

Clemson University

TigerPrints

All Dissertations

Dissertations

May 2020

Performance of Cross-Laminated Timber as a Residential Building Material Subject to Tornado Events

Michael W. Stoner

Clemson University, mwstone@g.clemson.edu

Follow this and additional works at: https://tigerprints.clemson.edu/all_dissertations

Recommended Citation

Stoner, Michael W., "Performance of Cross-Laminated Timber as a Residential Building Material Subject to Tornado Events" (2020). *All Dissertations*. 2639.

https://tigerprints.clemson.edu/all_dissertations/2639

This Dissertation is brought to you for free and open access by the Dissertations at TigerPrints. It has been accepted for inclusion in All Dissertations by an authorized administrator of TigerPrints. For more information, please contact kokeefe@clemson.edu.

PERFORMANCE OF CROSS-LAMINATED TIMBER AS A RESIDENTIAL
BUILDING MATERIAL SUBJECT TO TORNADO EVENTS

A Dissertation
Presented to
the Graduate School of
Clemson University

In Partial Fulfillment
of the Requirements for the Degree
Doctor of Philosophy
Civil Engineering

by
Michael Wallace Stoner
May 2020

Accepted by:
Dr. Weichiang Pang, Committee Chair
Dr. Patricia Layton
Dr. Thomas Cousins
Dr. Brandon Ross

ABSTRACT

Innovations in the use of wood as a structural material have included the invention of engineered wood products including Cross-Laminated Timber (CLT) for which markets are expanding. One such market is residential construction where many structures are built using light-frame construction techniques. These structures have shown vulnerabilities to hazards such as tornadoes; whereas, CLT has shown potential to withstand these hazards.

The project had two main components: an experimental test phase and an analytical phase. Results from experimental debris impact testing demonstrated that 3-ply CLT could reliably resist the debris associated with EF-2 and EF-3 level events while failing approximately 50% of the time when subject to EF-5 level hazards. CLT shear wall tests on assemblies with and without out-of-plane walls sought to quantify the performance of configurations that would likely be present in residential structures with more box-like geometries and behavior. In addition, it was determined that out-of-plane walls could resist the uplift forces that develop due to lateral loads. A simplified analytical method for determining the capacity of CLT shear wall assemblies was proposed based on the connection capacities of the assembly.

The analytical phase of the project included the development of a structural performance model for residential archetypes designed using CLT. Results from this study indicated that the archetypes experienced a 10% probability of failure in EF-4 events. In comparison, light-frame construction has shown vulnerabilities to EF-0 and EF-1 level events. In addition, the hazard assessment of light-frame structures based on historical

tornado data showed that significant portions of the United States exhibited a reliability index less than the target reliability described in ASCE 7-16, dropping to nearly 0% when built using CLT. A comparative cost analysis shows that for locations with high tornado hazard, it would take up to 100 years for CLT construction to be economically competitive with light-frame construction considering only the differences in upfront construction costs and tornado-induced losses.

Ultimately, CLT exhibits an increased level of performance compared to light-frame residential construction in tornado events. Further developments in the mass timber market could make such an alternative to light-frame construction more realistic.

DEDICATION

This work is dedicated to my wonderful, supportive, and loving wife, Rachel. Without her example of compassion, dedication, and faithfulness, I am sure I would be where I am today. I love you.

ACKNOWLEDGMENTS

I would like to thank the many people who have shaped my life both within and outside of the field of Civil Engineering. I thank my parents who opened my eyes to the curiosity and excitement that inspired my study of civil engineering. I thank my grandparents who gave me an example hard work and the showed me importance of time with family. I thank my brothers who inspired me to be better, work harder, and have fun. And to all my friends at Clemson, thank you for all the fun time together.

I thank my committee members who have been generous with their time and advice. To Dr. Layton, Dr. Ross, and Dr. Cousins who have each welcomed me into their home and showed incredible examples of passion for their field of study, thank you. To my advisor, Dr. Pang, I thank you for the time, dedication, patience, and understanding you have shown me the past 5 years.

I thank all the students who helped me discover my love for engineering. These include Graham Montgomery, Ross Phillips, Sara Albritton, Robert Gunter, Ben Reed, and many others who during my undergraduate time at Clemson, helped me every day. I also thank Eric Gu, Lancelot Reres, Bibek Bhardwaj, and others who helped with the completion of this research.

Finally, I would like to thank the sponsors of this research including the National Science Foundation, the U.S. Department of Agriculture, and Collum's Lumber for their support.

TABLE OF CONTENTS

	Page
TITLE PAGE.....	i
ABSTRACT.....	ii
DEDICATION.....	iv
ACKNOWLEDGMENTS	v
LIST OF TABLES.....	x
LIST OF FIGURES	xiii
1. INTRODUCTION	1
1.1 TORNADO HAZARDS.....	1
1.2 DEFINITION AND PROPERTIES OF CLT.....	2
1.3 SCOPE OF RESEARCH.....	4
1.4 REFERENCES.....	5
2. REVIEW OF RELEVANT STUDIES	7
2.1 TORNADO WIND DESIGN PROCEDURES.....	7
2.2 DEBRIS IMPACT TESTING PROCEDURES AND STUDIES	12
2.3 CROSS-LAMINATED TIMBER PRODUCTION AND DESIGN	24
2.4 STRUCTURAL PERFORMANCE MODELING.....	39
2.5 TORNADO HAZARD ESTIMATION	43
2.6 REFERENCES.....	45

TABLE OF CONTENTS (continued)

	Page
3. DEBRIS IMPACT PERFORMANCE OF CLT.....	51
3.1 INTRODUCTION:.....	52
3.2 EXPERIMENTAL TEST SETUP:.....	54
3.3 EXPERIMENTAL RESULTS:	59
3.4 DEVELOPMENT OF FRAGILITY CURVES:	70
3.5 CONCLUSIONS:.....	80
3.6 REFERENCES:.....	81
4. PERFORMANCE OF CLT SHEAR WALL ASSEMBLIES WITH OUT-OF- PLANE WALLS	83
4.1 INTRODUCTION.....	83
4.2 TEST BACKGROUND AND CONFIGURATION.....	84
4.3 CONNECTION TESTING AND HYSTERESIS PARAMETER DEVELOPMENT.....	86
4.4 FULL-SCALE TESTING	99
4.5 NUMERICAL MODELING	129
4.6 ANALYTICAL METHODOLOGY	135
4.7 CONCLUSIONS	139

TABLE OF CONTENTS (continued)

	Page
4.8 REFERENCES	140
5. STRUCTURAL PERFORMANCE MODEL OF RESIDENTIAL CLT	143
5.1 Introduction	144
5.2 Design of CLT Residential Archetypes.....	147
5.3 Determination of Tornado Wind Forces.....	152
5.4 Resistance of CLT Archetypes and Load Path Assumptions	157
5.5 Fragility Analysis of Residential Archetypes	164
5.6 Results of Fragility Analysis	169
5.7 Summary and Conclusions	178
5.8 References	180
6. HAZARD ASSESSMENT OF CROSS-LAMINATED TIMBER AND LIGHT- FRAME RESIDENTIAL CONSTRUCTION SUBJECT TO TORNADO HAZARDS	185
6.1 INTRODUCTION	186
6.2 TORNADO SIMULATION AND HAZARD QUANTIFICATION	188
6.3 COST ESTIMATION OF CLT RESIDENTIAL STRUCTURES	192
6.4 PERFORMANCE OF RESIDENTIAL WOOD STRUCTURES	195

TABLE OF CONTENTS (continued)

	Page
6.5 RISK ASSESSMENT OF CONTIGUOUS UNITED STATES.....	205
6.6 CASE STUDIES	209
6.7 CONCLUSIONS	214
6.8 REFERENCES.....	215
7. SUMMARY, CONCLUSIONS, AND RECOMMENDATIONS.....	219
7.1 SUMMARY OF STUDY.....	219
7.2 CONCLUSIONS	220
7.3 LIMITATIONS AND RECOMMENDATIONS OF FUTURE WORK ...	225
APPENDIX A: Detailed Debris Impact Testing Results.....	229
APPENDIX B: NDS Connection Capacity of Half-Lap Connection.....	253
APPENDIX C: Individual Fragilities for CLT Panels in Residential Archetypes	256
APPENDIX D: Wall and Roof Panel Parameters.....	274
APPENDIX E: CLT Design	276

LIST OF TABLES

Table	Page
Table 2.1: Increases in Design Loads using Tornado Factors (ASCE, 2016)	10
Table 2.2: Fujita/Enhanced Fujita Scale Correlation to 3-sec Gust Wind Speed (FEMA P-908)	11
Table 2.3: Tornado missile impact criteria for experimental debris impact testing	16
Table 2.4: Composition factors, k, for solid wood panels (Blass and Fellmoser 2004).....	28
Table 2.5: K_s values for different loading scenarios (Gagnon and Pirvu, 2011)	30
Table 2.6: Damage states for residential construction	42
Table 3.1: Number of failures for each failure mode and panel configuration tested.....	61
Table 3.2: Experimental test results of panel-to-panel connections	70
Table 3.3: Number of tests in each bin used to develop experimental fragility curves.....	73
Table 3.4: Lognormal parameters for experimentally derived fragility curves	74
Table 4.1: Peak values from monotonic tests of Simpson SD10212.....	87
Table 4.2: MSTEW parameters for AE 116 connectors in uplift and shear	95
Table 4.3: Stiffness estimates for dowel type fasteners in NDS and Eurocode.....	98

LIST OF TABLES (continued)

Table	Page
Table 4.4: Estimates of strength and stiffness of hold-down and screws not directly tested.....	98
Table 4.5: MSTEW Parameters for HD12, SDS25300, and SDWS 22800DB.....	99
Table 4.6: Instrumentation outline for shear wall assembly tests.....	102
Table 4.7: Results of stiffness tests performed on wall assembly 1	108
Table 4.8: Displacement procedure for destructive testing of wall assemblies.....	109
Table 4.9: Peak force and displacement of wall tests	110
Table 4.10: Description of member in <i>Timber3D</i> model.....	131
Table 4.11: Reference Allowable design loads for AE 116 connections	133
Table 4.12: ASD capacities and applied unit shear required to reach capacities in wall assembly 1 and 2.....	136
Table 4.13: Comparison of experimental and analytical deflection calculations	138
Table 5.1: Description of residential archetypes.....	148
Table 5.2: Material properties used for structural design of CLT elements	151
Table 5.3: Summary of values used in wind analysis.....	155
Table 5.4: External pressure coefficients, GC_P , used in wind analysis for structure Type 1	155
Table 5.5: Reference ASD loads for bracket-type connector	160

LIST OF TABLES (continued)

Table	Page
Table 6.1: Enhanced Fujita scale and corresponding wind speeds.....	187
Table 6.2: Targets size to determine tornado hazard	189
Table 6.3: Summarized cost information (Burback and Pei, 2017).....	193
Table 6.4: Degree of damage descriptions for one- and two-family residences.....	196
Table 6.5: Lognormal distribution parameters for light-frame and CLT construction	198
Table 6.6: Lognormal distribution parameters relating wind speed and area of roof failure	199
Table 6.7: Target reliability for load conditions that do not include earthquake, tsunami, or extraordinary events (ASCE, 2016).....	202
Table 6.8: Percentage of US by area with reliability index less than given value	207
Table 6.9: Tornado hazard equation coefficients for case study locations	210
Table 6.10: Summary of 1-year, 50-year, and 100-year P_F and β for Huntsville, AL	212
Table 6.11: Analysis of loss for comparison of light frame and CLT construction	213

LIST OF FIGURES

Figure	Page
Figure 1.1: Typical layout of 3-ply CLT	3
Figure 2.1: Typical debris generated from an EF3 tornado (FEMA, 2007)	14
Figure 2.2: Windborne debris damage from a 2x6 framing element	15
Figure 2.3: Impact locations for framed wall types (ICC, 2013).....	20
Figure 2.4: Impact resistance as a fraction of prescribed missile impact momentum	22
Figure 2.5: Panel layup for calculation of composition factors, k	28
Figure 2.6: Beam modeling using shear analogy method (Gagnon and Pirvu. 2011).....	29
Figure 2.7: Rocking (A), Sliding (B), Shear (C), and Bending (D) deformations	31
Figure 2.8: Simplified Kinematic Model for Lateral Load Resistance of CLT Panels.....	33
Figure 2.9: Half-lap (a) and surface spline (b) connections.....	36
Figure 2.10: Dowel-type connections between perpendicular mass timber elements	36
Figure 2.11: Metal bracket connections between perpendicular mass timber elements	37
Figure 2.12: Concealed beam hangers utilizing steel plates drilled into beam ends.....	37

LIST OF FIGURES (continued)

Figure	Page
Figure 2.13: Hurricane loss estimation method in HAZUS-MH (Vickery et al. 2006).....	41
Figure 2.14: Annual probability of exceedance for EF5 tornado in United States (Fan 2019).....	44
Figure 3.1: Pneumatic cannon used for experimental debris impact testing	55
Figure 3.2: Experimental test setup of (a) weak- and (b) strong-connection orientation.....	56
Figure 3.3: Experimental test setup of weak- and strong-axis orientations.....	56
Figure 3.4: Missile tracking process for determination of missile velocity.....	57
Figure 3.5: Panel-to-panel connections: half-lap (a) and surface spline (b).....	58
Figure 3.6: Measurement of missile penetration (a) and permanent deflection (b) after missile impact.....	59
Figure 3.7: Failure modes: perforation (a), permanent deflection (b), and dislodgement (c)	60
Figure 3.8: Relationship between missile penetrations and missile momentum (passed tests only).....	63
Figure 3.9: Relationship between backside deflection and missile momentum (passed tests only).....	64
Figure 3.10: Relationship between missile penetration and kinetic energy (passed tests only).....	65

LIST OF FIGURES (continued)

Figure	Page
Figure 3.11: Relationship between backside deflection and kinetic energy (passed tests only).....	66
Figure 3.12: Relationship between damage measurements and kinetic energy(all tests)	67
Figure 3.13: Relationship between damage measurements and missile momentum (all tests)	68
Figure 3.14: Damage photos of panel-to-panel connection tests.....	70
Figure 3.15: An example of the fragility curve analysis procedure.....	72
Figure 3.16: Plotted fragility curves for impact location.....	75
Figure 3.17: Plotted fragility curves for axis orientation.....	76
Figure 3.18: Plotted fragility curves for connection orientation.....	77
Figure 3.19: Fragility curve with missile speed as intensity measure for various debris masses	79
Figure 4.1: Simpson SD10212 screw tested in shear.....	87
Figure 4.2: Results of monotonic lateral test of Simpson SD10212 screws.....	87
Figure 4.3: Deformed shape of screw tested monotonically in shear	88
Figure 4.4: Test setup of uplift tests of AE 116 shear brackets	89
Figure 4.5: Monotonic and cyclic uplift response of AE 116 connector	90
Figure 4.6: Monotonic uplift testing failure.....	91
Figure 4.7: Cyclic uplift testing failure.....	92

LIST OF FIGURES (continued)

Figure	Page
Figure 4.8: Monotonic and cyclic shear response of AE 116 connector	93
Figure 4.9: Connector rotation and fastener shear typical of shear deformation of AE 116	94
Figure 4.10: Comparison of deformed shape after cyclic loading (left) with undeformed shear bracket (right)	94
Figure 4.11: Modified Stewart (MSTEW) hysteretic rule to describe connection behavior.....	95
Figure 4.12: SDWS screws used in connection between in-plane and out-of- plane walls	96
Figure 4.13: Simpson HD12 hold-down used in testing.....	97
Figure 4.14: Schematic setup of experimental test with out-of-plane walls.....	100
Figure 4.15: Schematic of experimental test setup with only in-plane walls	101
Figure 4.16: Instrumentation plan of wall assemblies	103
Figure 4.17: Progression of stiffness tests: in-plane only, one out-of-plane wall, two out-of-plane walls (top to bottom).....	105
Figure 4.18: Displacement time history procedure used to determine initial stiffness of wall assemblies	106
Figure 4.19: Force-displacement response of stiffness tests on wall assemblies.....	107

LIST OF FIGURES (continued)

Figure	Page
Figure 4.20: Force-displacement response of wall assemblies with and without out-of-plane walls.....	110
Figure 4.21: Measured deformations of string pots at displacement peaks for wall test with out-of-plane walls	112
Figure 4.22: Measured deformation of string pots at displacement peaks for wall test with in-plane walls only	113
Figure 4.23: Uplift of wall assembly in test with return walls	114
Figure 4.24: Uplift of wall assembly in test with in-plane walls only	115
Figure 4.25: Panel-to-panel displacement for wall test with out-of-plane walls	116
Figure 4.26: Panel-to-panel displacement for wall test with in-plane only walls.....	117
Figure 4.27: Sliding deformations at top and bottom of wall for wall test with out-of-plane walls.....	118
Figure 4.28: Sliding deformations at top and bottom of wall for wall test with in-plane walls only	119
Figure 4.29: Deformed shape of wall test with out-of-plane walls.....	120
Figure 4.30: Deformed shape of wall test with in-plane walls only	121
Figure 4.31: Failure of half-lap connection examined after wall assembly removal.....	122
Figure 4.32: Failure of AE116 connections at the bottom of in-plane walls.....	123

LIST OF FIGURES (continued)

Figure	Page
Figure 4.33: Failure of AE116 connections at the top of in-plane walls	124
Figure 4.34: Deformation of SD10212 screws used in AE116 connection	125
Figure 4.35: Deformation of AE116 at the top of out-of-plane wall	126
Figure 4.36: Deformations in connection between in-plane and out-of-plane walls.....	127
Figure 4.37: Crushing of wood at half-lap joint between in-plane wall	128
Figure 4.38: Timber3D representation of wall assemblies experimentally tested.....	130
Figure 4.39: Modified Stewart parameters taken from tests and estimation	132
Figure 4.40: Comparison of stiffness tests to Timber3D model.....	134
Figure 4.41: Comparison between experimental results and Timber3D model for wall assemblies 1 and 2	135
Figure 4.42: Shear of designated resisting elements in shear wall assembly 1 (left) and 2 (right)	137
Figure 5.1: Archetypes used in study of CLT residential structures (dimensions in m).....	148
Figure 5.2: Panel layout of structure 1	151
Figure 5.3: Representation of bracket-type connections used in simulations.....	159
Figure 5.4: Experimental uplift test data (top) and MSTEW hysteretic model rules (bottom)	163

LIST OF FIGURES (continued)

Figure	Page
Figure 5.5: Framework for development of fragility functions	165
Figure 5.6: Examples of panel fragilities developed for structure 1	170
Figure 5.7: Wall, roof, and system fragilities for structures 1, 3, and 5	171
Figure 5.8: Wall, roof, and system fragilities for structures 2, 4, and 6	172
Figure 5.9: Variation in performance based on change in spacing of bracket- type connections for structure 1	173
Figure 5.10: Variation in performance based on change in spacing of screw connections for structure 4	174
Figure 5.11: Simulated performance of all structure types compared to light- frame construction	178
Figure 6.1: Annual probability of experiencing EF-0 or greater for point size target (0.098 km ²)	190
Figure 6.2: Example of fitted asymptotic hazard curves, (left) log-log scale, and (right) linear scale.	192
Figure 6.3: Weighted average city cost index factor for locations in the United States.....	194
Figure 6.4: Estimated cost of CLT residential structure per square meter	195
Figure 6.5: Fragility analysis of light-frame and CLT residential structures showing probability of total structure failure	198

LIST OF FIGURES (continued)

Figure	Page
Figure 6.6: Relationship between wind speed and roof area failure for light-frame construction	200
Figure 6.7: Reliability index for light-frame (a) and CLT (b) residential construction subject to tornado hazards	206
Figure 6.8: Probability density function of reliability index for light-frame and CLT residential structures.....	207
Figure 6.9: Time before net present cost is equal for light-frame and CLT construction	209
Figure 6.10: Tornado hazard for case study locations	210
Figure 6.11: Hazard of tornado hazard and pdf of failure for CLT and light-frame for Huntsville, AL	211
Figure 6.12: Estimated cost due to initial construction and estimated tornado loss for case study locations	214

CHAPTER ONE

INTRODUCTION

1.1 TORNADO HAZARDS

Using engineering principles to design structures to withstand natural hazards has always had two distinct objectives, achieving the desired level of performance and creating a solution that remains economically cost-competitive. Innovation in structural materials has led to the development of new materials that have potential to achieve these two objectives. Exploring a new building material includes understanding the material limits and response to hazards as well as the opportunities to implement the material in different construction types. Tornadoes present a unique challenge both in terms of understanding the structural loads that develop due to the wind and predicting the occurrence of such storms. Tornadoes are violently rotating columns of air with wind speeds that can approach 134 m/s (300 mph) and form when warm and cold air interact to form these columns of air (Jones et al. 2001). Tornadoes have seen an increase in the insured and total losses due to their violent nature and lack of warning time as the average lead time before a storm hits can be as low as 15 minutes (KBRA, 2019). Unlike hurricanes, the affected area from a tornado is relatively smaller but often has generally more severe impact. Currently, around 1,200 tornadoes occur annually and cause anywhere from 20-60 deaths per year on average (NOAA, 2020). A significant amount of the insured and uninsured loss in tornado events come from damage to residential structures primarily built using wood framing techniques (Ellingwood and Rosowsky, 2004). The hazards associated with tornadoes can take the form of wind-induced pressures and windborne debris impact. The wind speeds in excess

of 89 m/s (200 mph) combined with the drop-in pressure in the center of the tornado vortex can impart pressures well above the capacity of residential structures. In the event of a tornado, hazardous material can be transported by the wind at speeds approaching 100 mph and impact the exterior of a structure endangering the occupants and potentially compromising the structural system. Current typical residential construction techniques have been shown to have vulnerabilities when subjected to these types of loads associated with tornado hazards.

1.2 DEFINITION AND PROPERTIES OF CLT

Cross-Laminated Timber (CLT) is an engineered wood panel typically consisting of three, five, or seven layers of dimension lumber oriented at right angles to one another and glued to form structural panels with high strength, dimensional stability, and rigidity. These properties make it suitable to resist loads associated with the hazards of tornadoes and hurricanes. A typical layout of a 3-ply CLT panel is shown in Figure 1.1 where three layers of solid sawn lumber are glued to create the solid panels. The resulting panels can be customized to produce large wall and floor panels that are versatile in the manufacture and application.



Figure 1.1: Typical layout of 3-ply CLT

In addition to CLT, there exist other engineered wood products that combine, through glue or mechanical fasteners, individual pieces of lumber to form panels, beams, and columns. These elements are commonly known as mass timber products and are characterized by the use of large wood panels. Other types of mass timber products include Nail-Laminated Timber (NLT), Glue-Laminated Timber (GLT), Dowel-Laminated Timber (DLT), and Massive Plywood Panels (MPP). Each of these products present their own benefits and advantages for use in construction and are worth exploring for their use as a construction material. For mass timber products, it is the task of engineering research to understand the behavior of these materials when subjected to the hazards of a given event and explore their potential to serve as a viable construction material. In the past

several decades, research has been done in an effort to understand the structural properties of CLT; however, gaps still exist in the knowledge that is needed to fully benefit from its advantages, especially in regard to the hazards associated with tornadoes.

1.3 SCOPE OF RESEARCH

The advantages of Cross-Laminated Timber and other mass timber products include the rigidity, material properties, and ability to be integrated with a light frame system. These benefits indicate the potential to resist the hazards associated with tornadoes in residential settings where wood construction materials are already utilized. As mentioned, much of the damage and loss due to tornadoes occurs in residential structures, so it is of interest to study the potential of CLT and other mass timber products to be used in such situations to resist the hazards of tornadoes. This includes determining the response of these products to debris impact loads and estimating their performance when subjected to the wind-induced pressures associated with tornadoes. The objectives presented in this study are as follows:

1. To determine the resistance to debris impact loads from a 2x4 for 3-ply Cross-Laminated Timber. This includes developing fragility curves which estimate the probability of failure given the physical properties of the 2x4 missile.
2. To investigate the lateral performance of CLT in a residential scenario. This includes the experimental lateral testing of a series of CLT wall elements to determine the influence of various connection types and out-of-plane walls common in low-rise and residential structures.

3. To review the literature on the design of CLT and develop archetype designs for residential structures based on design principles outlined in the National Design Specifications (NDS) and associated research and to develop a tornado structural performance models based on the developed archetypes which includes both the vertical and lateral load paths for CLT. The model will subject the various archetypes to tornado induced wind loading and debris impact loading using Monte Carlo Simulation to estimate performance.

4. A tornado simulation database (Fan and Pang, 2019) will be utilized to conduct a hazard assessment of residential structures subjected to tornadoes. This includes investigating the reliability and risk experienced by these structures when based on the geographic variation in the hazard associated with tornadoes as well as the differences in cost between light-frame and CLT residential structures due to upfront costs and tornado induced loss.

1.4 REFERENCES

Davies-Jones R., Trapp R.J., Bluestein H.B. (2001) Tornadoes and Tornadic Storms. In:

Doswell C.A. (eds) Severe Convective Storms. Meteorological Monographs.

American Meteorological Society, Boston, MA

Kroll Brand Rating Agency. (2019, March 28). KBRA Releases Insurance Research:

Insured Losses Rising for Tornadoes. Retrieved May 19, 2019. Retrieved from

<https://www.marketwatch.com/press-release/kbra-releases-insurance-research->

[insured-losses-rising-for-tornadoes-2019-03-28.](https://www.marketwatch.com/press-release/kbra-releases-insurance-research-)

- National Oceanic and Atmospheric Administration. (2020). Monthly and Annual U.S. Tornado Summaries. Retrieved January 14, 2020. Retrieved from <https://www.spc.noaa.gov/climo/online/monthly/newm.html#latestmts>.
- Ellingwood, B. R., & Rosowsky, D. V. (2004). Fragility Assessment of Structural Systems in Light-Frame Residential Construction Subjected to Natural Hazards. Structures 2004. doi: 10.1061/40700(2004)119
- Fan, F., & Pang, W. (2019). Stochastic Track Model for Tornado Risk Assessment in the U.S. *Frontiers in Built Environment*, 5. doi: 10.3389/fbuil.2019.00037
- Fan, F., (2019). "Tornado Hazard Analysis for the United States using a Stochastic Track Simulation Model." All Dissertations.

CHAPTER TWO

REVIEW OF RELEVANT STUDIES

2.1 TORNADO WIND DESIGN PROCEDURES

Naturally occurring events like tornadoes and hurricanes can cause several different types of hazards which must be considered in structural design. These hazards include wind-induced pressures, dynamic impact loads from flying debris, flooding hazards, and falling hazards from other damaged or fallen structures. In each case, these hazards can be difficult to quantify, but design and test standards have outlined the best practices to provide resistance suitable to provide life safety. Currently wind-induced pressures from straight-line hurricane winds are discussed in Chapters 26-31 of ASCE 7-16, *The Minimum Design Loads for Buildings and Other Structures* (ASCE, 2016). Two main procedures are used address the design of the main wind force resisting systems (MWFRS): the Envelope Procedure (Chapter 27) and the Directional Procedure (Chapter 26). Both methods are used to convert the 3-sec gust speed at 10 m (33 ft) above the ground in exposure category C. ASCE 7-10 provides the value of the 3-sec gust speed for the locations in the United States and its territories. The directional procedure converts the 3-sec gust wind speed, V , into a velocity pressure, q_z , through Equation 2.1.

$$q_z = 0.00256K_zK_{zt}K_dK_eV^2 \quad (2.1)$$

The velocity pressure exposure coefficient, K_z coefficient is meant to modify the pressure based on the height of the structure or the point along the structures at which the pressure is desired. The topographic factor, K_{zt} , modifies the pressure based on the effects of the terrain at isolated hills, ridges, and escarpments and is often set to unity unless

specific information is known about the topography of the site. The directionality factor, K_d coefficient is meant to modify the pressure based on the likelihood that a design level wind event aligns with the worst-case building aerodynamics (Laboy et al. 2012). The velocity pressure is further modified to a designed wind pressure, p , using Equation 2.2.

$$p = qGC_p - q_i(GC_{pi}) \quad (2.2)$$

This equation calculates the design wind pressures as a function of q , which is equal to q_z for windward walls located at a height z above the ground and equal to q_h for leeward walls, sidewalls, and roofs evaluated at the mean roof height, h . It is also a function of q_i , which can be taken conservatively as q_h . Finally, the velocity pressures are modified by the gust-effect factor, G , the external pressure coefficient, C_p , and the internal pressure coefficient, GC_{pi} . The gust-effect is meant to account for the “decorrelation of wind gusts over the size of the structure” (ASCE, 2016) and is set to a value for 0.85 for rigid buildings using these procedures. Alternative procedures are outlined by previous research to more accurately calculate the gust-effect factor for rigid buildings (Solari and Kareem 1998). The external pressure coefficient relates the design wind pressure to the external surface based on its location on the structure and its geometry relative to the wind. Finally, the internal pressure coefficient accounts for the difference in pressure between the outside and inside surface of the structural elements and is taken as both a positive and negative value. The internal pressure is set based on the enclosure classification of the structure. The possible enclosure classifications are enclosed, partially enclosed, partially open, and open and are based on the area of the openings in the exterior of the structure. Once the design wind pressure, p , is calculated for all surfaces and required wind directions, the structural

elements can be designed based on engineering principles and the applicable standard practices for design.

It is important to note that these procedures are meant to address straight-line wind only and not the wind-induced loads from tornadoes. In the case of pressures induced from a tornado event, there is also a significant load caused by the change in atmospheric pressure inducing a significant uplift on the structure. To indirectly account for these effects, the commentary of Chapter 26 describes two procedures for calculating the pressures due to a tornado event. The Extended Method modifies the wind pressure parameters (K_z , K_d , G) to calculate the increased pressures expected from a tornado. The exposure category used to determine K_z is set to exposure category C, the directionality factor is set to 1.0, and the gust-effect factor is increased to 0.9. For components and cladding loading, a reduction in the overall loading is permitted of 10% due to the relatively short duration of tornadoes. The typical components and cladding loads are calculated based on an event duration taken as 1-hour. Due to the high translational speed and relatively small impact area, tornadoes can have a duration of only a few minutes or even seconds. It is recommended that the structure be considered partially enclosed and the GC_{pi} value be taken as ± 0.55 due to the likelihood of a breach of the building envelope in a tornado.

Because the Extended Method requires the adjustment of many of the factors used in the Directional Procedure, the Simplified Method was developed to allow for the use of a single parameter to consider the effect of tornado induced wind loading. This factor is known as the tornado factor, TF , and was primarily developed based on research using a

tornado simulator and comparing the measured pressure coefficients to those calculated by ASCE 7-10 (ASCE, 2010). The factors are calculated based on a partially enclosed structure in exposure category C using a 9.14 m by 9.14 m (30-ft by 30-ft) building with mean roof height of 22-ft and 35° gable roof (Haan et al. 2010). The calculated tornado factors, TF , are applied to Equation 2.2 to give the following:

$$p = q_i \left(GC_p - (GC_{pi}) \right) \times TF \quad (2.3)$$

The tornado factors recommended by ASCE 7-16 are shown in Table 2.1 and vary based on the exposure category, enclosure classification, and whether they are applied to the Main Wind Force Resisting System (MWFRS) or to Components and Cladding (C&C).

Table 2.1: Increases in Design Loads using Tornado Factors (ASCE, 2016)

Original Enclosure Classification	Loading	Original Exposure B	Original Exposure C or D
Partially enclosed buildings	MWFRS	1.8	1.2
	C&C	1.6	1.1
Enclosed buildings ^a	MWFRS	2.5	1.6
	C&C	2.1	1.5

A final method for developing the design wind pressures from the wind velocity is outlined in FEMA P-361, *Safe Rooms for Tornadoes and Hurricanes: Guidance for Community and Residential Safe Rooms* (FEMA 2015) and ICC 500, *Standard for the Design and Construction of Storm Shelters* (ICC, 2013). Like the Extended Method, the guidance of FEMA P-361 modifies the wind pressure parameters, namely the wind directionality factor, K_d , to 1.0. The remaining calculations are the same as those outlined in the directional procedure from Chapter 27 of ASCE 7. It is also noted that the enclosure classification should be set to partially enclosed, regardless of the opening area within the

structure or safe room. Finally, FEMA recommends that all anchorage and connection be designed using the loads calculated the components and cladding procedures in Chapter 30 of ASCE 7 with the adjustments mentioned previously.

Calculating the pressures from wind at a given speed presents one challenge that is handled through the procedures outlined above; however, estimating the wind speed from a tornado can be another challenge. As it can be very difficult to directly measure the velocity of the wind in a tornado event, the Enhanced-Fujita scale is used to classify tornado intensity based on measures of the damage observed after the event. The original Fujita scale developed in 1971 by Dr. Tetsuya T. Fujita was correlated to the 3-sec gust speed used in the design process outlined by previously through post-tornado assessments. This scale was updated to the Enhanced Fujita scale in 2004 to improve the estimate of the 3-sec gust wind speeds (TTU, 2006) shown in Table 2.2.

Table 2.2: Fujita/Enhanced Fujita Scale Correlation to 3-sec Gust Wind Speed (FEMA P-

Fujita Scale	Fujita Scale: 3-Second Gust (mph)	EF Scale	EF Scale: 3-Second Gust (mph)
F0	45–78	EF0	65–85
F1	79–117	EF1	86–110
F2	118–161	EF2	111–135
F3	162–209	EF3	136–165
F4	210–261	EF4	166–200
F5	262–317	EF5	Over 200

mph = miles per hour; EF = Enhanced Fujita

While these estimates have been shown to relate the intensity of a tornado to its peak wind speed, they are empirically derived and based on damage assessments. Currently, there are Damage Indicators (DI) that categorize structures by use and type of structure. For each DI, there exists a set of damage descriptions with an assigned number termed the degree of damage (DOD). Each DOD corresponds to an EF-scale value and

subsequently to a 3-second gust wind speed. From this procedure, a given structure can be assigned a DI based on its construction and use, and after a tornado event, assigned a DOD based on the damage. The collection of corresponding EF-scale values for the given DOD are used to approximate the wind speed. In a comparison of code wind pressures to tornado induced wind pressures, an increase of up to 150% was measured in uplift pressures in the tornado simulator when compared to the ASCE 7-05 calculation procedures (Haan et al. 2010).

2.2 DEBRIS IMPACT TESTING PROCEDURES AND STUDIES

Another critical design objective is to protect a structure from windborne debris impact. Currently, ASCE 7-16 refers to ASTM E1886 and ASTM E1996 (ASTM, 2013; ASTM, 2014) as the primary standards for testing materials against debris impact loads. For a building's glazing elements to be subject to these ASTM standards, they must fall into either of the following categories: the structure is within 1 mile of coastal mean high water line with basic wind speed greater than or equal to 130 miles per hour, or the structure is within an area with a basic wind speed greater than or equal to 140 miles per hour. Once a structure is categorized as requiring glazing protection, it must pass the criteria outlined by the ASTM standards which indicate the missile type, weight, and velocity. For structures which are to be considered a "safe-room" there is additional direction given by FEMA P-361 and ICC 500. Because these documents address more than just the glazing, there are various impact locations to be tested and larger missile weights and speeds. Additionally, the failure criteria changes to match the failure modes of the wall material. Following these guidelines attempts to provide "near-absolute protection from the deadly

winds and wind-borne debris associated with extreme-wind events.” (FEMA 2015) In addition to the danger that wind-borne debris directly presents to the occupants of the structure, any breach in the building envelope can lead to an increased structural load due to pressurization. Continued research and observation are needed to further refine the procedures that have been outlined. The relatively violent and short duration of tornado events, precisely measuring their effects is difficult despite advances in wind load modeling. After tornado events, comparison between numerical models and observed damage needs to occur to further develop and refine the design procedures.

2.2.1 Development of Windborne Debris Impact Testing Standards

The debris produced by tornadoes and hurricanes is typically classified into three categories: small, medium, and large (FEMA 2015). Small debris can be roof aggregate or shingles, small tree limbs, or bricks. Medium debris can be appliances, longer framing members, wood sheathing, and roof coverings. Large debris is typically steel columns, roof trusses, large vehicles, and large trees. The standards for debris impact loading of safe rooms covered in FEMA P-361 are sufficiently conservative for small and medium debris loads, but the loads generated by excessively large debris may exceed the design procedures outlined for safe rooms and storm shelters. Typical debris associated with a tornado can be seen in Figure 2.1 where small, medium, and large debris was produced from an EF-3 tornado in Kansas in 2007 (FEMA, 2007).



Figure 2.1: Typical debris generated from an EF3 tornado (FEMA, 2007)

Post-tornado investigation led to the decision to use a 6.8 kg (15-pound) 2x4 as a representative missile (FEMA, 1999). It was considered particularly hazardous because it has a relatively high mass and small impact area and are commonly seen as medium sized debris in tornadoes. Following the tornadoes in Kansas and Oklahoma that occurred in 1999, observations of the damage showed significant damages in structures including existing storm shelters due to windborne debris (FEMA, 1999). Some of the debris observed in these events included 2x4 and 2x6 lumber that penetrated both wall assemblies and roof assemblies as shown in Figure 2.2. The debris associated with hurricane hazards led to the development of ASTM E1996 which requires the experimental debris impact testing of horizontal and vertical structural elements (roofs and walls) using a 9-pound 2x4

that is approximately 9-feet long at velocities at approximately 55 mph. Additionally, small steel balls are also used to imitate the small debris associated with hurricane hazards. These testing standards were first adopted in the 2000 edition of the *International Building Code* (ICC, 2000).



Figure 2.2: Windborne debris damage from a 2x6 framing element

The debris impact testing standards developed and implemented in the 2000 edition of the IBC were meant to reduce the damage from debris in hurricanes. FEMA P-361 was concerned more with occupant safety; therefore, a significantly higher level of performance was required for use in safe rooms and storm shelters. Furthermore, the relationship between the wind speeds and missile had not been extensively studied, so the assumption was made that for a design wind speed of 112 m/s (250 mph), the speed of a 6.8 kg (15-pound) 2x4 would approach 44.7 m/s (100 mph). In addition, the speed of debris on a

horizontal surface (roof) would be two thirds of the speed of the debris on a vertical surface (wall). The full table of debris speeds and associated EF level that is used for the design of safe rooms in FEMA P-361 is shown in Table 2.3.

Table 2.3: Tornado missile impact criteria for experimental debris impact testing

SAFE ROOM DESIGN WIND SPEED	MISSILE SPEED (OF 15-POUND 2X4 BOARD MEMBER) AND SAFE ROOM IMPACT SURFACE
250 mph	Vertical Surfaces: 100 mph Horizontal Surfaces: 67 mph
200 mph	Vertical Surfaces: 90 mph Horizontal Surfaces: 60 mph
160 mph	Vertical Surfaces: 84 mph Horizontal Surfaces: 56 mph
130 mph	Vertical Surfaces: 80 mph Horizontal Surfaces: 53 mph

Table notes: Walls, doors, and other safe room envelope surfaces inclined 30 degrees or more from the horizontal should be considered vertical surfaces. Surfaces inclined less than 30 degrees from the horizontal should be treated as horizontal surfaces.

In addition to the recommendations put forth in FEMA P-361 and ASTM E1996 other jurisdictions have addition or supplementary requirements for the debris impact performance of building materials. Most notably, Miami-Dade County in Florida references Testing Application Standards (TAS) 201, 202, and 203. TAS 201 *Large and Small Missile Test Standards*, TAS 202 *Uniform Structural Load Standards*, and TAS 203 *Uniform Cyclic Pressure Test Standards* are the standards that are required for product approval in Miami-Dade County. Testing according to these standards are further described in the Florida Building Code High Velocity Hurricane Zone test standard located in Chapter 16 Section 26 of the Florida Building Code. The required debris impact testing uses a 4.1 kg (9-pound) 2x4 travelling at 15.2 m/s (34 mph). This testing is required for “all parts or systems of a building or structure envelope such as, but not limited to, exterior walls, roof, outside doors, skylights, glazing and glass block shall meet impact test criteria or be protected with an external protection device that meets the impact test criteria”

(Florida Building Code, 2017). In addition to the large missile impact tests which require a 4.1 kg (9-pound) 2x4, small missile impact tests are required for assemblies and construction materials used 9.14 m (30 feet) above the ground elevation for any structure types. Small missiles impact tests use 10 steel balls having a mass of approximately 2 grams (0.07 oz) and measuring 7.9 mm (5/16 in) in diameter and are fired at a speed of 40 m/s (88.6 mph). Additional cyclic pressure testing is required for all assemblies per the TAS 203 standard.

The purpose of these debris impact testing standards varies per their application. The recommendations of FEMA P-361 and ICC 500 are meant to provide safety to the occupants against the most extreme tornado events, while the testing recommended by ASCE 7-16 and the Florida Building Code are meant to limit the damage from less severe hurricane events. Ultimately, it is difficult to accurately predict the debris that is likely in a tornado or hurricane event as it is a product of the neighboring structures, surrounding debris sources, and the exposure of the terrain. In addition, a windborne missile can be described by its mass, shape, velocity, angle of impact, and any additional movement at impact such as rotation. The magnitude of a missile's intensity can be quantified by the velocity of the missile, the momentum of the missile, or the energy of the missile. Based on whether the collision between the missile and the wall or roof assembly is largely elastic or inelastic, the momentum or kinetic (or impact) energy may be more suitable to quantify the intensity. The factors that determine the behavior of such collisions include the stiffness of the resisting system being impacted, the stiffness of the missile, the support conditions of the assembly being tested, and the material properties of the members

involved in the collisions. A missile's momentum is given by Equation 2.4 where the weight of the mass of the missile, m , is multiplied by its velocity, v . The kinetic (or impact) energy of a missile is calculated by equation 2.5 where the energy is the product of half of the missile's mass and velocity squared.

$$I = m \times v \quad (2.4)$$

$$KE = \frac{1}{2} \times m \times v^2 \quad (2.5)$$

The magnitude of the force that is imparted on the assembly being tested is a function of the amount of time it takes to decelerate the missile. In addition, the level of inelastic deformation and level of plasticity of the collision will affect the magnitude of the imparted force. Tests that measured the impulse of a 1.81 kg (4-pound) 2x4 striking a rigid impact plate travelling at 9.38 m/s (21 mph) produced a peak force approaching 44.5 kN (10,000-pounds) (Sciaudone 1996). At low missile velocities, impacts from a 2x4 have been observed to be relatively inelastic as the impulse, or change in momentum is closer to the initial momentum. As the missile velocity increases, the collisions become more elastic as the impulse becomes closer to twice the initial missile momentum. In all cases, the experimental tests fall between perfectly elastic and perfectly inelastic as crushing of the wood fibers in the missile. Due to the complex nature of the force transfer and mechanics of the collisions, it can be difficult to use a static or pseudo-static force to describe or predict the response of a given wall assembly and therefore typically requires vigorous experimental testing.

Research has attempted to quantify the debris risk and model the windborne debris, but many of these models are heavily based on assumptions of the debris generation and

surrounding conditions. An early implementation of the windborne debris risk assessment model for residential structures utilized wind-field models, wind-borne debris generation, impact, and trajectory (Twisdale et al. 1996). A simplified version of this model was ultimately used in the HAZUS-MH, a multi-hazard loss prediction model for earthquakes, hurricanes, floods, and other natural hazards. Additional debris risk models were developed to better understand and predict the behavior of windborne debris in high wind hazards, but still rely heavily on assumptions of the surrounding terrain and structures (Grayson et al., 2013, Lin et al., 2010). All models that have been created and standards for testing that have been put into practice make an effort to assure a level of performance that has been correlated to a level of hazard based largely on the empirical observations of events that produce windborne debris.

2.2.2 Experimental Debris Impact Setup, Testing, Results, and Analysis

The experimental test setup for debris impact testing is described in the associated testing standards, ASTM E1996, FEMA P-361, ICC-500 and TAS 201. Each of these standards require that a representative wall assembly be tested at a size of at least 4-foot by 4-foot. In addition, the boundary conditions should be representative of the conditions expected in its constructed state. The missile used for the testing is a Southern Yellow Pine 2x4 with a mass as dictated by the testing standard (usually 4.1 kg or 6.8 kg). Standards dictate that the missile's speed must also be measured by measurement devices that have a tolerance of 0.305 m/s (1 ft/s) (ICC, 2013) or have a calibrated speed measurement device like a high-speed camera with a frame rate of at least 500 frames per second (Florida Building Code, 1994). The cannon permitted for use in firing the missile must be either

pneumatically powered or elastically powered through elastic bands. The missile should not be accelerating upon impact due to the force of gravity and should be normal to the face of the assembly being tested. The location of the impacts is also controlled by the applicable standard and is meant to test the most vulnerable areas on the wall assembly. For most wall types, this includes impacts at the panel center, near the edge or any seam in the panel, and in the corner of the panel as shown in Figure 2.3 (ICC, 2013).

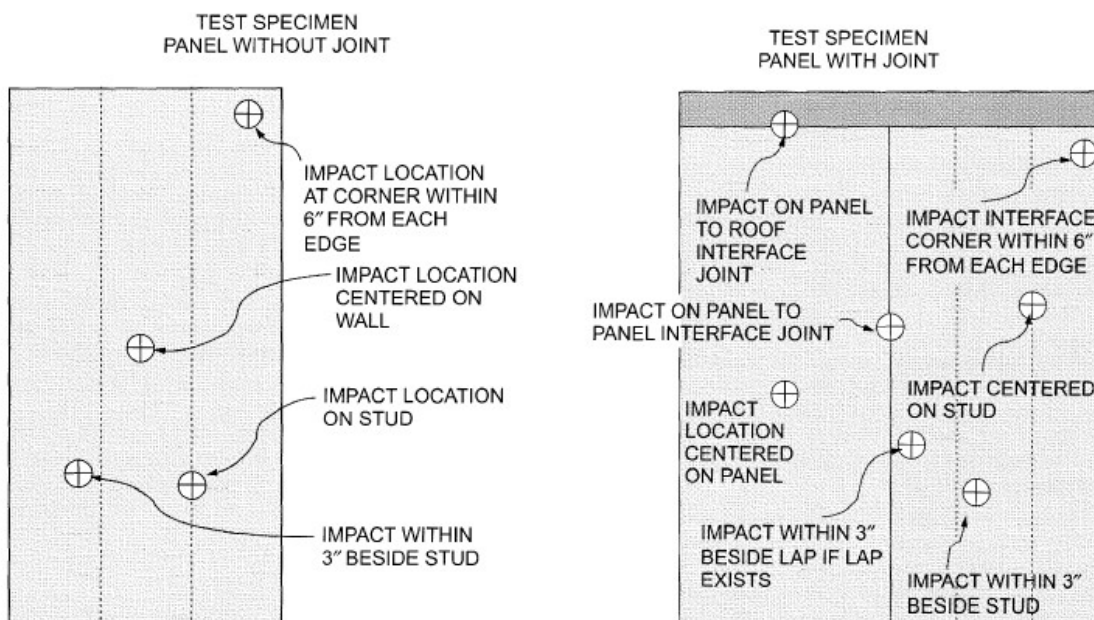


Figure 2.3: Impact locations for framed wall types (ICC, 2013)

The results of experimental debris impact tests are interpreted based on the applicable standard used to test them. Wall assemblies that are intended for use in safe rooms and storm shelter are subject to the descriptions of failure in ICC 500 and FEMA P-361 and are meant to ensure almost complete safety to the occupant. In ASTM E1996, the pass/fail performance is measured in terms of the opening in the assembly that is created by the windborne debris. ICC 500 defines failure any one of the following: perforation of the

missile, dislodgement of any components of the assembly that could pierce a 311 N (70-lb) piece of kraft paper installed within 5-inches of the test surface, spalling of the interior surface of the assembly, or permanent deformation of the assembly greater than 7.62 cm (3 in).

Experimental debris impact testing has been performed to these standards for many different building materials. The windborne debris impact resistance of residential glazing was determined experimentally through a series of impact tests (National Association of Home Builders, 2002). Traditional wall assemblies were studied through experimental debris impact tests conducted at Clemson University in 2000 for the Federal Emergency Management Association (FEMA) to compare the performance of traditional wall assemblies and composite assemblies. The study reported the fraction of impact momentum of a missile prescribed by the ICC 500 standards shown in Figure 2.4 and concluded that the impact resistance of a composite material was approximately equal to the sum of the experimentally calculated impact resistance of each layer.

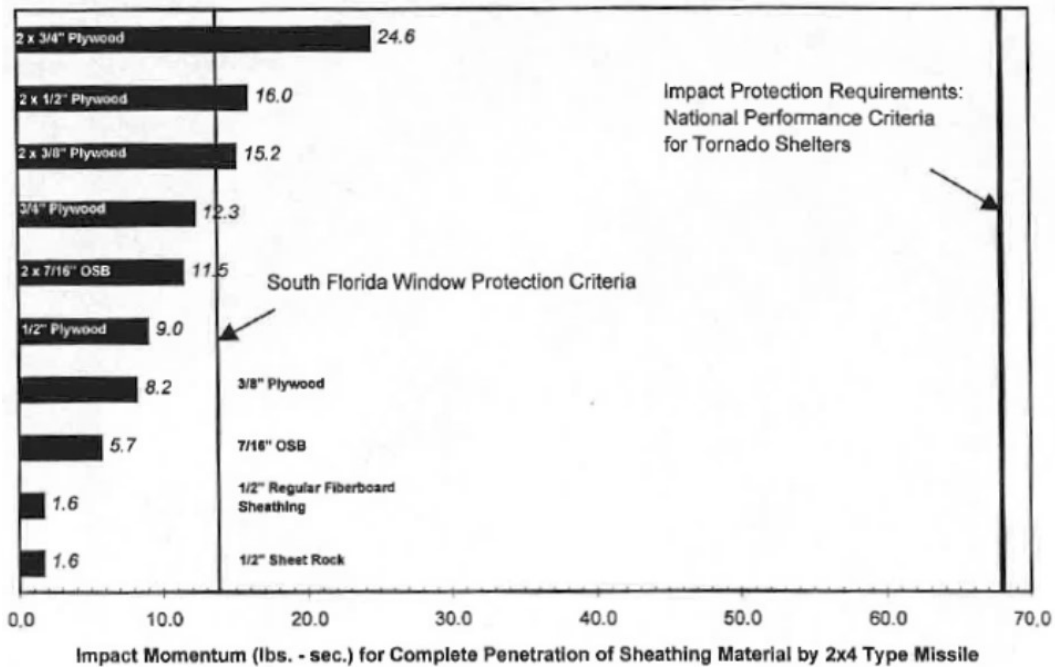


Figure 2.4: Impact resistance as a fraction of prescribed missile impact momentum

Many assemblies were tested at the Wind Science and Engineering Research Center at Texas Tech University from traditional reinforced concrete to masonry, to plywood wood assemblies, to composite wood and concrete or wood and steel sections. The tested assemblies were reported with a threshold missile speed, or missile speed of a 6.8 kg (15-pound) 2x4 that caused failure. Detailed, test-by-test reports with damage description is also reported in the final report which included additional testing by Florida A&M University, Florida State University, and the University of Florida (Texas Tech University, 2006). The results of these tests showed that traditional framing techniques are not capable of stopping a 2x4 missile at 23.7 m/s (53 mph). While the testing performed at Texas Tech University provided valuable information about the performance of wall assemblies, it only reported the threshold speed for which the wall assembly would fail an impact test. In these cases, the variability of the response of the various assemblies is not captured. Where

more information about the response of a structural material to various loadings is desired, fragility functions can be used. Fragility functions for structural performance are typically modeled using a lognormal distribution with a cumulative distribution function given by Eq. 2.6 where the probability of failure, $F(x)$ is given by the standard normal cumulative distribution function, Φ ; the logarithmic mean, μ ; and logarithmic standard deviation, σ for a given intensity measure, IM.

$$F(x) = \Phi \left[\frac{\ln(IM) - \mu}{\sigma} \right] \quad (2.6)$$

Fragilities have been created for residential construction types that consider the response to both wind-induced pressures and debris impact loading (Amini 2012, Alphonso 2014, and Maloney 2018). Analytical, numerical, and empirical approaches are also used in the creation of these fragility curves in order to reduce the number of physical experiments required. The benefits of these models include the expanded understanding of the material being tested, but they can often require significant additional modeling and experimental testing to develop confidence in their capabilities. Current standard practice remains to test the debris impact resistance of the building assemblies through experimental testing that corresponds to the guidelines of the standard describing the desired use of the material.

By experimentally testing the resistance to debris impact loads of CLT, information about the response and the behavior of the assemblies will be obtained. In addition, by quantifying the variation in performance using fragility curves, probabilistic models can

be developed that account for this variation and more accurately predict the response of CLT structures to tornado events.

2.3 CROSS-LAMINATED TIMBER PRODUCTION AND DESIGN

Cross Laminated Timber (CLT) was introduced as a building material in the early 1990s in Austria and Germany and has begun to gain popularity in North America as it offers a combination of structural performance and environmental benefits (Karacabeyli and Douglas, 2013). It has shown potential to serve as a sustainable and efficient material to resist the loads associated with tornadoes. A unified Canadian and United States performance and production standard for CLT was written in 2015 and updated in 2017 and 2018. *PRG-320, Standard for Performance-Rated Cross-Laminated Timber* provides information about the manufacturing tolerances in addition to the mechanical properties of CLT.

2.3.1 Manufacturing of Cross-Laminated Timber

The process of manufacturing CLT requires three main steps: surface preparation, gluing or bonding, and pressing. To begin, each piece of lumber must be planed to provide a surface free from anything detrimental to the gluing process. Adhesives used in the United States are subject to the requirements of *ANSI 405-Standard for Adhesives for Use in Structural Glued Laminated Timber* and *Department of Commerce Voluntary Product Standard PS 1-07* Section 6.1.3.4, a voluntary standard for structural plywood. The pressing stage of manufacturing is subject to the requirements of the specific adhesive used by the manufacturer. Several glues are used in pressing of CLT panels including Melamine Formaldehyde (MF), Phenol Resorcinol Formaldehyde (PRF), Polyurethane (PUR) and

Emulsion Polymer Isocyanate (EPI) all of which require a pressure of 1034 kPa (150 psi). Each of these glues have been used in the pilot study of Cross-Laminated Timber at Clemson University (Gu, 2015). Once panels have been pressed, they are typically cut to the custom sizes required by design. Using computer numeric controlled (CNC) cutting tools, openings are cut in the walls and floor panels. Panels can then be shipped to the construction site in the order in which they are to be placed by a crane leading to a relatively fast construction speed. Because the structural members can be cut to requires a high degree of coordination with other trades such as mechanical, electrical, and plumbing. The size of CLT panels are generally limited by the size of the trucks that transport material to a job site and the press size of CLT manufacturers in North America is typically around 3.05 m by 12.2 m (10 feet by 40 feet).

Currently, there are several producers of CLT in North America that have received product qualification from the Engineered Wood Product Association (APA) based on the requirements of *PRG-320*. Some of these include Structurlam Mass Timber Corporation, Freres Lumber Co., Inc (Massive Plywood Panels), D.R. Johnson Wood Innovations, Nordic Structures, and SmartLam, LLC. There are also more than a dozen manufacturers of CLT in Europe, some of whom supply North America with additional panels for construction projects. Three of the top producers in Europe include Stora Enso, Bienderholz, and KLH Massivholz. Additional manufacturers have begun to manufacture and build with CLT in Australia and Asia.

2.3.2 Gravity Design of Cross-Laminated Timber

There have been significant strides that have been made in the United States in mass timber research of these structures in both design and construction. The regulation of the performance of CLT in PRG-320 (APA, 2018) and NDS 2018 (AWC, 2018) gives production standards and design values and equation for gravity loads. These standards also address the design values for bending, modulus of elasticity, tension, compression, and shear for both the major and minor directions. Using these values, or those provided by the manufacturer, the traditional design procedure can be followed to determine the capacity and deflection of CLT subject to out-of-plane loading. An additional document published by FPInnovations and the Binational Softwood Lumber Council called *The CLT Handbook* gives an outline for the process of manufacture of CLT and provides comments and examples of structural design, lateral design, and connection design of CLT. Further information is also provided on the topics of vibration design, fire design, sound performance, and building enclosure detailing.

The gravity design of mass timber structures has become a relatively standard practice for mass timber products, specifically CLT and involves calculating three distinct quantities: bending, shear, and deflection. The stress limits for bending (F_b) and shear (F_v) are based on the grade and species of the wood used to create the CLT panels. For each of the bending, shear, and deflection calculations, the determination of the effective section properties presents the unique challenge in the design of CLT. A variety of methods have been used to determine the effective bending stiffness, EI_{eff} , including the “Mechanically Jointed Beams Theory” also known as the Gamma Method (EN 2004), the “Composite

Theory” also known as the K-method (Blass and Fellmoser 2004), and the “Shear Analogy” method (Kreuzinger 1995).

The “Mechanically Jointed Beam Theory” exists in Annex B of Eurocode 5 and calculates the effective beam stiffness based on the efficiency of the connection between layers represented by γ , with $\gamma=1$ representing a rigid connection between layers and $\gamma=0$ representing no connection between layers. This approach provides a closed form solution only to simply supported uniformly loaded beams, but differences for non-uniformly loaded scenarios are acceptable (Ceccotti 2003). The gamma factor is calculated through Equation 2.7 where E is the modulus of elasticity, A is the area of the cross section, s_{eff} is the effective fastener spacing of the connection between the layers, n is the number of rows of connectors, K is the stiffness of the spacing, and L is the span of the composite member.

$$\gamma_i = \left(1 + \frac{\pi^2 E_i \times A_i \times s_{eff}}{n \times K \times L^2}\right)^{-1} \quad (2.7)$$

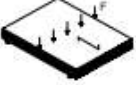
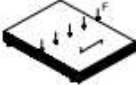
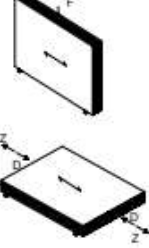
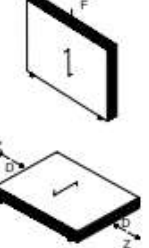
The effective bending stiffness, EI_{eff} , can then be taken as the application of the parallel axis theorem where the added term due to the distance between the centroid and the neutral axis is modified by the gamma term and is presented in Equation 2.8. Furthermore, the distance between each layer and the centroid of the, a_i , is the distance between the centroid of the composite shape and the centroid of layer i .

$$EI_{eff} = \sum_{i=1}^n (E_i I_i + \gamma_i E_i A_i a_i^2) \quad (2.8)$$

The “Composite Theory” or K-method predicts the section properties by calculated modification factors, or k-factors, depending on the loading orientation of the panels and the modulus of elasticity of each layer. In this method, the modulus of elasticity perpendicular to grain (E_{90}) is equal to the modulus of elasticity parallel to grain (E_0)

divided by 30. The calculation of these factors is shown in Table 2.4 and Figure 2.5. This method does not account for the shear deformations that are present under load and is typically only used for high span to depth ratios.

Table 2.4: Composition factors, k , for solid wood panels (Blass and Fellmoser 2004)

	k_i
	$k_1 = 1 - \left(1 - \frac{E_{90}}{E_0} \right) \cdot \frac{a_{m-2}^3 - a_{m-4}^3 + \dots \pm a_1^3}{a_m^3}$
	$k_2 = \frac{E_{90}}{E_0} + \left(1 - \frac{E_{90}}{E_0} \right) \cdot \frac{a_{m-2}^3 - a_{m-4}^3 + \dots \pm a_1^3}{a_m^3}$
	$k_3 = 1 - \left(1 - \frac{E_{90}}{E_0} \right) \cdot \frac{a_{m-2} - a_{m-4} + \dots \pm a_1}{a_m}$
	$k_4 = \frac{E_{90}}{E_0} + \left(1 - \frac{E_{90}}{E_0} \right) \cdot \frac{a_{m-2} - a_{m-4} + \dots \pm a_1}{a_m}$

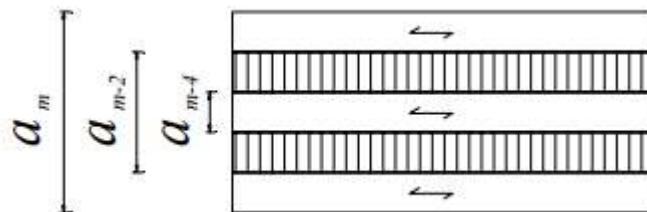


Figure 2.5: Panel layout for calculation of composition factors, k

The “Shear Analogy” is considered the most precise method for calculating the section properties of CLT (Blass and Fellmoser 2004). The characteristics of the multi-layer CLT cross section by separating the beam into two flexural beams, A and B. Beam A is the contribution of the flexural stiffness of each individual layer along its own neutral axis, and Beam B is given the flexural stiffness of the increase due to the distance between the neutral axis of each layer and the composite shape. In addition, Beam A is assigned an infinite shear stiffness, and Beam B is assigned the shear stiffness of the panel. The beam modeling is shown schematically in Figure 2.6.

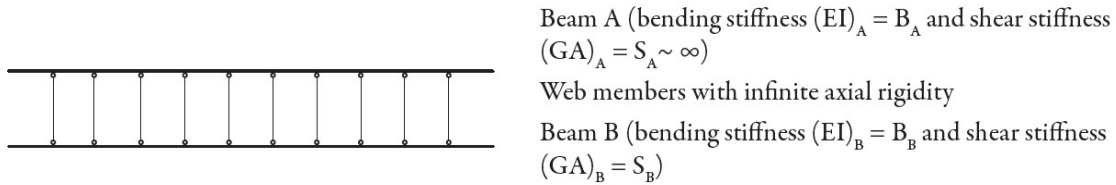


Figure 2.6: Beam modeling using shear analogy method (Gagnon and Pirvu. 2011)

The effective shear stiffness can be calculated using Equation 2.9 where h_i is the depth of layer i , b is the width of the section being considered, G_i is the shear modulus of layer i , and a is the distance between the centroid of the first layer and the centroid of the last layer.

$$GA_{eff} = \frac{a^2}{\left[\left(\frac{h_1}{2G_1b} \right) + \left(\sum_{i=2}^{n-1} \frac{h_i}{G_i b_i} \right) + \left(\frac{h_n}{2G_n b} \right) \right]} \quad (2.9)$$

The effective stiffness, EI_{eff} , can be calculated using the parallel axis theorem shown in Equation 2.10. This method is the same as the “Mechanically Jointed Beam Theory” except that $\gamma = 1$.

$$EI_{eff} = \sum_{i=1}^n (E_i I_i + E_i A_i a_i^2) \quad (2.10)$$

In the “Shear Analogy” the effective flexural stiffness is reduced to account for shear deformations. This yields the apparent bending stiffness, EI_{app} , from which the deflection of a uniformly loaded simply supported beam can be calculated. The equation which combines the effective flexural stiffness and the flexural shear stiffness is shown in Equation 2.11 where K_s is a constant that is derived based on the influence of the shear deformations. A variety of loading scenarios have been derived and are shown in Table 2.5.

$$EI_{app} = \frac{EI_{eff}}{1 + \frac{K_s EI_{eff}}{GA_{eff} L^2}} \quad (2.11)$$

Table 2.5: K_s values for different loading scenarios (Gagnon and Pirvu, 2011)

Loading	End Fixity	K_s
Uniformly distributed	Pinned	11.5
	Fixed	57.6
Concentrated at midspan	Pinned	14.4
	Fixed	57.6
Concentrated at quarter points	Pinned	10.5
Constant moment	Pinned	11.8
Uniformly distributed	Cantilevered	4.8
Concentrated at free-end	Cantilevered	3.6

In addition to determining the stiffness and associated deflection of CLT members, the effective bending stiffness is used to derive the effective section modulus, S_{eff} , shown in Equation 2.12. The effective section modulus is multiplied by the limiting bending stress, F_b , and a factor of 0.85 for conservatism as well as all appropriate adjustments per NDS to determine the moment capacity of the CLT section, M .

$$S_{eff} = \frac{2EI_{eff}}{E_1 h}; \quad M = 0.85F'_b S_{eff} \quad (2.12)$$

Finally, a simplified method for calculating the shear strength out of plane is used to calculate an effective $(Ib/Q)_{eff}$ shown in Equation 2.13 where the effective bending stiffness is divided by the product $E \times h \times z$ for half of the total layers. Often this calculation is performed by the manufacturer and the shear strength of the panel is reported directly.

$$(Ib/Q)_{eff} = \frac{EI_{eff}}{\sum_{i=1}^{n/2} E_i h_i z_i} \quad (2.13)$$

2.3.3 Lateral Design of Cross-Laminated Timber

While the gravity design of CLT elements has been codified, the lateral design procedure has not been standardized; however, there have been numerous tests attempting to quantify the resistance of CLT to lateral loads. In the calculation of the deflection due to shear forces, there are four factors that contribute to the result: rocking, slip, shear, and bending shown schematically in Figure 2.7. Because the CLT panels are relatively rigid in comparison to the connections, their response to lateral loads is controlled largely by the connections between the panels and the adjacent structural panels and the rocking or sliding deflection mechanisms. These are also the mechanisms through which ductility is ensured in the system in seismic applications where ductility is vital to a predictable and safe response of the structure.

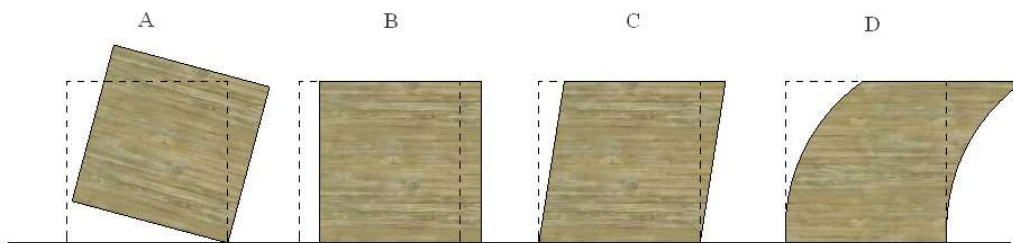


Figure 2.7: Rocking (A), Sliding (B), Shear (C), and Bending (D) deformations

In the case where rocking and sliding deflections are the most important contributions to the total deflection of the CLT wall under lateral load, it is important to understand the behavior of the connections used to transfer the vertical uplift forces and the horizontal shear forces. Different methods are assumed to simplify the statics of the shear force resolution at the base of the wall panel. The kinematic model of a CLT wall panel shown in Figure 2.8 is the method suggested by the CLT Handbook matching suitably the tests performed at FPInnovations (Popovski 2010). This model assumes rotation about the bottom corner of the panel, neglecting the compressive stresses that could include buckling out-of-plane and compression perpendicular to grain. For this simplified calculation, it is also assumed that there is no relative lateral slip between the wall and the ceiling/floor assemblies (Pei 2013). The resisting force of a wall at lateral displacement, D , is given by equation 2.14 where l_i , d_i , and f_i are the location, displacement, and force for connector i ; L , H , and G are the length, height, and gravity load for the entire panel.

$$F(D) \sum_{i=1}^n \frac{l_i}{H} f_i(d_i) + \frac{L}{2H} G \text{ and } d_i = \frac{l_i}{H} D \quad (2.14)$$

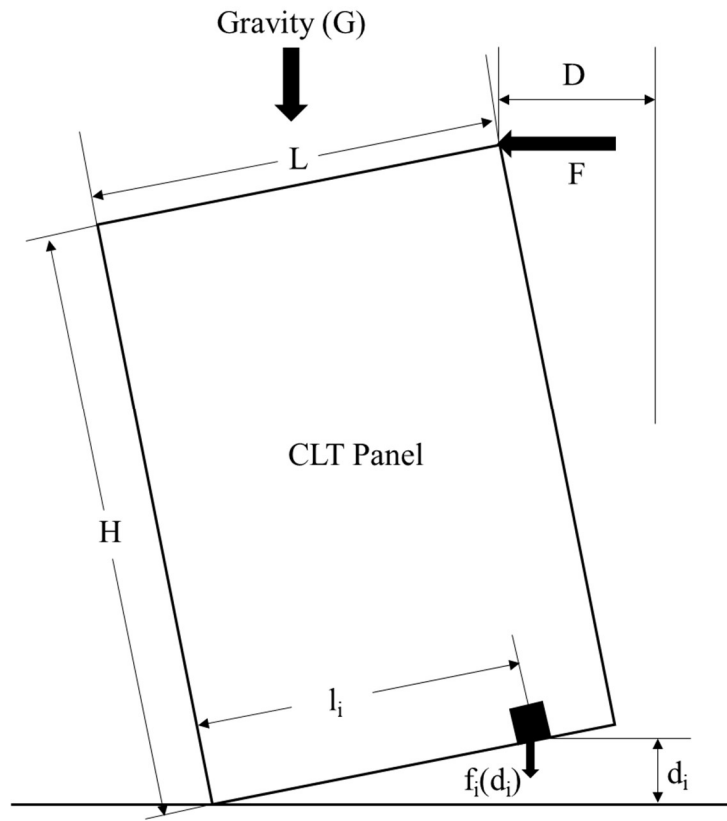


Figure 2.8: Simplified Kinematic Model for Lateral Load Resistance of CLT Panels

Other calculation methods consider connectors as either resisting uplift or lateral loads instead of both and assumed a zone of compression rather than rotation around a point. Still others include the contributions of panel bending, panel shear, and sliding deformations (Lukacs et al., 2019). Many of the design procedures do not account for any effects of out-of-plane walls present in platform construction and likely contributing to the behavior in smaller mass timber structures; however, some work has been done to quantify these effects analytically (Shahnewaz, 2018). These methods include modifications for the deformations due to sliding and rocking as they are affected by the presence of connecting walls and ceiling/floor panels. While these tests provide some guidance to the design of

CLT panels, some require an understanding of the entire force-displacement response of connections as each connection is loaded based on its location and some are iterative processes. Others only require the peak strength of each individual connector and makes assumptions about their loading to lead to a deterministic strength calculation. There are additional methods used to calculate the stiffness of CLT panels but also require information about the force-displacement of the connections. One example of the deflection of a CLT shear wall is shown in Equation 2.15. In this equation, the shear wall deflection, δ_{sw} , is a function of the bending deformation, shear deformation, and connection slip. In this equation, the panel width, b_s , panel height, h , bending stiffness, EI_{eff} , and shear stiffness, GA_{eff} all play roles in the deflection equation. In addition, the connection slip at design loads for the horizontal connections, $\Delta_{nail\ slip, h}$, vertical connection, $\Delta_{nail\ slip, v}$, and hold downs, Δ_a are also required to calculate the anticipated deflection at the design shear load, v .

$$\delta_{SW} = \frac{576vb_s h^3}{EI_{eff}} + \frac{vb_s}{GA_{eff}} + 3\Delta_{nail\ slip, h} + 2\Delta_{nail\ slip, v} \frac{h}{b_s} + \Delta_a \frac{h}{\Sigma b_s} \quad (2.15)$$

This equation mimics the deflection equations present in the wood design standards (AWC 2018) for light-frame walls where the various forms of shear wall deflection are considered. For strength design, details about the connections to adjacent panels and panels above and below as well as the panel aspect ratio will likely be controlled by the NDS. Continued research on unique connection types and configuration would further seek to take advantage of the properties of CLT to serve as a lateral system.

2.3.4 Connections in Mass Timber

There are a variety of methods that have been used to connect mass timber elements to each other and to other structural members. The CLT Handbook outlines five types of connection in CLT construction:

- Panel-to-panel connections
- Wall-to-wall connections
- Wall-to-floor connections
- Roof-to-wall connections
- Wall-to-foundations connections

Of these connection types, they typically utilize two types of fasteners: dowel type fasteners like nails, self-tapping screws, and bolts and metal plate connectors like brackets, shear plates, or specialty beam hangers. There have also been specialty connectors developed in order to serve specific purposes as well as more traditional joinery that relies on wood bearing between elements. The dowel type connections that are common to mass timber products take many forms, but two of the more common are the half-lap and the surface spline shown in Figure 2.9. Additionally, dowel type connections are also used to connect perpendicular elements as shown in Figure 2.10. The design of these connections is governed by the fasteners (either screws or nails) connecting the pieces of wood. Their capacity is dictated by equations in the National Design Specification based on the European Yield Theory. Significant testing has also been performed on these types of connection to determine both their capacity and load-displacement behavior.

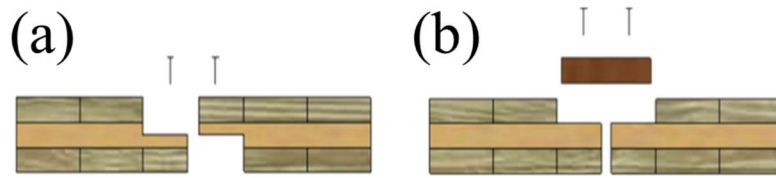


Figure 2.9: Half-lap (a) and surface spline (b) connections

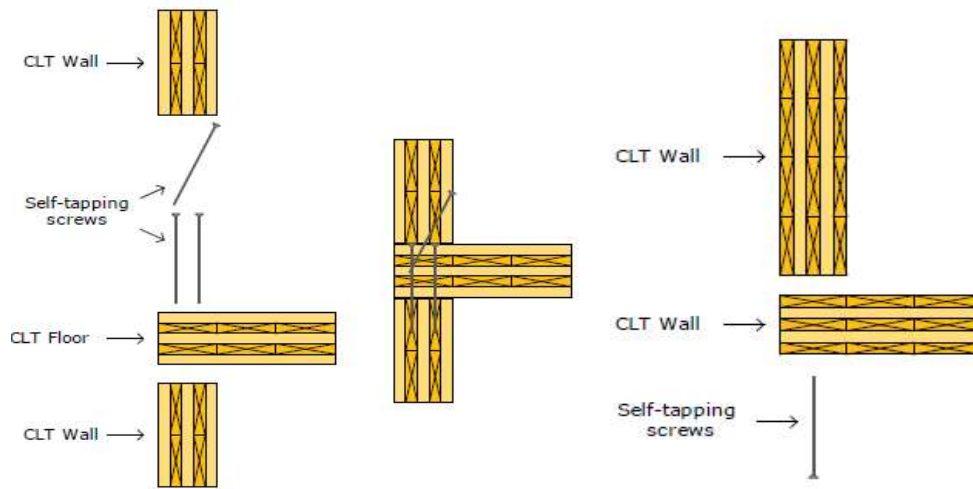


Figure 2.10: Dowel-type connections between perpendicular mass timber elements

There are many metal connection types utilized in mass timber structures that are used for many different purposes. Bracket type connections are frequently used to connect perpendicular elements such as walls to floor or perpendicular walls such as those shown in Figure 2.11. Concealed and partially concealed beam connections are also vital to the connection of mass timber beam members. They have taken many forms in order to provide structural performance and protect the connections from fire as they can be totally concealed as shown in Figure 2.12. Even proprietary products meant to connect mass timber in innovative ways have been developed. Continued innovation in the area of

connections will lead to more efficiently construction and cost-effective building solutions for mass timber.

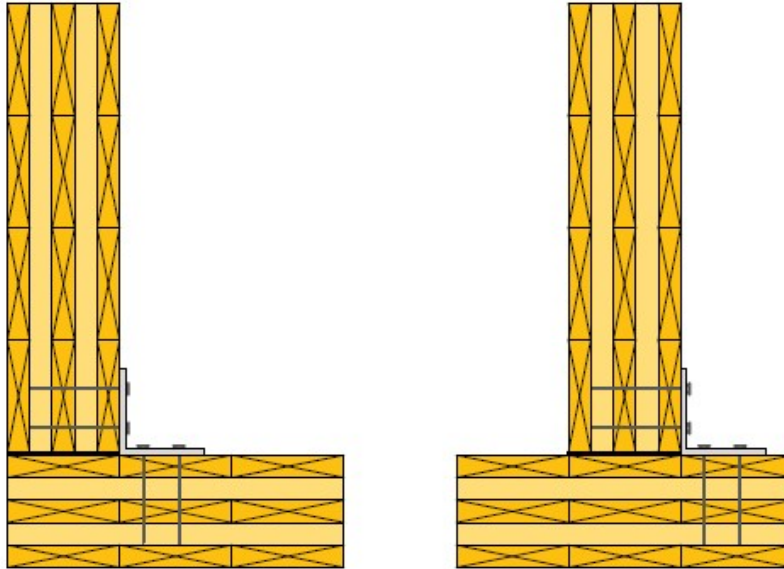


Figure 2.11: Metal bracket connections between perpendicular mass timber elements

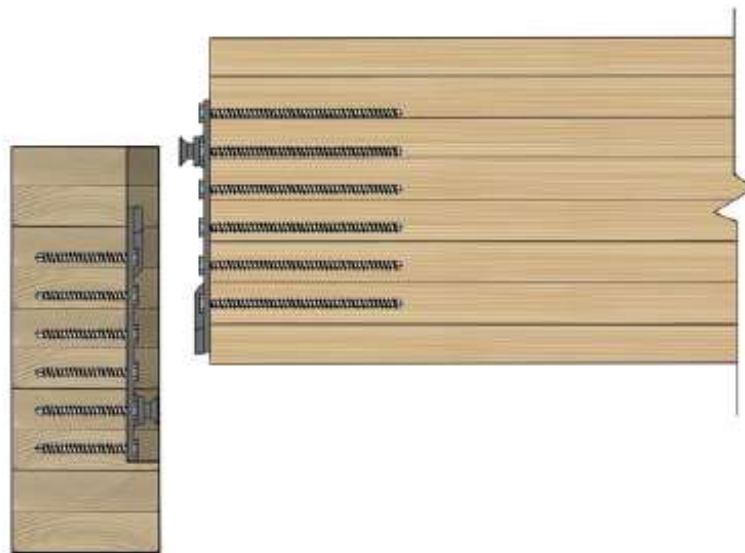


Figure 2.12: Concealed beam hangers utilizing steel plates drilled into beam ends

As connections continue to be developed and tested, their performance is crucial to the development of mass timber as a building material. Because the connections contribute so significantly to the deformation of mass timber lateral systems, their performance determines the factors used in design, especially with regards to seismic hazards. In addition, it becomes difficult to standardize the capacities and design parameters for each individual manufacturer, efforts have been made to develop design procedures for generic angle brackets (Amini et al. 2016; Pei et al. 2013). Eventually, the lateral design of mass timber elements including shear walls and diaphragms will be covered in the NDS.

Despite the advancements in understanding of the lateral performance of CLT assemblies, there exists a need for additional research and experimental testing. In order to further estimate the performance of residential CLT structures and their response to tornado events, information about the interaction between in-plane and out-of-plane walls is necessary. These interactions can be critical when it comes to the performance of residential structures where out-of-plane walls are common. While the work of Shahnewaz (2018) analytically addressed these configurations and experimental shake table tests were performed with the presence of out-of-plane walls (Amini, 2018), experimental testing has not taken place to directly quantify the effects these walls have on the strength and stiffness of the shear wall assemblies. Having the ability to analyze and predict that performance will lead to better design tools beyond the applications in residential CLT construction.

2.4 STRUCTURAL PERFORMANCE MODELING

Experimental testing often serves the purpose of determining the performance of components of a structural system whether that be the gravity resisting elements like floors and columns or the lateral resisting elements like shear walls and diaphragms. With the knowledge of the performance of the structural components, assumptions are made about both the load path and load distribution based on the distribution of applied forces and applied stiffness. Structural analysis programs such as SAP2000 and ETABS can be used to model the linear and non-linear stiffness of elements for a structure. These program aid in the design of structural elements through building codes and standards that are built into the program. These programs can be extremely useful in the design of structural elements and apply the appropriate safety factors and design methodologies. Additional modeling programs are used specifically for estimating the behavior of physical elements based on their material properties and the principles of the Finite Element Method. Well known programs such as ABAQUS or ANSYS are commonly used to perform Finite Element Analyses. Other open source programs are used for modelling various structural elements including OpenSees and Timber3D (Pang et al. 2012). OpenSees was developed primarily to explore the performance of structures subject to earthquake loads and was created through the National Science Foundation Pacific Earthquake Engineering Center (PEER). *Timber3D* is a 3D numerical software based in MATLAB that is meant to analyze the performance of wood structures using two-node, 12 degree-of-freedom frame elements that are connected using frame-to-frame (F2F) elements. Each of these programs deal with

explicit modelling of component strength and stiffness properties and their interaction to predict on a detailed level the response to the external inputs associated with hazards.

Other programs are meant to estimate the performance of structures subject to external loads based on probabilistic assumptions of material capacity and hazard demand. Most notably, HAZUS-MH is a multi-hazard software that predicts the performance of various structure types subject to hazards like hurricanes, floods, earthquakes, and tsunamis. The goal of HAZUS-MH is to estimate the physical, economic, and societal losses associated with these natural hazards based on Geographic Information Systems (GIS) technology that communicates the risk of hazards spatially due to the geography and risk of hazard. While programs like OpenSees, Timber3D, ABAQUS, and others give explicit response of a well-known structure with defined material properties and known loading scenarios, HAZUS-MH relies on the probabilistic risk of various hazards and the approximate performance of structures based on construction type and date as well as geography to determine the risk to larger regions.

HAZUS-MH predicts the performance of many building types and many construction materials. An overview of the hurricane methodology used is shown in Figure 2.13 where the performance or loss estimation models are created by modeling the hazard track and wind-field model to produce the pressures and expected loads on the structure. These loads are compared to the building resistance which is estimated based on the applicable building code used to design and construct the structure as well as the building

material used. The predicted failures are compared on a component basis with data collected in post-event surveys (Vickery et al. 2006).

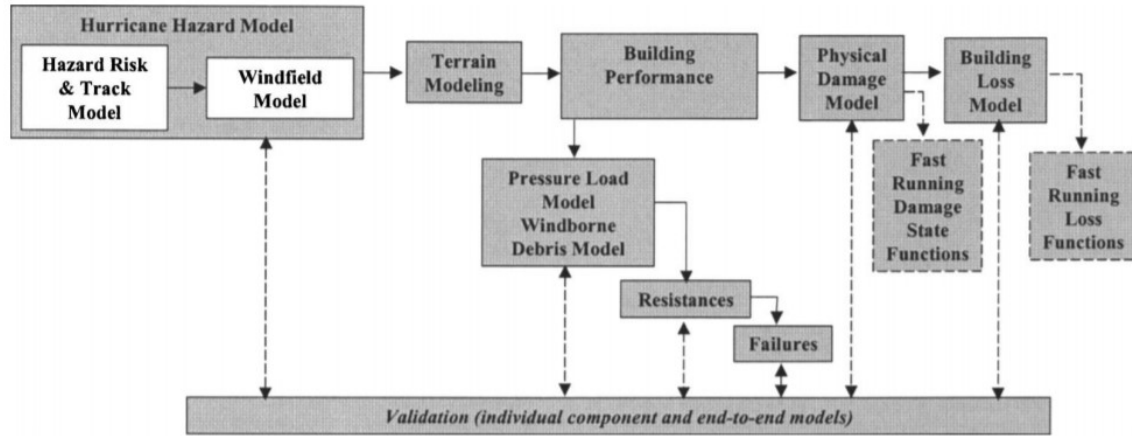


Figure 2.13: Hurricane loss estimation method in HAZUS-MH (Vickery et al. 2006)

When quantifying the performance of a given building stock it can be useful to quantify the various damage states that are observed to categorize the response into discrete states. For residential structures, HAZUS-MH quantifies the damage states as one of five categories of damage like the DOD indicators that are observed after a tornado event. For residential structures, the description of the damage state for each of the categories are described in Table 2.6 and include roof cover failure, window or door failures, roof deck failure, missile impacts to walls, roof structure failure, and wall structure failure. Based on the structural models that were produced assuming building geometry, terrain, structural details, and member capacities, fragility curves were developed that predict the probability of exceeding a specific damage state. Examples of the fragility curves developed for single story gable residential structures include curves for structures with 6d nails as roofing attachment relating the wind speed with an expected probability of failure. With a large database of similar fragility curves, the HAZUS-MH program can provide detailed

estimates of community level risk given a description of the types of buildings, surrounding terrain, and level of hazard for a given community.

Table 2.6: Damage states for residential construction

Damage State	Qualitative Damage Description	Roof Cover Failure	Window Door Failures	Roof Deck	Missile Impacts on Walls	Roof Structure Failure	Wall Structure Failure
0	No Damage or Very Minor Damage Little or no visible damage from the outside. No broken windows, or failed roof deck. Minimal loss of roof over, with no or very limited water penetration.	≤2%	No	No	No	No	No
1	Minor Damage Maximum of one broken window, door or garage door. Moderate roof cover loss that can be covered to prevent additional water entering the building. Marks or dents on walls requiring painting or patching for repair.	>2% and ≤15%	One window, door, or garage door failure	No	<5 impacts	No	No
2	Moderate Damage Major roof cover damage, moderate window breakage. Minor roof sheathing failure. Some resulting damage to interior of building from water	>15% and ≤50%	> one and ≤ the larger of 20% & 3	1 to 3 panels	Typically 5 to 10 impacts	No	No
3	Severe Damage Major window damage or roof sheathing loss. Major roof cover loss. Extensive damage to interior from water.	>50%	> the larger of 20% & 3 and ≤50%	>3 and ≤25%	Typically 10 to 20 impacts	No	No
4	Destruction Complete roof failure and/or, failure of wall frame. Loss of more than 50% of roof sheathing.	Typically >50%	>50%	>25%	Typically >20 impacts	Yes	Yes

Other research has attempted to take the methodologies developed for HAZUS-MH and apply them to the hazards associated with tornadoes. Studies have shown that a significant proportion of the damage from tornadoes occurs in residential structures (Ellingwood and Rosowsky 2004). In addition, deaths due to tornadoes are most likely to occur in mobile homes and permanent residential structures (Ashley 2007). Extensive studies have attempted to quantify the performance of residential structures, most of constructed using wood framing techniques when subjected to tornado hazards. Some have relied heavily on empirical data (Roueche et al. 2017, Alfano et al 2015) while other have performed detailed analysis of archetype residential structures using methodologies like those implemented in HAZUS. Conclusion by these studies suggest that light frame wood

construction experience median probabilities of failure in the EF-1 to EF-2 range. Empirically derived fragility curves by Roueche et. al exhibit a higher degree of uncertainty than those numerically derived by Amini et al. Those derived by Amini et al. referenced specific building geometries with general assumptions made about load path, construction techniques, and member spacing, while those developed by Roueche et al. were based on the observations in a post storm event.

As the techniques for analyzing the performance of various structure types and construction materials continue to evolve, it is useful to apply these strategies to a new material like Cross-Laminated Timber especially in situations where its structural properties lend itself to perform well when subject tornado hazards. Probabilistic models will be created based on the detailed component level results of previous experimental testing, experimental testing developed by this study, and assumptions about the load path associated with residential CLT structures subject to tornadoes. The goal of this portion of the study will be to estimate the response of residential CLT structures subject to a tornado event. This information will attempt to reliably predict the increase in safety associated with a CLT structure as compared to light-frame residential structures studied by previous research.

2.5 TORNADO HAZARD ESTIMATION

Research has been performed to study the nature of tornado hazards and their variance across the United States. Unlike the straight-line winds covered by the designed standards, the risk assessment of tornados is far less understood. During the period of 1950-2015, the United States experienced over 60,000 tornadoes, but because of the

localized nature, it is difficult to fully understand the hazard using only the raw historical data. Extensive work has been done to perform stochastic simulation of tornado tracks and parameters to create a database of 1 million years of simulated tornadoes (Fan and Pang, 2019). From this database, tornado hazard maps were created for the United States as shown in Figure 2.15. These maps relate the annual probability of exceedance to geographic locations in the United States based on the size of the target of interest. By fitting this data to a hazard curve, it can be coupled with the performance models developed for CLT structures.

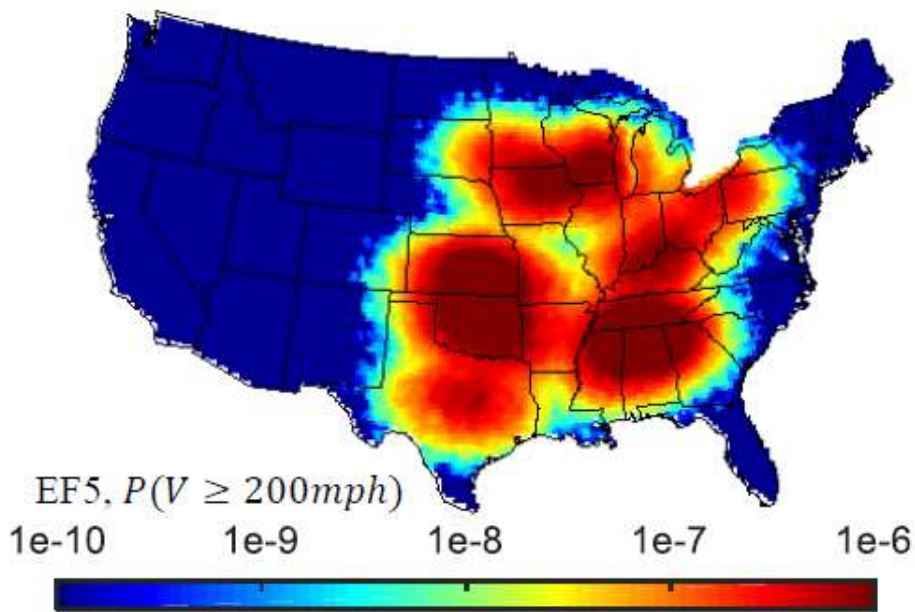


Figure 2.14: Annual probability of exceedance for EF5 tornado in United States (Fan 2019)

The hazard associated with tornadoes exhibits significant geographic variation, just as seismic hazards and hurricane hazards do. Using the database developed by Fan and Pang, analysis of the annual probability of failure of CLT structures and light-frame

structures can be predicted based on the results of the structural performance model and previous studies on the performance of light-frame. In addition to the annual probability, the reliability index can be used as a measure of the baseline level of safety targeted by the design codes. Detailed information about the hazard and the response to the hazard means that the estimated loss due to tornado events can be quantified and compared for CLT and light-frame structures.

2.6 REFERENCES

- ASCE. (2016). "Minimum design loads for buildings and other structures." Structural Engineering Institute, Reston, VA.
- Laboy, S. T., Kalisz, S., Gurley, K., & Masters, F. (2012). Considering the Directionality Factor in ASCE 7. *Advances in Hurricane Engineering*. doi: 10.1061/9780784412626.001
- Solari, G., and Kareem, A. (1998). "On the formulation of ASCE 7-95 gust effect factor." *J. Wind Eng. Indust. Aerodyn.*, Vols. 77–78, 673–684.
- ASCE. (2010). "Minimum design loads for buildings and other structures." Structural Engineering Institute, Reston, VA.
- Haan, F. L., Balaramudu, V. K., and Sarkar, P. P. (2010). "Tornado-induced wind loads on a low-rise building," *J. Struct. Eng.*, 10.1061/(ASCE)ST.1943-541X.0000093, 106–116.

- FEMA, (2015). Design and Construction Guidance for Community Safe Rooms. Second Edition. FEMA P-361. Federal Emergency Management Association, Washington, D.C., 374 pp.
- ICC/NSSA, (2013). Standard for the Design and Construction of Storm Shelters. International Code Council/National Storm Shelter Association. ICC 500. American National Standard Institute, Washington, DC.
- Texas Tech University, (2006.) A Summary Report on Debris Impact Resistance of Building Assemblies.
- ASTM, 2013. Standard Test Method for Performance of Exterior Windows, Curtain Walls, Doors, and Impact Protective Systems Impacted by Missile(s) and Exposed to Cyclic Pressure Differentials. ASTM E1886, West Conshohoken, PA.
- ASTM, 2014. Standard Specification for Performance of Exterior Windows, Curtain Walls, Doors, and Impact Protective Systems Impacted by Windborne Debris in Hurricanes. ASTM E1996, West Conshohoken, PA.
- FEMA, (2007). Tornado Damage Investigation Greensburg, Kansas. FEMA 1699 DR-KS. Federal Emergency Management Association, Washington, D.C., 29 pp.
- FEMA, (1999). Midwest Tornadoes of May 3, 1999: Observations, Recommendations and Technical Guidance. FEMA P-342. Federal Emergency Management Association, Washington, D.C., 220 pp.
- ICC. (2000). International Building Code, Country Club Hills, IL.
- Florida Building Code, (2017). “2017 Florida Building Code-Test Protocols for High Velocity Hurricane Zone.” Sixth Edition. TAS 201-94. Florida, USA

- Sciaudone, J., (1996). "Analysis of Wind Borne Debris Impact Loads." All Dissertations.
- Twisdale, L. A., Vickery, P. J., and Steckley, A. C. (1996). Analysis of hurricane windborne debris impact risk for residential structures, State Farm Mutual Automobile Insurance Companies, Bloomington, IL.
- Grayson, J. M., Pang, W., & Schiff, S. (2013). Building envelope failure assessment framework for residential communities subjected to hurricanes. *Engineering Structures*, 51, 245–258. doi: 10.1016/j.engstruct.2013.01.027
- Lin, N., & Vanmarcke, E. (2010). Windborne debris risk analysis - Part I. Introduction and methodology. *Wind and Structures An International Journal*, 13(2), 191–206. doi: 10.12989/was.2010.13.2.191
- NAHB (National Association of Home Builders), 2002. Wind-Borne Debris Impact Resistance of Residential Glazing. Upper Marlboro, MD.
- Amini, M., and van de Lindt, J. (2013). "Quantitative insight into rational tornado design wind speeds for residential wood-frame structures using fragility approach." *J. Struct. Eng.*, 10.1061/(ASCE)ST.1943-541X.0000914, 04014033.
- Alphonso, T.C., Barbato, M., 2014. Experimental fragility curves for aluminum storm panels subject to windborne debris impact. *J. Wind Eng. Ind. Aerod.* 134, 44–55.
- Maloney, T., Ellingwood, B., Mahmoud, H., Wang, N., Wang, Y., & Lin, P. (2018). Performance and risk to light-framed wood residential buildings subjected to tornadoes. *Structural Safety*, 70, 35–47. doi: 10.1016/j.strusafe.2017.10.004
- Karacabeyli, E., Douglas, B., 2013. CLT Handbook: Cross-Laminated Timber. FPInnovations, Pointe-Claire, QC.

- Gu, Mengzhe, (2017). “Strength and Serviceability Performances of Southern Yellow Pine Cross-Laminated Timber (CLT) and CLT-Glulam Composite Beam.” All Dissertations.
- AWC. (2018). National Design Specification for Wood Constructions (NDS). Forest Product Association.
- APA-The Engineered Wood Association. (2018). Standard for performance rated cross laminated timber. ANSI/APA PRG 320. Tacoma, WA:
- European Committee for Standardization, 2004. Eurocode 5: Design of timber structures. Part 1-1: General – Common rules and rules for buildings. EN 1995-1-1. Brussels: CEN, 124 p.
- Blaas H.J., and P. Fellmoser. 2004. Design of solid wood panels with cross layers. In Proceedings of the 8th World Conference on Timber Engineering, June 14-17, 2004. Lahti, Finland, 2:543-548.
- Kreuzinger H. 1995. Mechanically jointed beams and columns. In Timber Engineering – STEP 1, ed. H.J. Blaas et al. B11/1-8. Almere, The Netherlands: Centrum Hout.
- Kreuzinger H. 1995. Mechanically jointed beams and columns. In Timber Engineering – STEP 1, ed. H.J. Blaas et al. B11/1-8. Almere, The Netherlands: Centrum Hout.
- Gagnon, S. and C. Pirvu. (2011). CLT Handbook: Cross-Laminated Timber. Canadian ed. Special Publicatio SP-528E. Quebec, QC: FPInnovations. 1 v.
- Popovski, M., Schneider, J. & Schweinsteiger, M. (2010). “Lateral Load Resistance of Cross-Laminated Wood Panels.” In Proc., World Conf. on Timber Engineering. Trentino, Italy, WCTE.

- Pei, S., Popovski, M., & Lindt, J. W. V. D. (2013). Analytical study on seismic force modification factors for cross-laminated timber buildings. *Canadian Journal of Civil Engineering*, 40(9), 887–896. doi: 10.1139/cjce-2013-0021
- Lukacs, I., Björnfot, A., & Tomasi, R. (2019). Strength and stiffness of cross-laminated timber (CLT) shear walls: State-of-the-art of analytical approaches. *Engineering Structures*, 178, 136–147. doi: 10.1016/j.engstruct.2018.05.126
- Shahnewaz, M. Tannert, T., Popovski, M., & Alam, M. (2018). “Deflection of CLT Shear Walls in Platform Construction.” In Proc., World Conf. on Timber Engineering. Seoul, South Korea, WCTE.
- Amini, M. et al. (2016). “Determination of Seismic Performance Factors for CLT Shear Wall Systems.” In Proc., World Conf. on Timber Engineering. Vienna, Austria, WCTE.
- Vickery, P. J., Lin, J., Skerlj, P. F., Twisdale, L. A., & Huang, K. (2006). HAZUS-MH Hurricane Model Methodology. I: Hurricane Hazard, Terrain, and Wind Load Modeling. *Natural Hazards Review*, 7(2), 82–93. doi: 10.1061/(asce)1527-6988(2006)7:2(82)
- Vickery, P. J., Skerlj, P. F., Lin, J., Twisdale, L. A., Young, M. A., & Lavelle, F. M. (2006). HAZUS-MH Hurricane Model Methodology. II: Damage and Loss Estimation. *Natural Hazards Review*, 7(2), 94–103. doi: 10.1061/(asce)1527-6988(2006)7:2(94)

- Ellingwood, B. R., & Rosowsky, D. V. (2004). Fragility Assessment of Structural Systems in Light-Frame Residential Construction Subjected to Natural Hazards. *Structures* 2004. doi: 10.1061/40700(2004)119
- Ashley, W. S. (2007). Spatial and Temporal Analysis of Tornado Fatalities in the United States: 1880–2005. *Weather and Forecasting*, 22(6), 1214–1228. doi: 10.1175/2007waf2007004.1
- Roueche, D. B., Lombardo, F. T., & Prevatt, D. O. (2017). Empirical Approach to Evaluating the Tornado Fragility of Residential Structures. *Journal of Structural Engineering*, 143(9), 04017123. doi: 10.1061/(asce)st.1943-541x.0001854
- Standohar-Alfano, C. D., Freyne, S., Graettinger, A. J., Floyd, R. W., & Dao, T. N. (2015). Performance of Residential Shelters during the May 20, 2013, Tornado in Moore, Oklahoma. *Journal of Performance of Constructed Facilities*, 29(5), 04014143. doi: 10.1061/(asce)cf.1943-5509.0000636
- Fan, F., & Pang, W. (2019). Stochastic Track Model for Tornado Risk Assessment in the U.S. *Frontiers in Built Environment*, 5. doi: 10.3389/fbuil.2019.00037

CHAPTER THREE

DEBRIS IMPACT PERFORMANCE OF CLT

Taken from: *Development of a windborne debris impact fragility curve for Cross-Laminated Timber using experimental testing* (Journal of Wind Engineering and Industrial Aerodynamics)

ABSTRACT: Cross-Laminated Timber (CLT) is an engineered wood product with high rigidity, dimensional stability, and desirable environmental properties. Because of these characteristics, it presents the potential to resist the impact loads associated with windborne debris in both tornadoes and hurricanes. Full-scale experimental debris impact testing was performed on 3-layer CLT in order to determine its response to debris impact loading scenarios. A variety of missile masses, speeds, and impact locations were tested to determine this response. Various forms of failure were observed including missile perforation, excessive backside deflection, and dislodgement of debris on the backside of tested panels. Analysis of the experimental data was then performed with the goal producing a debris impact fragility curve for CLT. The resulting curves were based on relating a missile's kinetic energy with the probability of failure as defined by relevant testing standards. The results of this study point towards 3-ply CLT having a high likelihood of surviving impacts from EF-2 and EF-3 level missiles with a decreased likelihood of surviving debris from EF-4 and EF-5 level events. For qualification as a material for safe rooms, thicker panels and additional connection design would be required.

3.1 INTRODUCTION:

Cross Laminated Timber (CLT) was introduced as a building material in the early 1990s in Austria and Germany and has begun to gain popularity in North America as it offers a combination of structural performance and environmental benefits (Karacabeyli and Douglas, 2013). CLT is made by gluing alternating layers of solid sawn lumber to form large panels providing dimensional stability and a relatively high degree of rigidity. As the markets for CLT in the United States grow, it becomes worthwhile to examine its capabilities to resist the loads associated with hazards present in the region, namely hurricanes, tornadoes and the windborne debris associated with them.

Windborne debris has long been known to be a significant contributor to damage in hazardous wind events such as tornadoes and hurricanes. The response of building envelope to the debris associated with these events is critical to the overall performance of a structure (Minor, 2005). Additional research shows a strong link between damage to the building envelope and the total loss associated with a hazardous wind event (Sparks et al., 1994). In order to standardize the experimental qualification of material to resist windborne debris impacts several guidelines were written to describe the procedure for such tests (ASTM, 2013; ICC, 2013; FEMA, 2015). These standards require testing with a 2 by 4 (3.8 cm by 8.9 cm) framing member propelled at various velocities depending on the level of the hazard and the desired level of protection. For wall assemblies to be used in a storm shelter or safe room, a 2 by 4 (3.8 cm by 8.9 cm) missile with mass of 6.8 kg (15-lb) and velocity of 44.7 m/s (100 mph) is used to represent the hazard of a tornado with a magnitude of 5 on the Enhanced Fujita (EF) scale. Several typical wall assemblies were

experimentally tested at the Wind Science and Engineering Research Center at Texas Tech University to determine the threshold missile speed at which a 6.8 kg (15-lb) 2 by 4 caused failure (Texas Tech University, 2006). Additional research was performed to attempt to understand the intensity measures associated with debris impact loading including missile momentum and kinetic energy and concluded that due to energy losses during impact that missile momentum would likely be a better measure of hazard intensity than energy (National Association of Home Builders, 2002). This assumption and the variation in behavior with different impact locations was tested through experimental tests in the study. Studies have determined the response of CLT to debris impact loads showing the ability of 5-ply CLT to resist a 6.8 kg (15-lb) 2 by 4 with a velocity of approximately 45 m/s (100 mph) with minimal damage (Bridwell et al. 2013; Falk et al. 2015).

Experimental testing beyond the determination of threshold missile velocity has been performed in an effort to quantify either the material variability or the variability of the windborne debris by varying the location, mass, and velocity of the debris. These studies produced vulnerability curves for structurally insulated panels (Chen et al. 2015) and fragility curves for corrugated steel panels (Chen et al. 2015; Herbin and Barbato, 2012; Alphonso and Barbato, 2014). These studies used a combination of several experimental debris impact tests and numerical simulations to develop the fragility curves that captured the non-linear behavior of the wall panels as well as the various failure modes that were observed.

In this study, the capacity of 3-ply CLT to resist debris impact loads was determined through experimental testing, and fragility curves were developed to quantify the variability in the performance of the CLT panels.

3.2 EXPERIMENTAL TEST SETUP:

The experimental debris impact testing was conducted using a pneumatic air cannon shown in Figure 3.1. The cannon was pressurized and released to launch a 3.8 cm by 8.9 cm (1.5 inch by 3.5 inch; nominally 2 by 4) piece of No. 2 southern yellow pine at the desired velocity. The mass, length, and velocity of the missile was controlled for each of the impact tests to determine the response to a variety of intensity measures. The velocity of the missile was measured using a Photron Fastcam Mini high-speed camera filming perpendicular to the plane of the missile's trajectory and tracking discrete points marked on the missile. A series of test shots were performed to develop the relationship between the pressure in the pneumatic cannon, the mass of the missile, and the velocity of the missile at impact.



Figure 3.1: Pneumatic cannon used for experimental debris impact testing

Fourteen 3-ply CLT panels made of spruce, pine, fir lumber were manufactured for experimental testing. Each panel measured between 2.44 m by 2.54 m (96 inches by 100 inches) and 2.44 m by 2.33 m (96 inches by 91.75 inches) and was 10.5 cm (4.125 inches) thick. The panels were made such that the center-to-center span of the panel was exactly 2.44 m (96 inches). Each test panel was supported by 35.6 cm (14 inch) strips of CLT and secured using 15.2 cm (6 inch) long, 0.7 cm (0.27 inch) diameter lag screws which were anchored to W6 steel supports acting as a supporting frame. The connections were meant to imitate realistic boundary conditions for the connection of perpendicular panels. The panels were tested using both the strong and weak orientation of the connection shown in Figure 3.2. In addition, the CLT panels were tested such that the outer layer of the test panel was oriented vertically (weak axis span) and horizontally (strong axis span) shown in Figure 3.3.

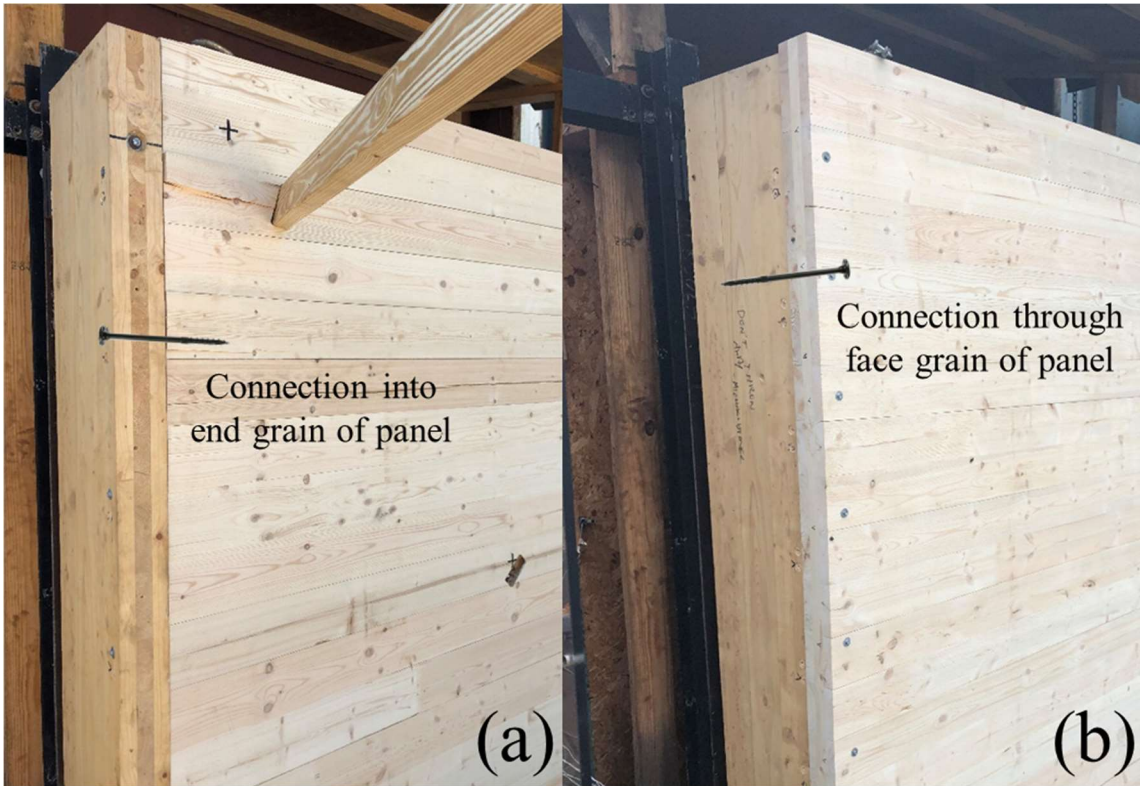


Figure 3.2: Experimental test setup of (a) weak- and (b) strong-connection orientation



Figure 3.3: Experimental test setup of weak- and strong-axis orientations

Videos captured by Photron Fastcam Mini high-speed camera at 2,000 frames per second were analyzed in order to determine a precise measurement of the missile velocity and develop an empirical relationship between the pressure in the cannon and the missile's mass and velocity. The initial linear portion of the displacement versus time graph of the missile was fit using a linear regression whose slope was used to estimate of the missile velocity, shown in Figure 3.4.

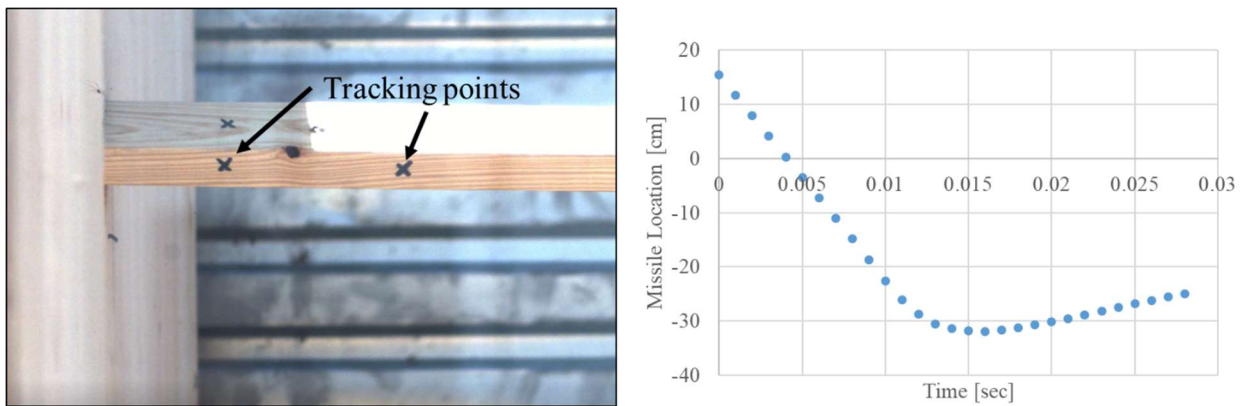


Figure 3.4: Missile tracking process for determination of missile velocity

Each panel was impacted at least three times; once in the center of the panel, once on the edge of the panel within 15.2 cm (6 inches) of the support, and once on the corner of the panel within 15.2 cm (6 inches) of the corner of the panel. After each impact, the penetration of the missile and the permanent displacement at the back of the panel were measured. The experimental test plan varied the mass, velocity, and location of the missile impact in order to test a range of intensity measures dictated by the recommendations of FEMA P-361 and ICC 500. The test matrix included 6.8 kg (15-pound), 5.4 kg (12-pound), and 4.1 kg (9-pound) pieces of lumber travelling between 26.6 m/s (59.5 mph) and 53.4

m/s (119.4 mph). More experimental tests were performed at intensities that caused failure to better understand the failure mechanisms of the panels

In addition to solid 3-ply CLT panels, two different panel-to-panel connections were tested. A half lap panel-to-panel connection occurs when half of a CLT panel's depth is removed and overlapped on an adjacent panel cut in the same fashion. A surface spline panel-to-panel connection occurs when two panels are connected using a spline that is routed into each panel to the depth of the spline member. The half lap and surface spline panel-to-panel connections are shown in Figure 3.5a and 3.5b respectively and were tested using the strong connection to the supports. The half lap connection used 6.4 mm x 76 mm (1/4" x 3") screws with 76 mm (3 inch) spacing in a staggered row. The surface spline connection used the same screws with two rows of staggered screws with 152 mm spacing in each panel. Each set of panels measured 2.44 m by 2.44 m (96 in by 96 in), and two sets of each panel-to-panel connection test were performed, one with each axis orientation.

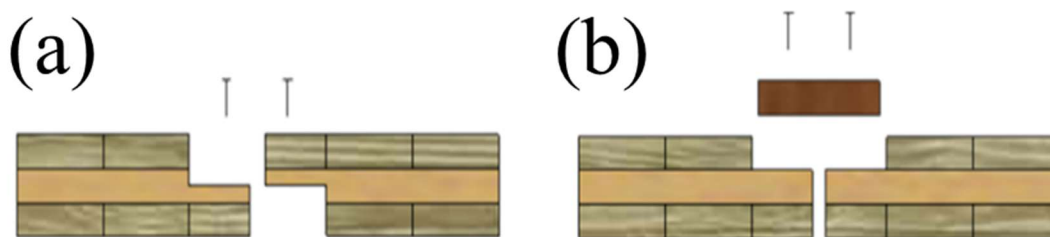


Figure 3.5: Panel-to-panel connections: half-lap (a) and surface spline (b)

3.3 EXPERIMENTAL RESULTS:

Of the fourteen experimental panels, seven were tested with the weak axis and strong connection orientation, three were tested with the strong axis and strong connection orientation, two panels were tested with weak axis and weak connection orientation, and two panels were tested with the strong axis and weak connection orientation. An example of both the penetration and the permanent deflection measured after each test is shown in Figure 3.6 and were the primary damage indicators used to judge the response of the CLT panel.

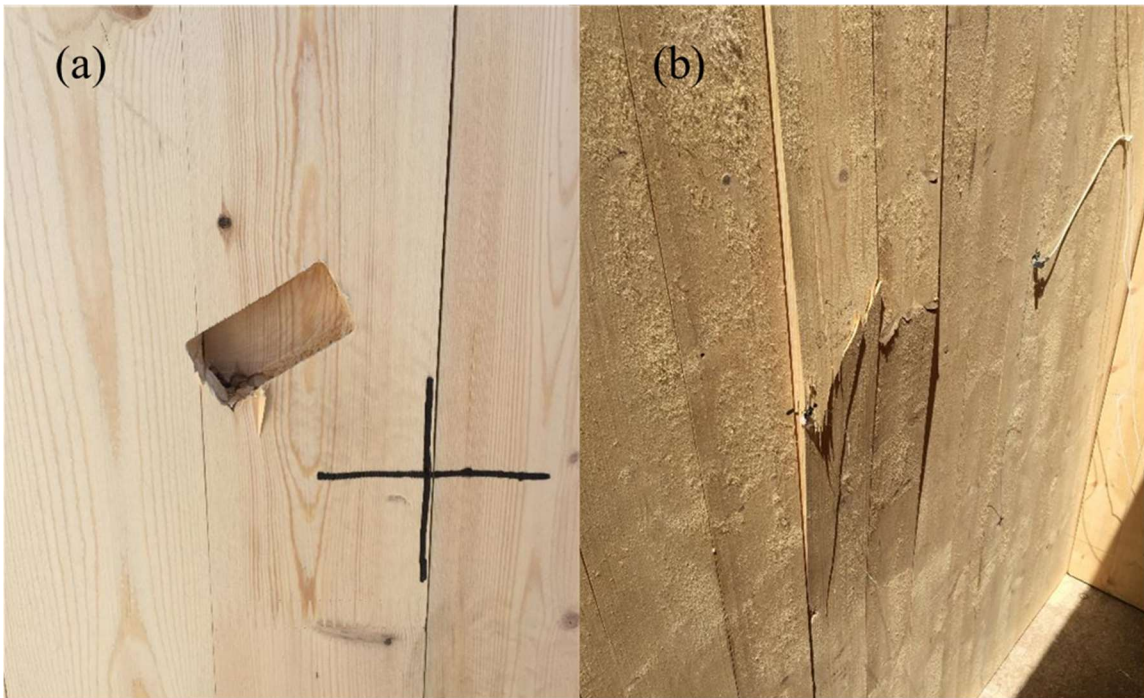


Figure 3.6: Measurement of missile penetration (a) and permanent deflection (b) after missile impact

Each test was determined to be a passing or failing test based on the criteria set by FEMA P-361 and ICC 500. These documents determine failure any one of three criteria: perforation, permanent deflection, and/or dislodgement. Perforation occurs when the missile punctures through the wall assembly and is visible on the interior of the panel. Permanent deflection of the backside of the panel greater than 7.62 cm (3 inches) also constitutes a failure. Finally, any piece of the wall that is ejected from the inside of the panel deemed to cause a risk to the occupants is considered a failure. An example of each of the failure mechanisms, perforation, permanent, deflection, and dislodgement, is shown in Figure 3.7.

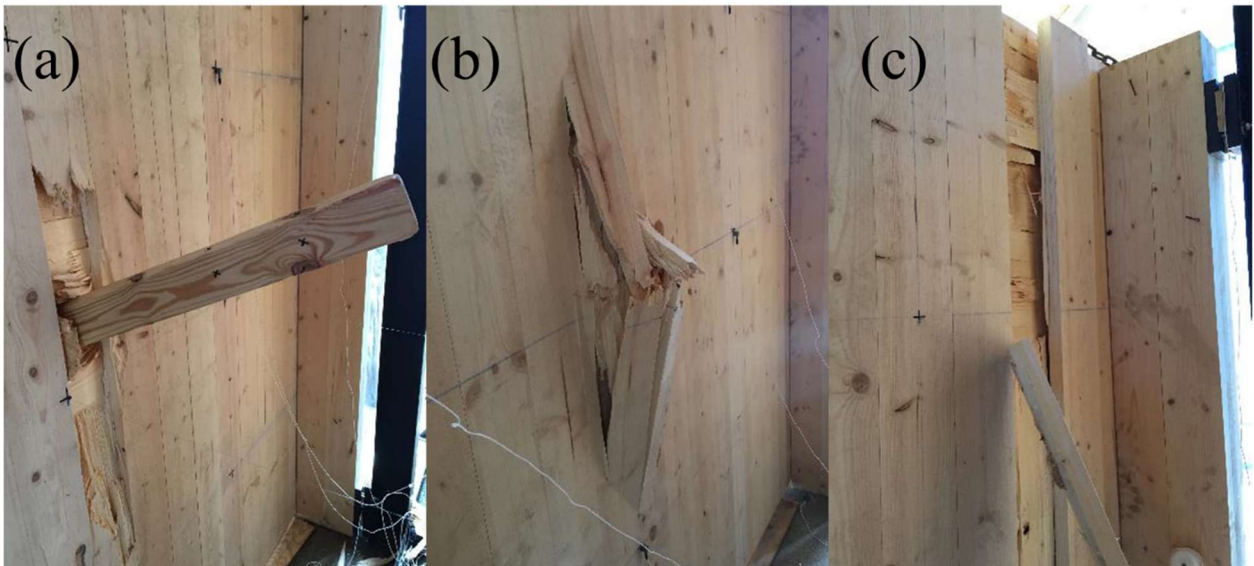


Figure 3.7: Failure modes: perforation (a), permanent deflection (b), and dislodgement (c)

The distribution of failure mechanisms based on impact location, axis orientation, and connection orientation gave insight to the behavior of the CLT panels. Table 3.1 shows the breakdown of failures due to perforation, permanent deflection, and dislodgement for

each of the configurations tested. With regards to impact location, failure due to deflection occurred only in impacts that occurred in the center and edge, while the corner experienced primarily perforation failure. As the stiffness of the panel increases closer to the supported edges, perforation becomes a more likely failure mechanism than deflection as the panel can dissipate less energy through elastic deflections. Examining the distribution of failures based on axis orientation showed that only the weak axis panel orientation was susceptible to dislodgement failures and both weak and strong axis orientations were subject to perforation and deflection failures. Finally, connection orientation exhibited the vulnerability to perforation failures for weak connection orientations as all six failures occurred due to perforation.

Table 3.1: Number of failures for each failure mode and panel configuration tested

Panel Configuration	Failure Mechanism		
	Perforation	Deflection	Dislodgement
All Configurations	11	4	2
Center	1	2	0
Edge	3	1	1
Corner	7	1	1
Weak Axis	6	2	2
Strong Axis	5	2	0
Weak Connection	6	0	0
Strong Connection	5	4	2

To establish a relationship between the various intensity measures of the missile and the performance of the CLT panels, the damage measures (missile penetration and permanent panel deflection) were plotted against the missile's momentum and kinetic energy. Plotting both the permanent deflection and penetration of the missile against the

missile's momentum and kinetic energy gave indications of increasing trends, but still exhibited significant variation as shown in Figures 3.8-3.11. In addition, these figures only contained information from tests that passed the impact test, as any panel with a perforation or dislodgement failure made the penetration and/or backside deflection measurement difficult or impossible to measure. Using the final position of the missile measured from the front surface of the panel as the penetration value and adding it to the information from passed tests further underscored the variability in the panel's behavior. The maximum value of the measured missile penetration and permanent deflection was 121.9 cm (48 in) because this was the distance between the inside of the panel and the back of the test frame. Figures 3.12-3.13 show the relationship between the measured damage and the missile intensity for all tests. It was clear that no defined relationship existed for all missile impact locations, panel axis orientation, and connection orientations. Because so many configurations were tested, further dividing the experimentally measured response to distinguish the change in behavior did not provide enough information to develop consistent relationships.

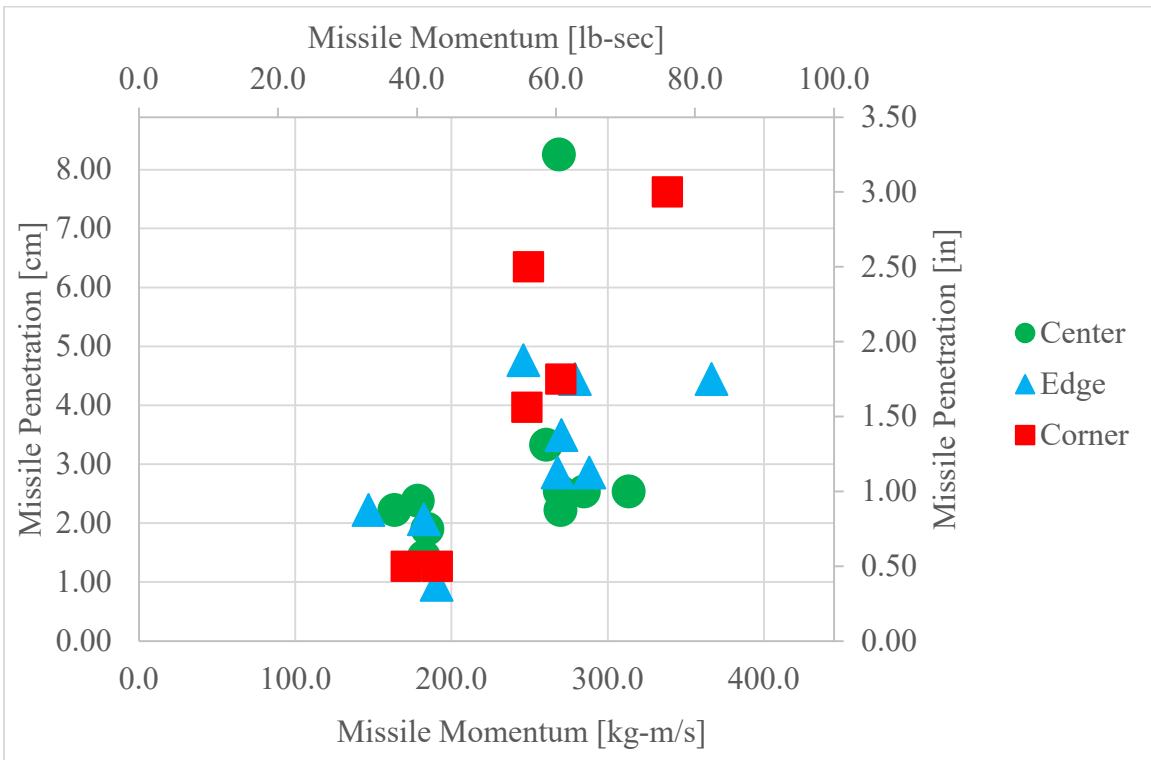


Figure 3.8: Relationship between missile penetrations and missile momentum (passed tests only)

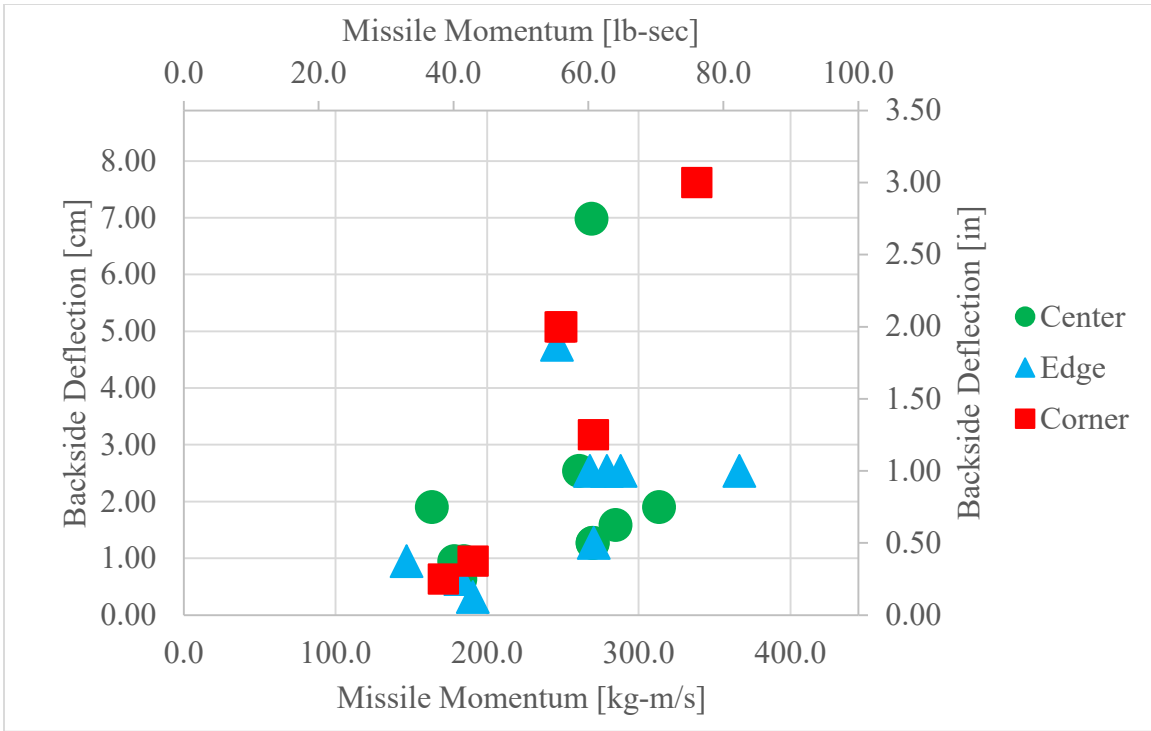


Figure 3.9: Relationship between backside deflection and missile momentum (passed tests only)

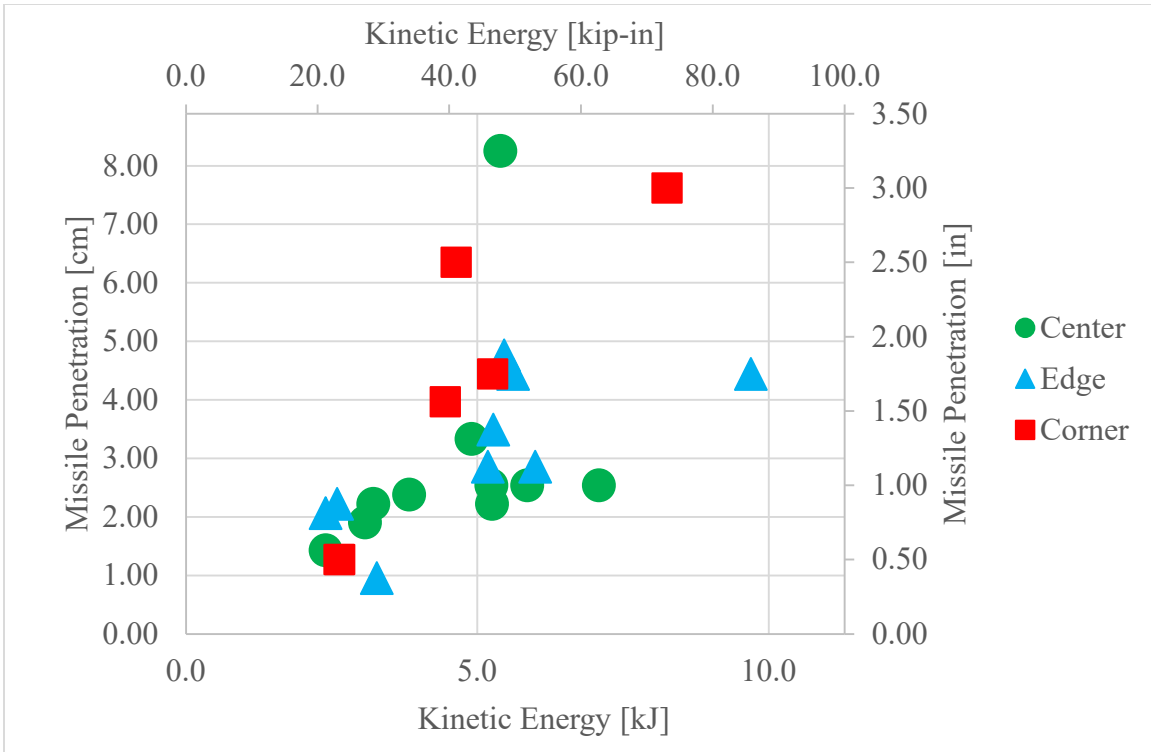


Figure 3.10: Relationship between missile penetration and kinetic energy (passed tests only)

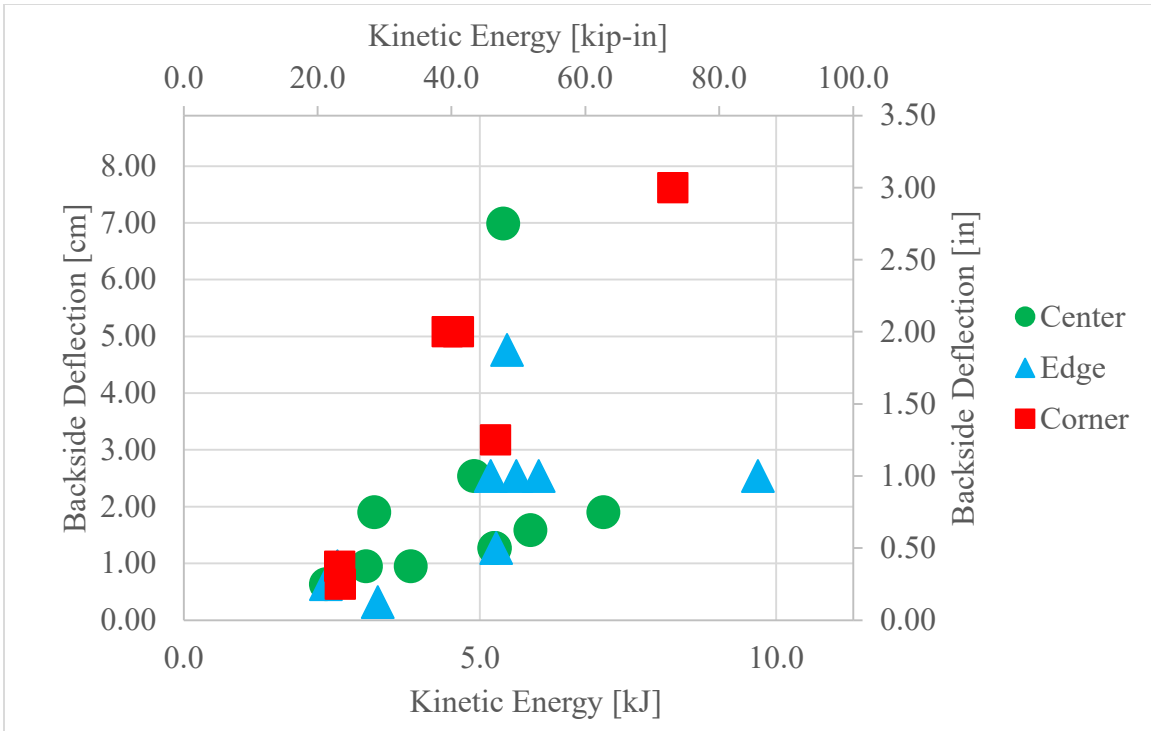


Figure 3.11: Relationship between backside deflection and kinetic energy (passed tests only)

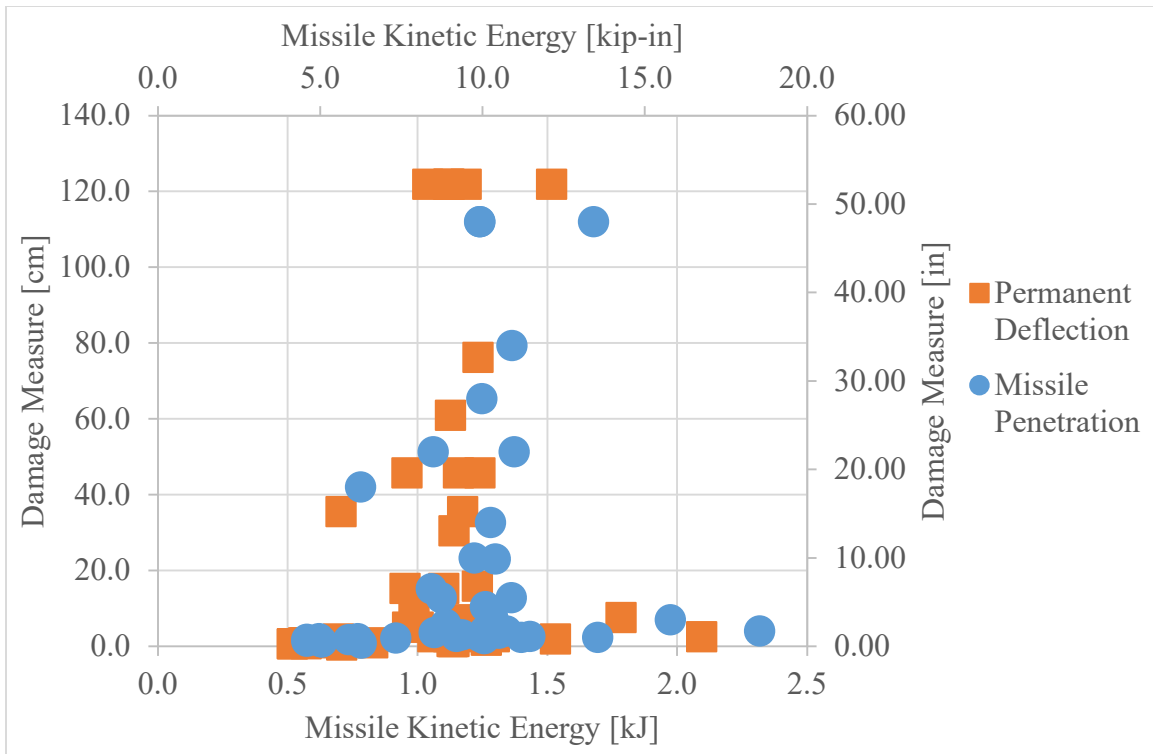


Figure 3.12: Relationship between damage measurements and kinetic energy(all tests)

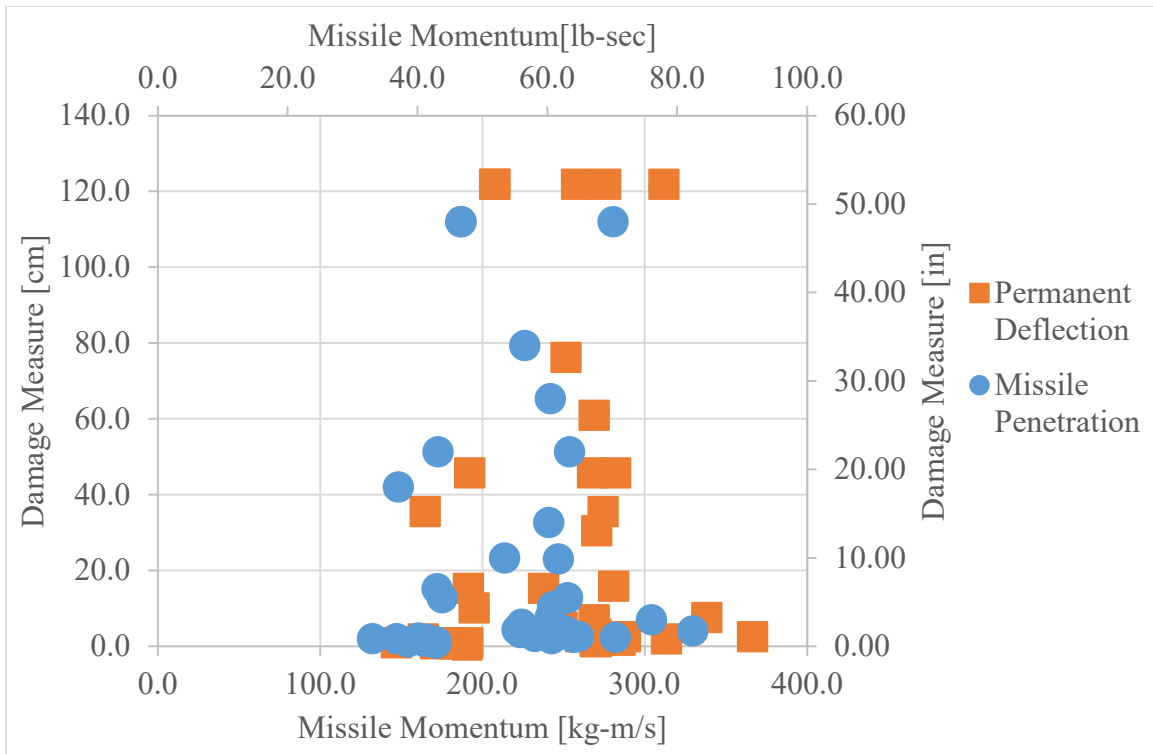


Figure 3.13: Relationship between damage measurements and missile momentum (all tests)

Plotting the damage indicators with the missile's intensity measure allowed for a comparison of the missile intensity measures to determine which served as a better predictor for failure. For all plots a power model was selected to relate the missile intensity with the damage indicator as it provided the best fit. The difference between the fitted power model equation and the experimentally collected data was calculated. The dispersion of the calculated error terms gave an indication of the variability in the data and was used to decide intensity measure was better suited for predicting the response of the panel. For predicting the missile's penetration, momentum had a dispersion of the lognormally distributed error of 0.42, while of 0.39 indicating it was a slightly better

measure of the missile's intensity. For predicting the panel's permanent deflection, momentum had a dispersion of the lognormally distributed error of 0.63, while kinetic energy had a dispersion of 0.60, also indicating that the kinetic energy did a slightly better job of measuring the intensity of the missile. Based on these results, the kinetic energy was used as the primary intensity measure in the development of the fragility curves.

A total of four panel-to-panel debris impact tests also were conducted. Each connection was tested in both the weak- and strong-axis orientation. A summary of these impact tests is shown in Table 3.2 with images of damage shown in Figure 3.14. Significant transient deflection was also observed during the debris impact test for the panels with a weak axis orientation. This was expected as panel-to-panel connections are not designed to withstand out-of-plane loads while spanning in the weak axis orientation. The performance of the panel-to-panel connections with the strong axis orientation showed significantly better results. Vulnerability to perforation was evident as even strong axis orientation panels experienced this failure mechanism. With only one panel test of each configuration, it was difficult to differentiate the performance of the half-lap and surface spline; however, a reduction in performance was observed when compared to solid panels of the same axis and connection orientation. Future panel-to-panel connection impact tests would be required to develop statistics on their performance and determine a better understanding of their response.

Table 3.2: Experimental test results of panel-to-panel connections

Panel No.	Connection Type	Axis Orientation	Missile Mass [kg]	Missile Velocity [m/s]	Result
1	Half-Lap	Weak	6.8	30.6	Some damage to panel, no failure
2	Half-Lap	Strong	6.8	37.2	Perforation of missile - failure
3	Surface Spline	Weak	6.8	34.1	No perforation, high deflection - failure
4	Surface Spline	Strong	6.8	38.0	Damage, backside deflection - no failure



Figure 3.14: Damage photos of panel-to-panel connection tests

3.4 DEVELOPMENT OF FRAGILITY CURVES:

Fragility functions for structural performance are typically modeled using a lognormal distribution with a cumulative distribution function given by Equation 3.1 where the probability of failure, $F(x)$ is given by the standard normal cumulative distribution function, Φ ; the logarithmic mean, μ ; and logarithmic standard deviation, σ for a given intensity measure, IM .

$$F(IM) = \Phi \left[\frac{\ln(IM) - \mu}{\sigma} \right] \quad (3.1)$$

The method for calculating fragility curves included assigning each experimental test a binary probability of failure based on whether the test was a passed test or a failed

test as defined by FEMA P-361 and ICC 500. Experimental tests which passed according to these standards were assigned $P_f = 0$ while tests which failed were assigned $P_f = 1$. Beginning at the smallest experimentally tested intensity level (kinetic energy) a collection of experimental tests was grouped based on a ‘bin width’ and the probability of failure calculated by Equation 3.2 where the probability of failure at a given intensity measure, IM , was the sum of the binary probabilities of failure in each bin divided by the number of tests in each bin, n_{IM} .

$$F(IM) = \frac{\sum_{i=1}^{n_{IM}} P_{f,i}}{n_{IM}} \quad (3.2)$$

The ‘bin’ was shifted to capture the next group of experimental tests until all experimental tests were captured. The discrete points along the failure curve were then fit to a lognormal distribution using maximum likelihood and weighting each bin equally. An example of this process is shown in Figure 3.15. Initially, bin widths of 0.8 kJ, 1.6 kJ, and 2.4 kJ (7 kip-in, 14 kip-in, and 21 kip-in) were used to calculate fragility possible curves. Ultimately, a bin width of 1.6 kJ (14 kip-in) was used to calculate the final fragility curves for each of the configurations. The number of tests in each bin followed the distribution of experimental tests and are shown in Table 3.3. In all cases, where the most tests were performed in the range of 3.9 kJ to 5.5 kJ. This occurred as each configuration was tested an increasing level of intensity until failures were observed. Repeated tests were performed at intensity where failures occurred to produce more data around the failure threshold. Additionally, tests were performed with various masses to assure that the measured performance was not dependent on a single missile mass. Because the number of

experimental tests in each bin was not exactly uniform, this method did not necessarily equally weight each test; however, it assured that the most data was collected at the point where failure was measured.

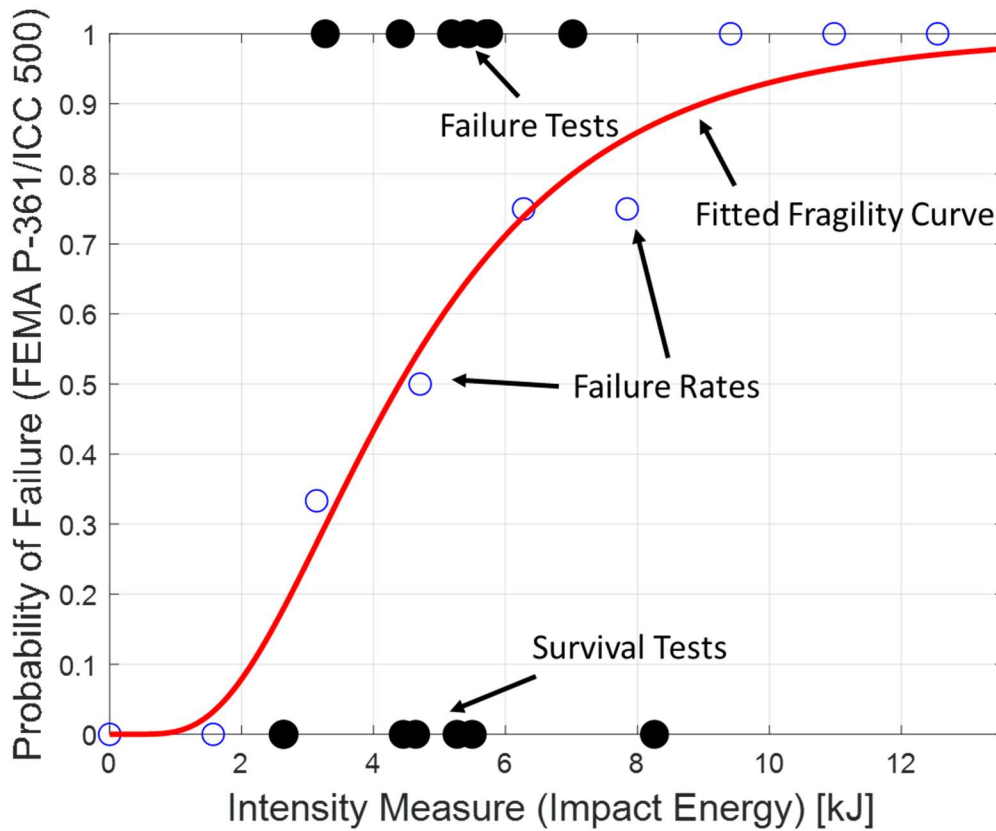


Figure 3.15: An example of the fragility curve analysis procedure

Table 3.3: Number of tests in each bin used to develop experimental fragility curves

Missile Energy [kJ]	Number of Tests in Each Bin				
	3.1	4.7	6.3	7.8	9.4
All Configurations	10	21	8	2	1
Center	4	7	2	1	0
Edge	3	8	2	0	1
Corner	3	6	4	1	0
Weak Axis	9	13	5	0	0
Strong Axis	1	8	3	2	1
Weak Connection	3	6	3	0	0
Strong Connection	7	15	5	2	1

The individually fit lognormal distribution location (μ) and scale (σ) parameters calculated using this analysis method are shown in Table 3.4. The fitted fragility curves are plotted with the associated configurations in Figures 3.16-3.18. As expected, including all experimental data lead to a fragility curve with the highest variability. For fragilities separated by impact location, impacts at the center performed better than impacts at both the edge and the corner. For lower levels of intensity, the edge impacts showed performance closer to impacts at the center. At relatively higher levels of intensity, edge impacts showed performance closer to corner impacts. Comparing the calculated fragility curves based on axis orientation showed only slight differences between strong axis orientations and weak axis orientations. The weak axis orientation panels did perform slightly better, likely because the weak axis allowed more deformation and absorption of energy than the strong axis panels. Finally, the comparison of the calculated fragility curves based on connection orientation showed significant improvement in the

performance when the strong connection was used. The performance of strong connection panels provided a more direct load path in the form of bearing as opposed to the weak connection panels which relied on the shear performance of the lag screw connection. This method for calculating the debris impact fragility curves produced results consistent with the observed failure mechanisms from the experimental tests.

Table 3.4: Lognormal parameters for experimentally derived fragility curves

Location, Axis Orientation, Connection Configuration	Lognormal Location Parameter, μ	Lognormal Scale Parameter, σ
All Impacts	1.85	0.61
Center	1.84	0.43
Edge	1.66	0.34
Corner	1.48	0.56
Strong Axis	1.54	0.48
Weak Axis	1.78	0.28
Strong Connection	1.99	0.51
Weak Connection	1.39	0.50

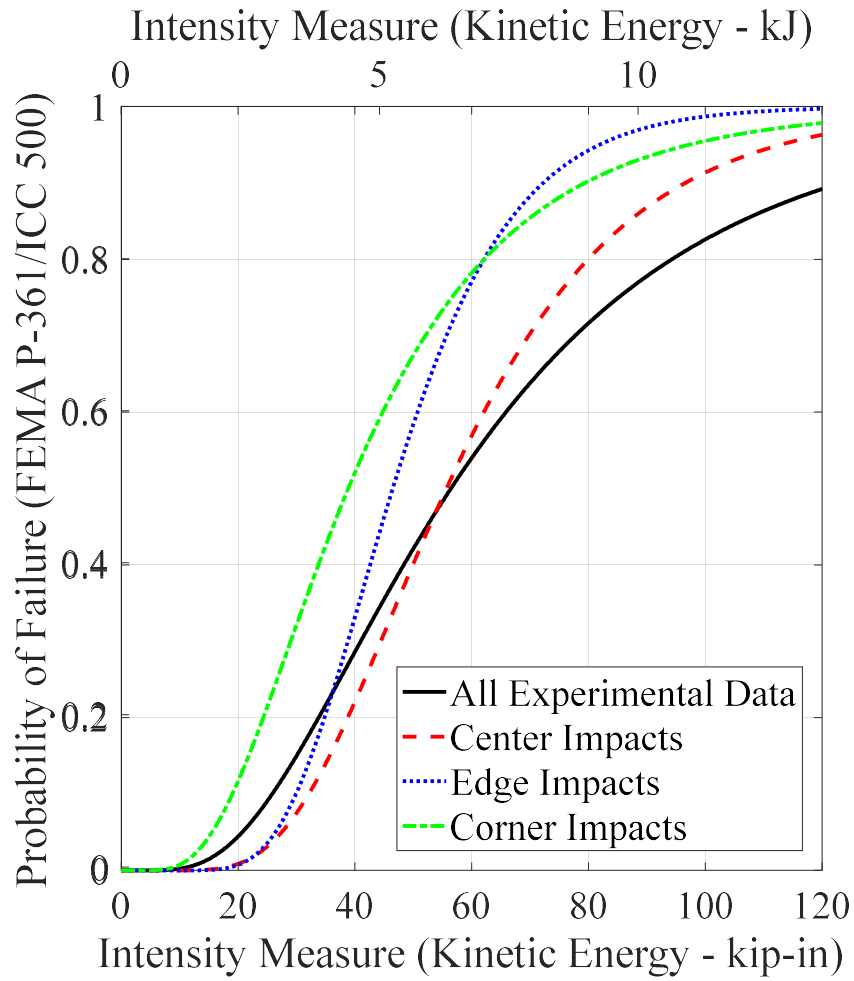


Figure 3.16: Plotted fragility curves for impact location

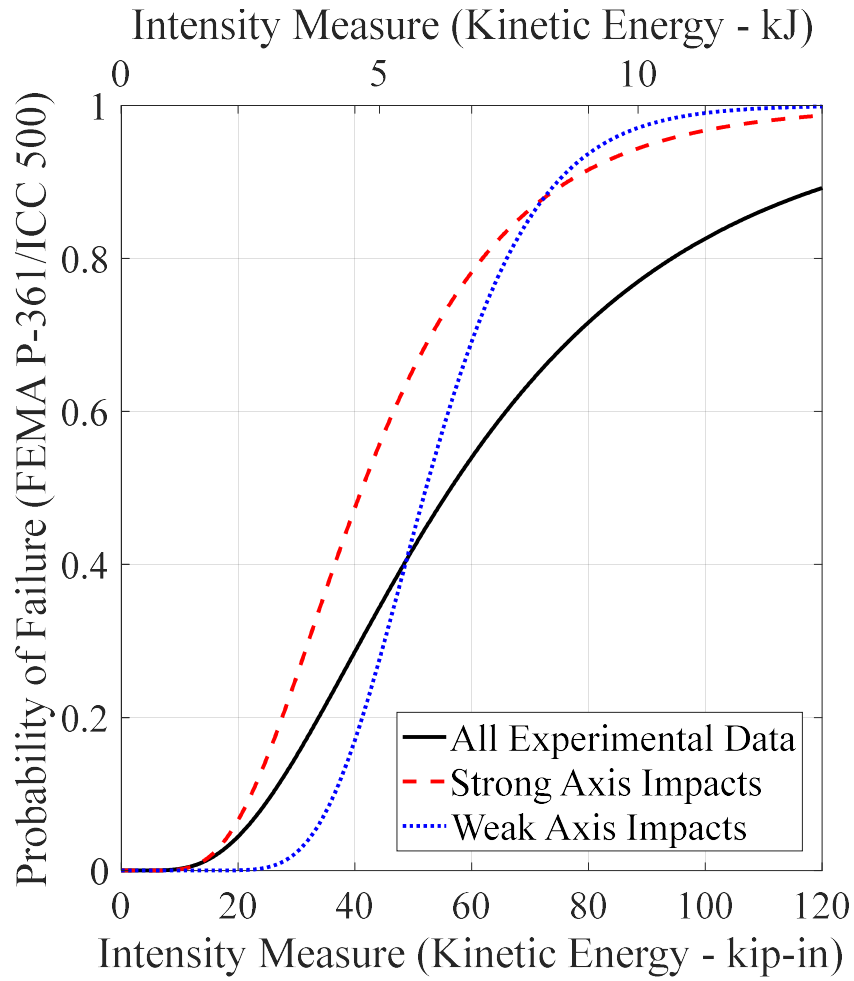


Figure 3.17: Plotted fragility curves for axis orientation

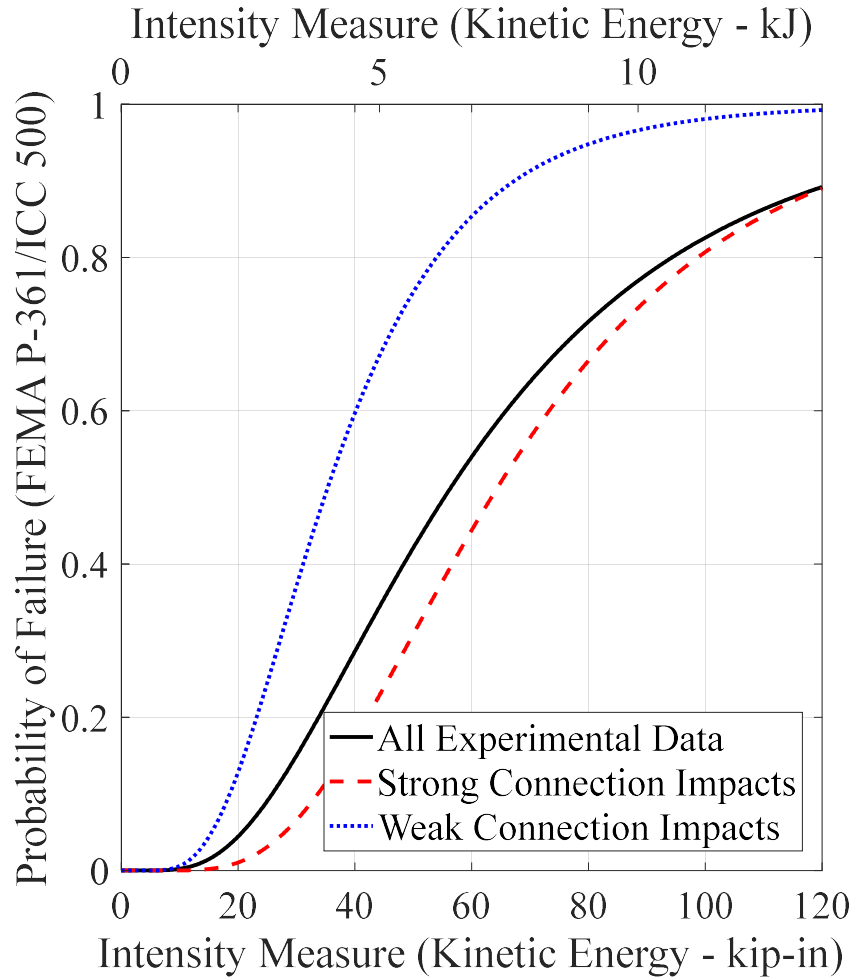


Figure 3.18: Plotted fragility curves for connection orientation

The performance of the 3-ply CLT panels were then compared to the intensities of windborne debris outlined by FEMA P-361 and ICC 500. For EF-2, EF-3, EF-4, and EF-5, the kinetic energy of the missile was calculated to be 4.4 kJ, 4.8 kJ, 5.5 kJ, and 6.8 kJ (38.5 kip-in, 42.6 kip-in, 48.7 kip-in, and 60.2 kip-in) based on these documents. These energies represent a 6.8 kg (15-pound) 2x4 travelling at 35.8, 37.6, 40.2, and 44.7 m/s respectively (80, 84, 90, and 100 mph respectively). For all experimental impact test configurations, the probabilities of failure due to windborne debris from EF-2 through EF-

5 tornadoes were approximately 26%, 32%, 40%, and 54% respectively. In order to reduce these probabilities of failure, a 4-ply or 5-ply panel could be used. Furthermore, engineering a connection between perpendicular wall panels like a box joint would provide stronger performance in impacts to a panel's edge and corner and would remove the need to test multiple connection configurations.

Because a missile's speed can be more easily estimated or measured than its kinetic energy, the presented fragility curves were converted into fragility curves using missile speed as the intensity measure on the horizontal axis. To do this, the mass of the missile was assumed, and the fragility curve was scaled to the associated velocity. Three fragility curves are shown in Figure 3.19 corresponding to 4.1 kg, 5.4 kg, and 6.8 kg (9-pound, 12-pound, and 15-pound) missiles. For comparison, a 6.8 kg (15-pound) at 44.7 m/s (100 mph) would have a predicted probability of failure of 60% while a 4.1 kg (9-pound) missile at 44.7 m/s (100 mph) would only have a predicted probability of failure of 28%.

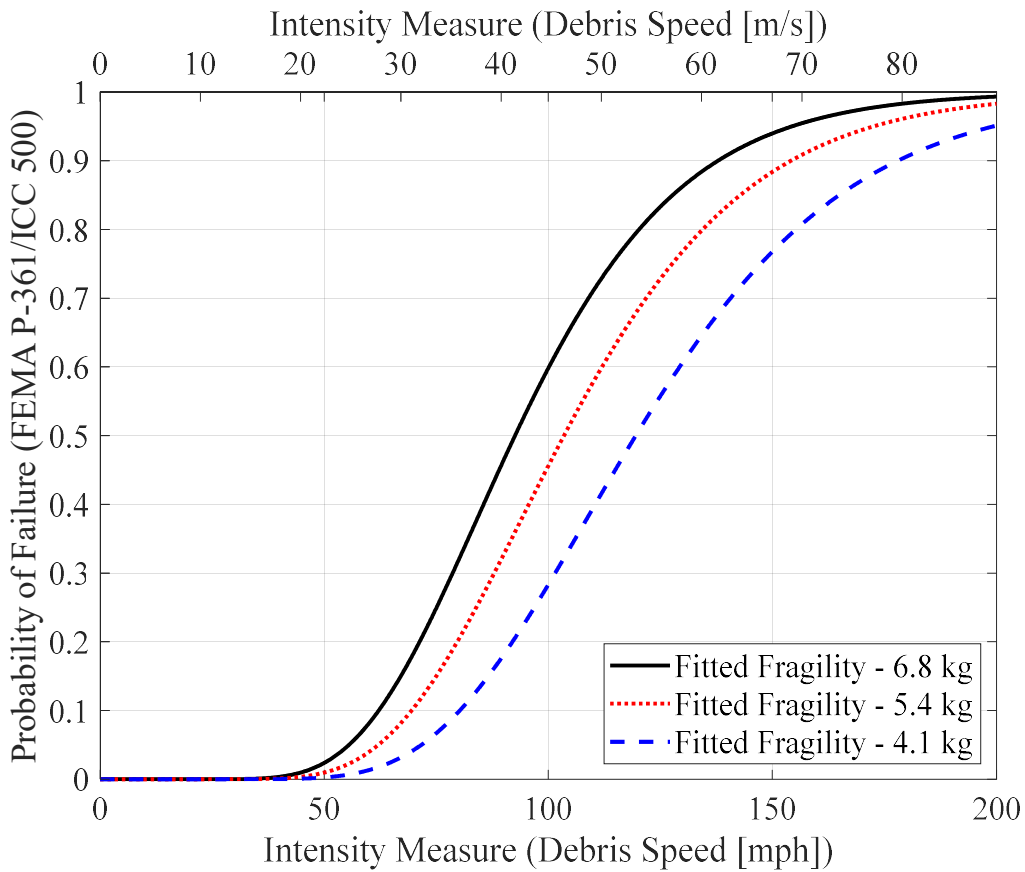


Figure 3.19: Fragility curve with missile speed as intensity measure for various debris masses

The variability in the performance of CLT panels was significant as the impacted location was relatively small in comparison to the size of the panel. Minor defects in individual pieces of lumber sometimes lead to diminished performance of an otherwise suitably strong panel accounting for the high variability in panel performance observed in this study. The calculated fragility curves are useful as they attempt to quantify this variability and can be utilized in loss models that attempt to quantify the performance of CLT structures in tornadoes and hurricanes.

3.5 CONCLUSIONS:

Cross-Laminated Timber shows potential as an engineered wood product to resist the debris loads associated with hurricanes and tornadoes due to its dimensional stability and rigidity. Standards that describe the recommended experimental testing suggest using a wood 2 by 4 to approximate the most dangerous debris produced by these events. Experimental debris impact testing was performed on a series of 3-ply CLT panels to quantify their performance in such hazardous events. Missile perforation and excessive panel deflection were the primary failure mechanisms that were observed in the experimental testing setup. Using the information from experimental debris impact tests, separate fragility curves were calculated for each impact location, axis orientation, and connection orientation. Ultimately, the 3-ply CLT panels were most vulnerable in the corners of panels, with the strong axis orientation, and with the weak connection orientation. These fragility curves showed that for missiles expected in an EF-2 level tornado, there was a 26% probability of failure, while for an EF-5 level missile, there was a 54% probability of failure when all experimental tests were considered. It is likely that testing of 4-ply or 5-ply CLT panels would demonstrate the ability to better resist the high intensity debris impact loads associated with more hazardous tornadoes and hurricanes. Because the probability of such events is very low, 3-ply CLT panels would offer enough strength to provide an acceptable performance in lower intensity, higher probability events. Additional testing of two different panel-to-panel connections showed a decreased performance of the connection in comparison to solid panels. In order to qualify CLT panels for used as safe rooms or storm shelters as recommended in FEMA P-361 and ICC

500, thicker panels and additional connection design and testing would be necessary.

Appendix A contains photo of all debris impact tests.

3.6 REFERENCES:

Alphonso, T.C., Barbato, M., 2014. Experimental fragility curves for aluminum storm panels subject to windborne debris impact. *J. Wind Eng. Ind. Aerod.* 134, 44–55.

ASTM, 2013. Standard Test Method for Performance of Exterior Windows, Curtain Walls, Doors, and Impact Protective Systems Impacted by Missile(s) and Exposed to Cyclic Pressure Differentials. ASTM E1886, West Conshohocken, PA.

Bridwell, J.J., Ross, R.J., Cai, Z., Kretschmann, D.E., 2013. USDA Forest Products Laboratory's Debris Launcher. <https://doi.org/10.2737/fpl-rn-0329>.

Chen, Wensu, Hao, Hong, Li, Jun, 2015. Fragility curves for corrugated structural panel subjected to windborne debris. In: International Conference on Performance-Based and Life-Cycle Structural Engineering, Brisbane, QLD, Australia, pp. 9–11. <https://doi.org/10.14264/uql.2016.509>. December 2015. 877–883.

Falk, R.H., Bridwell, J., Hermanson, J., 2015. Tornado Safe Rooms from Commodity Wood Products: Wall Development and Impact Testing. Res. Paper FPL-RP-681. U.S. Department of Agriculture, Forest Service, Forest Products Laboratory, Madison WI.

FEMA, 2015. Design and Construction Guidance for Community Safe Rooms. Second Edition. FEMA P-361. Federal Emergency Management Association, Washington, D.C., 374 pp.

- Herbin, A., Barbato, M., 2012. Fragility curves for building envelope components subject to windborne debris impact. *J. Wind Eng. Ind. Aerod.* 285–298.
- ICC/NSSA, 2013. Standard for the Design and Construction of Storm Shelters. International Code Council/National Storm Shelter Association. ICC 500. American National Standard Institute, Washington, DC.
- Karacabeyli, E., Douglas, B., 2013. CLT Handbook: Cross-Laminated Timber. FPInnovations, Pointe-Claire, QC.
- Minor, J.E., 2005. Lessons learned from failures of the building envelope in windstorms. *J. Archit. Eng.* 11 (1), 10–13.
- National Association of Home Builders, 2002. Wind-Borne Debris Impact Resistance of Residential Glazing. Upper Marlboro, MD.
- Sparks, P.R., Schiff, S.D., Reinhold, T.A., 1994. Wind damage to envelopes of houses and consequent insurance losses. *J. Wind Eng. Ind. Aerod.* 145–155.
- Texas Tech University, 2006. A Summary Report on Debris Impact Resistance of Building Assemblies.

CHAPTER FOUR

PERFORMANCE OF CLT SHEAR WALL ASSEMBLIES WITH OUT-OF-PLANE WALLS

4.1 INTRODUCTION

As Cross-Laminated Timber (CLT) continues to grow in popularity in the United States, its applications as a structural material grow. CLT was developed in Europe for mixed-use and light commercial structures. It is made when dimensioned lumber is glued in orthogonal layers to create larger and stronger structural elements when compared to traditional light-frame wood construction. In addition to the environmental benefits, an increased resistance to fire and its relatively high out-of-plane strength have made it a suitable option for mid-rise platform-style construction. The out-of-plane behavior of CLT panels has been experimentally tested and analytically derived to the point that it is addressed in the United States design specification for wood (AWC, 2018). The in-plane behavior of CLT panels used as a lateral force resisting system has been studied widely, and the performance is largely based on the connections between vertical panels and between vertical and horizontal elements. Kinematic models that estimate the strength and stiffness of CLT panels used as lateral force resisting elements have been developed that combine the effects of panel in-plane bending, in-plane shear, sliding, and rocking (Lukacs et al, 2019). Further analytical study has attempted to quantify the effect on stiffness of vertical CLT elements perpendicular to the in-plane CLT elements; configurations that are common in platform construction (Shahnewaz, 2018).

For the purposes of determining the response of a CLT residential structure when subjected to tornado induced loading, a series of experimental tests were conducted. The primary goal of this study was to determine whether in-plane walls could sufficiently transfer uplift forces to out-of-plane walls. In residential structures, the presence of out-of-plane walls is common and likely influences the response to lateral loads. In order to determine the benefits of perpendicular member in terms of strength and stiffness, a series of experimental tests were performed on full-scale CLT shear walls with and without perpendicular wall elements. Furthermore, models were created for each configuration based on the tested connection behavior and spacing. To develop these preliminary models, a series of single-fastener tests were performed on the component connections that make up the shear wall assembly. In addition, a simplified analytical approach was developed to estimate the strength of the wall assemblies.

4.2 TEST BACKGROUND AND CONFIGURATION

The performance of CLT walls as lateral force resisting elements is controlled largely by the connections between panel elements. Both the strength and stiffness of such assemblies relies on the strength and stiffness of shear-resisting elements, hold-downs, and panel-to-panel connections. Connections typically include dowel type fasteners such as self-tapping screws or nails, bracket-style connections, threaded rod or traditional hold-down systems. Each of these elements have unique stiffnesses and force-displacement that, with the material properties of CLT elements contribute to the behavior of CLT shear wall systems. Generally, design methodologies rely heavily on the strength of the various components to estimate the strength of the overall assembly, where the relative stiffness of

the connections to resist sliding and overturning contribute heavily deformed shape. Extensive research has examined the performance of CLT shear wall assemblies designed with aspect ratios between 2:1 and 4:1 to calibrate seismic performance factors with designated design methods and connections that are standardized (Amini et al. 2018). The result of these studies presents a method for CLT shear walls where the strength is controlled by the amount of shear capacity provided by angle brackets at the top and bottom of the wall elements and the connection between in-plane panels. Furthermore, a method for calculating the deflection at a given load is given which consists of a linear approximation of the deflection as a result of bending, shear, sliding, and overturning. Equation 4.1 describes the shear wall deflection, δ_{sw} , as a function of the bending deformation, shear deformation, and connection slip. In this equation, the panel width, b_s , panel height, h , bending stiffness, EI_{eff} , and shear stiffness, GA_{eff} all play roles in the deflection equation. In addition, the connection slip at design loads for the horizontal connections, $\Delta_{nail\ slip,h}$, vertical connection, $\Delta_{nail\ slip,v}$, and hold downs, Δ_a are also required to calculate the anticipated deflection at the design shear load, v .

$$\delta_{sw} = \frac{576vb_s h^3}{EI_{eff}} + \frac{vb_s}{GA_{eff}} + 3\Delta_{nail\ slip,h} + 2\Delta_{nail\ slip,v} \frac{h}{b_s} + \Delta_a \frac{h}{\Sigma b_s} \quad (4.1)$$

The measured force-deformation response of the wall assembly will be compared to the results of this equation. Results of the tests will be compared with connection level testing and manufacturer literature to determine the adequacy of calculating strength based on the shear resisting elements and panel-to-panel connections. In order to accurately determine and predict and analyze the behavior of these wall assemblies, connection level tests on the various components were performed.

4.3 CONNECTION TESTING AND HYSTERESIS PARAMETER DEVELOPMENT

As the performance of the various connecting elements plays such a significant role in the overall behavior of CLT shear wall systems, some of the individual components that make up the final tested assembly were individually experimentally tested.

4.3.1 Monotonic Testing of SD10212

The first experimental test examined the lateral performance of Simpson SD10212 screws which were used in the AE116 angle brackets. The calculation of the lateral capacity of the screw fasteners following the National Design Specification for Wood Construction (AWC, 2018) produced an ASD capacity of 1.28 kN (287 pounds) when assuming a duration factor, $C_D = 1.6$. This calculation assumed connection between Spruce-Pine-Fir CLT ($SG = 0.42$) with an 11-gauge steel side plate (0.125 in, 3.18 mm). The shaft diameter (0.162 in, 4.12 mm) was used for the purpose of the calculations as it was assumed that the threaded portion of the fastener was sufficiently far away from the connector shear plane as referenced by Appendix I of NDS 2018 (AWC, 2018). The controlling yield mode was found to be yield mode IIIs where a plastic hinge develops, and crushing occurs in the side member. The reference lateral design value, Z , was found to be 0.8 kN (179.9 pounds). A total of 5 screws were tested monotonically to determine their performance. The test setup tested the lateral capacity of the 6.35mm x 63.5mm (0.25in x 2.5in) screws shown in Figure 4.1. The results of each of the tests is shown in Figure 4.2 and with peak values reported in Table 4.1.



Figure 4.1: Simpson SD10212 screw tested in shear

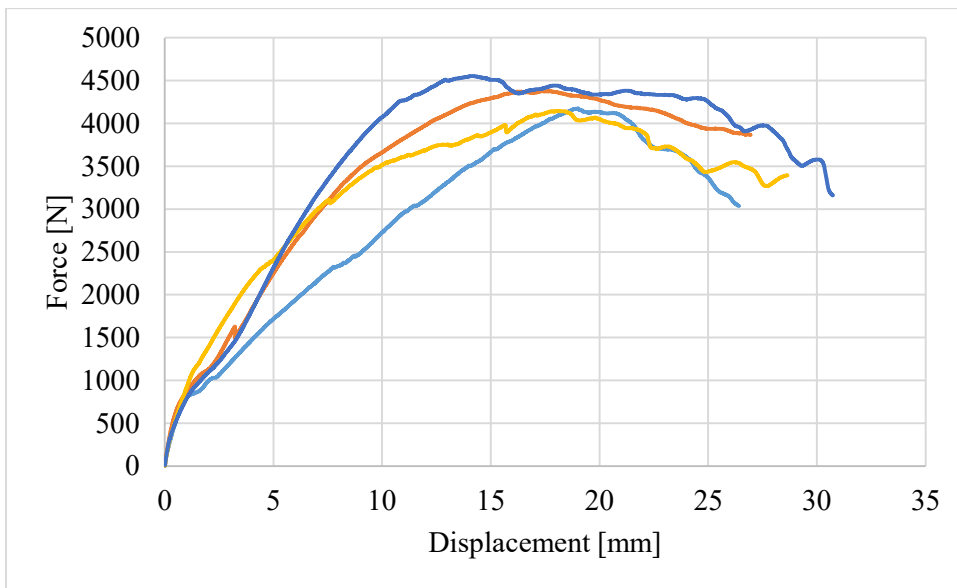


Figure 4.2: Results of monotonic lateral test of Simpson SD10212 screws

Table 4.1: Peak values from monotonic tests of Simpson SD10212

Test No.	Value	Units
Test 1	4.15	kN
Test 2	4.38	kN
Test 3	4.18	kN
Test 4	4.56	kN
Average	4.32	kN
Standard Dev.	0.191	kN

The results of the monotonic tests produced peak values averaging 4.32 kN (970 pounds) with a standard deviation of 0.191 kN (43 pounds). The resulting factor of safety averages 3.38. The deformed shape of the screw after testing presented a combination of Mode IIIs and Mode IV yielding. This is likely because the oversized hole in the connector allowed for rotation of the fastener at early levels of load after which yielding occurred at both the interface and the point at which the threads begin. Figure 4.2 shows the deformed screw after the monotonic testing exhibiting two plastic hinges.



Figure 4.3: Deformed shape of screw tested monotonically in shear

4.3.2 Uplift Testing of AE 116

In addition to the screws tested in shear, the fully attached Simpson AE116 angle brackets were also tested in uplift and shear. The testing plan for the Simpson AE 116 angle brackets shown in Figure 4.4 included both monotonic and cyclic tests. These tests correspond to the performance of the connector in the F_1 and F_4 directions.

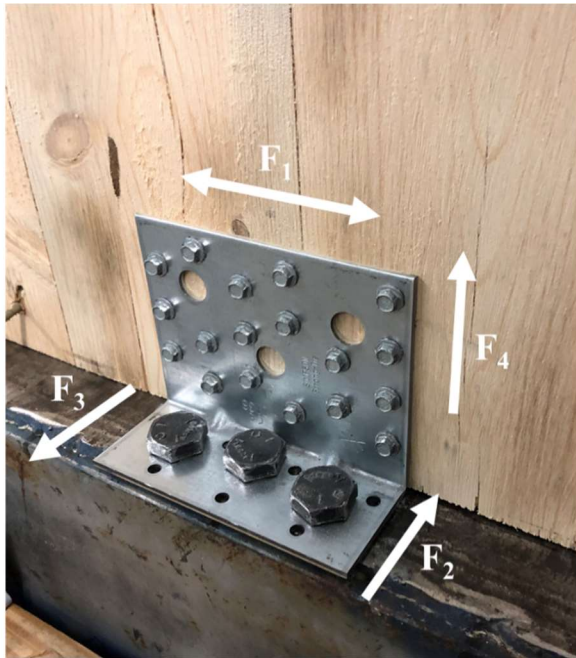


Figure 4.4: Test setup of uplift tests of AE 116 shear brackets

Each of the angle brackets were tested using (18) Simpson SD10212 screws to connect the vertical leg of the bracket and (3) 12.7 mm (0.5 in) bolts to connect the horizontal member per the manufacturer recommendation. The test schedule included one monotonic test and three one-sided cyclic tests. The force displacement response of the monotonic uplift tests is shown in Figure 4.5 measured as an average of the two corners of the angle bracket as measured by string potentiometers.

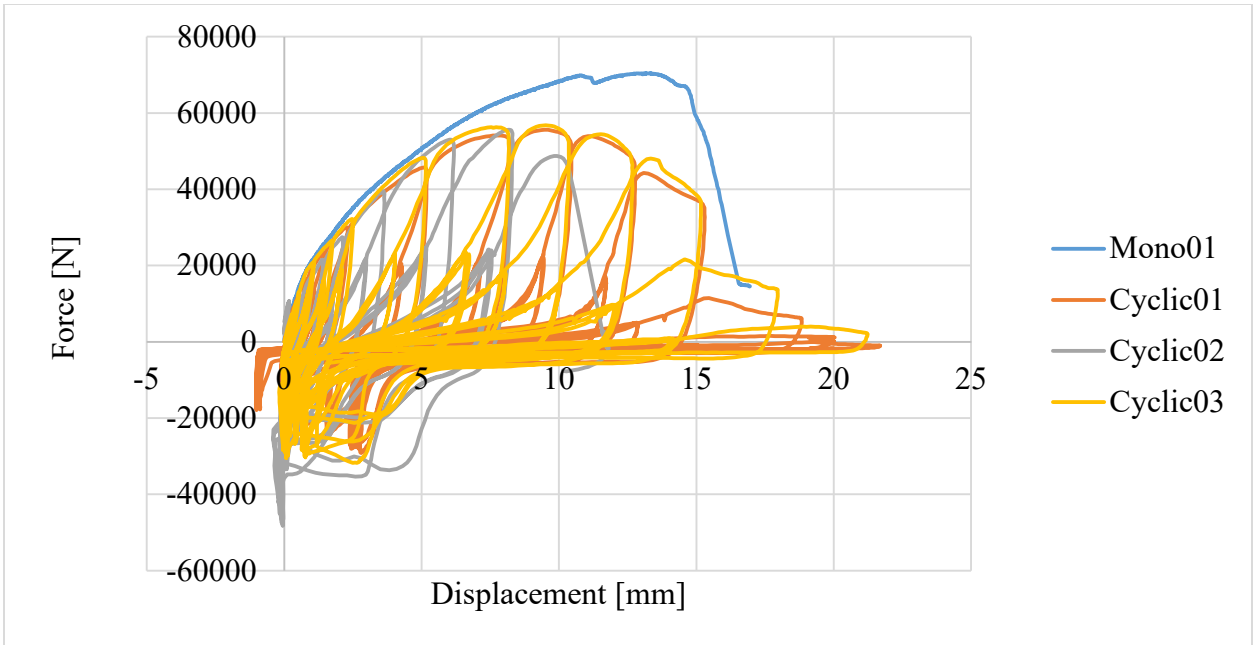


Figure 4.5: Monotonic and cyclic uplift response of AE 116 connector

Results of the monotonic tests resulted in a peak force of 70.4 kN (15.8 kip) at approximately 12.7 mm (0.5 in) displacement. The failure mechanism of the monotonic tests was rupture of the bracket as shown by Figure 4.6. In addition, the deformation occurred primarily in the bending of the bracket and shear of the fasteners.



Figure 4.6: Monotonic uplift testing failure

Based on the results of the monotonic testing, a modified one-sided CUREE protocol (CUREE, 2001) with a reference displacement of 10.2 mm (0.4 in) where instead of cycling between positive and negative displacements, each cycle returned to 0 displacement. The cyclic performance of the brackets in uplift exhibited different behavior than the monotonic tests as the fasteners were the primary failure and displacement mechanism as illustrated by Figure 4.7. This was likely due to the wedging that occurs as fasteners were loaded at lower intensity cycles. The changes in failure mechanism corresponded to a 20% drop in the peak load. Peak loads in the cyclic testing reached an

average of 56 kN (12.6 kip) with a standard deviation of 0.67 kN (0.15 kip). The peak force occurred at approximately 8.4 mm (0.33 in).



Figure 4.7: Cyclic uplift testing failure

4.3.3 Shear Testing of AE 116

The shear testing of the AE 116 connector followed a similar testing schedule as the uplift testing. A monotonic test was followed by two fully reversed cyclic tests. The results of the three experimental tests are shown in Figure 4.8. Peak load for the monotonic test was 39.3 kN (8.8 kip) occurring at approximately 28 mm (1.1 in). The load was applied at approximately the centerline of the fasteners in the vertical leg of the bracket. For cyclic loading, the reference displacement was set to 20.3 mm (0.8 in). Peak loads and deformation at peak load were consistent between cyclic and monotonic loads averaging

40.1 kN (9.02 kip) at a deformation of 25.4 mm (1 in). The primary deformation mechanism was fastener shear and connection rotation as shown in Figure 4.9. The connector rotation is likely due to the eccentricity between the application of the load and the plane of resistance of the bolts. The connector rotation is further shown in Figure 4.10 with a deformed shear bracket (left) compared to an undeformed bracket (right).

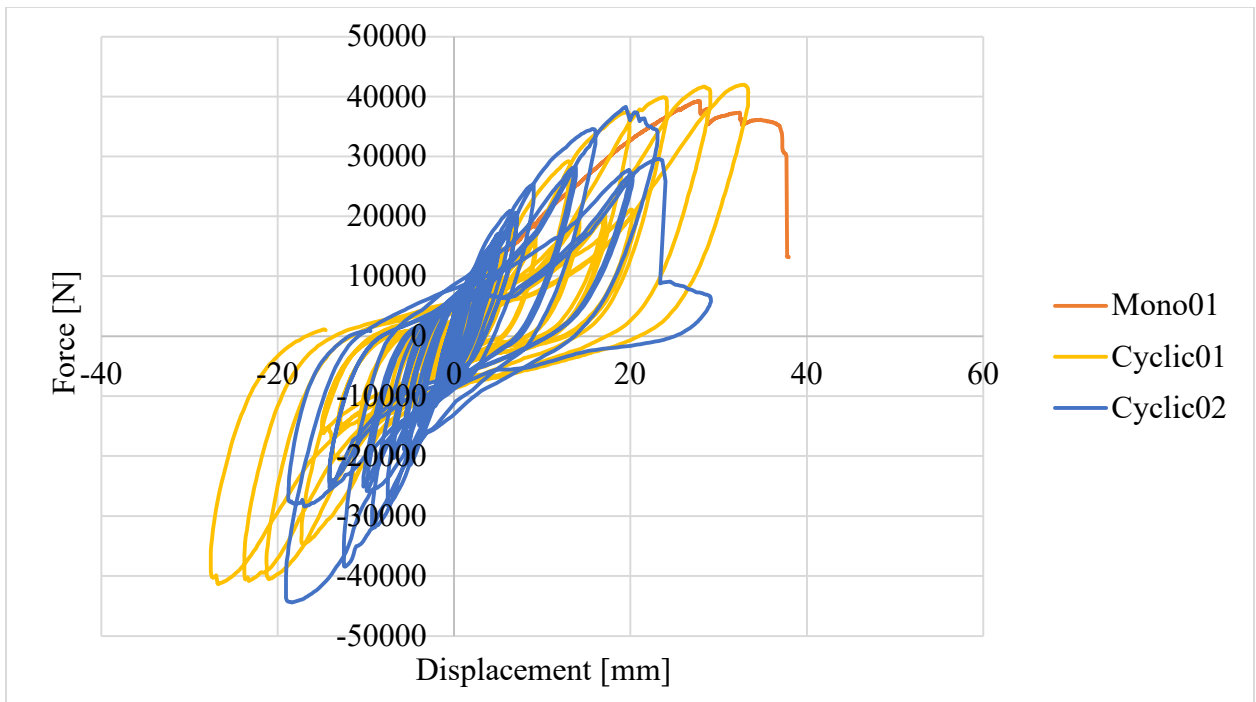


Figure 4.8: Monotonic and cyclic shear response of AE 116 connector



Figure 4.9: Connector rotation and fastener shear typical of shear deformation of AE 116



Figure 4.10: Comparison of deformed shape after cyclic loading (left) with undeformed shear bracket (right)

4.3.4 Hysteresis Parameters

In order to utilize the performance of the connectors in numerical models, the cyclic performance the AE 116 brackets was fit to a set of parameters known as the Modified STEWart (MSTEW) model, also referred to as the CUREE model (Folz and Filiatrault 2001). This hysteretic model consists of 10 parameters (K_o , r_1 , r_2 , r_3 , r_4 , F_o , F_i , δ_u , α , and β) that are depicted by Figure 4.11 and is used to describe timber engineering connections and assemblies. The uplift and shear parameters are given in Table 4.2.

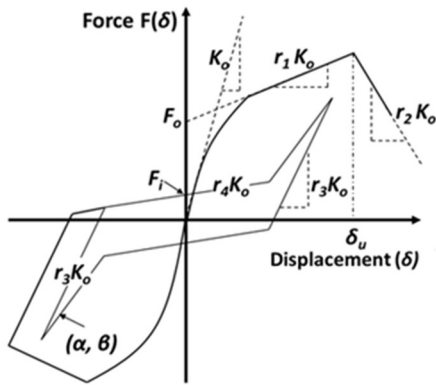


Figure 4.11: Modified Stewart (MSTEW) hysteretic rule to describe connection behavior

Table 4.2: MSTEW parameters for AE 116 connectors in uplift and shear

Parameter	Shear	Uplift
K_o [N/mm]	4.12	21.88
r_1 [-]	0.21	0.09
r_2 [-]	-0.17	-0.15
r_3 [-]	1.00	1.00
r_4 [-]	0.01	0.03
F_o [kN]	16.7	41.8
F_i [kN]	2.67	3.34
δ_u [mm]	28.96	8.89
α [-]	0.80	0.80
β [-]	1.10	1.10

Additional connection parameters were taken from previous experimental testing to estimate the parameters representing the performance of the screws used to connect two perpendicular wall elements and connection between in-plane walls. The connection between out-of-plane and in-plane walls was made using Simpson SDWS 22800DB measuring 5.6 mm x 203 mm (0.22 in x 8 in). The parameters used were based on monotonic tests of the screw shown in Figure 4.12 (B. Bhardwaj, personal communication, October 26, 2019).



Figure 4.12: SDWS screws used in connection between in-plane and out-of-plane walls

The connection used in half-lap was made using Simpson SDS25300 screws measuring 6.4 mm x 76.2 mm (0.25 in x 3 in). All hold-downs used in testing were Simpson HD12 shown in Figure 4.13. The parameters for the panel-to-panel connections and hold-downs were estimated based on the comparison of the experimental tests of Simpson SD10212 to values of strength and stiffness calculated by NDS 2018 and Eurocode 5 (EN-1995, 2004). The equation describing stiffness of a dowel type fastener,

γ , from NDS and Eurocode are shown in Table 4.3 for metal-to-wood connections, where D is the diameter of the fastener and ρ is the density of the wood member.



Figure 4.13: Simpson HD12 hold-down used in testing

Table 4.3: Stiffness estimates for dowel type fasteners in NDS and Eurocode

	NDS 2018	EN 1995-2004
Wood-to-Wood	$\gamma = 180,000 \times D^{1.5}$ [lb/in]	$\gamma = \rho^{1.5} \times D / 23$ [N/mm]
Metal-to-Wood	$\gamma = 270,000 \times D^{1.5}$ [lb/in]	$\gamma = (2 \times \rho)^{1.5} \times D / 23$ [N/mm]

Both the NDS and Eurocode equations overestimate the initial stiffness of the tested Simpson SD10212 screw assemblies. In order to estimate the initial stiffness of screw connections using SDS25300 screws and HD12 hold-downs, half of the stiffness produced from the Eurocode 5 equations was used to determine the initial stiffness of these connections. In order to estimate the peak strength of these connections, the ratio of ASD design to peak ultimate force measured in the test of the Simpson SD10212 screws was used to estimate the peak force from the ASD design value per the manufacturer literature for the hold-down (Simpson Strong Tie, 2019) and yield mode equations in NDS for the screw connection. The estimates for strength and stiffness are shown in Table 4.4. In addition, the full set of MSTEWS parameters are shown in Table 4.5 for each of the connection types including the SDWS screws.

Table 4.4: Estimates of strength and stiffness of hold-down and screws not directly tested

Connection Description	Published/Calculated ASD Strength [kN]	Estimated Peak Load [kN]	Estimated Connection Stiffness (EC5) [kN/mm]
SD25300	1.03	3.48	2.71
HD12	45.3	153	108

Table 4.5: MSTEWS Parameters for HD12, SDS25300, and SDWS 22800DB

Parameter	HD12	SDS25300	SDWS 22800DB
K_0 [N/mm]	53.7	1.35	0.67
r_1 [-]	0.04	0.019	0.076
r_2 [-]	-0.2	-0.15	-0.5
r_3 [-]	1	1	1
r_4 [-]	0.01	0.01	0.005
F_0 [kN]	111.3	2.9	12.1
F_i [kN]	15.6	0.3	2.1
δ_u [mm]	29.5	30.5	64.9
α [-]	0.5	0.5	0.75
β [-]	1.1	1.1	1.2

4.4 FULL-SCALE TESTING

4.4.1 Experimental Test Setup

A series of full-scale experimental lateral tests were performed to determine the effect of the out-of-plane walls on the strength and stiffness of the assembly and whether this contribution could be analytically derived from the behavior of the various connections. Two wall assemblies were tested, one with out-of-plane walls and one with only in-plane walls. The test setup consists of two 1.18 m x 2.44 m (46.5 in x 96 in) 3-ply CLT walls connected with half-lap connections. In addition, there were 1.22 m x 2.44 m (48 in x 96 in) walls as the out-of-plane walls used in one of the experimental tests to demonstrate its effect on the performance of the assembly. The bottom and top of each wall panel, both in-plane and out-of-plane, were connected using two AE116 connections. Each end of the bottom of the in-plane and out-of-plane walls were connected using

Simpson HD12 hold-downs. A schematic of the test setup is shown in Figure 4.14 with the presence of the out-of-plane walls. The in-plane only wall test is shown in Figure 4.15.

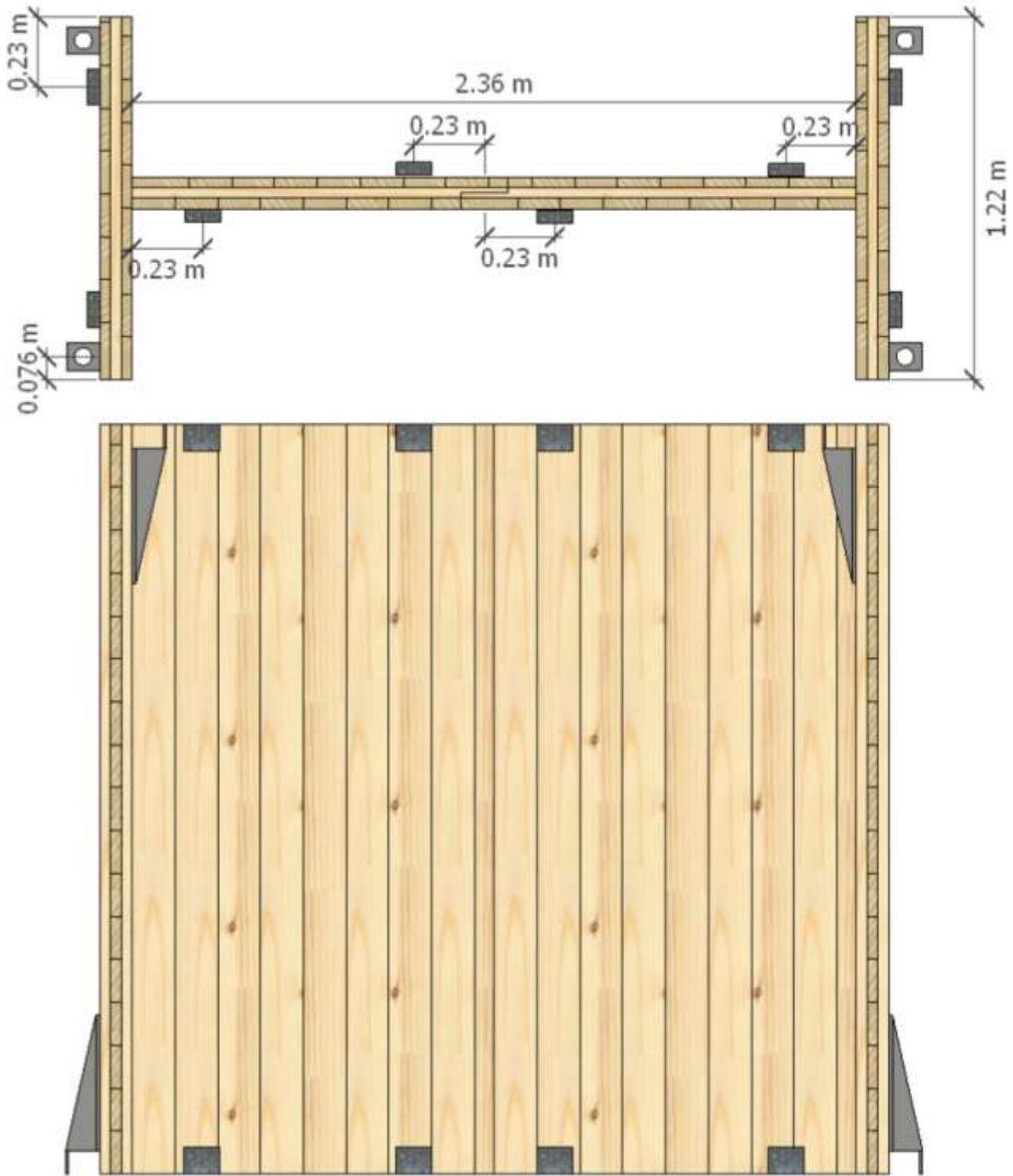


Figure 4.14: Schematic setup of experimental test with out-of-plane walls

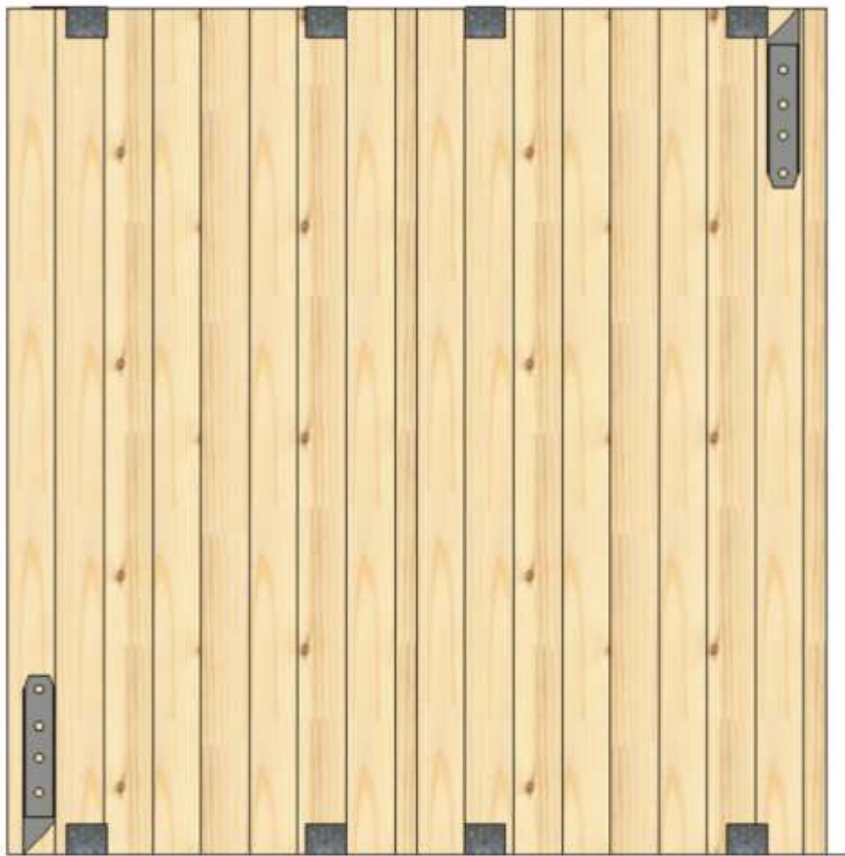
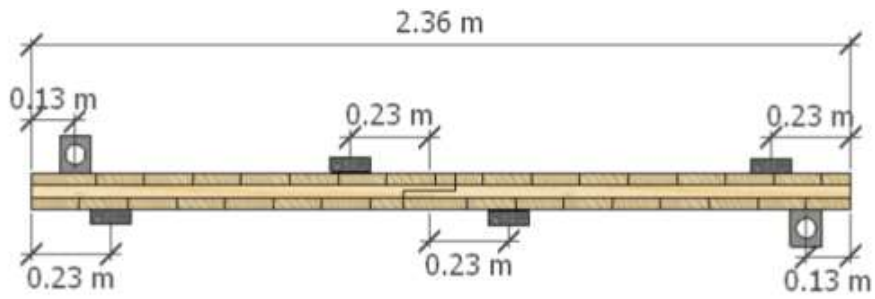


Figure 4.15: Schematic of experimental test setup with only in-plane walls

The instrumentation plan for the wall assembly tests were meant to capture the various deformations associated with the global deformations of the system. In total, 14 string potentiometers and four load cells will be used to track the component deformations

and load in each hold-down. Table 4.6 and Figure 4.16 outline the location and purpose of each of the sensors utilized in the testing assembly.

Table 4.6: Instrumentation outline for shear wall assembly tests

Sensor Number	Measurement Type	Description
1	Displacement	Total deformation of wall
2	Displacement	Sliding of wall at base
3*	Displacement	Uplift of right out-of-plane wall
4	Displacement	Uplift of right in-plane wall (right end)
5*	Displacement	Uplift of right in-plane wall (left end)
6*	Displacement	Uplift of left in-plane wall (right end)
7	Displacement	Uplift of left in-plane wall (left end)
8*	Displacement	Uplift of left out-of-plane wall
9*	Displacement	Slip between out-of-plane and in-plane wall (right)
10	Displacement	Slip between in-plane walls (center)
11*	Displacement	Slip between out-of-plane and in-plane wall (left)
12	Displacement	Diagonal 1
13	Displacement	Diagonal 2
14	Displacement	Sliding of wall at top
15	Force	Hold-down 1
16*	Force	Hold-down 2
17	Force	Hold-down 3
18*	Force	Hold-down 4

*Only present in tests with out-of-plane walls

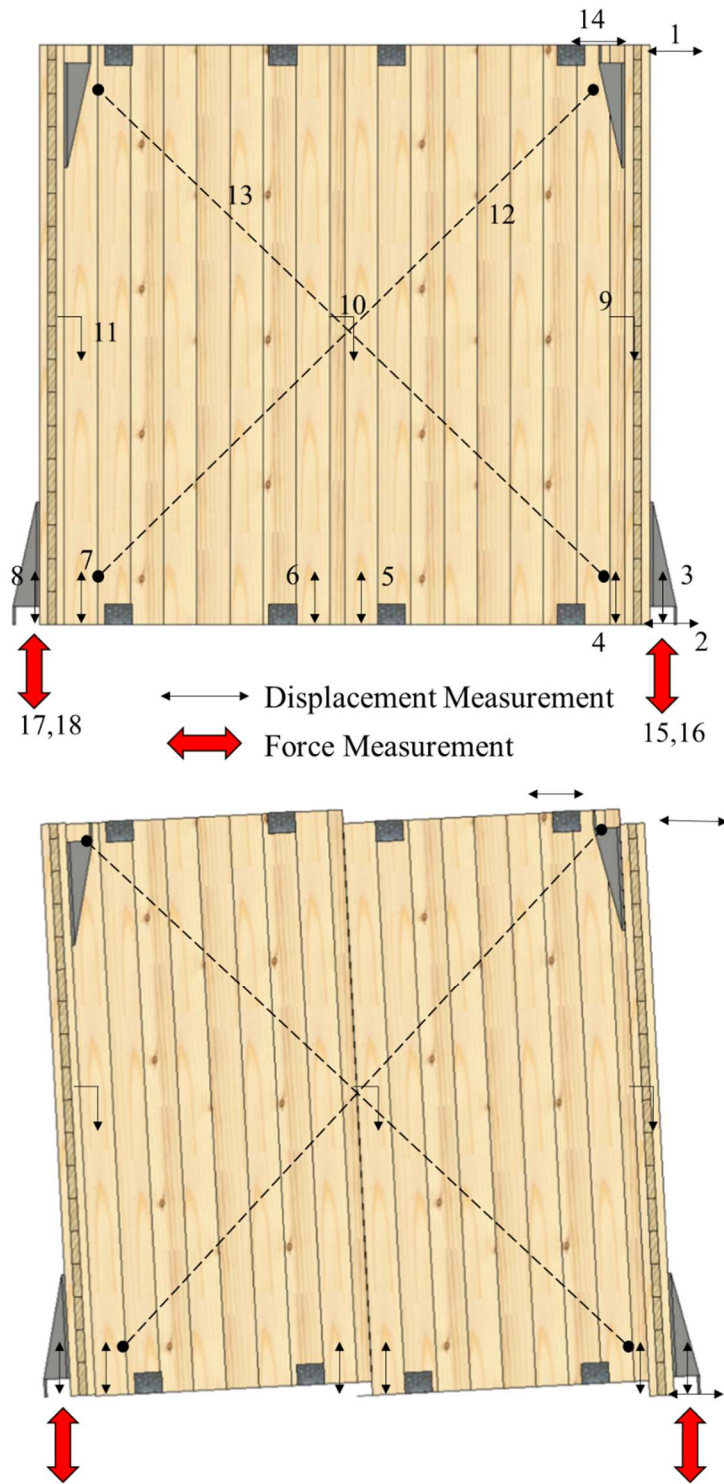


Figure 4.16: Instrumentation plan of wall assemblies

4.4.2 Stiffness Test of Wall Assemblies

In addition to destructive cyclic testing, incremental tests were performed to capture the stiffness of each of the components and the stiffness of the final assembly. The first measurement of stiffness was taken when the wall assembly had only the in-plane walls installed. Next, the assembly was tested with the right out-of-plane wall installed. Finally, the stiffness was measured with both out-of-plane walls installed. This progression of the stiffness test assemblies is shown in Figure 4.17. The stiffness of each segment was measured by performing cycles at low levels of displacement up to 1.25 mm (0.05 in) of top of wall displacement as measured at the actuator. The protocol of this stiffness test is shown in Figure 4.18 showing the displacement time history of the actuator.



Figure 4.17: Progression of stiffness tests: in-plane only, one out-of-plane wall, two out-of-plane walls (top to bottom)

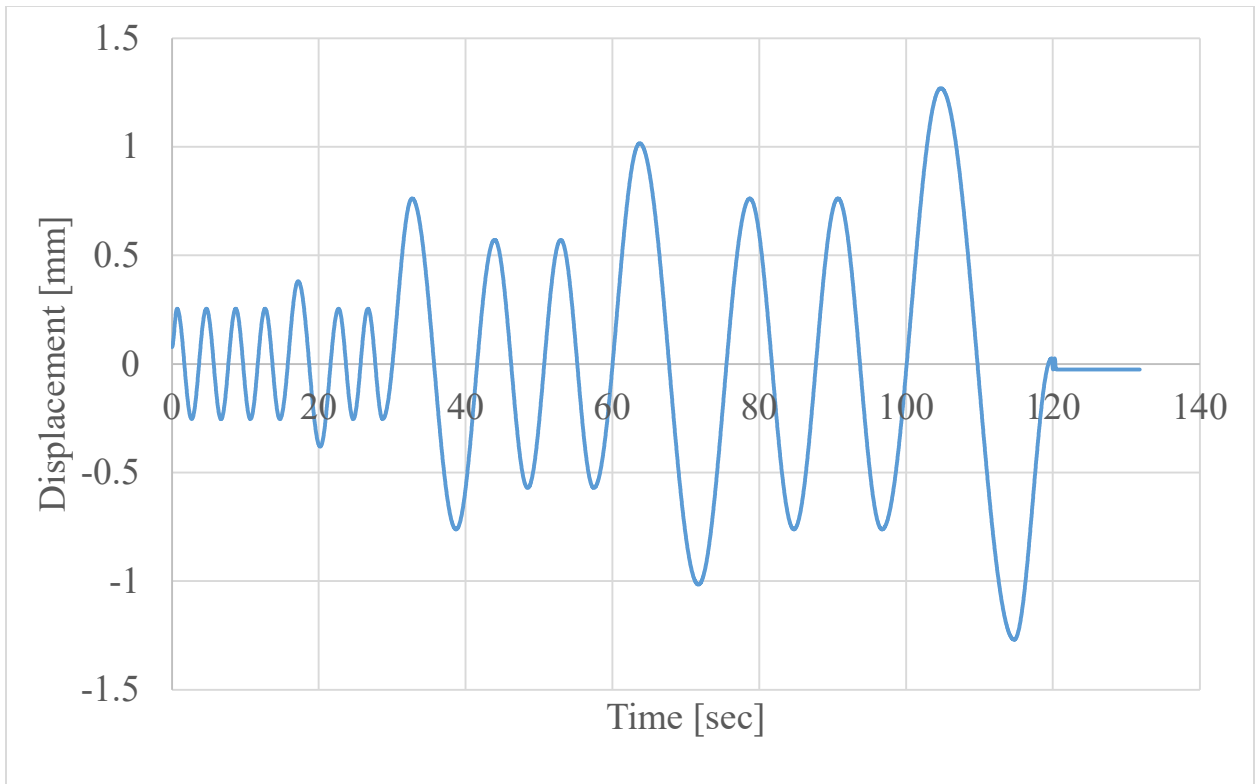


Figure 4.18: Displacement time history procedure used to determine initial stiffness of wall assemblies

Results of the stiffness test underscored the influence of the out-of-plane walls and their connections on the stiffness of the assembly. Figure 4.19 shows the force-displacement response of each of the assemblies subjected to the displacement protocol.

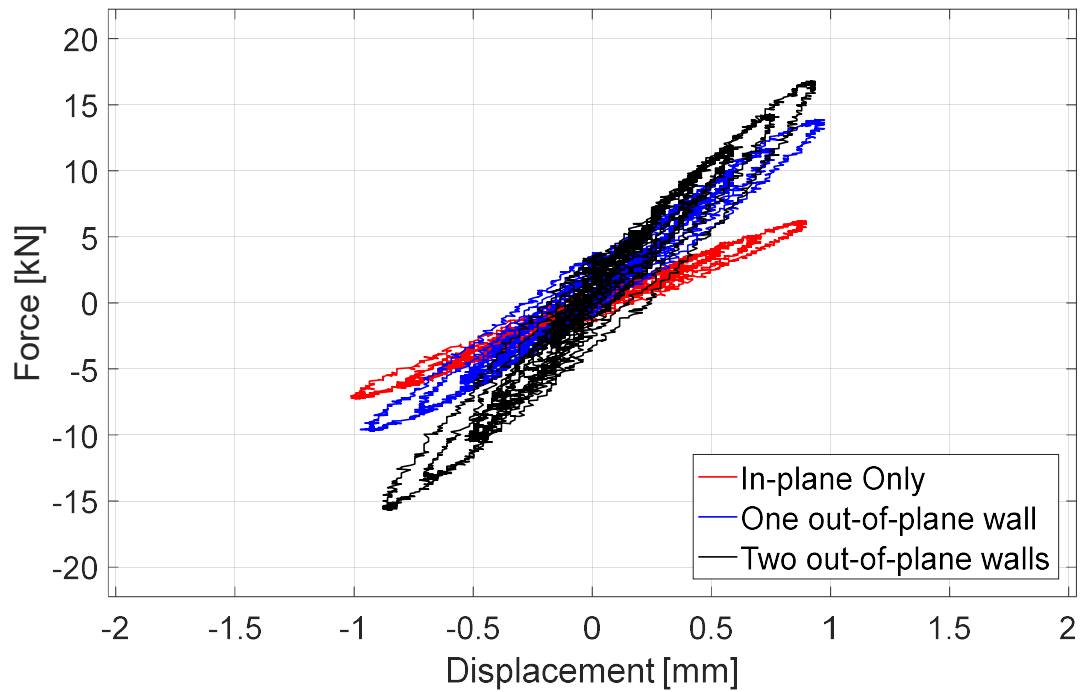


Figure 4.19: Force-displacement response of stiffness tests on wall assemblies

The approximate linear stiffness of each of the three stiffness tests is shown in Table 4.7 and illustrates in the added stiffness that comes with the out-of-plane walls. For symmetrical tests 1 and 3, the positive and negative stiffness values are comparable; however, for the second stiffness test, the out-of-plane wall helps significantly more in tension (actuator push cycle) than it does in compression (actuator pull cycle). Increases in stiffness were due to both the additional hold-down restraint and the resistance to shear and uplift deformations from the additional AE1 16 connectors on the out-of-plane walls.

Table 4.7: Results of stiffness tests performed on wall assembly 1

Stiffness Test No.	Description	Positive Stiffness at 1 mm [kN/mm]	Percent Increase from Test 1 - Positive	Negative Stiffness at 1 mm [kN/mm]	Percent Increase from Test 1 - Negative
1	In-plane walls only	7040	-	7300	-
2	One out-of-plane wall	14830	111%	10340	42%
3	Both out-of-plane walls	18330	160%	18240	150%

4.4.3 Destructive Testing of Wall Assemblies

The destructive test of wall assemblies 1 and 2 followed the CUREE hysteresis protocol outlined in ASTM E2126 Method C (ASTM, 2018). For this test, a reference displacement of 19 mm (0.75 in) was used to develop the protocol. This estimate was based on the component level testing of connections in the assembly which exhibited failure at relatively low displacement levels, understanding that the system may produce a more ductile response. The protocol used is shown in Table 4.8. where $\alpha = 0.2$.

Table 4.8: Displacement procedure for destructive testing of wall assemblies

Step	Number of Cycles	Amplitude (% of reference displ.)
1	6	5
2	1	7.5
3	6	5.625
4	1	10
5	6	7.5
6	1	20
7	3	15
8	1	30
9	3	22.5
10	1	40
11	2	30
12	1	70
13	2	52.5
14	1	100
15	2	75
16	1	$100 + 100\alpha$
17	2	$0.75 \times (100 + 100\alpha)$

The global force-displacement response of wall assemblies 1 and 2 are both shown in Figure 4.20. The results show that the out-of-plane walls increased the strength and stiffness of the assembly when compared to a traditional, in-plane only wall assembly. The ultimate strength, displacement at ultimate strength, and ultimate unit shear are summarized in Table 4.9.

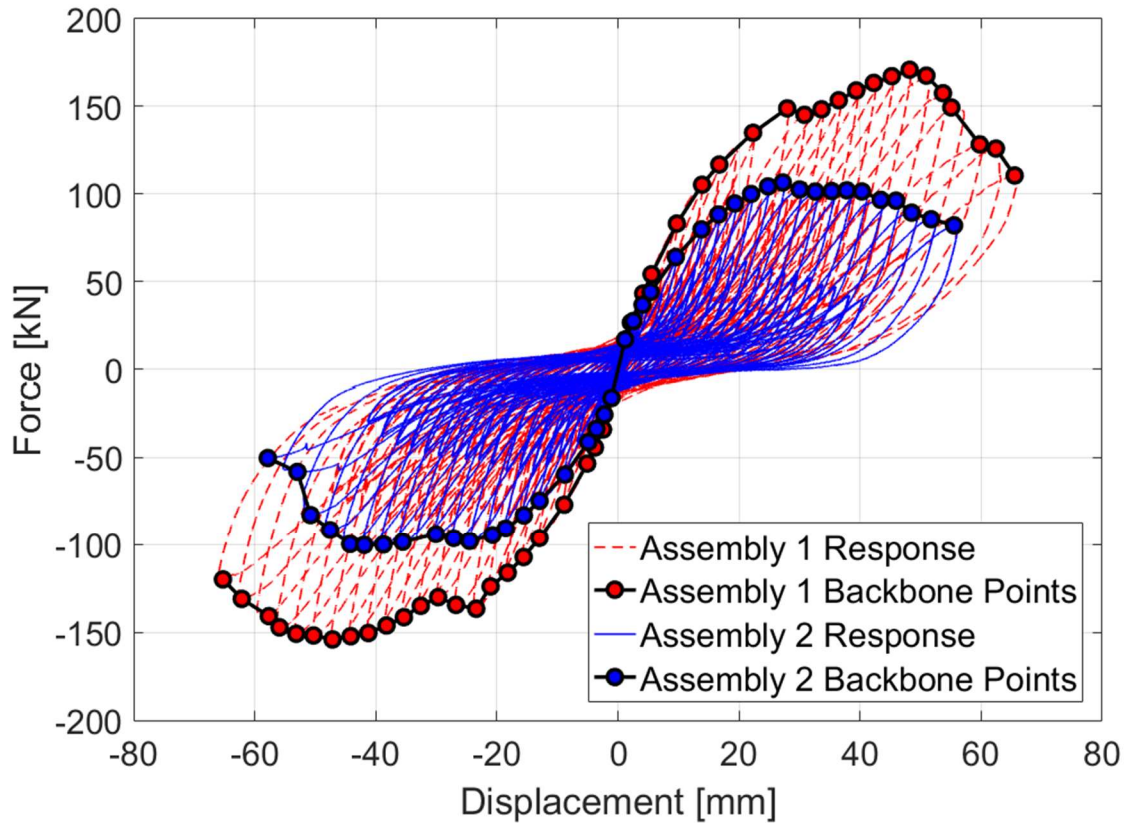


Figure 4.20: Force-displacement response of wall assemblies with and without out-of-plane walls

Table 4.9: Peak force and displacement of wall tests

Test No.	Peak Positive Force [kN]	Displacement at Peak Positive Force [mm]	Peak Negative Force [kN]	Displacement at Peak Negative Force [mm]	Average Peak Unit Shear [kN/m]
1	171.0	48	154.2	47	68.8
2	106.5	27	100.2	42	43.8

To understand the deformation behavior of the wall assemblies, the displacement of the string pots at the peaks of the cyclic protocol was plotted as a function of time in Figures 4.21 and 4.22 for wall assemblies 1 and 2 respectively. In wall assembly 1, this

comparison shows that comparatively, the deformation is dominated by the panel-to-panel connection (SP10). The deformations are mirrored by the uplift at the base of the wall assembly at the panel-to-panel connection (SP5 and SP6). Later in the test, the sliding deformations (SP14) increase. Similar trends are seen in wall assembly test 2 where deformations at the panel-to-panel connection (SP10). Deformations due to rocking were approximately equal for the panel ends (SP4 and SP7) as they were at the base of the assembly at the panel-to-panel connection (SP5 and SP6). Sliding deformations again began to increase near the very end of the test.

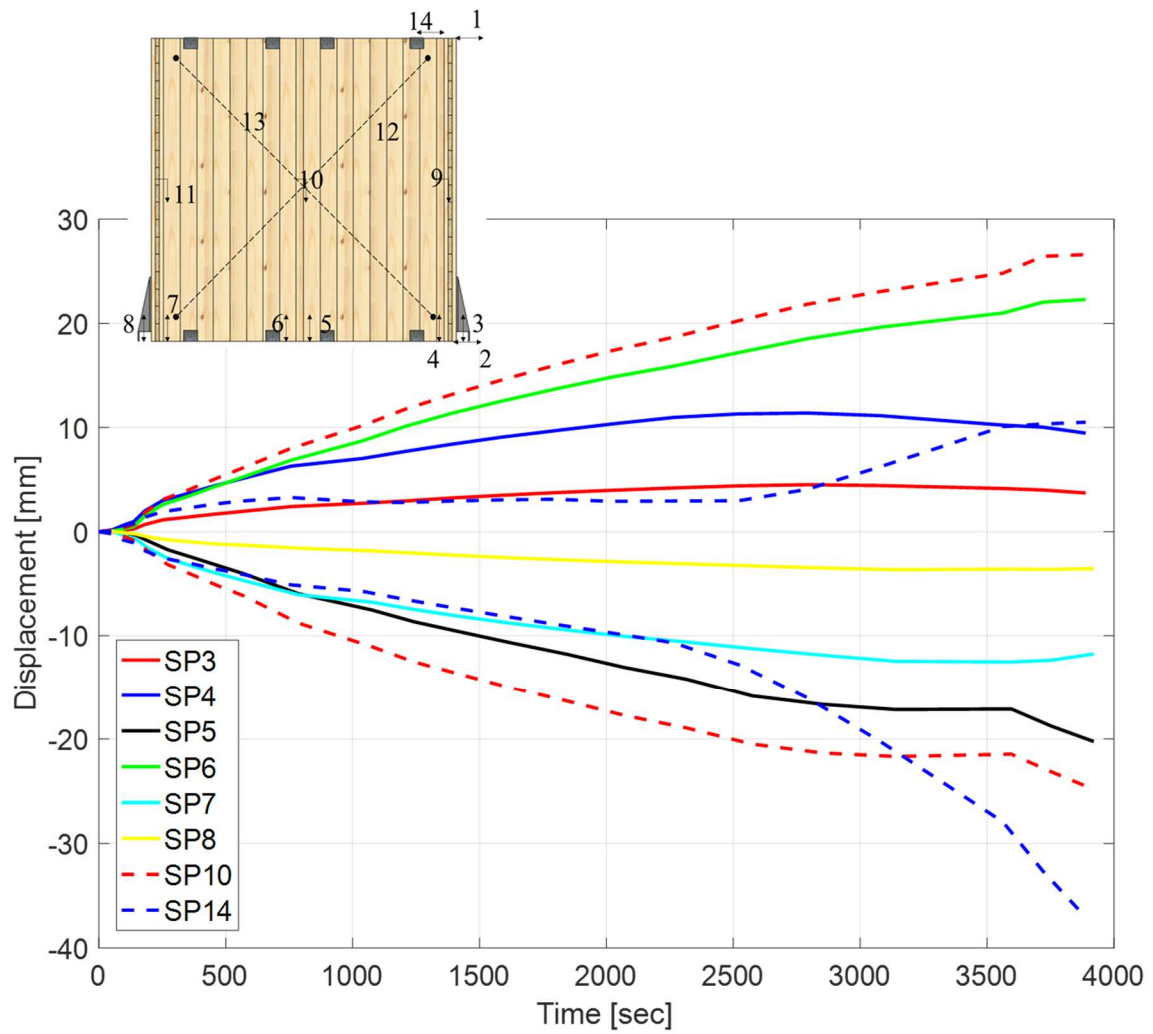


Figure 4.21: Measured deformations of string pots at displacement peaks for wall test with out-of-plane walls

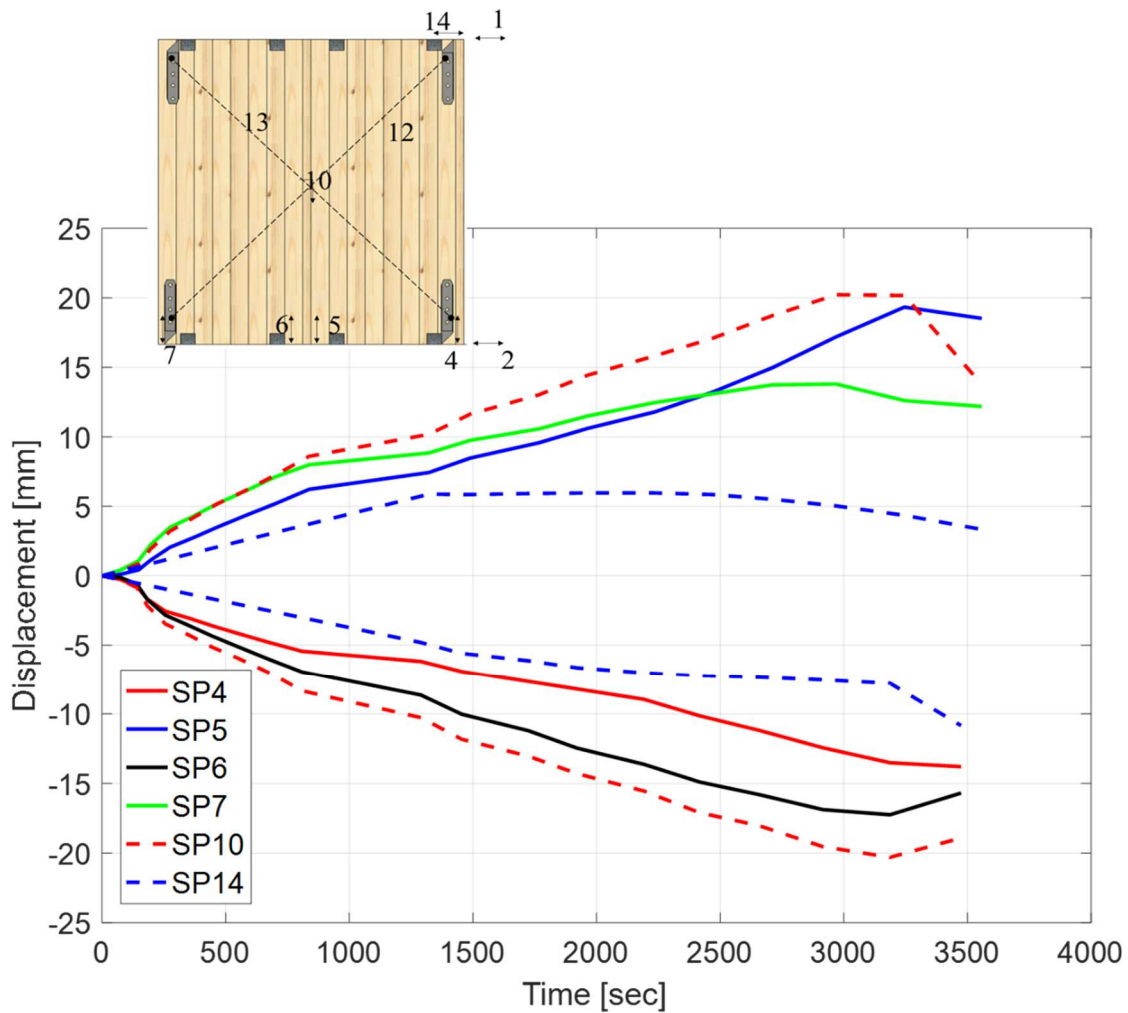


Figure 4.22: Measured deformation of string pots at displacement peaks for wall test with in-plane walls only

Detailed information about the rocking of the panel assembly is shown in Figure 4.23 for test number 1 and Figure 4.24 for test number 2, which show that for both tests, uplift deformations were predominately in SP5 and SP6 indicating panel uplift at the center of the wall. In the results from test number 1 the uplift of the return walls (SP3 and SP8) is relatively low compared to the uplift at the panel-to-panel connection. This also indicates that hold downs are activated and restricting the deformation at the wall boundaries.

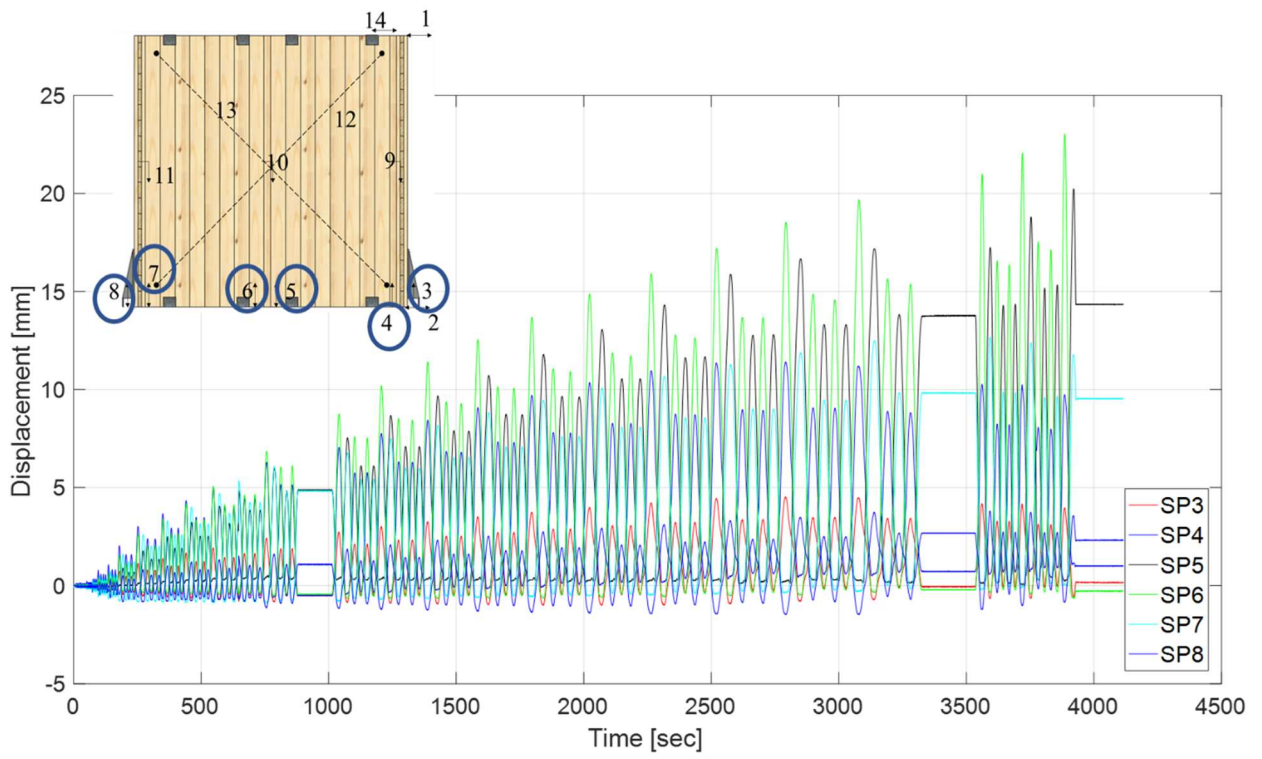


Figure 4.23: Uplift of wall assembly in test with return walls

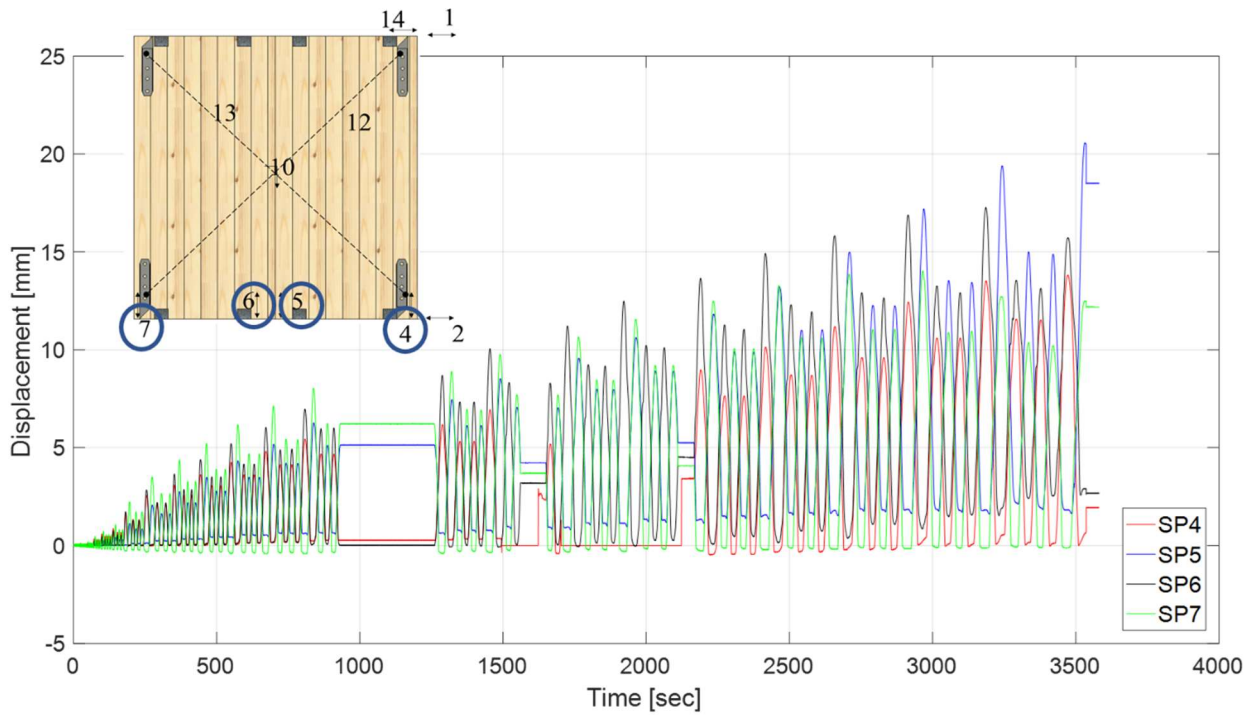


Figure 4.24: Uplift of wall assembly in test with in-plane walls only

The panel-to-panel deformations at the half-lap connection and connection between in-plane and out-of-plane panels for test number 1 also indicated that the half-lap connection was the primary deformation mechanism throughout most of the test. Figure 4.25 and Figure 4.26 for tests 1 and 2 respectively. The slip between panels measured by SP10 is significantly more than the slip between in-plane and out-of-plane walls (SP9 and SP11) for wall test 1.

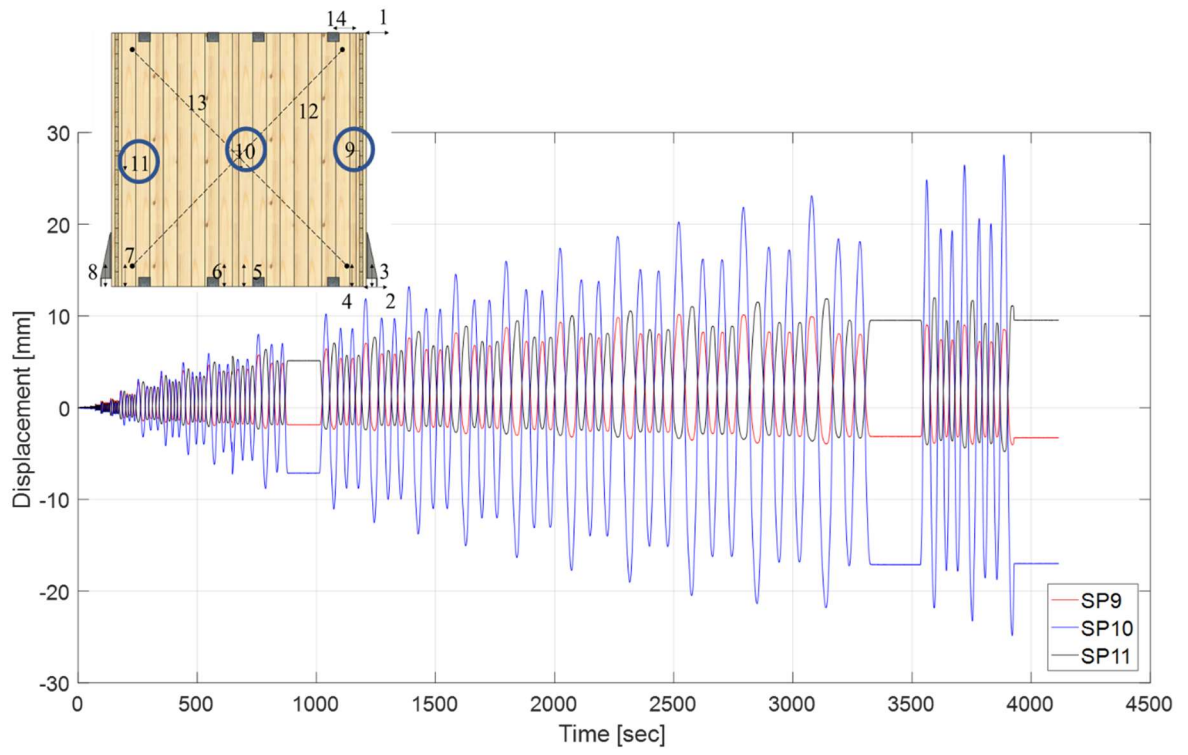


Figure 4.25: Panel-to-panel displacement for wall test with out-of-plane walls

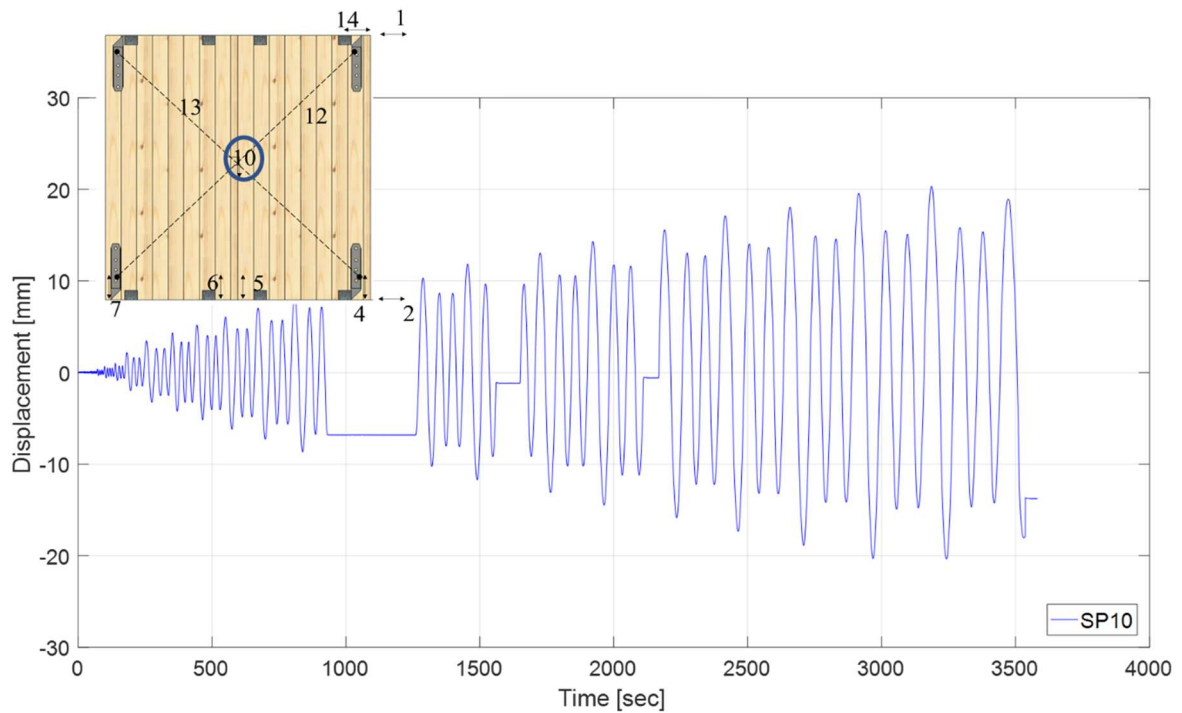


Figure 4.26: Panel-to-panel displacement for wall test with in-plane only walls

The sliding deformation at the top and bottom of the wall were also tracked as a function of time and showed that sliding deformations remained relatively low until later in the test. These deformations are shown in Figures 4.27 and 4.28 for test numbers 1 and 2 respectively. The deformation in both tests was larger at the top of the wall than it was at the bottom of the wall for both tests until the very end of test 2 where the sliding deformation at the bottom approached 15 mm (0.59 in). At the end of test 1, the sliding deformation at the top of the wall began to significantly increase approaching 35 mm (1.4 in).

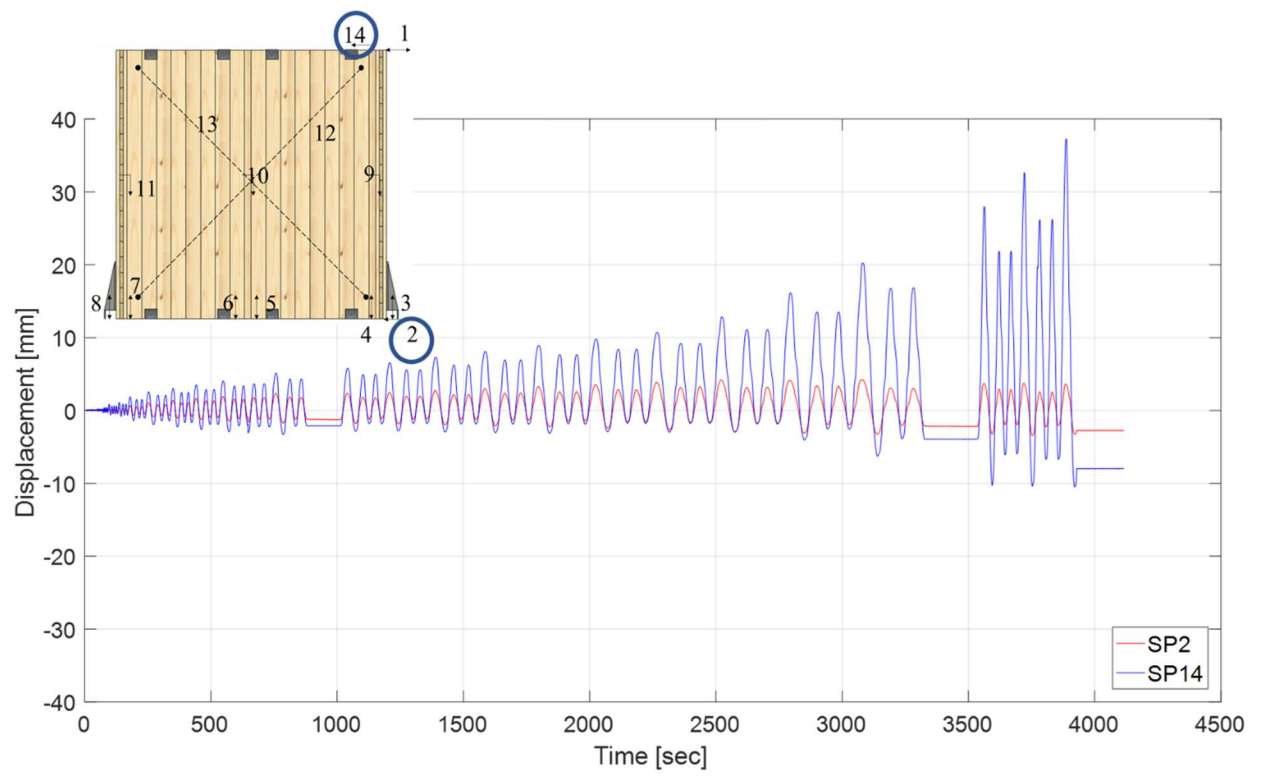


Figure 4.27: Sliding deformations at top and bottom of wall for wall test with out-of-plane walls

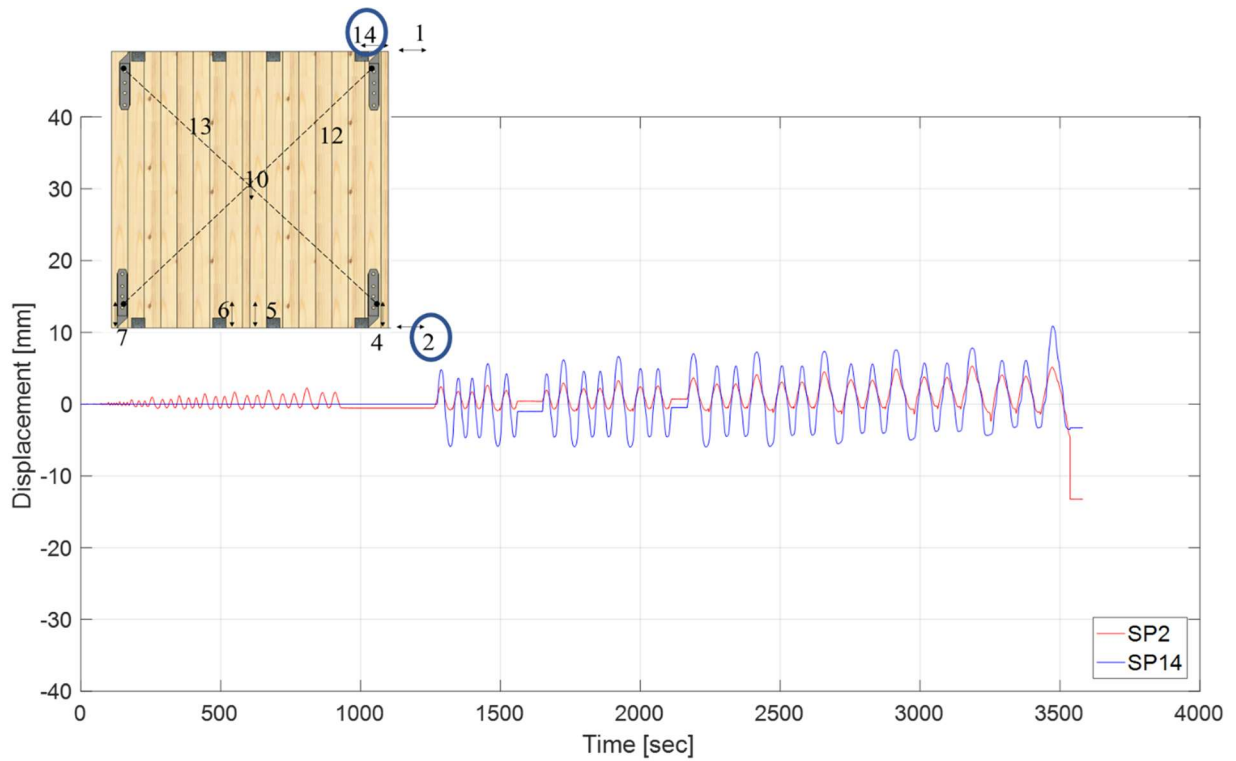


Figure 4.28: Sliding deformations at top and bottom of wall for wall test with in-plane walls only

4.4.4 Failure Analysis of Destructive Testing

Analysis of the failure of both wall assemblies indicated that fastener failure, primarily in the panel-to-panel connection and AE116 connections. The deformed shape at the end of each of the tests is shown in Figures 4.29 and 4.30 for wall tests 1 and 2 respectively. The primary deformations of rocking and panel-to-panel connection deformations are evident in the uplift at each end of the in-plane walls. In addition, there is separation of the in-plane walls in test 2. With the presence of the out-of-plane walls in test 1, there was little separation between in-plane panels as evident in test 2.



Figure 4.29: Deformed shape of wall test with out-of-plane walls



Figure 4.30: Deformed shape of wall test with in-plane walls only

Because of the nature of the spline connection, it was not possible to view the damage at the connection until after the wall was disassembled. Figure 4.31 shows the spline connection after the two in-plane walls were separated and the SDS screws after failure. All screws in the spline connection failed as shown.



Figure 4.31: Failure of half-lap connection examined after wall assembly removal

Failure was also evident in the in-plane AE 116 connections at the top and bottom of the walls. The failure of the in-plane AE116 connections at the bottom of the wall failed due to rupture of the connection as shown in Figure 4.32. This failure was like the failure experienced by the single connection tests performed previously. Failure at the top of the in-plane walls was due to fastener withdrawal and shear shown in Figure 4.33. Because the connection of both the vertical and horizontal leg of the AE 116 connection were made using screw connections, the screws in the horizontal leg incrementally withdrew from the bracket connection and ultimately failed in shear as portions of the SD10212 screws completely sheared. Screws with various states of deformation are shown in Figure 4.34. In addition, AE 116 connections located near the panel-to-panel connection experienced more damage due to the increased displacement demand on those connections.



Figure 4.32: Failure of AE116 connections at the bottom of in-plane walls

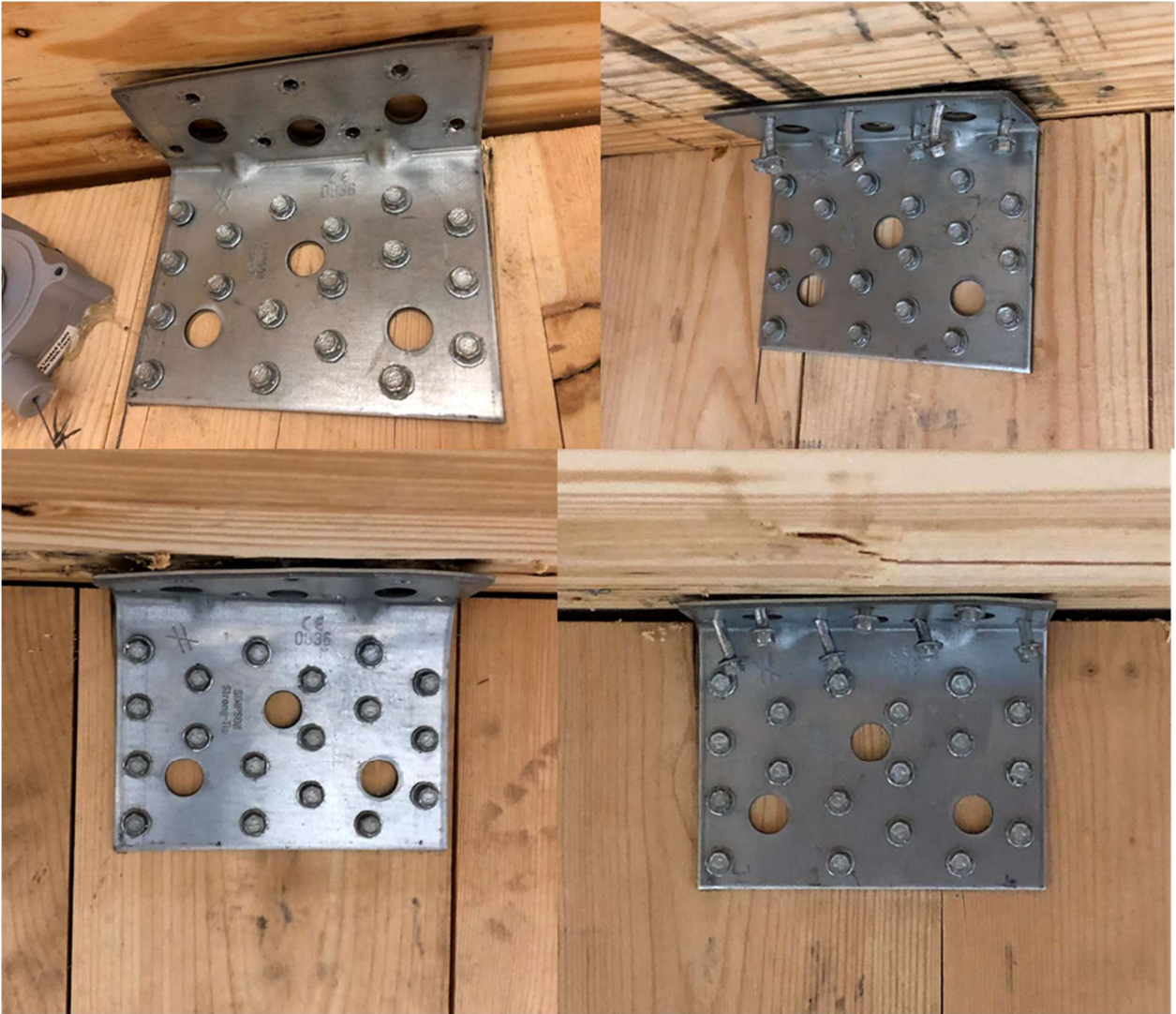


Figure 4.33: Failure of AE116 connections at the top of in-plane walls



Figure 4.34: Deformation of SD10212 screws used in AE116 connection

Additionally, deformations were observed in the out-of-plane AE116 connections present in wall test 1. These deformations were present only in the top of the out-of-plane walls as shown in Figure 4.35 and exhibited connection bending and some screw withdrawal.



Figure 4.35: Deformation of AE116 at the top of out-of-plane wall

There were also small deformations observed in the connection between in-plane and out-of-plane walls for wall test 1. These deformations are apparent in the form of screw head compression into the out-of-plane wall element shown in Figure 4.36.



Figure 4.36: Deformations in connection between in-plane and out-of-plane walls

In addition to the observable damage in the connection, minor damage was observed in the compression end of the in-plane walls. Crushing of the wood fiber was observed on the in-plane wall at the half-lap connection and shown in Figure 4.37. This crushing occurred at the half-lap due to the reduced wood section at the connection.



Figure 4.37: Crushing of wood at half-lap joint between in-plane wall

In summary, the deformation and failure of both wall tests followed the sequence shown below:

- Wall acts as single element with primary deformations due to rocking with all elements acting as a composite structure
- Panel-to-panel half-lap connection becomes primary deformation source and each panel rocks relatively independently
- AE 116 connectors near panel-to-panel connections at top and bottom experience deformations primarily due to uplift
- As half-lap connections fail and AE 116 fail in uplift, shear capacity begins to drop and sliding deformations become more significant

4.5 NUMERICAL MODELING

4.5.1 Introduction to and parameters used in *Timber3D*

Numerical models of the tested shear wall configurations were created in *Timber3D*, a three-dimensional model originally developed to capture the non-linear dynamic response and seismic performance of light-frame wood buildings (Pang, 2012). *Timber3D* operates through the Matlab platform and was created based on a co-rotational formulation and large displacement theory. Models are built using 3-dimensional, 2-node, 12-degree of freedom (DOF) beam elements called Frame3D elements. Connections between elements are modeled using 6-DOF Frame-to-Frame (F2F) link elements. Each of the 6-DOF can be assigned a different hysteretic performance including linear, non-linear elastic (NLE), MSTEW, among others. To simulate the performance of the experimental setup, each of the experimental test configurations was modeled to estimate and calibrate the performance based on the component strength and stiffness. An example of the *Timber3D* model is shown in Figure 4.38 labelling the Frame3D elements (left) and F2F link elements (right). In addition, the elements are described in Table 4.10. Figure 4.39 summarizes the parameters taken both from testing and estimated.

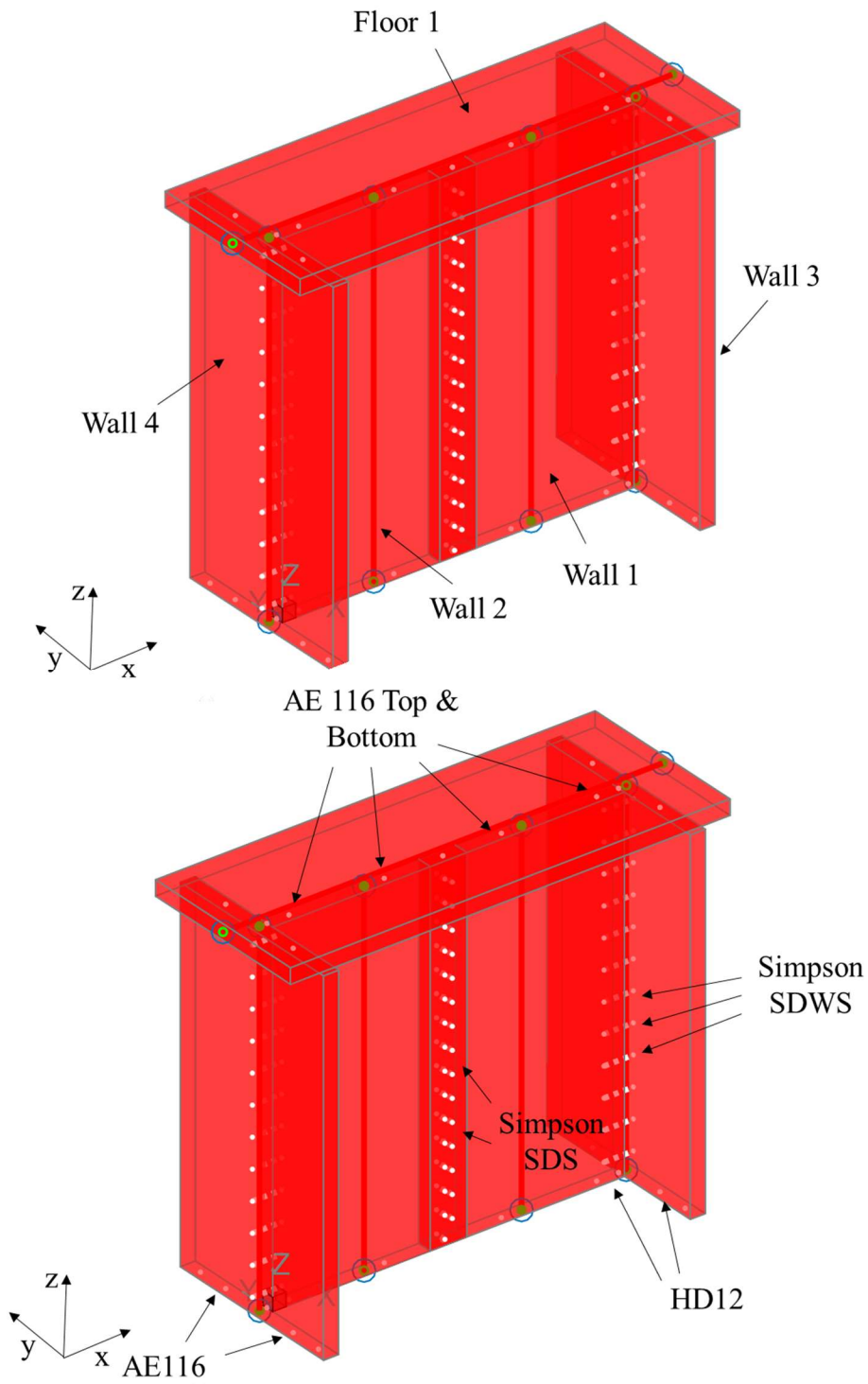


Figure 4.38: *Timber3D* representation of wall assemblies experimentally tested

Table 4.10: Description of member in *Timber3D* model

Element Name	Element Type	Parameter	Notes
Floor 1	Frame3D	Elastic Beam	Member to which load is applied
Wall 1	Frame3D	Elastic Beam	In-plane Wall (right)
Wall 2	Frame3D	Elastic Beam	In-plane Wall (left)
Wall 3	Frame3D	Elastic Beam	Out-of-plane Wall (right)
Wall 4	Frame3D	Elastic Beam	Out-of-plane Wall (left)
AE116	F2F	MSTEW	Uplift + shear values from testing; other directions have no strength/stiffness
HD12	F2F	MSTEW	Stiffness/strength estimated from manufacturer literature
SDWS Screws	F2F	MSTEW	Screw parameters estimated for connection between in-plane and out- of-plane walls
SDS Screws	F2F	MSTEW	Screw parameters estimated for half- lap connection
Bearing Elements	F2F	Non-linear Elastic	Keeps beam elements from going below base of wall and act as bearing between beam elements

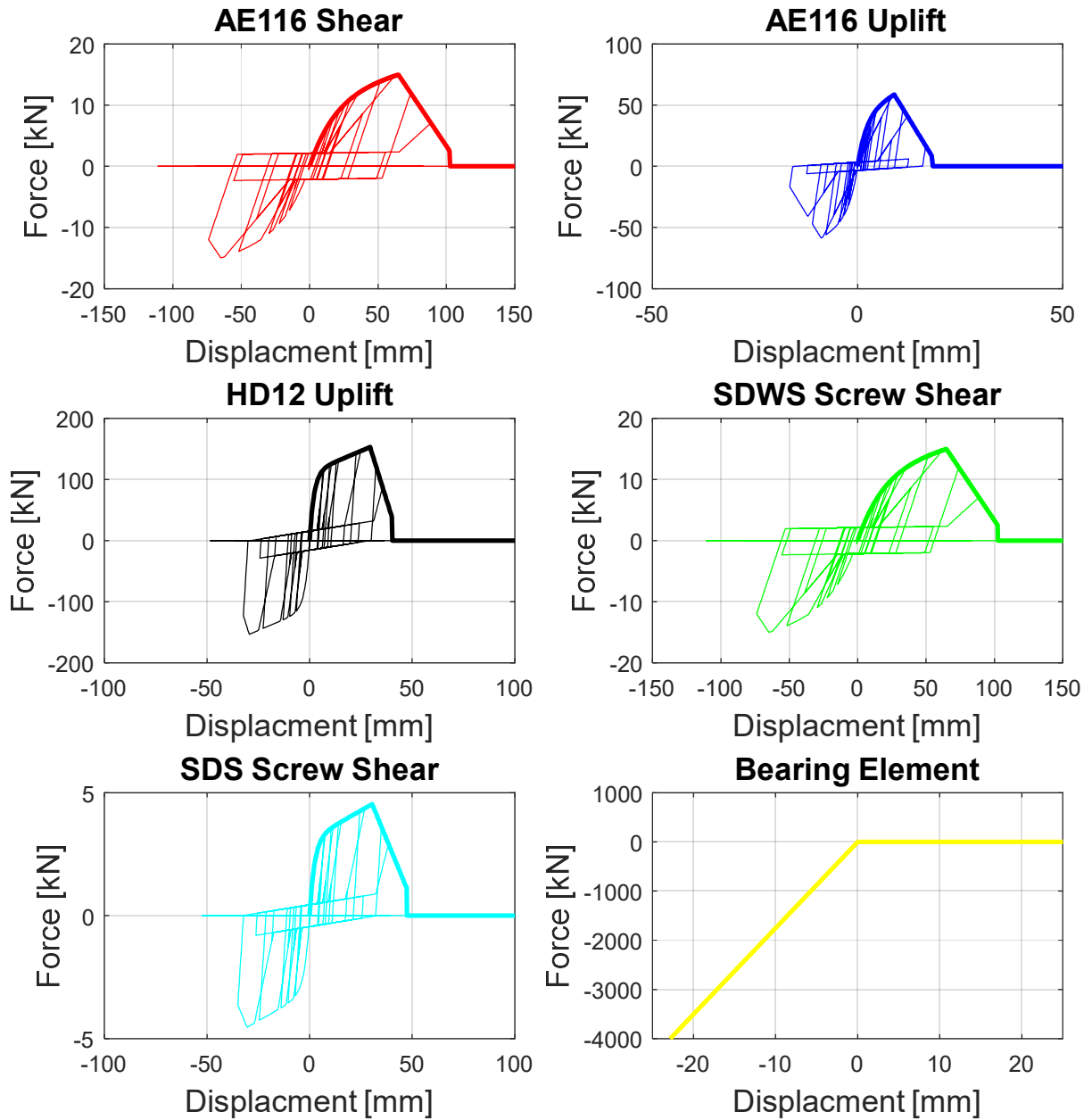


Figure 4.39: Modified Stewart parameters taken from tests and estimation

The wall assembly was restricted in the y-direction to assure only in-plane deformations. The shear resistance of hold-down F2F elements was neglected in the modelling due to the tendency to rotate. In addition, the out-of-plane behavior of the

AE116 connection (F_2 and F_3 in Figure 4.4) was assumed to follow the same shape as the tested shear connection but have a ratio of strength based on the manufacturer published values. The scaled parameters used to estimate the out-of-plane behavior of AE 116 elements are based on the published ASD strength values shown in Table 4.11 for F_2 and F_3 (Simpson Strong Tie, 2020).

Table 4.11: Reference Allowable design loads for AE 116 connections

Value	Reference Allowable Load [kN]
F ₁	16.7
F ₂	6.4
F ₃	14.1
F ₄	17.0

4.5.2 Comparison to Experimental Results

The results of the experimental stiffness and destructive tests were compared to the numerical models created in *Timber3D*. A comparison of the stiffness test force-displacement time histories is shown in Figure 4.40. From the comparison the model does an adequate job of estimating the stiffness of the various wall assemblies.

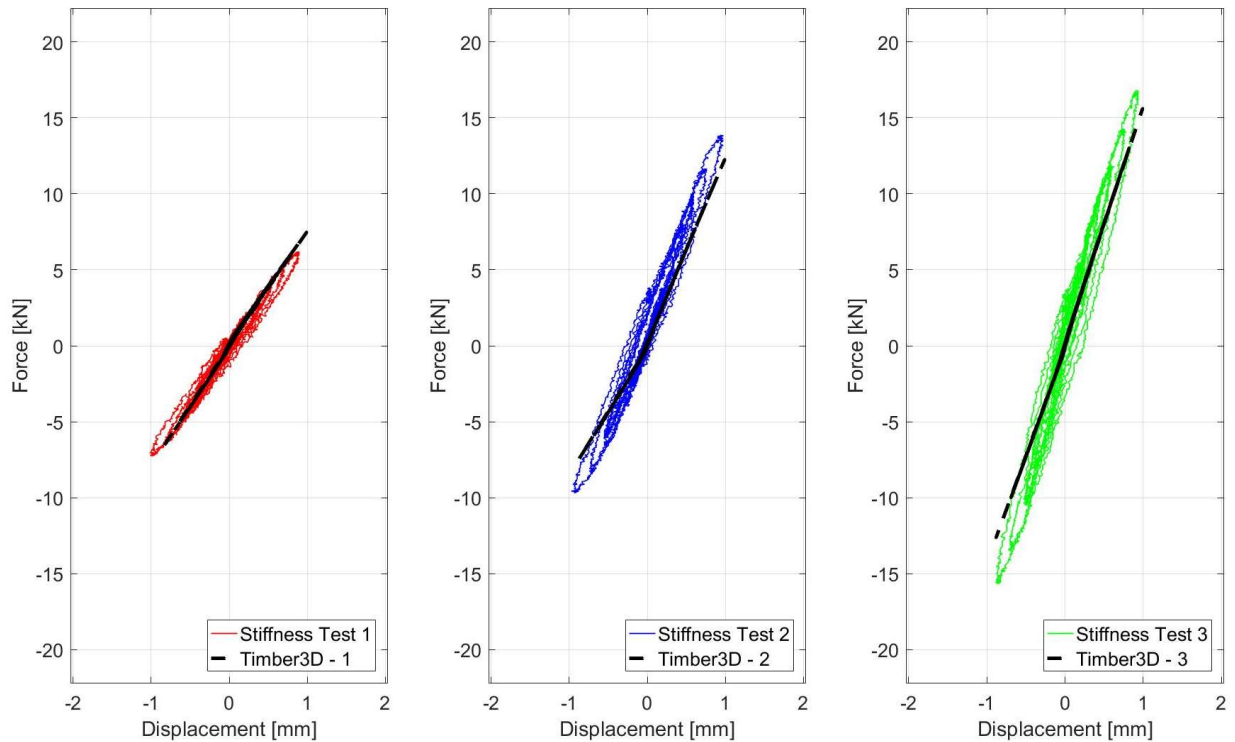


Figure 4.40: Comparison of stiffness tests to *Timber3D* model

In addition to stiffness comparisons, strength comparisons between *Timber3D* models and the destructive tests for wall assemblies 1 and 2 were performed. The results of these comparisons are shown in Figure 4.41 which indicates that the numerical models developed in *Timber3D* overestimate the strength of each assembly. The differences in the estimates may be due to errors in the estimation process of connection components which were not directly tested experimentally. In addition, the model does not account for interaction between uplift and shear likely present in the experimental test. Other discrepancies could be explained by the linear bearing elements not accounting for things like crushing of the CLT panels while rocking. Further experimental testing of connections

and modeling of non-linear bearing and friction could lead to numerical models which better match the results of the experimental testing.

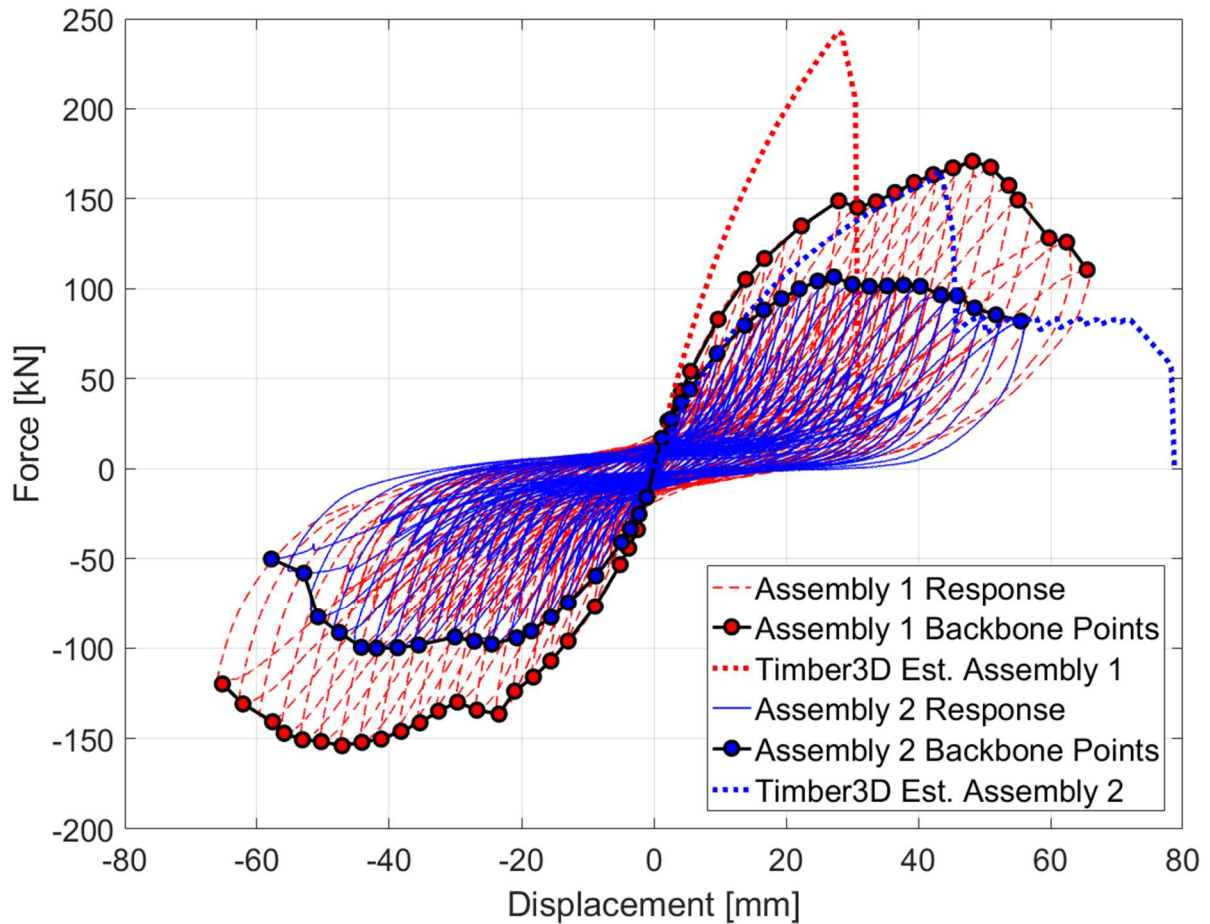


Figure 4.41: Comparison between experimental results and *Timber3D* model for wall assemblies 1 and 2

4.6 ANALYTICAL METHODOLOGY

The analytical approach used to determine the strength and stiffness of the tested wall assemblies was based on the ASD capacities of the elements that resist the applied loads. In the case of wall test 1 with out-of-plane walls, these elements included the shear capacity of the AE116 connectors in-plane at the top and bottom of the panel, the shear

capacity of the half-lap panel-to-panel connection, the capacity of the hold-downs, and the capacity of the connection between in-plane and out-of-plane walls. The ASD capacities of each of these elements are shown in Table 4.12 and represented in Figure 4.42 and calculated by taking published manufacturer data (Hold-down, AE116, out-of-plane to in-plane) or NDS calculations (panel-to-panel) shown in Appendix B.

Table 4.12: ASD capacities and applied unit shear required to reach capacities in wall assembly 1 and 2

Wall Assembly 1 Connection	ASD Capacity	Unit Shear Applied to reach ASD Capacity [kN/m]	Color in Figure 4.42
AE116 - Top	8.2 kN	13.9 kN/m	Green
AE116 - Bottom	16.7 kN	28.4 kN/m	Orange
Panel-to-Panel	11.6 kN/m	11.6 kN/m	Blue
Out-of-plane to in-plane	14.6 kN/m	14.6 kN/m	Red
Hold-Down	45.3 kN	19.6 kN/m	Black
Wall Assembly 2 Connection	ASD Capacity	Unit Shear Applied to reach ASD Capacity [kN/m]	Color in Figure 4.42
AE116 - Top	8.2 kN	13.9 kN/m	Green
AE116 - Bottom	16.7 kN	28.4 kN/m	Orange
Panel-to-Panel	11.6 kN/m	11.6 kN/m	Blue
Hold-Down	45.3 kN	17.6 kN/m	Black

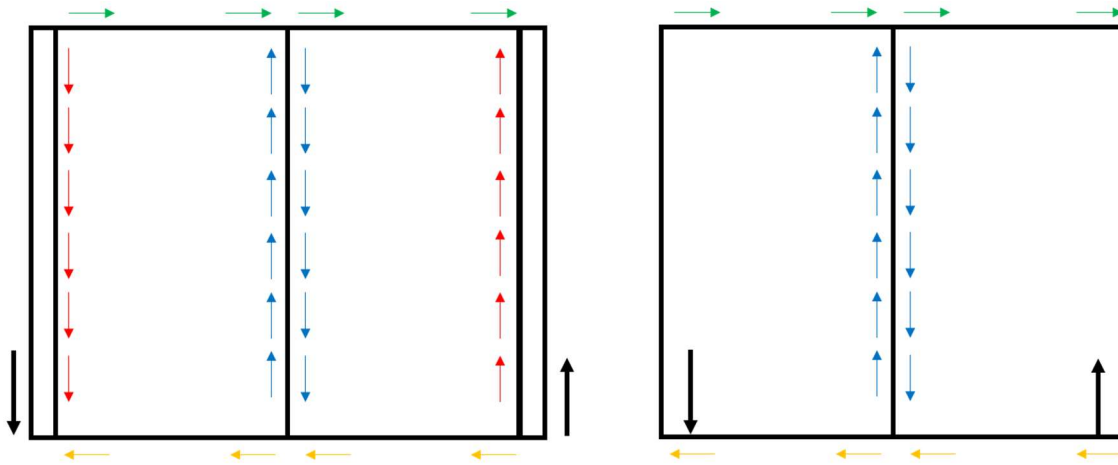


Figure 4.42: Shear of designated resisting elements in shear wall assembly 1 (left) and 2 (right)

Examining the values in Table 4.12 shows that the limiting capacity was the panel-to-panel connection with a unit shear of 11.6 kN/m (792 plf). The ratio of the controlling unit shear and the ultimate applied force was 5.8 and 3.7 for wall assemblies 1 and 2 respectively. In addition, the displacement at the analytically derived ASD capacity was 2.5 mm (0.1 in) and 2.7 mm (0.12 in) for wall assemblies 1 and 2 respectively. Using an approach which calculates the capacity of the wall assembly based on the panel-to-panel connection adequately estimates the strength of the wall assembly with in-plane walls only, but neglects the increase in strength that was observed in wall assembly 1 with out-of-plane walls. The presence of additional AE 116 connections and the connection between the in-plane and out-of-plane elements is not accounted for in this simplified analytical approach. A comparison of the magnitude of the in-plane shear strength of the wall assembly to light-frame shear walls shows that the ASD strength is comparable to a 12 mm (15/32") Structural I plywood with 10d nails at between 76 mm and 100 mm (3 to 4 inches) on

center in wind applications and 10d nails at approximately 50 mm (2 inches) on center in seismic applications. These light-frame systems are closer to the upper limit of strength possible for light-frame applications. Alternatively, the analytical capacity of the CLT shear wall assemblies has the potential for increased strength by increasing the shear strength of the panel-to-panel connections.

The deflection at design level load was also estimated based on Equation 4.1 with results shown in Table 4.13. Estimates from the analytical equation overestimated the deflection of the wall assembly by a factor of 1.9 and 1.6 for wall tests 1 and 2 respectively. The calculations of bending deformation were in accordance with Blass and Fellmoser (2004) and for shear deformation with Flaig M. and Blass H. (2013). Estimates of horizontal slip and vertical slip were taken from experimental testing or from numerical estimation. A potential source of the differences is that the analytical estimates do not account for the hold down restraint of the AE116 connectors both in-plane and out-of-plane. In addition, the deformation due to panel bending seems to overestimate the actual bending deformations measured by the experimental tests.

Table 4.13: Comparison of experimental and analytical deflection calculations

Configuration	Bending	Shear	Deformations [mm]			Total
			Horizontal Slip	Vertical Slip	Anchorage Slip	
Analytical Approach	0.94	0.04	0.90	2.32	0.50	4.7
				Wall Assembly 1		2.5
				Wall Assembly 2		3.0

4.7 CONCLUSIONS

The primary purpose of the experimental testing of CLT shear walls with and without out-of-plane walls was to determine whether out-of-plane walls could resist the uplift forces associated with lateral loads. Based on the results of the two wall tests, including the out-of-plane walls increased both the strength and stiffness of the assembly. In addition, the deformation mechanisms present in the test with only in-plane walls were also present in the test with out-of-plane walls meaning their presence did little to affect the behavior or ductility of the system. It can be concluded that out-of-plane walls can serve to anchor the in-plane walls given that their attachment is suitable to resist the shear demand at the interface between the two elements.

In addition, the development of an analytical method for estimating strength of the wall system was important for determining the performance of CLT walls that may be subject to loads associated with tornadoes. Analysis of the tested wall assemblies showed that the minimum capacity of the following elements served as a good estimate of the capacity of the entire assembly: shear capacity at top and bottom of wall, panel-to-panel connection shear capacity, hold-down capacity, and shear capacity of connection between in-plane and out-of-plane walls when present. For both tested assemblies, the panel-to-panel connection limited the analytical estimate of the wall assembly capacity and experienced the highest levels of deformation at design loads validating the simplified analytical approach.

Experimental testing of two wall assemblies was preceded by connection testing of the elements that made up the wall assemblies, namely the screws used in the shear

brackets and the uplift and shear performance of the brackets as installed. These results were used to aid preliminary numerical models used to match the behavior of the wall assemblies. With further refinement and additional experimental testing, a better match between experimental results and numerical models is likely. The results of the experimental testing and analysis demonstrates that the connection and detailing used in CLT shear wall assemblies is the most significant factor affecting the overall performance of the structure. Further testing, innovation, and development of these connection will lead to more efficient systems that can be implemented by engineers as lateral force resisting systems.

4.8 REFERENCES

- AWC. (2018). National Design Specification for Wood Constructions (NDS). Forest Product Association.
- Shahnewaz, M. Tannert, T., Popovski, M., & Alam, M. (2018). “Deflection of CLT Shear Walls in Platform Construction.” In Proc., World Conf. on Timber Engineering. Seoul, South Korea, WCTE.
- Lukacs, I., Björnfot, A., & Tomasi, R. (2019). Strength and stiffness of cross-laminated timber (CLT) shear walls: State-of-the-art of analytical approaches. *Engineering Structures*, 178, 136–147. doi: 10.1016/j.engstruct.2018.05.126
- Shahnewaz, M. Tannert, T., Popovski, M., & Alam, M. (2018). “Deflection of CLT Shear Walls in Platform Construction.” In Proc., World Conf. on Timber Engineering. Seoul, South Korea, WCTE.

- Amini, M. et al. (2016). “Determination of Seismic Performance Factors for CLT Shear Wall Systems.” In Proc., World Conf. on Timber Engineering. Vienna, Austria, WCTE.
- CUREE. (2001), Development of a Testing Protocol for Woodframe Structures, CUREE W-02, prepared by H. Krawinkler, F. Parisi, L. Ibarra, A. Ayoub, and R. Medina for Consortium of Universities for Research in Earthquake Engineering, Richmond, California.
- Simpson Strong Tie, (2019). “Wood Construction Connectors.” Retrieved from <https://www.strongtie.com/resources/literature/wood-construction-connectors-catalog>
- Folz, B., and Filiatrault, A. (2001). “Cyclic analysis of wood shear walls.” *J. Struct. Eng.*, 127(4), 433–441
- Bhardwaj, B. (2019, October 26). Email with M. Stoner
- European Committee for Standardization, 2004. Eurocode 5: Design of timber structures. Part 1-1: General – Common rules and rules for buildings. EN 1995-1-1. Brussels: CEN, 124 p.
- ASTM, 2018. Standard Test Methods for Cyclic (Reversed) Load Test for Shear Resistance of Vertical Elements of the Lateral Force Resisting Systems for Buildings. ASTM E2126, West Conshohoken, PA.
- Pang, W., Ziaei, E., Filiatrault, A. [2012] “A 3D Model for Collapse Analysis of Soft-story Light-frame Wood Buildings,” Proceedings of the 2012 World Conference on Timber Engineering (2012 WCTE), Auckland, New Zealand.

Simpson Strong Tie, (2020). “Connectors & Fasteners for Mass Timber Construction.”

Retrieved from <https://www.strongtie.com/resources/literature/mass-timber>

Blass H.J., and P. Fellmoser. 2004. Design of solid wood panels with cross layers. In

Proceedings of the 8th World Conference on Timber Engineering, June 14-17, 2004.

Lahti, Finland, 2:543-548.

Flaig M. and Blass H (2013). Shear strength and shear stiffness of CLT-beams loaded in

plane. CIB-W18 Meeting 46, Vancouver

CHAPTER FIVE

STRUCTURAL PERFORMANCE MODEL OF RESIDENTIAL CLT

Taken from: *Simulated Performance of Cross-Laminated Timber Residential Structures Subject to Tornadoes* (A paper in submission for *Frontiers in the Built Environment – Wind and Wood Frame Construction*)

Abstract

Tornadoes are some of the most severe and devastating natural events and cause significant damage to structures in the United States. Light-frame wood residential structures have shown vulnerabilities to these events, but they are not explicitly addressed in the design requirements due to their infrequent occurrence, relatively small impact area (compared to hurricanes), and complex wind profile. This paper explores the potential of Cross-Laminated Timber (CLT) to serve as a residential building material, specifically with regards to its performance in tornado events. CLT is an engineered wood product made when orthogonal layers of dimensioned lumber are glued to create panels. To compare the tornado performance of CLT buildings, six archetype residential buildings were each designed using CLT and light-frame wood in accordance to the appropriate US building code provisions and engineering principles. The capacity of each of the structural components was simulated using Monte Carlo Simulation based on the panel spans and connections of the panel boundaries. In addition, the resistance to structure sliding and combined uplift and overturning was simulated using engineering principles based on the load path of a CLT residential structure. Analysis of tornado induced wind loading was performed using recommendations from the 2016 ASCE-7 commentary and applicable

literature that attempts to account for the wind-induced pressures caused by tornadoes. Fragility analysis was performed to determine the probability of failure for a given estimated tornado wind-speed. When compared to the wind speeds of the Enhanced Fujita (EF) scale, the CLT residential archetypes showed wind speeds resulting in 10% probability of failure were in the range of EF-4 level events. Factors such as the connection spacing, and roof panel spans had the most significant effect on the simulated performance of the residential archetypes. Thicker panels, more robust connections, or tighter connection spacing could also lead to residential CLT structures that withstand EF-5 level events.

5.1 Introduction

As Cross-Laminated Timber (CLT) becomes a more widely used and readily available building material, its uses and performance continue to be studied. CLT was developed as a structural building material in Europe in the 1990's (Podesto, 2011). Each panel is created by pressing orthogonal layers of dimensional lumber to create large panels that can be manufactured with a great deal of precision (Karacabeyli and Douglas, 2013). CLT panels are cut to dimension using computer navigated cutting (CNC) which ensures both precision and customization. Due to the cross-laminations, CLT panels exhibit stiffness in both planar directions. This property ensures ease of installation as well as dimensional stability when subject to changes in moisture. While compared to light-frame construction, there is relatively more lumber used in CLT panels, their increased structural properties may be beneficial when subject to extreme natural hazards such as tornadoes.

Tornadoes have seen an increase in the insured and total losses due to their violent nature and lack of warning time, as the average lead time before a tornado hits can be as low as 15 minutes (KBRA, 2019), and unlike hurricanes, the affected area from a tornado is relatively small. Over the past 20 years, around 1,200 tornadoes occur annually and cause approximately 75 deaths in the United States (Insurance Information Institute, 2019). A significant amount of the insured and uninsured loss in tornado events comes from damage to residential structures primarily built using wood framing techniques (Ellingwood and Rosowsky, 2004). The hazards associated with tornadoes can take the form of wind-induced pressures and debris impact loads. The wind speeds in excess of 89.4 m/s (200 mph) combined with the drop in atmospheric pressure in the center of the tornado vortex can impart pressures well above the capacity of light-frame residential structures. In the event of a tornado, hazardous material can be transported by the wind at speeds approaching 44.7 m/s (100 mph) and impact the exterior of a structure, endangering the occupants and potentially compromising the structural system. In addition to the economic damages, deaths due to tornadoes are most likely to occur in mobile homes and permanent residential structures (Ashley, 2007).

Studies have attempted to quantify the performance of residential structures constructed using wood framing techniques when subjected to tornado hazards. Some have relied heavily on empirical data (Roueche et al. 2017, Alfano et al 2015) while other have performed detailed analysis of archetype residential structures using engineering principles that assume a load path through the structure (Amini and van de Lindt 2013). Empirically derived fragility curves by Roueche et. al (2017) exhibit a higher degree of uncertainty than

those numerically derived by Amini and van de Lindt (2013). The resulting fragility curves referenced specific building geometries with general assumptions made about load path, construction techniques, and member spacing, while those developed by Roueche et al. (2017) were based on the observations in a post storm event. Conclusions from these studies indicate that, in general, light-frame wood construction using typical practices and hardware would experience moderate damage during EF-2 level events and expect failure of the main wind force resisting system (MWFRS) in EF-3 level events.

Following the methodologies by previous analytical studies, the expected performance of a series of residential CLT structures was quantified following the damage states outlined by Amini and van de Lindt (2013). The damage states including loss of roof sheathing material great than 25% and failure of systems due to wall racking and uplift. The design of the archetype structures used in this study was based on the guidelines of the National Design Specification for Wood Construction (NDS 2018) and the recommendation of the CLT handbook (Karacabeyli and Douglas, 2013). Archetypes like those developed by Amini and van de Lindt (2013) for residential light-frame construction and the model developed by Raymond (2019) for CLT were used as a set of archetype structures. Using assumptions about the structural load path, analysis of wind-induced pressures, and Monte Carlo Simulations, fragility curves were developed. These fragility curves were examined to determine the vulnerabilities of the CLT residential archetypes as well as the expected performance given a tornado event.

5.2 Design of CLT Residential Archetypes

In order to compare the performance of a CLT structure to that constructed using light-frame wood, a series of five archetype structures were taken from Amini and van de Lindt (2013) and the single structure developed by Raymond (2019). These structures were developed to generalize the performance of residential structures and give an indication of the variation of performance based on various building geometries. Each of the six structures are shown with arrows indicating the span of the CLT elements in Figure 5.1, summarized in Table 5.1, and were designed using CLT panels for the roof and wall structure. Each of the residential archetypes developed by Amini and van de Lindt were used to generalize the performance of different structures geometries. The archetype developed by Raymond was developed specifically to maximize the efficiencies and performance of the CLT elements in a tornado event. For this study, the five light-frame archetypes were used as a comparison to the performance of light-frame residential structures, while the CLT archetype was used to investigate the potential for CLT to resist tornadoes when tornado wind design was considered in the panel layout and overall structural geometry. The development of the each of the archetypes using CLT followed gravity and straight-line wind design with a wind speed of 67 m/s (150 mph) outlined in ASCE 7-16 (ASCE, 2016).

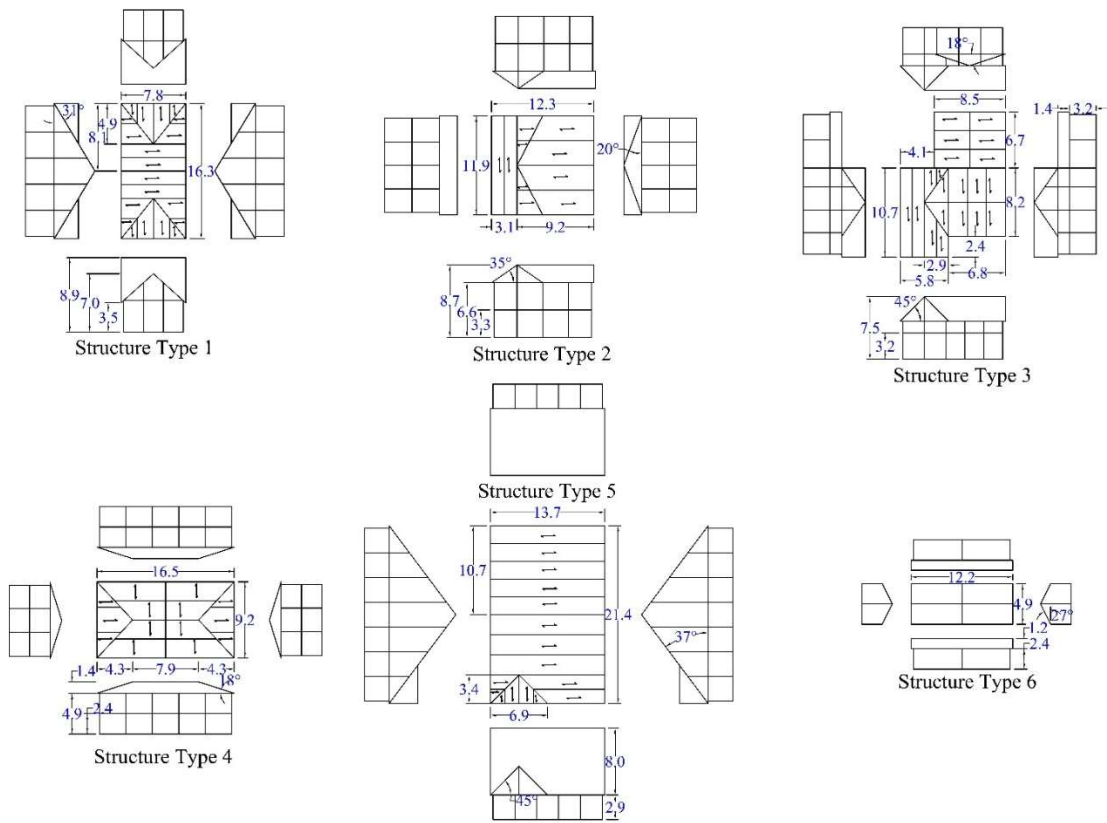


Figure 5.1: Archetypes used in study of CLT residential structures (dimensions in m)

Table 5.1: Description of residential archetypes

Structure Number	1*		2*		3*		4*		5*		6**
Plan Width	7.2 m		12.3 m		12.5 m		9.1 m		13.7 m		4.9 m
Plan Length	16.2 m		13.8 m		17.4 m		16.2 m		21.3 m		12.2 m
No. of Stories	1		2		1		2		2		1
Roof Type	Gable		Gable		Gable		Hip		Gable		Gable
Roof Side	N-S	E-W	N-S	E-W	N-S	E-W	N-S	E-W	N-S	E-W	E-W
Roof Slope	7:12	11:12	4:12	8:12	8:12	4:12	4:12	4:12	9:12	12:12	5:12
*Amini and van de Lindt (2013)											
**Raymond (2019)											

The roof and wall assemblies for each of the structure types were designed based on the guidance of the CLT handbook (Karacabeyli and Douglas, 2013) for shear, moment, and deflection due to dead load and roof loading. Design of panels for vibration and fire were not considered. In addition, panel dimensions were limited by maximum panel dimensions of 3.05 m by 12.2 m (10 feet by 40 feet) due to shipping limitations and typical CLT press sizes. CLT panels were assumed to bear on exterior walls, and where supported by interior member, glulam beams were utilized. These members would be typical where changes in roof pitch occur as well as in locations where double or triple span conditions exist. These additional supporting elements were not designed for each archetype, nor were they considered for the fragility analysis of this study as they were assumed to have the capacity to develop the strength required to support the CLT panels. In addition, 70% of the exterior CLT walls was assumed to be full height CLT walls, consistent with the assumptions of Amini and van de Lindt (2013). For the purpose of the analysis of CLT structures, the percentage of full-length wall affected the number of connections at the base of each wall line. The original spacing of the connectors was determined based on the straight-line wind analysis of with a wind speed of 67 m/s (150 mph). The spacing was varied in the Monte Carlo Simulation to determine the spacing's effect on the performance of the archetypes.

A three-layer CLT panel was assumed for all roof and wall elements where each layer measured 35 mm (1.375 inches) and the total panel depth measured 105 mm (4.125 inches). The panel's structural properties were taken for a V3 layup where all longitudinal layers are No. 2 Southern pine lumber and all transverse layers are No. 3 Southern pine

lumber (ANSI/APA, 2018). The bending strength of the CLT panel is given by Equation 1 where the maximum bending moment, M_b , is a function of the effective section modulus, S_{eff} , and the allowable or ultimate bending stress, F_b , multiplied by all applicable adjustment factors present in Chapter 10 of the National Design Specification (AWC, 2018).

$$M_b = 0.85F_b'S_{eff} \quad (5.1)$$

The effective section modulus was taken from the effective bending stiffness, EI_{eff} , and was calculated using one of several mechanical models used to predict the stiffness of composite elements. The shear analogy method described in Kreuzinger (1995) was used in this study to calculate the effective section properties of the composite CLT section. In this method, the effective bending stiffness is reduced to account for shear deformations when calculating deflections. A summary of the strength properties and adjustment factors used for design and the resulting Allowable Stress Design (ASD) values and limiting spans are described in Table 5.2. Using the span limitations, CLT panels were arranged to minimize the number of panels and necessary interior supports. Where possible, double and triple span configurations were used. An example of the layout for panel walls (numbers) and roof (letters) is shown in Figure 5.2. Each panel is labelled individually based on geometry and unique loading due to tornado induced forces. The panel layout for all structures is shown in Appendix C with wind load statistics for wall and roof panels in Appendix D. The design parameters and analysis of a V3 CLT panel is shown in Appendix E.

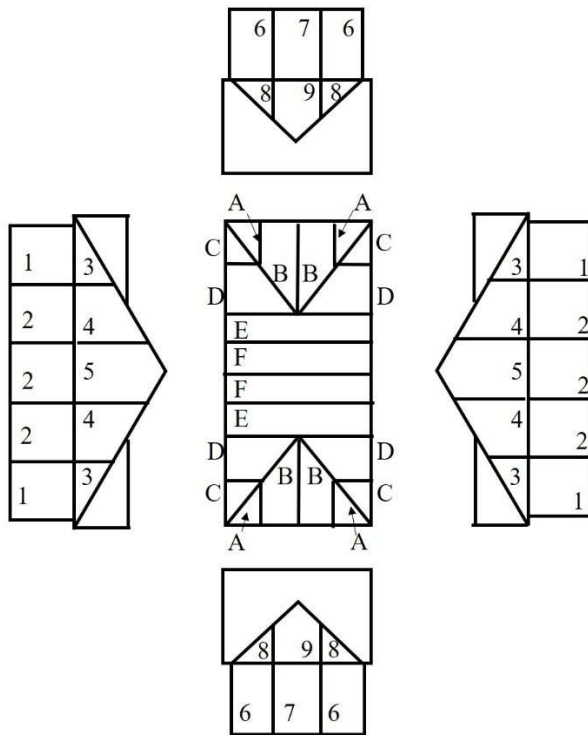


Figure 5.2: Panel layout of structure 1

Table 5.2: Material properties used for structural design of CLT elements

Variable	Value
Self-Weight [kPa]	0.57
Roof Live [kPa] (Slope less than 4:12)	0.96
Roof Live [kPa] (Slope greater than 4:12)	0.72
CLT Grade	V3 - Major
Modulus of Elasticity ($\times 10^3$ MPa)	9.7
Modulus of Elasticity, Perp. ($\times 10^3$ MPa)	9.0
Bending Stress, F_b [kPa]	5170
Shear Stress, F_s [kPa]	380
Specific Gravity	0.55
Moisture Adjustment Factor, C_M	1
Temperature Adjustment Factor, C_t	1
Effective Section Modulus, $Seff$ [mm^3]	5.38×10^5
Moment Capacity, LRFD [kN-m/m]	13.4
Limiting Moment Span [m]	6.9
Shear Capacity, LRFD [kN]	15.1
Effective Moment of Inertia, EI_{eff} [kN-m ² /m]	892
Limiting Deflection Span - Single Span $L/180$ [m]	4.6
Limiting Deflection Span - Double Span $L/180$ [m]	5.9

5.3 Determination of Tornado Wind Forces

The current state of codified wind design in the United States describes procedures to only consider straight line winds; however, methods for considering the wind-induced loads from tornado events are provided in the Commentary of ASCE 7-16 (ASCE, 2016). The two methods that are presented are termed the *Extended Method* and the *Simplified Method*. The *Extended Method* modifies the directional procedure present in Chapter 27 of ASCE 7-16 shown in Equations 2 and 3.

$$q_z = 0.613K_zK_{zt}K_dK_eV^2 \quad (5.2)$$

$$p = qGC_p - q_i(GC_{pi}) \quad (5.3)$$

In Equations 2 and 3, K_z = velocity pressures exposure coefficient, K_{zt} = topographic factor, K_d = wind directionality factor, K_e = ground elevation factor, V = basic wind speed (m/s), and q_z = velocity pressure at height z (N/m²). In Equation 3, the design wind pressure p (N/m²), is calculated from the velocity pressures q evaluated at either height z or mean roof height h depending on which walls/roof elements are being considered. In addition, G = the gust-effect factor, C_p = the external pressure coefficient, and GC_{pi} = the product of the gust-effect factor and the internal pressure coefficient.

The commentary addresses the differences in wind-induced pressures from tornado winds and the wind-induced pressures from other windstorms by increasing the directionality factor, K_d , from 0.85 to 1.0 and increasing the gust-effect factor, G , from 0.85 to 0.90. The increase in the directionality factor results from the rotational winds in a tornado increasing the likelihood that at the building will experience the maximum wind velocity at the same time it experiences the worst-case wind direction. The increase in the

gust-effect factor to remove the 0.925 calibration factor used to derive $G = 0.85$ for rigid buildings (ASCE, 2017). It is also recommended that component and cladding (C&C) loads be decreased by 10%, due to the short duration of tornado events (Kopp and Morrison, 2011). Finally, the internal pressure coefficient, GC_{pi} , be set to ± 0.55 to account for the likelihood that there is damage to the building envelope increasing the internal pressure.

The *Simplified Method* considers tornado induced wind loading by modifying the traditional equation for the calculation of design wind pressures by a Tornado Factor, TF , as shown in Equation 4. The Tornado Factor is meant to address the changes in pressure due to the central pressure drop measured by Haan et al. (2010). In this research, a 9.14m x 9.14m (30-ft by 30-ft) building with a mean roof height of 6.71m (22-ft) and gable roof angle of 35° was studied in a tornado simulator. The tornado simulator created vortices simulating the wind behavior associated with tornadoes on a 1:100 scale model of the structure. These studies were performed with the explicit goal of comparing the pressures measured on the model to those calculated by straight-line wind provisions in ASCE 7-10. The resulting ratio between measured pressure and calculated pressures range from 1.1 to 2.5 based on enclosure and exposure category. In this equation, the velocity pressure, q_i , is multiplied by the product of the external pressure coefficient and gust factor, GC_p , combined with the internal pressure coefficient, GC_{pi} , to give the design wind pressure, p .

$$p = q_i \left(GC_p - (GC_{pi}) \right) \times TF \quad (5.4)$$

For this study, the *Extended Method* was utilized in determining the forces that result from tornado events.

Wind load statistics used in the simulation of the forces on structural elements were taken from ASCE as well as literature relevant to the study of the performance of structures in tornadoes. Values for K_{zt} , K_d , and K_e were set to unity, while values for K_z , GC_p , and GC_{pi} were normally distributed with coefficients of variation (CoV) based on work done by Lee and Rosowsky (2005) summarized in Table 5.3. The panel's dead load with mean of 0.575 kPa (12 psf) and superimposed dead load with mean of 0.575 kPa (12 psf) was also simulated using a normal distribution and a CoV of 0.10. Values of external pressure coefficients were calculated based on a weighted average approach for the various zones of pressure present on wall and roof panels. CLT wall and roof panels and their boundary connections were subjected to the C&C pressure coefficients referenced by ASCE 7 Chapter 30. For system level failures such as uplift, overturning, and sliding, forces were calculated using pressure coefficients associated with the MWFRS). Examples of the pressure coefficients calculated for CLT wall and roof panels are shown in Table 5.4 for structure Type 1. The CoV used for all GC_p values was 0.12. For each of the values of the velocity pressure coefficient, K_z , and external pressure coefficients, GC_p , a nominal-to-mean ratio of 1.05 consistent with studies by Lee and Rosowsky (2005) and Amini and van de Lindt (2013).

Table 5.3: Summary of values used in wind analysis

Variable	Mean Value	Coefficient of Variation	Distribution Type	Reference
K_z	Vary by Structure Type	0.14	Normal	Amini and van de Lindt (2013)
K_{zt}	1.0		Deterministic	ASCE 7 (2016)
K_d	1.0		Deterministic	ASCE 7 (2016)
K_e	1.0		Deterministic	ASCE 7 (2016)
GC_p	Vary by Panel	0.12	Normal	Amini and van de Lindt (2013)
GC_{pi}	0.46 (Partially enclosed)	0.33	Normal	Lee and Rosowsky (2005)
GC_{pi}	0.15 (Enclosed)	0.33	Normal	Lee and Rosowsky (2005)
Super-imposed Dead Load	0.575 kPa	0.10	Normal	Lee and Rosowsky (2005)

Table 5.4: External pressure coefficients, GC_p , used in wind analysis for structure Type 1

Wall Panel	Nominal C&C GC_p	Roof Panel	Nominal C&C GC_p
1	-0.92	A	-1.81
2	-0.90	B	-1.20
3	-1.04	C	-2.13
4	-0.93	D	-1.25
5	-0.90	E	-1.19
6	-0.94	F	-1.19
7	-0.90		
8	-1.00		
9	-0.95		

For design purposes, it is recommended that due to the likelihood of breach of building envelope caused by windborne debris, a partially enclosed internal pressure coefficient be used to calculate the wind-induced forces on a structure. Using CLT as the exterior of the residential structures would provide more resistance to windborne debris impact; however, vulnerable areas including building fenestrations are likely to limit the

enclosure classification. In order to study the potential improvement the added resistance of CLT would have on the residential structure, debris impacts were considered parametrically. The debris impact performance (or fragility) of 3-ply CLT was experimentally determined in a previous study that subjected CLT panels to windborne debris impacts in the form of a 2x4 dimension lumber (Stoner and Pang, 2019). The mass and velocity of the simulated debris corresponded to the debris found in EF-2 and EF-3 level events as defined by FEMA P-361 (FEMA, 2015). The experimental data collected in (Stoner and Pang, 2019) was fit to a lognormally distributed fragility curve, which relates the debris speed of a 6.8 kg (15-lb) 2x4 lumber to impact failure probability. The relationship between wind speed and debris speed was estimated using the recommendations of FEMA P-361 where the debris speed is listed for a given design tornado wind speed. These debris speeds give an indication of the maximum hazard from windborne debris that can be expected in a tornado event. Using the lognormal distribution parameters from the study, the response to debris impact of the CLT structures was simulated where surviving structures used an enclosed internal pressure coefficient, and structures that experienced failure due to debris impact used a partially enclosed internal pressure coefficient. The response to debris impact loads relies heavily on assumptions made about the number and severity of debris that impact a structure during a tornado event both of which are functions of the surrounding terrain and available debris. To study the effect of such debris, the number of impacts each structure was exposed to during a single event simulation was varied between 0 and 5 for a 6.8 kg (15-lb) 2x4. Results from this analysis would give an indication of the performance of a CLT structure if both the

fenestrations were protected and the performance of the CLT wall and roof assemblies was considered. For all other simulations, the structure was assumed to be partially enclosed for all wind speeds.

5.4 Resistance of CLT Archetypes and Load Path Assumptions

In order to determine the performance of residential CLT structures, the CLT panel strength and connection strength was determined. The true mean bending capacity of the panels used in this study was calculated based on the required characteristic value referenced in PRG-320, *Standard for Performance-Rated Cross-Laminated Timber* (APA 2018). This standard provides guidance regarding the performance of CLT used in the United States and Canada including the required characteristic values derived from the 5th percentile with 75% confidence of an experimental test series representing the population. To arrive at the ASD design value reported by manufacturers, the characteristic test values are taken from the statistical analysis of the test results and divided by a factor of 2.1 per PRG-320. To ratio of mean value to characteristic value was taken from tests by Gu (2017) on Southern Yellow Pine CLT where this ratio was found to be 1.4. Combining the ratios ($1.4 \times 2.1 = 2.94$) gives an estimate of the ratio between the true mean capacity and the published ASD value. Simulations of the capacity of CLT panels utilized this factor to predict the bending strength of a 3-ply V3 CLT panel.

Connections between wall and roof panels used screws that measured 5.6mm x 203mm (0.22 in x 8 in). These connections were also used between perpendicular wall panels at the corners of the residential structures. The spacing of the screws significantly affects the capacity of the structure in both uplift and shear and was varied between 15.2

cm and 30.5 cm (6 in and 12 in) in this study. The average screw spacing of 22.9 cm (9 in) was based on a straight-line wind design of 67 m/s (150 mph). Reference allowable withdrawal and shear values were taken from literature provided by screw manufacturers (Simpson Strong Tie, 2019). The reference allowable withdrawal load for southern pine was given as 47.5 N/mm of penetration into the main member (214 lb/in) with a maximum value of 2,600 N (590 lb). The reference allowable shear value for southern pine was 1.76 kN (395 lb) for a side member thickness of 105 mm (4.125 in). For both withdrawal and shear, the calculated design value was multiplied by a factor of 3 to estimate the mean strength value from a design level strength.

Connections between CLT walls and floor or foundations were made using bracket style connectors, namely Simpson Strong-Tie AE 116 brackets measuring 90 x 48 x 116 mm (3.5 x 1.9 x 4.6 in) and 3 mm thick (0.12 in). The vertical face of the bracket-type connector is fastened using (18) screws measuring 3.1mm x 63.5mm (0.122" x 2.5"). The horizontal face was fastened using (7) screws when attaching two CLT surfaces and (3) 12.7mm (0.5 in) bolts when attaching to the foundation at the first floor as shown in Figure 5.3. The ASD capacities in each direction are given in Table 5.5. No hold downs were assumed to be present in the structures as the gravity load and uplift capacity of the bracket-type connectors were assumed to resist the uplift loads associated with the straight-line wind design. Bracket-type fasteners were assumed to be connected on the inside of the exterior walls where forces resulting from positive wind pressures would be compared to the value, F_3 in Figure 5.3 and forces from negative wind pressures would be compared to the value F_2 in Figure 5.3. Like the screwed connection between perpendicular elements,

the bracket style connection used a ratio of 3 to calculate the mean strength for values of F_1 , F_2 , and F_3 from the ASD capacity published by the manufacturer. Experimental testing was used to determine the behavior of the connection in uplift, F_4 . In addition, connections were assigned a coefficient of variation of 0.15 consistent with testing of similar various configurations of bracket-type connectors (Schneider et al. 2013, Gavric et al. 2014, Liu and Lam 2018, MahdaviFar et al. 2018).

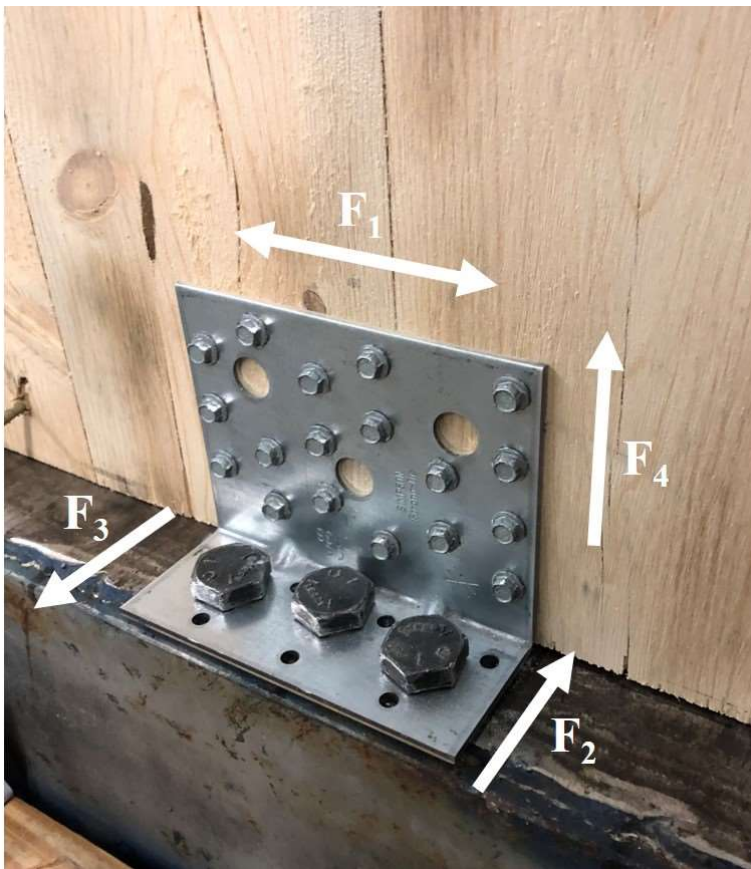


Figure 5.3: Representation of bracket-type connections used in simulations

Table 5.5: Reference ASD loads for bracket-type connector

Value	Reference Allowable Load [kN]	CoV
F ₁	16.7	0.15
F ₂	6.4	
F ₃	14.1	
F ₄	17.0*	
*Reported values were replaced by results of experimental testing		

In addition to the failure of CLT components and their connections, the failure of the structure due to sliding, and combined uplift and overturning was considered. For the sliding of each structure, exterior walls were assumed to resist all the base shear demand produced by the wind-induced pressures. Principles of tributary area were used to determine the out-of-plane demand for each connector. The out-of-plane and in-plane walls were analyzed separately to determine their resistance to the shear forces generated from MWFRS pressure coefficients on the entire structure.

The total uplift on the structure was divided between the exterior walls and interior supports by tributary area. The percentage of the uplift tributary to each of the exterior wall lines was determined and assumed to act uniformly on each of the bracket-type connectors present at the base of each wall. In addition, the contribution of overturning to the vertical component of the force on each connector was determined by assuming a percentage of the overall overturning moment be resisted by the in-plane walls. Analytical models have been developed to predict the stiffness contribution due to out-of-plane walls (Shahnewaz et al. 2019); however, there is little information on the strength contribution of out-of-plane walls to the overturning resistance of a platform framed CLT structure. For

this study, the ratio of global overturning moment taken by the in-plane walls was defined as the overturning ratio. It was assumed that all remaining overturning moment was taken by the out-of-plane walls. The overturning ratio resisted by the in-plane walls was varied between 50% and 100% to determine the affect this assumption had on the predicted performance of the structure. It is understood that there will be some contribution by the out-of-plane walls which relies heavily on the connection between in-plane and out-of-plane walls. For the baseline structural model, it was assumed that 75% of the overturning ratio was taken by the in-plane walls.

Many methods have been developed for determining the strength of CLT shear walls that assume different contributions due to bending, shear, sliding, and rocking (Lukacs et al. 2018, Popovski et al. 2011, Pei et al. 2013, Reynolds et al. 2017, Shahnewaz et al. 2018). Ultimately, a simplified kinematic model presented in the CLT Handbook (Popovski et al., 2011) was utilized in determining the strength of the in-plane CLT walls. In this method, the CLT panels are assumed to rotate about their corner and all lateral forces are resisted by the connections at the base as a function of their distance from the point of rotation. This model is represented by Equation 5 where the lateral force, F , and resulting deformation, D , is resisted by the force in each connector, f_i . The force in each connector is calculated based on its distance to the point of rotation, l_i , and deformation, d_i . In addition, the contribution of the gravity load on each panel is assumed to resist the rocking action based on the length of the CLT panel, L , and height of panel, H .

$$F(D) \sum_{i=1}^n \frac{l_i}{H} f_i(d_i) + \frac{L}{2H} G \text{ and } d_i = \frac{l_i}{H} D \quad (5.5)$$

This kinematic model assumes pure rotation about the bottom corner and neglects the compressive stresses and associated deformations due to rocking. In addition, panel-to-panel connections were assumed to resist the required shear demand between panels. The lateral strength of the CLT walls was controlled by the length of wall and the vertical capacity of the bracket-type connectors used in each exterior wall. In order to determine the strength of the wall, information about the force-deformation response of the bracket-type connectors present at the base of the wall was required. To obtain a more detailed understanding of the performance of the connectors in uplift, a series of connection tests were performed to further quantify the vertical force-displacement behavior, F_v . Based on a series of monotonic and cyclic uplift tests of the bracket-type connections, this response was quantified on the connection level. The one-sided response of the bracket-type connection was quantified using the Modified Stewart (MSTEW) model, also commonly known as the CUREE hysteresis model (Folz and Filiatrault, 2001), shown in Figure 5.4. For full cyclic data, the MSTEW model uses a 10-parameter model to describe the hysteresis behavior. Where only the backbone is described by the hysteretic model, only

5 parameters are required, K_0 , r_1 , r_2 , F_0 , and Δ_u . The backbone parameters fit to the test results are shown in Figure 5.4.

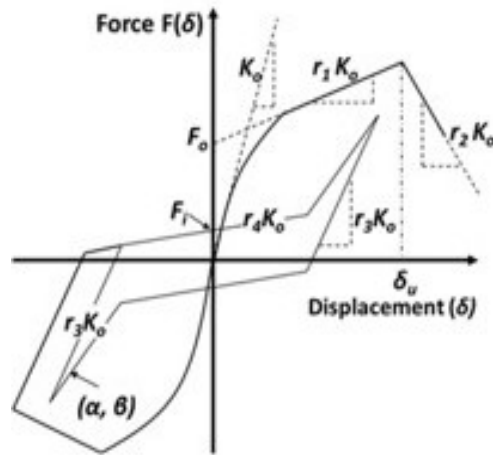
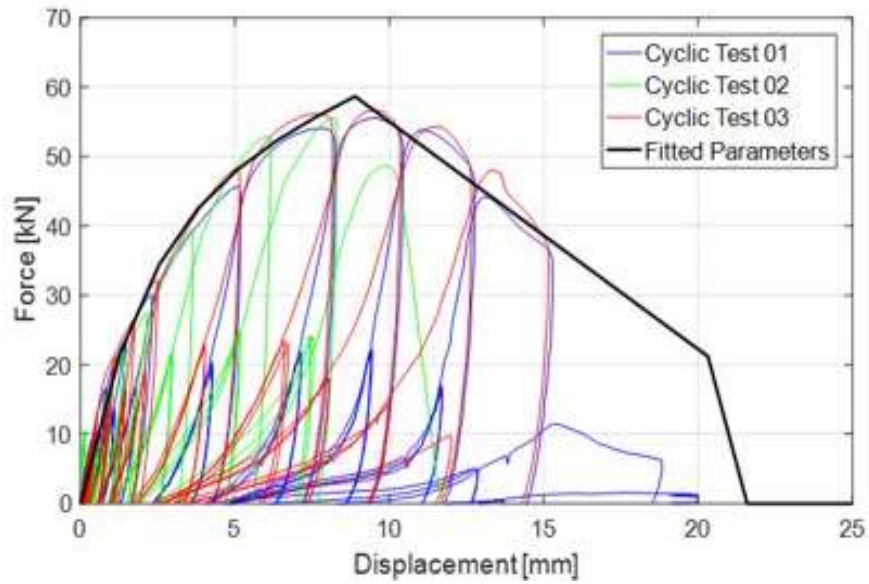


Figure 5.4: Experimental uplift test data (top) and MSTEW hysteretic model rules (bottom)

Using the force-displacement relationship of the bracket-type connections derived from experimental testing, the strength of the exterior walls of the residential archetypes could be calculated and simulated. For each of the exterior walls, the peak capacity of each connector was estimated with a mean directly taken from the experimental testing and CoV of 0.15.

5.5 Fragility Analysis of Residential Archetypes

Fragility functions have been used to quantify the variability in structural performance most often using a lognormal cumulative distribution function to relate the probability an event occurs given the occurrence of a specific intensity measure. The lognormal fragility function is represented in Equation 6 where the probability of exceeding a damage threshold, P_f , given an estimated tornado wind speed, WS , is a function of the standard normal cumulative distribution function, Φ , and lognormal distribution parameters representing the logarithmic mean, μ , and logarithmic standard deviation, σ . The lognormality of the fragilities was verified after all the limit states were defined.

$$P_f(WS) = \Phi \left[\frac{\ln(WS) - \mu}{\sigma} \right] \quad (5.6)$$

Figure 5.5 represents the procedures used to develop the fragility functions for each of the components in the structural system and the total structure fragility. Once the building geometry, panel layouts, and connection spacing was determined, the wind load statistics were calculated, the design wind pressure could be simulated. In the case of the study on the potential influence of debris impact resistant wall assembly on the structural performance, the debris was simulated in order to calculate the wind load statistics and the design wind pressures. For each wall and roof panel, fragilities were calculated for failure

due to exceeding the moment capacity of the panel as well as connection failures at the panel boundaries. These fragilities were used to develop overall roof fragilities based on 25% failure of the roof by area and wall fragilities based on the failure of any wall panel. In addition, systems level failures such as sliding and combined rocking and uplift were calculated.

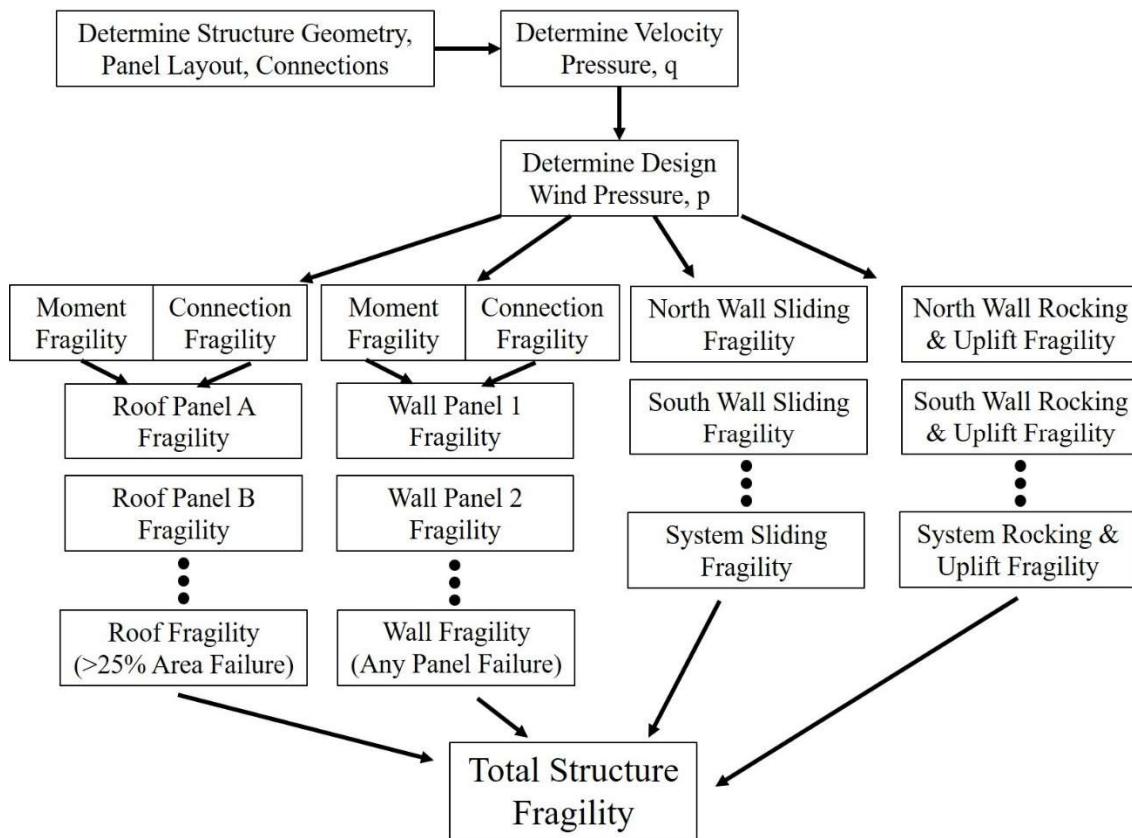


Figure 5.5: Framework for development of fragility functions

5.5.1 Flexural Failure of Wall and Roof Elements

Failure of the CLT roof and wall panels in flexure due to uplift forces was determined through the limit state function given in Equation 7 where the limit state, $g_{flexure}(WS)$, is given by the difference in the simulated moment capacity, M_{cap} , and simulated demand, M_{demand} , with added moment due to the dead load of the panel, M_{DL} .

Dead load was only considered in the fragility functions for roof elements. In addition, the positive wind pressure was checked where the moment due to dead load, M_{DL} , was added to the positive wind pressure. Each panel was assumed to span in the direction of its strong axis. For triangular panels, the longest span was assumed to calculate the moment capacity, demand, and moment due to dead load.

$$g_{flexure}(WS) = M_{cap} - M_{demand}(WS) + M_{DL} \quad (5.7)$$

Lognormal fragility curves were developed for each CLT panel and its boundary connections by simulating the pressure resulting from a given estimated tornado wind speed, WS .

5.5.2 Connection Failure of Wall and Roof Elements

The connection capacity of each CLT panel was taken as the total capacity the connections on the panel's perimeter to supporting elements. For roof panels, this included screws in withdrawal, while for wall panels, this was composed of a combination of screws in withdrawal and/or shear and bracket-type connections in shear. The out-of-plane capacity of the panel-to-panel connection was neglected in the estimation of the connection capacity. If a significant pressure differential existed between adjacent panels, it is not likely that the panel would transmit a significant amount of force through the panel-to-panel connection which is not designed to resist such loading. It is noted that there could be damage to the panel-to-panel connection compromising its ability to transmit shear forces to adjacent panels but was neglected from these limit state definitions. The limit state for panel failure due to negative pressure connection failure, $g_{connection}(WS)$, is demonstrated in Equation 8 where the capacity is given by the capacity of a connector in

shear, F_{shear} , times the number of connectors in shear, n_{shear} , and the capacity of a connector in withdrawal, F_{with} , times the number of connectors in withdrawal, n_{with} . The capacity is compared to the total suction force on the panel, $F_{suction}$.

$$g_{connection}(WS) = F_{shear}n_{shear} + F_{with}n_{with} - F_{suction} \quad (5.8)$$

5.5.3 Structure Sliding Failure

In addition to the component fragilities for each panel in the residential archetypes, the system level limit states of sliding and combined uplift and rocking were analyzed. The limit state function for sliding was determined by comparing the shear from wind-induced pressure, $V(WS)$, to the shear capacity of the bracket-type connection at each perimeter wall given as F_i , where there exist n exterior walls (Equation 9).

$$g_{sliding}(WS) = [\sum_{i=1}^n F_i] - V(WS) \quad (5.9)$$

5.5.4 Structure Uplift and Overturning Failure

The limit state function for panel combined uplift and rocking was determined through Equation 10 where the capacity of each connector in uplift, F_i , was compared to the forces generated by uplift, F_{uplift} , and rocking, $F_{rocking}$. Uplift forces were determined through the contribution of overall uplift taken by each of the exterior walls. The rocking forces were determined by calculating the peak force developed in the connectors based on Equation 10 assuming rocking behavior of the in-plane walls.

$$g_{rocking+upli}(WS) = F_i - F_{uplift} - F_{rocking} + DL \quad (5.10)$$

The demand on the system level limit states changed with wind direction due to the geometry of the structure archetypes; therefore, each of the cardinal wind directions was simulated through Monte Carlo Simulation.

5.5.5 Calculating Total Structure Fragilities

To determine the component fragilities for each wall/roof panel, the limit states of connection failure and moment failure were combined to determine its probability of failure by either negative pressure connection failure or flexural failure by Equation 11. The compliment of the flexural limit state for panel i , $g_{flexure,i}$ is multiplied by the compliment of the connection limit state, $g_{connection,i}$, and subtracted from 1.

$$g_{wall/roof,i}(WS) = 1 - \left(1 - g_{flexure,i}(WS)\right) \times \left(1 - g_{connection,i}(WS)\right) \quad (5.11)$$

Where there were multiple wall panels with the same limit state function, the compliment of the limit state function was raised to the power, n_p , representing the number of panels in the structure with the given limit state and n unique panels in the structure as shown in Equation 12.

$$g_{wall}(WS) = 1 - \prod_{i=1}^n (1 - g_{wall,i}(WS))^{n_p} \quad (5.12)$$

In the case of roof panels, the probability of failure exceeding 25% of the roof area was used as the threshold for ‘failure’, which was calculated through Monte Carlo Simulation and fit to a lognormal distribution function to determine the limit state g_{roof} . The threshold for failure of 25% roof failure by area was used to match the threshold for light-frame structures in the analysis by Amini and van de Lindt (2013). For wall panels, any wall failure was considered to exceed the damage threshold associated with ‘failure’.

The performance of a structure considering all limit states, $G(WS)$, was determined using Equation 13 where the limit state function for limit state functions for roof panels, wall panels, system sliding, and system rocking and uplift are combined by multiplying their compliments and subtracting the result from 1.

$$G(W S) = 1 - \left(1 - g_{roof}(W S)\right) \times \left(1 - g_{wall}(W S)\right) \times \left(1 - g_{sliding}(W S)\right) \times \left(1 - g_{rocking+uplift}(W S)\right) \quad (5.13)$$

The lognormality of the limit state fragilities was verified by comparing the sum of the squared error terms for a lognormal distribution to that of a normal and Weibull distribution. In the case of each panel component fragility and system failure fragility, the failures simulated by the limit state equations were fit to a lognormal distribution, a normal distribution, and a Weibull distribution. The sum of the squared error terms for each distribution type was the primary measure of fit. In all cases, the lognormal distribution produced the least error and was considered appropriate to describe the fragility function. The total lognormal error was 17% and 2% of the normal error and Weibull error, respectively.

5.6 Results of Fragility Analysis

Fragility analysis of each of the residential CLT archetypes gave insight into not only the expected performance in the event of a tornado, but also the most susceptible components and effect specific load path assumptions had on the resulting performance of the structure. A baseline structure connection spacing and set of assumptions was used to compare the influence of assumptions including the overturning ratio (75% of overturning taken by in-plane walls) and connector spacing (23 cm for screws, 91.4 cm for bracket-type connectors).

Examples of the component fragilities calculated for structure Type 1 are shown in Figure 5.6. Each panel had a fragility developed for moment and connection failure from wind-induced pressures. The panels experienced variations in predicted performance due

to the change in external pressure coefficients, maximum span, and connection at the perimeter. Panel 2 was the most vulnerable wall panel due to the connections only at the base to the foundation and above to the floor plate. Similarly, Panel E was the most vulnerable roof panel due to its large span (3.9 m).

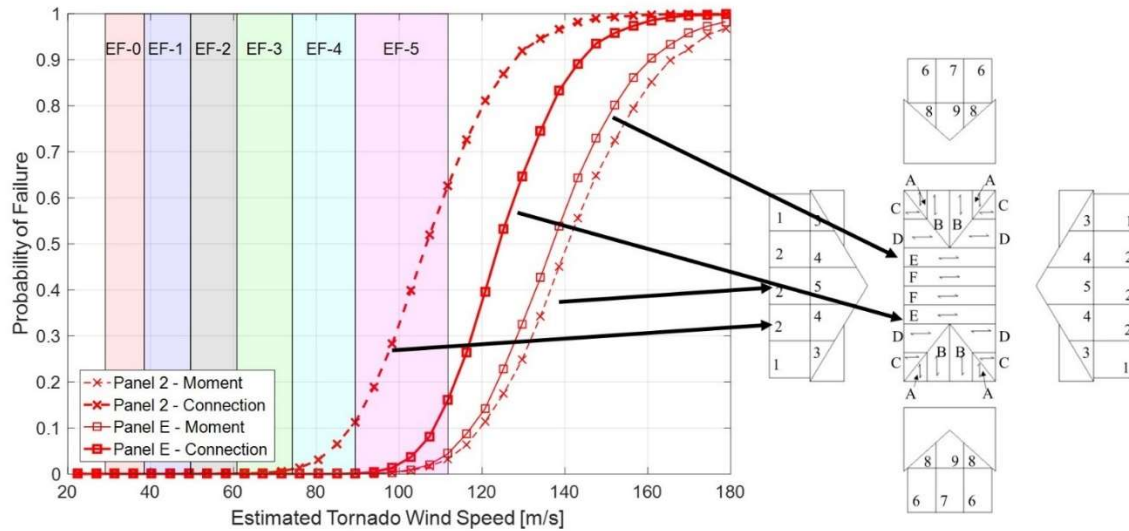


Figure 5.6: Examples of panel fragilities developed for structure 1

The total structure fragility for each structure type was plotted along with the wall, roof, sliding, and combined uplift and overturning fragilities in Figures 5.7 and 5.8 where the shaded areas represent the estimated wind speed for each of the levels on the EF scale 0-5. The performance of each of the six archetype structures was dominated primarily by failures of the wall and roof panels (due to bending and negative pressure connection failures) and sliding failure. Structure Types 1, 2, and 3 were controlled largely by the wall component fragilities, while structure Types 4 and 5 were controlled by the roof fragilities. System level failures associated with sliding were a contributing failure mechanism for Structure Types 1, 3, and 5.

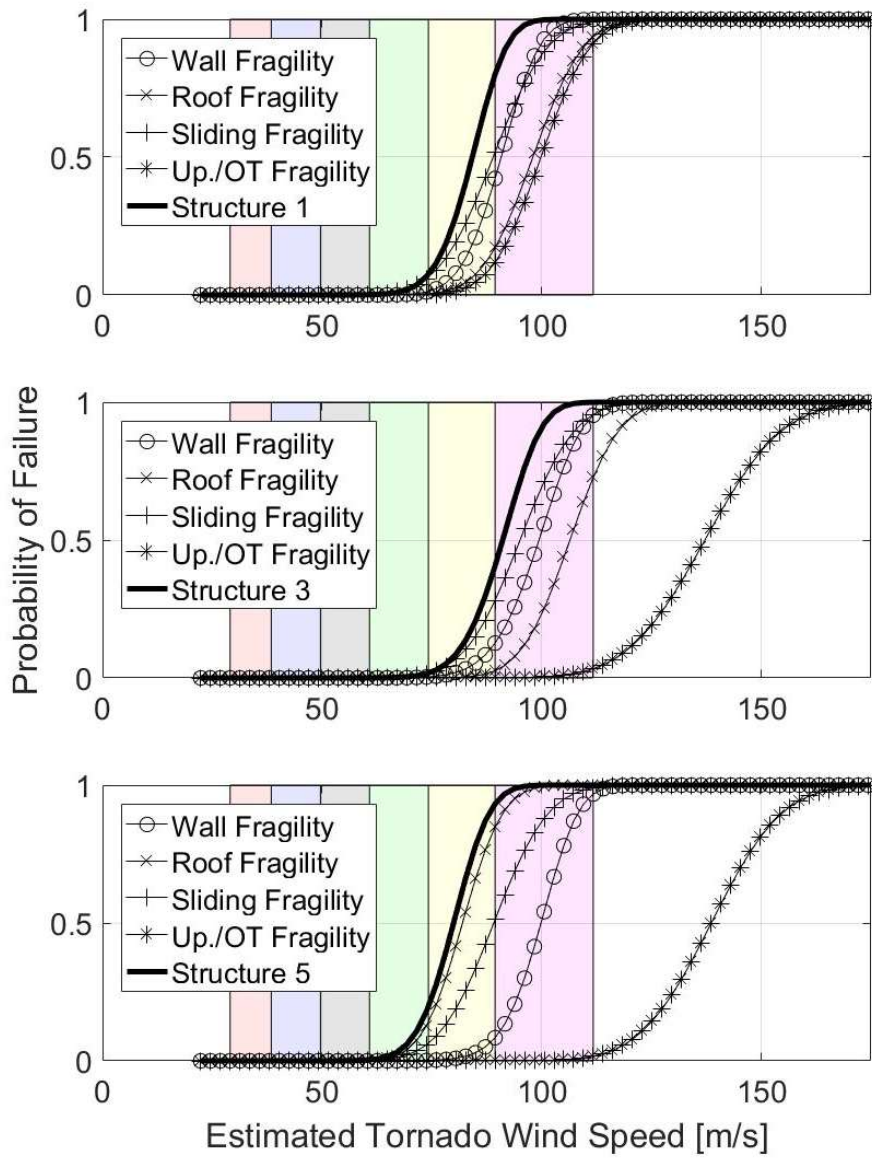


Figure 5.7: Wall, roof, and system fragilities for structures 1, 3, and 5

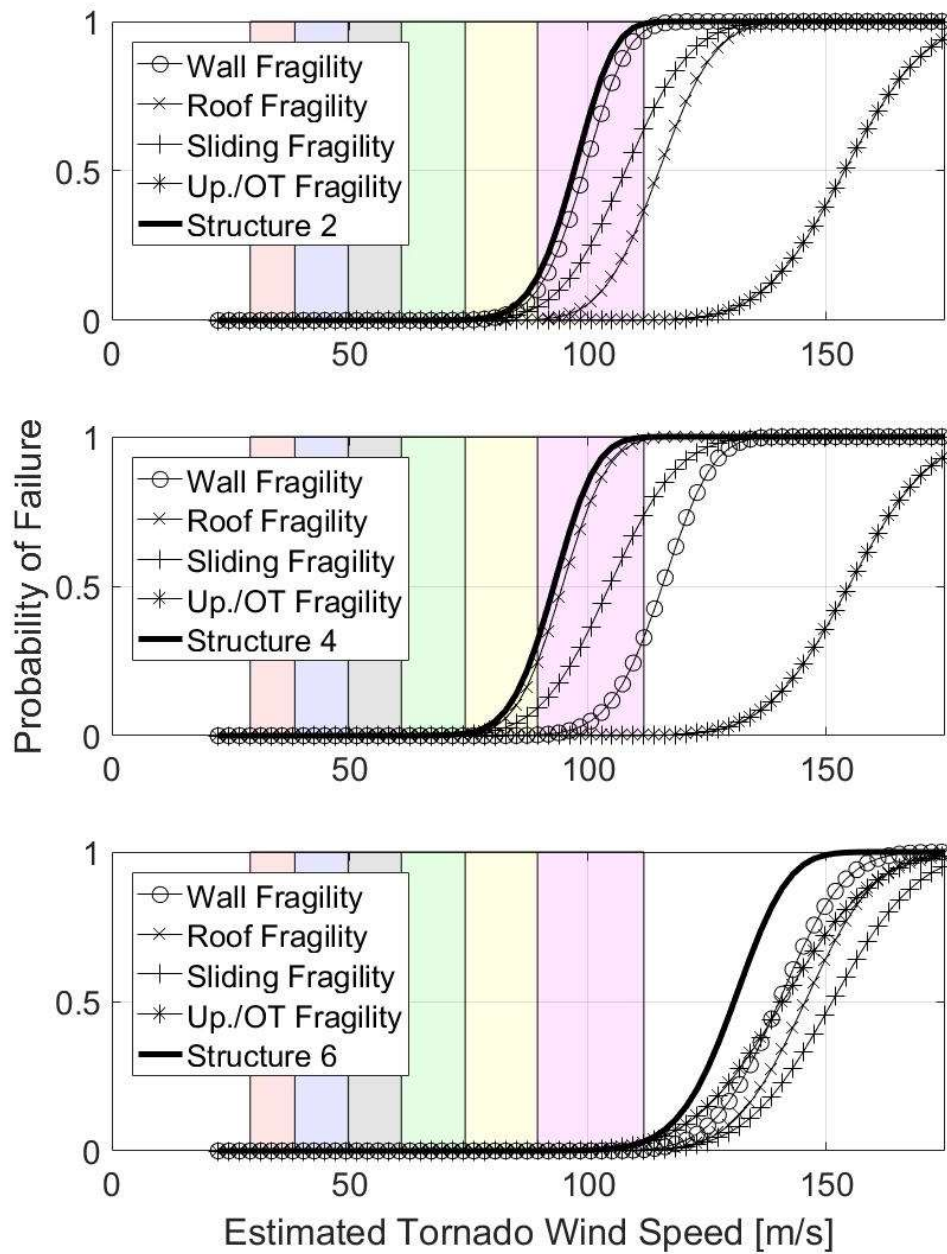


Figure 5.8: Wall, roof, and system fragilities for structures 2, 4, and 6

The bracket-type connector spacing was found to have a significant impact on the simulated performance as shown in Figure 5.9 for Structure 1. The windspeed resulting in 10% probability of failure increased from 65.8 m/s (147 mph) to 86.0 m/s (193 mph) when

the spacing decreased from 122 cm (48 in) to 61 cm (24 in). An increase of 32% and 29% in windspeed resulting in 10% probability of failure probability was also experienced for structure Types 2 and 3 where spacing of connection in wall elements had a more significant impact on the performance of the entire structure. Increases in median failure probability for structure Types 4 and 5 was only in the range of 9-10% where the failure was controlled more by the screw connection at the roof.

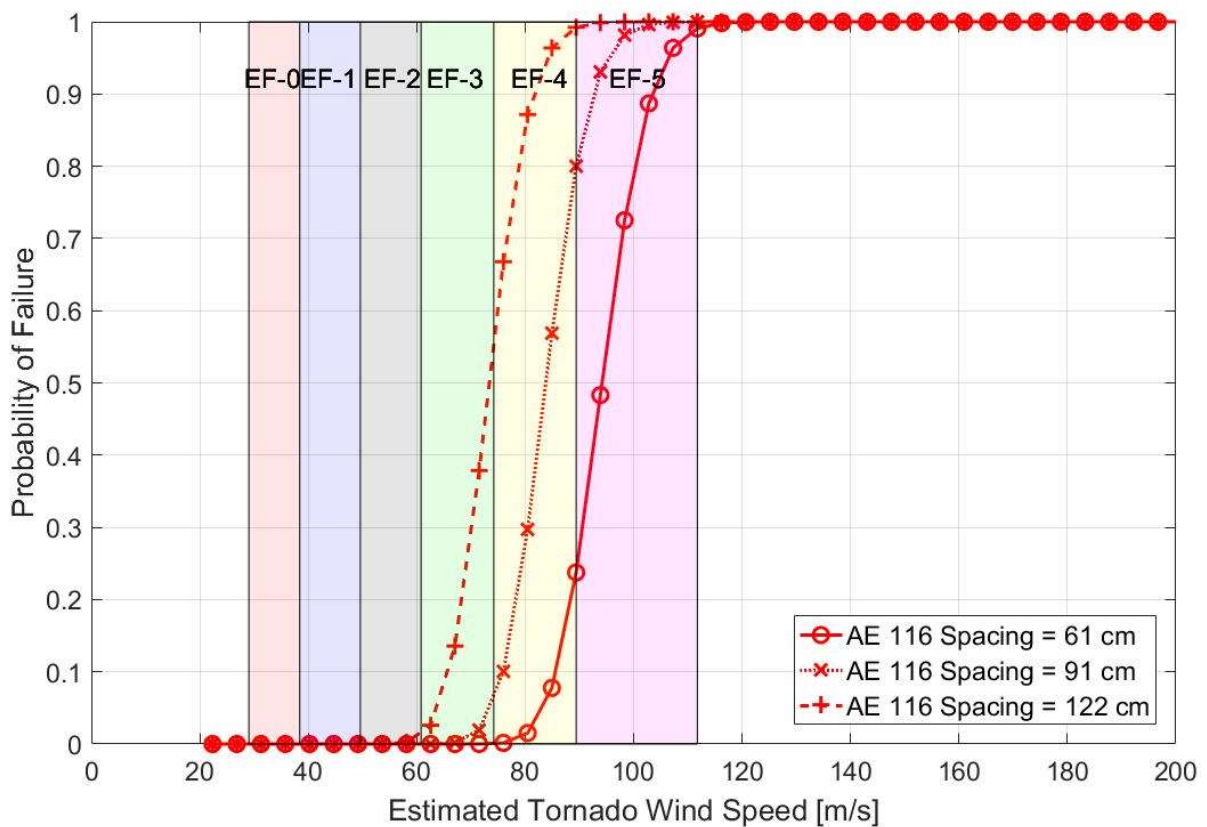


Figure 5.9: Variation in performance based on change in spacing of bracket-type connections for structure 1

Where failure of the roof components played greater role in the simulated performance of the structure, the spacing of the boundary screw connections had a more

significant impact on the simulated performance as with structure Types 4, 5, and 6. The variation in simulated performance of structure Type 4 is shown in Figure 5.10 where there was an increase in the windspeed resulting in 10% probability of failure from 74.9 m/s (168 mph) to 90.8 m/s (203 mph) when the screw spacing decreased from 30.5 cm (12 in) to 15.2 cm (6 in). Other archetypes experienced increases in the windspeed resulting in 10% probability of failure that ranged from 1% for structure Types 1, 2, and 3 to 21% for structure Types 4, 5, and 6.

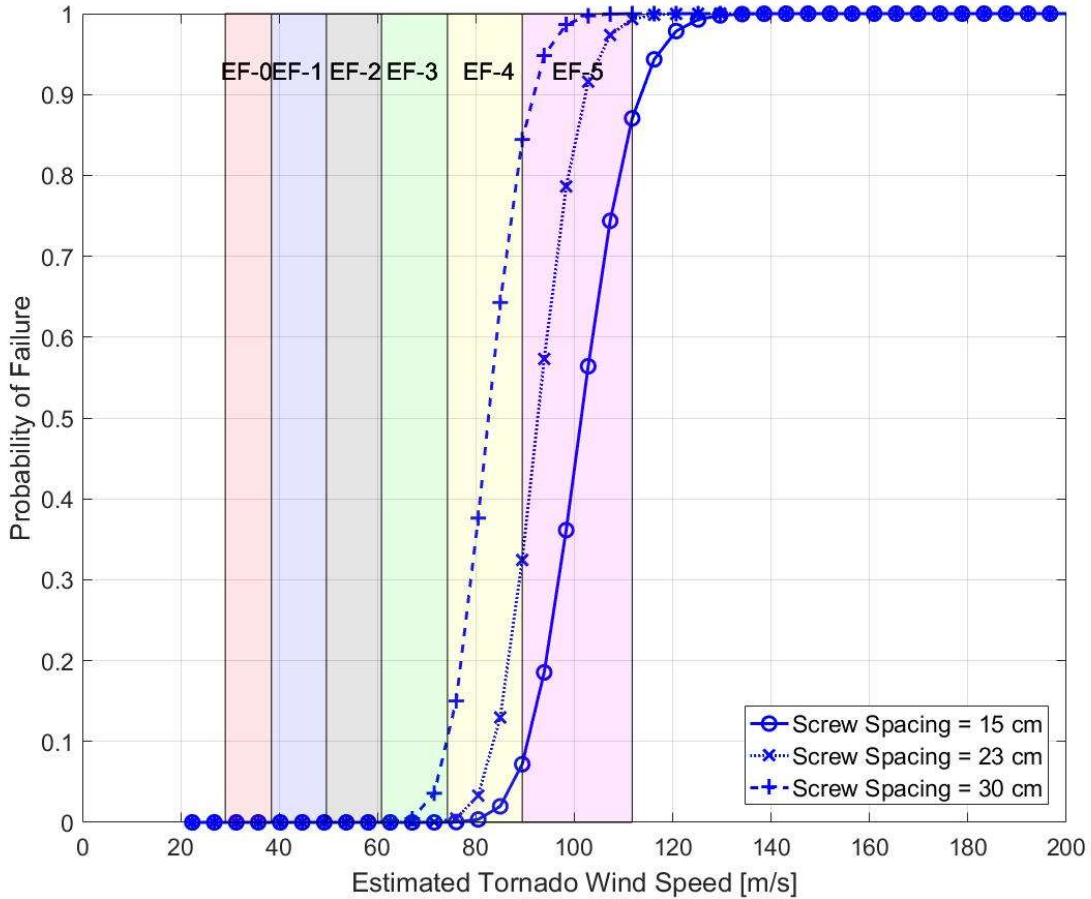


Figure 5.10: Variation in performance based on change in spacing of screw connections for structure 4

The debris impact performance of the CLT structures was considered by assuming the internal pressure coefficient be enclosed for the portion of the analysis where the CLT elements resisted simulated debris impacts. The windspeed resulting in 10% probability of failure decreased by 10-15% between the simulations with 0 debris impacts and 1 debris impact. Increasing the number of debris impacts to 2 caused an additional 1-2% reduction in the windspeed resulting in 10% probability of failure. After 3 severe impacts to the structure, the performance of the archetypes remains largely unchanged with additional simulated impacts. Furthermore, simulations where the internal pressure classification was set to partially enclosed for the entirety of the simulation showed little difference compared those where 3-5 debris impacts were simulated. This indicates that while the debris impact performance may reduce the direct hazard to occupants of a structure, it may not significantly influence structural performance when only the internal pressure coefficient is considered. The response to debris impact loads may also have a negative effect on the connection or panel capacities, but were neglected in this study. Vulnerabilities such as building fenestrations may also lead to a partially enclosed structure. If sufficient coverings were applied to building fenestrations and the performance of 3-ply CLT was considered, an increase of up to 10-15% could be achieved.

Assumptions about the amount of overturning taken by the in-plane walls as a percentage of the total global overturning moment were found to have a small effect on the overall simulated performance of the structure. This is in large part due to the dominance of the component fragilities in the simulated response of the structures. When the overturning ratio was varied between 50% and 100% the change in the windspeed resulting

in 10% probability of failure was only between 2% and 4% for all archetypes. This is likely because system overturning was not the most significant failure mechanism for any of the archetypes due to the relatively high ratio between the building plan dimensions and structural height. Taller, more slender structures would likely exhibit a higher vulnerability to rocking and uplift failure.

The results of the fragility analysis comparing the entire structure are shown in Figure 5.11 and indicate that structure Type 5 is most vulnerable to tornado events with a windspeed resulting in 10% probability of failure of 71.9 m/s (161 mph) while structure Type 6 is least vulnerable with a windspeed resulting in 10% probability of failure of 119 m/s (266 mph). Windspeed resulting in 10% probabilities of failure were found to be in the range of EF-4 level events. The increased performance observed for structure Type 6 was due to the small footprint, low roof height, relatively small panel spans, and large number of base connections per square foot. In addition, this archetype was developed specifically to maximize the performance of a CLT residential structure and demonstrates the potential for peak levels of safety achievable with CLT. The performance of all archetype structures was significantly linked to the panel spans and connection spacing associated with the structural layout. Consequently, design considerations and architectural preferences would likely have an impact on the performance of residential structures constructed using CLT.

In addition to the performance of CLT archetypes, the performance of light-frame construction archetypes was plotted in Figure 5.11 for comparison. In the plotted fragilities, the archetypes considered 8d nails with 150mm/150mm (6in/6in) spacing and

hurricane clip connections between roof trusses and wall elements with fragility parameters taken directly from the study by Amini and van de Lindt (2013). The windspeed resulting in 10% probabilities of failure increased from EF-0 and EF-1 levels to EF-4 when built with CLT instead of light-frame construction. This increase is to be expected as the volume of wood and production costs of CLT increase the overall cost of a CLT residential structure compared to one built using light-frame construction techniques. Studies concerning the feasibility of residential CLT construction estimate a 20-30% increase in the upfront cost of CLT based on the current market state of mass timber in the Denver, CO area (Burback and Pei, 2017). An analysis of the likelihood of tornado hazards would indicate whether such a premium on CLT construction would be offset by the improvement in performance.

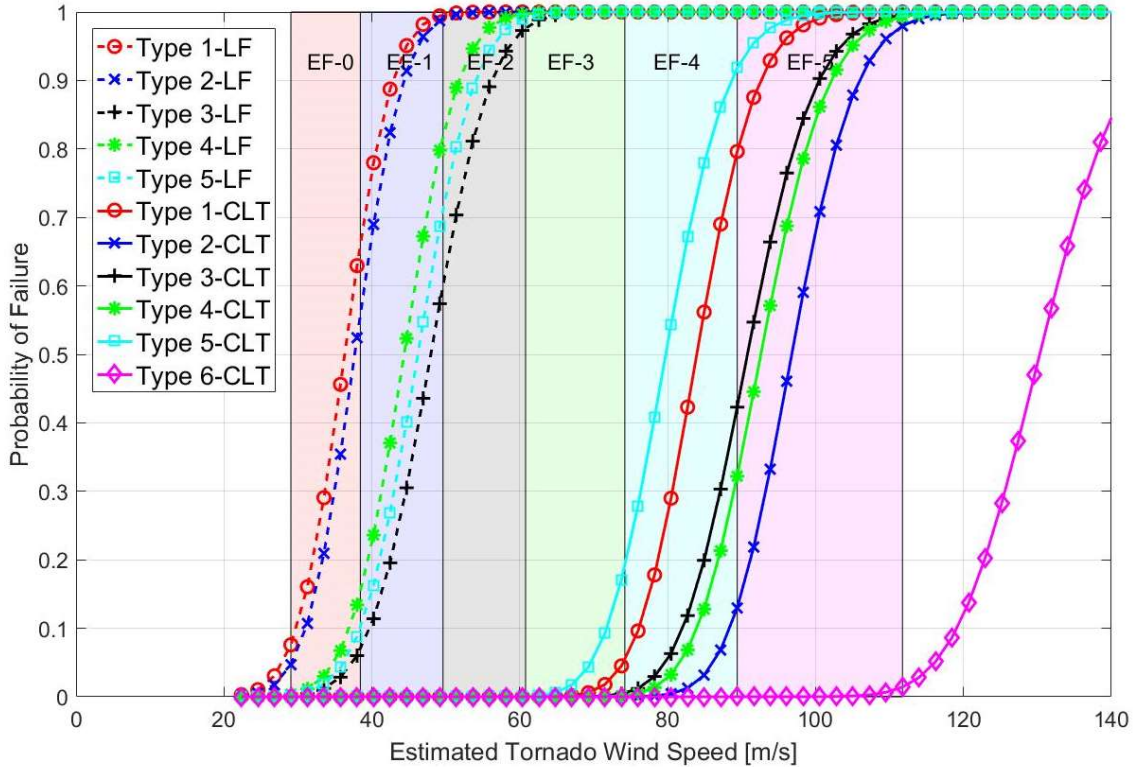


Figure 5.11: Simulated performance of all structure types compared to light-frame construction

5.7 Summary and Conclusions

The purpose of this study was to determine the potential improvement in expected performance of residential structures built using Cross-Laminated Timber subject to tornado hazards. In order to compare to previous studies on light-frame residential archetypes, a set of consistent archetypes was used to simulate a portion of the residential building stock. The design the envelope of these structures followed applicable design standards for both gravity load and straight-line wind to produce spans and panel layouts that attempt to maximize the efficiency CLT as a panelized product. This design approach neglected the vibration and fire design of the CLT elements. Using typical connections,

the probability of failure in the event of tornadoes was simulated through Monte Carlo Simulation and tornado wind analysis consistent with the procedures outlined in design recommendations was performed. Failure was controlled largely by the roof and wall components, their connections. In addition, the sliding failure played a role in the performance of the structures. Overturning and uplift of the structure did not play a significant role due to the geometry and aspect ratios of the archetypes. With taller and more slender structures, overturning and uplift would likely be a more significant failure mode. Studying the potential increases in resistance to debris impact loads associated with CLT by simulating the internal pressure coefficient (enclosed or partially enclosed based on simulation results) showed an improvement in the performance of the structures of approximately 10%. Analysis of the uplift and overturning fragilities showed that the amount of overturning taken by the in-plane walls as a percentage of the overall overturning moment had little effect on the final simulated fragilities. This is due to the fact that the dominant failure mechanisms were the components of the wall and roof structure as well as system sliding. Other residential structure geometries and connection types and spacings could have a higher vulnerability to system level failures of uplift and overturning.

Ultimately, the CLT archetypes used in the study were found to have experience approximately 10% probability of failure during EF-4 level events as compared to EF-0 and EF-1 for light-frame residential structures. By limiting spans and increasing the number of connections, performance of the residential archetypes could be further improved. As much as improved performance is to be expected, the cost of CLT would be

higher than traditional light-frame building techniques. Further study of the economics of CLT as a residential construction material coupled with the improved structural performance and geographic variations in hazard would give additional information about the applicability of such construction materials and techniques. In addition, empirical evidence of the performance of such structures, whether through full-scale testing or post-storm events, would be needed to further confirm Cross-Laminated Timber's performance as a residential building material subject to tornadoes.

5.8 References

Podesto, L. (2011). The coming of Cross-Laminated Timber. *The Construction Specifier*, Buffalo, United States. 45-55.

Karacabeyli, E., Douglas, B. (2013). *CLT Handbook: Cross-Laminated Timber*. FPInnovations, Pointe-Claire, QC.

Kroll Brand Rating Agency. (2019, March 28). KBRA Releases Insurance Research: Insured Losses Rising for Tornadoes. Retrieved May 19, 2019. Retrieved from <https://www.marketwatch.com/press-release/kbra-releases-insurance-research-insured-losses-rising-for-tornadoes-2019-03-28>.

Facts Statistics: Tornadoes and thunderstorms. (n.d.). Retrieved May 19, 2019, from <https://www.iii.org/fact-statistic/facts-statistics-tornadoes-and-thunderstorms>.

Ellingwood, B. R., & Rosowsky, D. V. (2004). *Fragility Assessment of Structural Systems in Light-Frame Residential Construction Subjected to Natural Hazards*. Structures 2004. doi: 10.1061/40700(2004)119

- Ashley, W. S. (2007). Spatial and Temporal Analysis of Tornado Fatalities in the United States: 1880–2005. *Weather and Forecasting*, 22(6), 1214–1228. doi: 10.1175/2007waf2007004.1
- Roueche, D. B., Lombardo, F. T., & Prevatt, D. O. (2017). Empirical Approach to Evaluating the Tornado Fragility of Residential Structures. *Journal of Structural Engineering*, 143(9), 04017123. doi: 10.1061/(asce)st.1943-541x.0001854
- Standohar-Alfano, C. D., Freyne, S., Graettinger, A. J., Floyd, R. W., & Dao, T. N. (2015). Performance of Residential Shelters during the May 20, 2013, Tornado in Moore, Oklahoma. *Journal of Performance of Constructed Facilities*, 29(5), 04014143. doi: 10.1061/(asce)cf.1943-5509.0000636
- Amini, M., and van de Lindt, J. (2013). “Quantitative insight into rational tornado design wind speeds for residential wood-frame structures using fragility approach.” *J. Struct. Eng.*, 10.1061/(ASCE)ST.1943-541X.0000914, 04014033.
- ASCE. (2016). “Minimum design loads for buildings and other structures.” *Structural Engineering Institute*, Reston, VA.
- AWC. (2018). *National Design Specification for Wood Constructions (NDS)*. Forest Product Association.
- Raymond, Augustus L., (2019). "An Exploration into Tornado Resistant Residential CLT Structures". All Theses. 3095. https://tigerprints.clemson.edu/all_theses/3095
- Kreuzinger H. 1995. Mechanically jointed beams and columns. In *Timber Engineering – STEP I*, ed. H.J. Blaas et al. B11/1-8. Almere, The Netherlands: Centrum Hout.

European Committee for Standardization, 2004. Eurocode 5: Design of timber structures. Part 1-1: General – Common rules and rules for buildings. EN 1995-1-1. Brussels: CEN, 124 p.

Blass H.J., and P. Fellmoser. 2004. Design of solid wood panels with cross layers. In Proceedings of the 8th World Conference on Timber Engineering, June 14-17, 2004. Lahti, Finland, 2:543-548.

Kopp, G. A., and Morrison, M. J. (2011). Discussion of “Tornado-induced wind loads on low-rise buildings” by F. L. Haan, V. K. Balaramudu, and P. P. Sarkar, J. Struct. Eng. 137, 1620–1622.

Haan, F. L., Balaramudu, V. K., and Sarkar, P. P. (2010). “Tornado-induced wind loads on a low-rise building,” J. Struct. Eng., 10.1061/(ASCE)ST.1943-541X.0000093, 106–116.

Lee, K. H., and Rosowsky, D. V. (2005). “Fragility assessment for roof sheathing failure in high wind regions.” Eng. Struct., 27(6), 857–868, 10.1016/j.engstruct.2004.12.017.

APA-The Engineered Wood Association. (2018). Standard for performance rated cross laminated timber. ANSI/APA PRG 320. Tacoma, WA:

Gu, Mengzhe, (2017). “Strength and Serviceability Performances of Southern Yellow Pine Cross-Laminated Timber (CLT) and CLT-Glulam Composite Beam.” All Dissertations.

Simpson Strong Tie, (2019). “Wood Construction Connectors.” Retrieved from <https://www.strongtie.com/resources/literature/wood-construction-connectors-catalog>

- Schneider, J., Shen, Y., Stiemer, S., & Tesfamariam, S. (2015). Assessment and comparison of experimental and numerical model studies of cross-laminated timber mechanical connections under cyclic loading. *Construction and Building Materials*, 77, 197–212. doi: 10.1016/j.conbuildmat.2014.12.029
- Gavric, I., Fragiaco, M., & Ceccotti, A. (2014). Cyclic behaviour of typical metal connectors for cross-laminated (CLT) structures. *Materials and Structures*, 48(6), 1841–1857. doi: 10.1617/s11527-014-0278-7
- Liu, J., & Lam, F. (2018). Experimental test of coupling effect on CLT angle bracket connections. *Engineering Structures*, 171, 862–873. doi: 10.1016/j.engstruct.2018.05.013
- MahdaviFar, V., Barbosa, A. R., Sinha, A., Muszynski, L., Gupta, R., & Pryor, S. E. (2019). Hysteretic Response of Metal Connections on Hybrid Cross-Laminated Timber Panels. *Journal of Structural Engineering*, 145(1), 04018237. doi: 10.1061/(asce)st.1943-541x.0002222
- Shahnewaz, M. Tannert, T., Popovski, M., & Alam, M. (2018). “Deflection of CLT Shear Walls in Platform Construction.” In Proc., World Conf. on Timber Engineering. Seoul, South Korea, WCTE.
- Lukacs, I., Björnfot, A., & Tomasi, R. (2019). Strength and stiffness of cross-laminated timber (CLT) shear walls: State-of-the-art of analytical approaches. *Engineering Structures*, 178, 136–147. doi: 10.1016/j.engstruct.2018.05.126
- Popovski, M., Karacabeyli, E., and Ceccotti, A. (2011). Seismic Performance of Cross-Laminated Timber Buildings - Chapter 4. *CLT Handbook - Cross-Laminated*

Timber, FPInnovations Special Publication SP-528E, Canadian Edition, ISBN 978-0-86488-547-0.

Pei, S., Popovski, M., & Lindt, J. W. V. D. (2013). Analytical study on seismic force modification factors for cross-laminated timber buildings. *Canadian Journal of Civil Engineering*, 40(9), 887–896. doi: 10.1139/cjce-2013-0021

Reynolds, T., Foster, R., Bregulla, J., Chang, W.-S., Harris, R., & Ramage, M. (2017). Lateral-Load Resistance of Cross-Laminated Timber Shear Walls. *Journal of Structural Engineering*, 143(12), 06017006. doi: 10.1061/(asce)st.1943-541x.0001912

Shahnewaz, M., Popovski, M., & Tannert, T. (2019). Resistance of Cross-Laminated Timber Shear Walls for Platform-Type Construction. *Journal of Structural Engineering*, 145(12), 04019149. doi: 10.1061/(asce)st.1943-541x.0002413

Folz, B., and Filiatrault, A. (2001). “Cyclic analysis of wood shear walls.” *J. Struct. Eng.*, 127(4), 433–441.

Burback, B., & Pei, S. (2017). Cross-Laminated Timber for Single-Family Residential Construction: Comparative Cost Study. *Journal of Architectural Engineering*, 23(3), 06017002. doi: 10.1061/(asce)ae.1943-5568.0000267

CHAPTER SIX

HAZARD ASSESSMENT OF CROSS-LAMINATED TIMBER AND LIGHT-FRAME

RESIDENTIAL CONSTRUCTION SUBJECT TO TORNADO HAZARDS

Taken from: *Tornado Hazard Assessment of Residential Structures Built Using Cross-Laminated Timber and Light-Frame in the United States* (A paper in preparation)

ABSTRACT: Research has continued to broaden understanding of tornadoes and their effect on civil infrastructure. Because a significant portion of the losses associated with tornado events impact residential structures, it is appropriate to conduct a risk-based hazard assessment of these structures, particularly those constructed using wood since more than 90 percent of residential buildings are constructed of wood. In addition, alternatives to light-frame construction, including Cross-Laminated Timber (CLT), provide stronger and more resilient structures. CLT is an engineered wood product made of gluing orthogonal layers of dimensioned lumber to produce panels. In this study, the performance of traditional light-frame construction and CLT archetypes was used to calculate the risk associated with tornadoes. In addition, a tornado hazard database was utilized to determine the geographic variation in risk associated with residential structures built using CLT and light-frame construction. This risk was quantified in terms of the annual probability of failure, reliability index, and the expected average annual loss. Comparisons of annual probability of failure and reliability index show that, for large portions of the United States, light-frame construction following the current practice does not exhibit the level of reliability recommended by design standards. In those same areas, CLT structures designed in accordance to the current code standards and engineering principles exhibited

a significantly smaller annual probabilities of failure and larger reliability index. A comparison of cost (direct building and content losses) shows that tornado hazards alone do not make it economically advantageous to build using CLT; however, consideration of additional hazards (e.g., non-tornadic wind and earthquake) and other indirect losses (e.g., interruption cost and loss of lives) could make it an alternative worth considering.

6.1 INTRODUCTION

Tornadoes are the product of a violently rotating column of air that can produce wind speeds in excess of 134 m/s (300 mph). These natural hazards can cause significant damage in the form of economic and social losses due to damage of property and loss of life. They are particularly devastating due to their violent nature and lack of warning time where storms can form in as little as 15 minutes (KBRA, 2019). While recommendations are made in the commentary of American design standards, ASCE 7-16, *Minimum Design Loads and Associated Criteria for Buildings and Other Structures* (ASCE, 2016), tornado hazards are not explicitly addressed in requirements for structural design. Research has explored the hazard associated with tornadoes in the United States, but the relatively small impact area and high level of hazard make the risk difficult to quantify. Such research has relied heavily on simulating tornado risk based on historical data gathered on the occurrence, size, intensity, and path of tornadoes in the United States (Fan and Pang 2019 Strader et al. 2015). This research attempts to quantify the hazard associated with tornadoes, which can be used to simulate and study the performance of various structures which are subject to tornado hazards. In general, these studies present the probability of exceeding various tornado hazard levels over a given span of time. Tornado intensity scale

is quantified through the Enhanced-Fujita scale (EF-scale) which categorizes tornadoes with a magnitude between 0 and 5 based on the maximum estimated wind speed that occurs during the event (McDonald and Mehta 2006). The EF-scale and estimated tornado wind speed is shown in Table 6.1.

Table 6.1: Enhanced Fujita scale and corresponding wind speeds

Magnitude	F-Scale wind speed [kph]		EF-scale wind speed [kph]	
	Lower Bound	Upper Bound	Lower Bound	Upper Bound
0	72	126	105	137
1	127	189	138	176
2	190	260	177	221
3	261	337	222	269
4	338	421	270	321
5	422	510	322	377

Studies have shown that a significant portion of the economic impact of tornadoes affects residential structures which are built primarily using conventional wood framing techniques (Ellingwood and Rosowsky, 2004). Furthermore, historical data has shown that deaths that occur as a result of tornadoes are most likely to occur in mobile homes and permanent residential structures (Ashley, 2007). This information has led to studies into the performance of wood-frame residential structures subject to tornado hazards that both predict the performance of structures (Amini and van de Lindt 2013, Masoomi et. al 2018) and use post-event analysis of damage to determine the performance of such structures (Alfano et. al 2015, Roueche et. al 2017). The results of these studies showed that wood-frame residential structures would experience damage and possible failure from EF-1 and EF-2 level events and quantify structural performance through fragility curves. These

curves relate the intensity measure, most often wind speed, with the probability of exceeding a given damage state. With vulnerabilities to tornadoes in traditional wood-frame construction, alternative construction materials for residential structures have been considered. Cross-Laminated Timber (CLT) offers a stronger wood alternative to light-frame construction techniques that could be used to construct residential structures where tornadoes are found to be particularly vulnerable. CLT panels are made by gluing orthogonal layers of dimensioned lumber to create 3-layer, 5-layer, or 7-layer panels that exhibit a high degree of dimensional stability and increased resistance to the hazards that are associated with tornadoes, namely wind-induced pressures and windborne debris.

In this study, the risk of loss due to tornado was quantified for the contiguous United States by defining the hazard associated with tornadoes with data gathered through simulation of historical tornado observations. Once the hazard is defined for locations in the US, it was combined with the performance of traditional wood-frame construction as well as with CLT residential construction. With an understanding of both the hazard and performance, statistics about the structural reliability were determined. In addition, a comparison of the estimated losses due to tornado induced wind-pressures was performed to establish the financial impact of building residential structures using CLT.

6.2 TORNADO SIMULATION AND HAZARD QUANTIFICATION

Previous research on tornado simulation (Fan and Pang, 2019) developed a stochastic model for tornado track simulation. This model includes a genesis model, a tracking model, and a wind field model that are based on historical observations made from a time period of 1951-2015. Based on the historical data, tornado tracks, intensities, and

wind field statistics were simulated for 1 million years in the contiguous United States. From these simulations, data was captured about the tornado hazard associated with a grid of latitude and longitude points. As the hazard associated with tornadoes is largely influenced by both the impact area of the tornado, the size of the structure, significantly affects the level of hazard (Twisdale 1983). Results of the simulations (Fan and Pang, 2019) utilized a grid of points separated by 24.1 km (15 miles). The hazard associated with each grid point was calculated for four different circular target sizes summarized in Table 6.2. For analysis regarding residential structures, only the point target size and small target size were considered applicable as most residential structures are relatively small; whereas, medium and large size targets would be more applicable for infrastructure such as schools or airports.

Table 6.2: Targets size to determine tornado hazard

Target Size	Radius [m]	Area [km ²]
Point	-	-
Small	89	0.025
Medium	177	0.098
Large	715	1.606

The hazard for each grid point and target size was determined for each of the EF-scales, EF-0 to EF-5, and were reported as an annual probability of exceedance. The annual probability of experiencing tornado winds of EF-0 and higher ($V \geq 29$ m/s) with a point target size in the contiguous United States is shown in Figure 6.1. The data presented shows the increased hazard in the states located within Tornado Alley, the area of the central United States where tornadoes are known to be frequent.

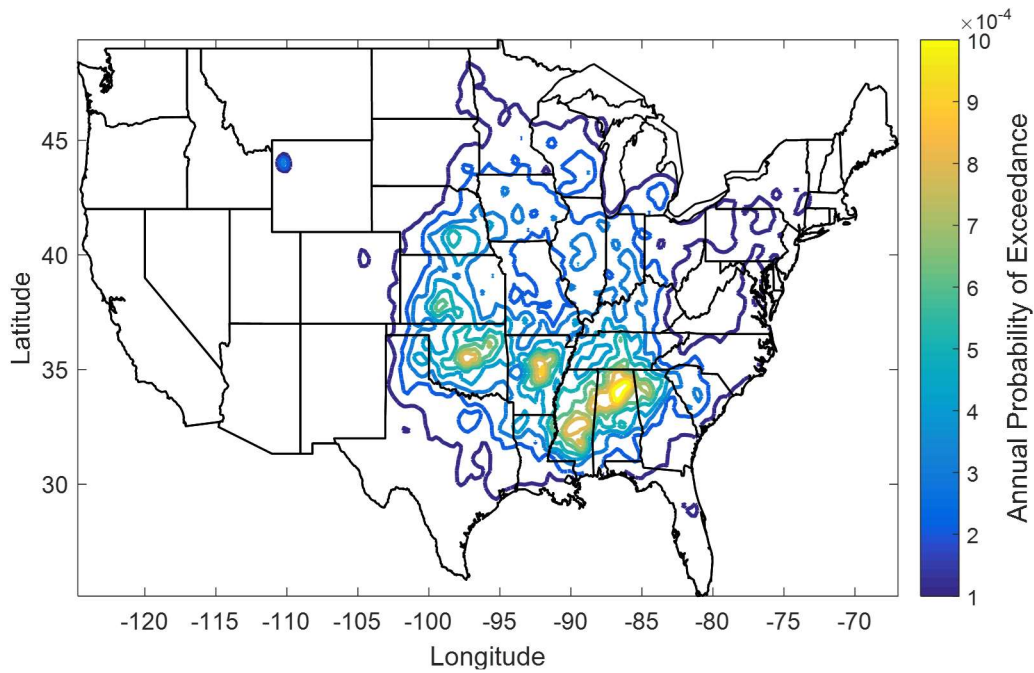


Figure 6.1: Annual probability of experiencing EF-0 or greater for point size target (0.098 km²)

In order to better utilize the hazard information from each of the grid points, the data points corresponding to each of the EF-scale tornadoes were fit to a function typically used to describe seismic hazard and shown modified in Equation 6.1 (Bradley et. al 2007). In this equation, the annual probability of exceedance, APE , is a function of fitted parameters, APE_0 and α , as well as a maximum estimated wind speed, V_{max} and the input wind speed, V . Graphically, the function represents a hyperbola in log-log space with asymptotes represented by the horizontal asymptote, APE_0 , and vertical asymptote, V_{max} . The parameters V_{max} , α , and APE_0 were fit to create a hazard function for each of grid points in the study domain. Where probabilities of exceedance for EF-3, EF-4, and EF-5 tornadoes were 0, for a given data point, the value of V_{max} was defined as the upper bound wind speed corresponding to the highest intensity tornado event observed.

$$APE(V) = APE_0 e^{\frac{\alpha}{\ln(\frac{V}{V_{max}})}} \quad (6.1)$$

An example of the parametrically fit equation and the simulated annual probability of exceedance for each EF-level representing represents Huntsville, AL (Latitude: 34.7304° N, Longitude: 86.5861° W) is shown in Figure 6.2 in both log-log space (left) and linear space (right). A non-linear least square regression was used to fit the data where the logarithms of the error were minimized so that the fit would not be weighted toward the larger values of annual probability of exceedance corresponding to lower intensity tornado events. As a point of comparison, the ASCE 7-16 wind hazard has been plotted in the log-log space to give an indication of its intensity compared to tornado hazards. For this study, only the hazard associated with tornado events was considered for calculations regarding the risk associated with residential structures.

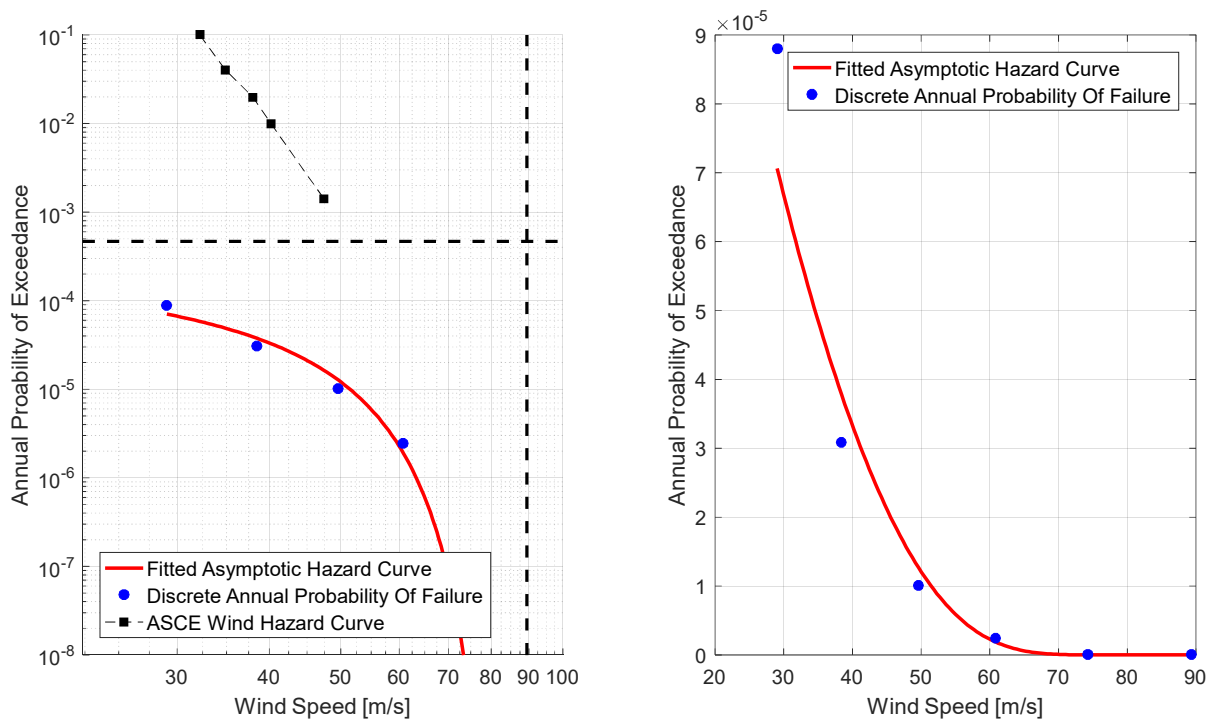


Figure 6.2: Example of fitted asymptotic hazard curves, (left) log-log scale, and (right) linear scale.

6.3 COST ESTIMATION OF CLT RESIDENTIAL STRUCTURES

To fully quantify the performance of wood residential structures in a tornado, financial information comparing traditional wood-frame construction to CLT construction was required. Research efforts have been made to determine the feasibility of CLT as a residential construction material (Burback and Pei, 2017). In this study, a 172 m² (1,850 sf) residential structure was designed as light-frame construction, CLT construction, and an optimized CLT design that utilized CLT, dimensioned lumber, and glulam elements to provide a more efficient and economic design. A cost breakdown of each of the three configurations was reported based on quotes from manufacturers and contractors presented with the plans. The cost breakdown reported is summarized in Table 6.3 based on the structure being built in Arvada, CO. To apply this design specific information to the residential archetypes used to estimate the performance wood residential structures, the cost information was normalized on a square meter (square foot) basis.

Table 6.3: Summarized cost information (Burbach and Pei, 2017)

Project Task	Light-Frame		CLT		Optimized CLT	
	Total Cost	Cost per m ² (ft ²)	Total Cost	Cost per m ² (ft ²)	Total Cost	Cost per m ² (ft ²)
Project Preparation	\$153,300	\$892 (\$82.86)	\$153,780	\$895 (\$83.12)	\$153,780	\$895 (\$83.12)
Foundation	\$29,780	\$173 (\$16.10)	\$29,780	\$173 (\$16.10)	\$29,780	\$173 (\$16.10)
Frame Work	\$44,220	\$257 (\$23.90)	\$153,270	\$892 (\$82.85)	\$120,270	\$700 (\$65.01)
Exterior Work	\$31,295	\$182 (\$16.92)	\$31,295	\$182 (\$16.92)	\$31,295	\$182 (\$16.92)
Interior Work	\$42,930	\$250 (\$23.21)	\$44,860	\$261 (\$24.25)	\$44,860	\$261 (\$24.25)
Interior Work Final	\$50,560	\$294 (\$27.33)	\$51,360	\$299 (\$27.76)	\$51,360	\$299 (\$27.76)
Final Details	\$41,000	\$239 (\$22.16)	\$45,200	\$263 (\$24.43)	\$45,200	\$263 (\$24.43)
Total	\$393,085	\$2,288 (\$212.48)	\$509,545	\$2,966 (\$275.43)	\$476,545	\$2,774 (\$257.59)

The cost information had to be adjusted based on geographic variations on both material and labor. This information on the geographic variations in price is available through RSMeans (Plotner, 2019) and is referred to as the city cost index, which modifies the cost of building materials and labor across the United States. The index is normalized to a value of 100 such that cities with a cost index greater than 100 are more expensive and those with an index less than 100 are less expensive. RSMeans reports three distinct values that represent the material cost, labor cost, and a total value which combines all aspects of the construction process. In addition, cost index values are given for different construction division including site preparation, concrete, metals, finishes, and a weighted average of all categories. For this study, the value given for a weighted average of all categories was used as an estimate compare the cost of a CLT residential structure across the United States. The meshed grid of city cost index factors for the weighted average of all given US cities is shown in Figure 6.3.

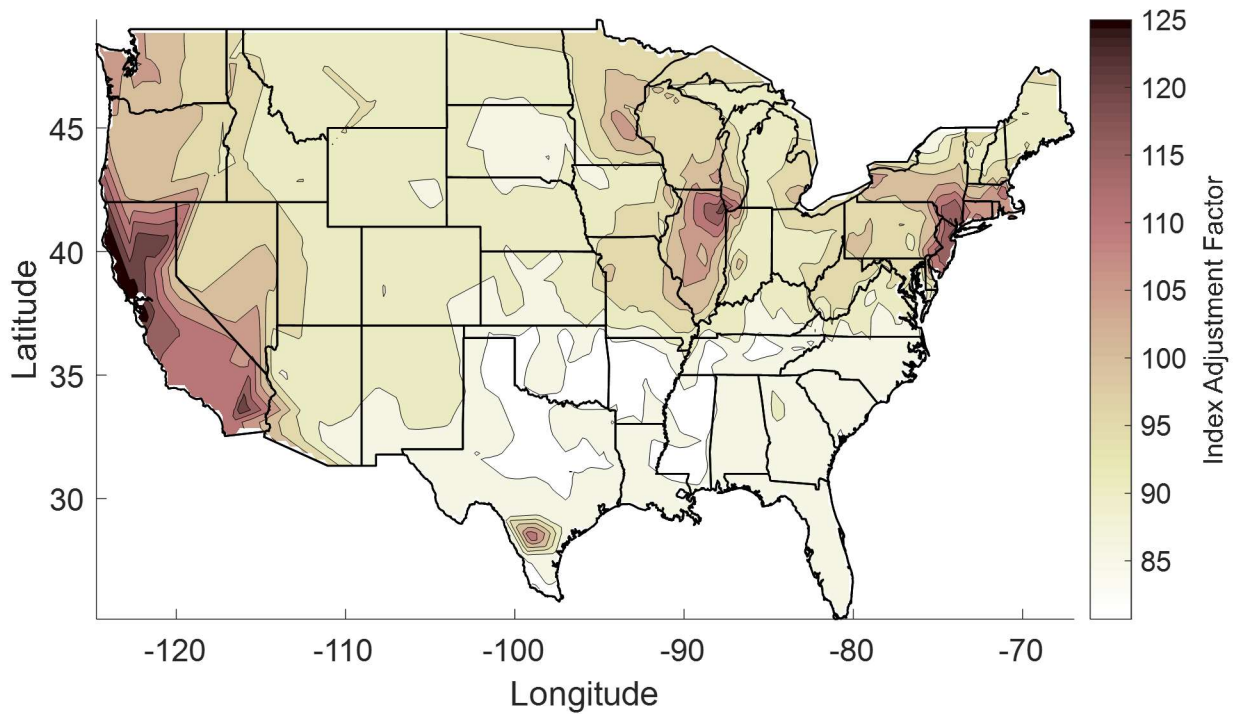


Figure 6.3: Weighted average city cost index factor for locations in the United States

Additionally, the cost of shipping CLT was considered by determining the distance to the nearest manufacturer of CLT. Currently, there are eight manufacturers of CLT in the United States and Canada which were considered in the cost of shipping. For each of the points in the study domain, the approximate cost of shipping was calculated by determining the distance to the nearest manufacturer and an estimated cost of shipping equal to \$1.86/km (\$3/mi) (Truck Freight Rates, 2017). The variation in the up-front cost

of a CLT residential structure are shown in Figure 6.4 on a cost per square meter basis.

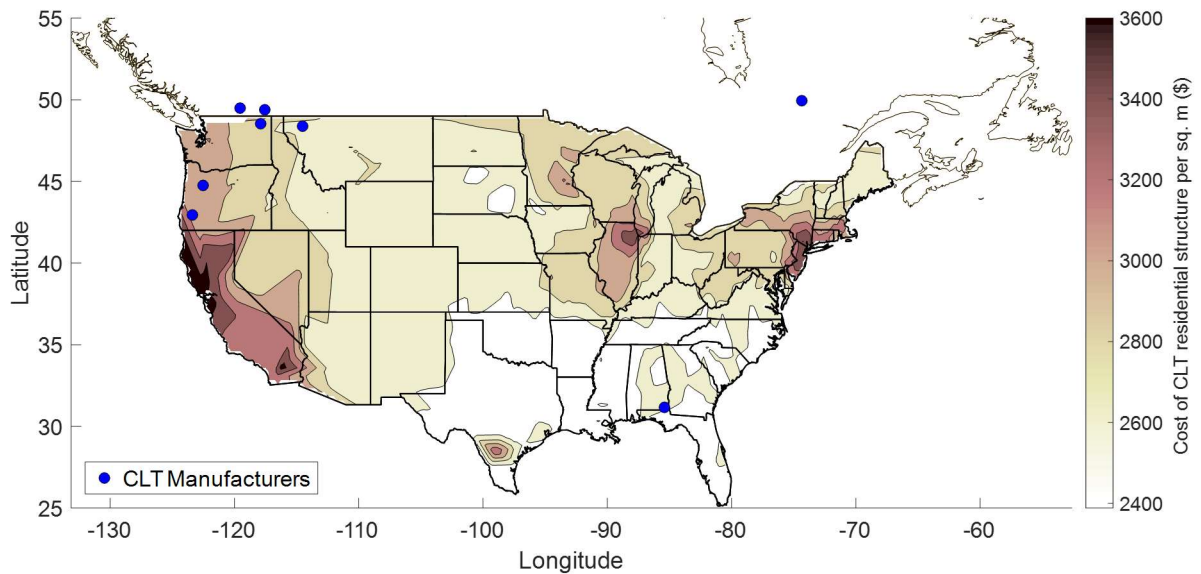


Figure 6.4: Estimated cost of CLT residential structure per square meter

6.4 PERFORMANCE OF RESIDENTIAL WOOD STRUCTURES

With the hazard defined for each of the points in the grid of the contiguous United States, it was used to define the risk associated with wood residential structures located across the United States. To quantify the risk due to tornadoes, the performance of wood residential structures had to be established. Studies by Amini and van de Lindt (2013) used a fragility approach to define the performance of a set of archetype residential structures using light-frame wood construction. Additional work was done to quantify the performance of the same archetypes constructed using 3-ply CLT (Stoner and Pang, 2020). Typically, lognormal distribution functions are used to describe fragility functions related to the structural performance various building types shown in Equation 6.2. In this equation, the probability of failure, $P_f(V)$, is a function of the wind speed, V , and the

standard normal cumulative distribution function, Φ , and lognormal distribution location and scale parameters, μ and σ .

$$P_f(V) = \Phi \left[\frac{\ln(V) - \mu}{\sigma} \right] \quad (6.2)$$

The performance of structures in tornado events is categorized into damage states called degrees of damage (DOD). The DOD used to describe the damage from a tornado varies based on the type of construction and material. For typical one- and two-family residences, the degrees of damage are described in Table 6.4 (McDonald and Mehta 2006), of which, DOD4 through DOD9 deal with and describe failures that deal with structural failures.

Table 6.4: Degree of damage descriptions for one- and two-family residences

DOD	Damage Description
1	Threshold of visible damage
2	Loss of roof covering material (<20%), gutters and/or awning; loss of vinyl or metal siding
3	Broken glass in doors and windows
4	Uplift of roof deck and loss of significant roof covering material (>20%); collapse of chimney; garage doors collapse inward; failure of porch or carport
5	Entire house shifts off foundation
6	Large sections of roof structure removed; most walls remain
7	Exterior walls collapsed
8	Most walls collapsed, except small interior rooms
9	All walls collapsed
10	Destruction of engineered and/or well-constructed residence; slab swept clean

For comparison between light-frame construction and CLT for the residential archetypes, the onset of DOD4 was used to determine the difference in performance. The

onset of DOD1 through DOD3 would remain the same given similar roof covering, windows, and doors. Lognormal distributions were used to describe the system response at which roof sheathing loss is equal to or greater than 25% and limit states such as system level failures to lateral support and anchorage occur are shown for light-frame residential construction (Amini and van de Lindt, 2013) and CLT construction (Stoner and Pang, 2020) and are represented in Figure 6.5. Conclusions by the study on light-frame residential construction suggest that, for the archetypes considered, 8d nails with 150mm/150mm (6in/6in) spacing, hurricane clip connections between roof trusses and wall elements would produce a structure with an approximately 50% probability of failure for an EF1 level event (29.2-38.3 m/s; 85-110 mph). This level of design corresponds to relatively typical nail spacing, connection types, and adequate anchorage for shear and uplift that satisfy the design standards for residential construction. The decreased performance of the examined archetypes is due to increased structural demand from the tornado induced wind forces such as the pressure drop that occurs during such events.

The total structure fragilities describing CLT residential construction used 3-ply CLT panels and screwed connections to supporting elements spaced at 230 mm (9 in). It also utilized shear and overturning restraint spaced at 910 cm (36 in). The studied archetypes had approximately 50% probability of failure when subjected to EF4 level events (75-89.2 m/s; 168-199 mph). The lognormal fragility parameters used in this study represent the average of five residential archetypes used in the studies of light-frame and CLT residential construction and are shown in Table 6.5.

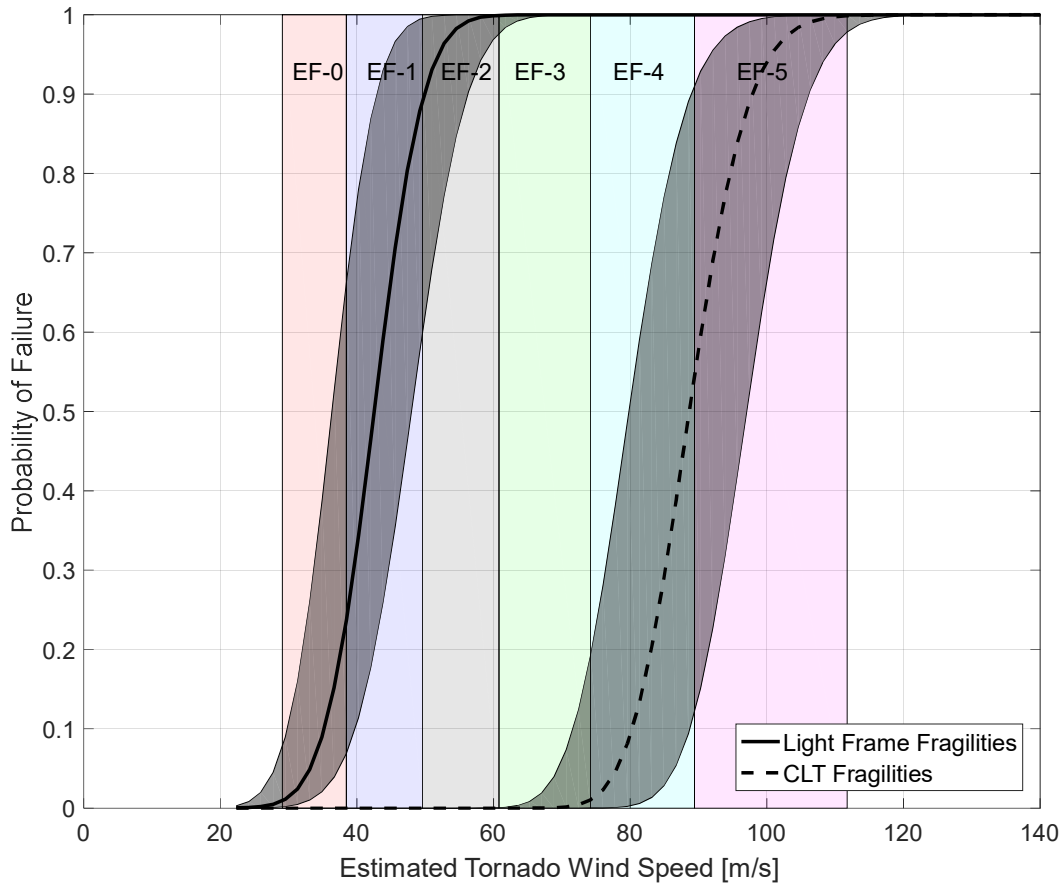


Figure 6.5: Fragility analysis of light-frame and CLT residential structures showing probability of total structure failure

Table 6.5: Lognormal distribution parameters for light-frame and CLT construction

Lognormal Distribution Parameters - Total Failure		
Construction Type	λ	ξ
LF	4.546	0.1333
CLT	5.280	0.0771

In addition to the system level fragilities used in this study, detailed information about the roof sheathing or panel failure was derived from the previously mentioned

studies. In the case of the performance of CLT residential structures, the relationship between estimated tornado wind speed and roof area failure represented by the cumulative distribution function, $F_{roof,CLT}$, was directly calculated. The lognormal distribution parameters representing $F_{roof,CLT}$ are shown in Table 6.6.

Table 6.6: Lognormal distribution parameters relating wind speed and area of roof failure

Lognormal Distribution Parameters - Total Failure		
Construction Type	λ	ξ
CLT	5.427	0.0789

For the study of light-frame residential structures, was reported as four separate fragilities describing each of four damage states. These damage states 1-4 represent 0 sheathing failures, less than or equal 1 sheathing failure (2% by area), less than or equal to 10% failure by area, and less than or equal to 25% failure by area respectively. Using the lognormal distribution parameters describing all five archetypes (Amini, 2012) and Monte Carlo simulation, the relationship between wind speed and roof area failure could be developed. This relationship is shown for all archetypes in Figure 6.6. The relationship between wind speed and roof area failure was used to develop estimates of the comparative losses associated with such failures.

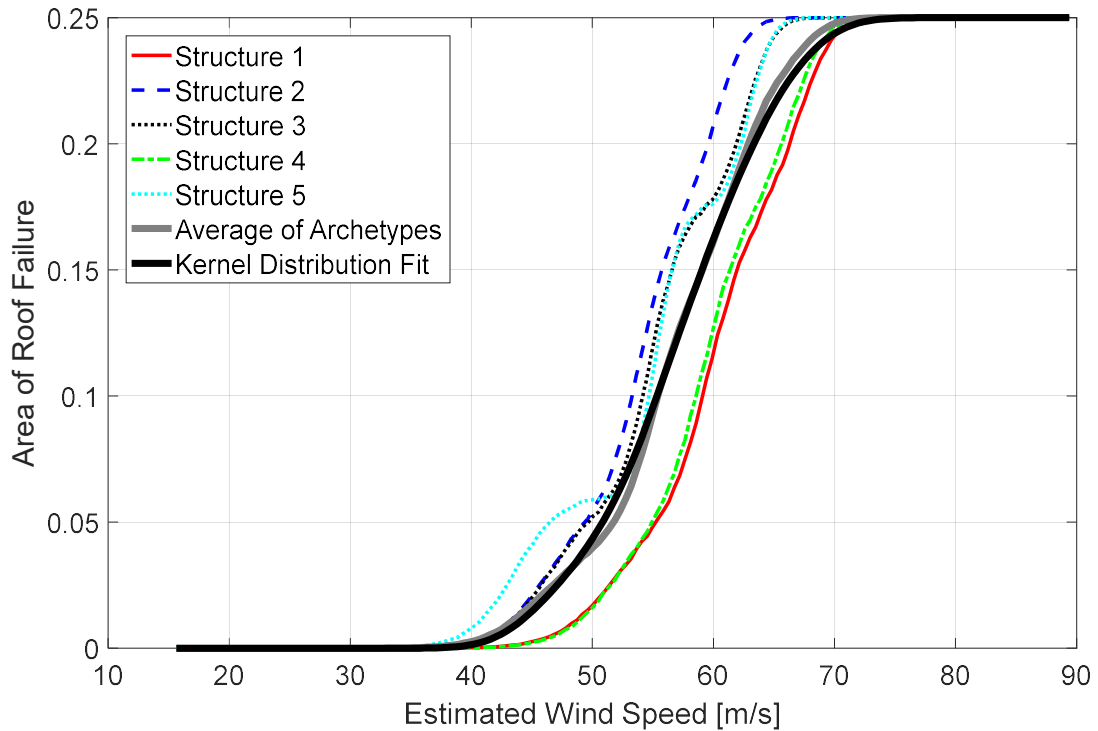


Figure 6.6: Relationship between wind speed and roof area failure for light-frame construction

In order to use the relationship between estimated tornado wind speed and roof area failure, the distribution was described using a kernel distribution function with bandwidth equal to 6.891. The fitted distribution is also shown in Figure 6.6 and referred to as $F_{roof,LF}$.

6.4.1 Annual Probability of Failure

With the performance of wood residential structures for a given wind speed quantified and the hazard associated with gridded points across the United States, the annual expected probability of failure could be computed by convolving the hazard curve and fragility curve. This operation is shown in Equation 6.3, where the annual probability of failure P_{fl} , is the integration over the hazard domain of the product of the function

describing the hazard, $H(V)$, and the probability density function (pdf) describing the lognormally distributed fragility curve, $f(V)$. To determine the probability of failure over a period of n years, Equation 6.4 is utilized. In addition, this equation assumes that the tornado hazard and failure probability are identically distributed and independent from year to year.

$$P_{f1}(WS) = \int_0^{\infty} H(WS) \times f(WS) dWS \quad (6.3)$$

$$P_{f,n} = 1 - (1 - AP_f)^n \quad (6.4)$$

6.4.2 Reliability Index

The risk associated with residential structures due to tornado hazards was further quantified in terms of the reliability index, β . Values for the reliability index give an indication of the likelihood of failure where larger number correspond to a lower probability of failure. In this case, the reliability index is calculated through Equation 6.5 where the probability of failure in n years, $P_{f,n}$, is used with the standard normal distribution function, Φ .

$$\beta_n = -\Phi[P_{f,n}] \quad (6.5)$$

For structural applications guidance is given about the target reliability index in 50-years. Eurocode recommends reliability indices based on three distinct consequence classes that differentiate between structures with high consequences of failure and those with low consequences of failure. For these consequence classes the reliability index ranges from 4.8 to 3.3 for high to low consequences, respectively (EN-1990, 2002). Similarly, ASCE 7-16 gives indication of the values of reliability index as shown in Table

6.7 (ASCE, 2016) based on the risk category and the consequence of failure where values ranged from 2.5-4.5.

Table 6.7: Target reliability for load conditions that do not include earthquake, tsunami, or extraordinary events (ASCE, 2016)

Basis	Risk Category			
	I	II	III	IV
Failure that is not sudden and does not lead to widespread progression of damage	$P_F = 1.25 \times 10^{-4}/\text{yr}$ $\beta=2.5$	$P_F = 3.0 \times 10^{-5}/\text{yr}$ $\beta=3.0$	$P_F = 1.25 \times 10^{-5}/\text{yr}$ $\beta=3.25$	$P_F = 5.0 \times 10^{-6}/\text{yr}$ $\beta=3.5$
Failure that is either sudden or leads to widespread progression of damage	$P_F = 3.0 \times 10^{-5}/\text{yr}$ $\beta=3.0$	$P_F = 5.0 \times 10^{-6}/\text{yr}$ $\beta=3.5$	$P_F = 2.0 \times 10^{-6}/\text{yr}$ $\beta=3.75$	$P_F = 7.0 \times 10^{-7}/\text{yr}$ $\beta=4.0$
Failure that is sudden and results in widespread progression of damage	$P_F = 5.0 \times 10^{-6}/\text{yr}$ $\beta=3.5$	$P_F = 7.0 \times 10^{-7}/\text{yr}$ $\beta=4.0$	$P_F = 2.5 \times 10^{-7}/\text{yr}$ $\beta=4.25$	$P_F = 1.0 \times 10^{-7}/\text{yr}$ $\beta=4.5$

Other studies aimed directly at the reliability analysis of residential construction in the United States (Rosowsky, 2001) suggested that the reliability of roof sheathing attachment ranged from 1.8 to 3.5. Analysis of the target reliability of residential structures located in the Netherlands indicated that an annual probability of failure of 1×10^{-6} , or $\beta_{50} = 3.89$, was deemed acceptable (JCSS, 2001). In this study, the reliability index of residential structures constructed using both light-frame and CLT will be compared directly with a $\beta_{50} = 3.50$, consistent with ASCE recommendations for failure that is either sudden or leads to widespread progression of damage in Risk Category II which is defined as all structures that are not essential facilities, structures whose failure poses a substantial risk to human life, or structures that represent a low risk for human life given failure.

6.4.3 Comparative Estimated Loss

To calculate the estimated financial loss due to a tornado event, the annual probability of failure was multiplied by the consequence of failure, in this case a portion

of the cost of the residential structure. The calculation of loss in residential structures has been categorized into several causes of economic loss. Loss estimation methodologies for hurricanes separate economic into roof cover loss, roof sheathing or panel loss, loss due to failure of windows and doors from windborne debris, loss due to water infiltration, and total loss due to structural failure including loss of use. In this case, the loss due to roof sheathing or panel failure and the total loss due to structural failure were calculated as loss to roof cover, failure of windows and doors, and water infiltration would remain the same or be similar for light-frame and CLT construction.

The predicted performance of light-frame residential construction and CLT residential construction was taken directly from the component fragilities of the studies on light-frame and CLT respectively. These component fragilities related the estimated tornado wind speed with the percentage of roof sheathing or panel failure. The calculation of loss due to total structure failure was the annual probability of total structure failure multiplied by the total cost of the structure. The annual loss due to total structural failure, C_{bld} can be represented in Equation 6.6 using the probability density function of total building failure, f_{bld} and the hazard curve, H . In this case the probability density function takes the place of the loss function as the loss associated with building failure can be compared directly with the probability of failure multiplied by the total cost of the structure. These functions are convolved over the hazard domain and multiplied by the total cost of the structure including contents, C_{tot} , to give the average annual loss due only to total structural failure.

$$C_{bl} = C_{tot} \int_0^{\infty} H(V) \times f_{bld}(V) dV \quad (6.6)$$

The calculation of loss due to roof sheathing or panel failure was taken from the methodology used in HAZUS-MH (Vickery et al. 2006), a multi-hazard analysis tool that estimates loss due to hurricanes. In this methodology the loss due to roof sheathing loss is estimated by Equation 6.7 where the ratio of interior finish and content loss, L_C , is a function of the cumulative distribution function of the ratio of roof sheathing loss by area, F_{roof} , describing either CLT or light-frame construction. The contents within the structure were assumed to be half the total initial construction cost of the structure. The result was a loss function that assumes total loss of interior finishes and content at 25% roof sheathing loss by area and a linear relationship below this threshold.

$$L_C = 4F_{roof}, \quad F_{roof} < 0.25 \quad L_C = 1.0, \quad F_{roof} \geq 0.25 \quad (6.7)$$

Using the associated distributions for light-frame, $F_{roof,LF}$, and CLT, $F_{roof,CLT}$, functions could be developed for the cumulative distribution function of loss, L_C , and probability density function, l_C , were developed. The loss due to roof sheathing or panel failure is computed in Equation 6.8, C_{roof} . In this equation, the loss function is calculated by taking the probability density function of the loss function, l_C , convolving convolved over the hazard domain, H , and multiplying by the cost of interior finishes and contents, $C_{i,c}$, given by Equation 6.8.

$$C_{roof} = C_{i,c} \int_0^{\infty} H(V) \times l_C dV \quad (6.8)$$

Calculating the sum of these two estimates, C_{bld} and C_{roof} , allows for comparison of the difference in average annual loss due to tornadoes for light-frame and CLT residential structures. This value will be referred to as the comparative estimated loss as it only

includes the losses that would be useful for comparison and neglects the losses that would be the same for both light-frame and CLT structures.

6.5 RISK ASSESSMENT OF CONTIGUOUS UNITED STATES

Considering the geographic variation tornado hazard underscores locations where the increased performance of CLT residential structures has a more significant impact. The primary points for comparison of risk between CLT and light-frame residential construction were the reliability index and net present cost (initial construction cost + comparative estimated loss adjusted for inflation). The reliability indices are plotted for the contiguous United States in Figure 6.7 with a solid line indicating the reliability index equal to 3.5.

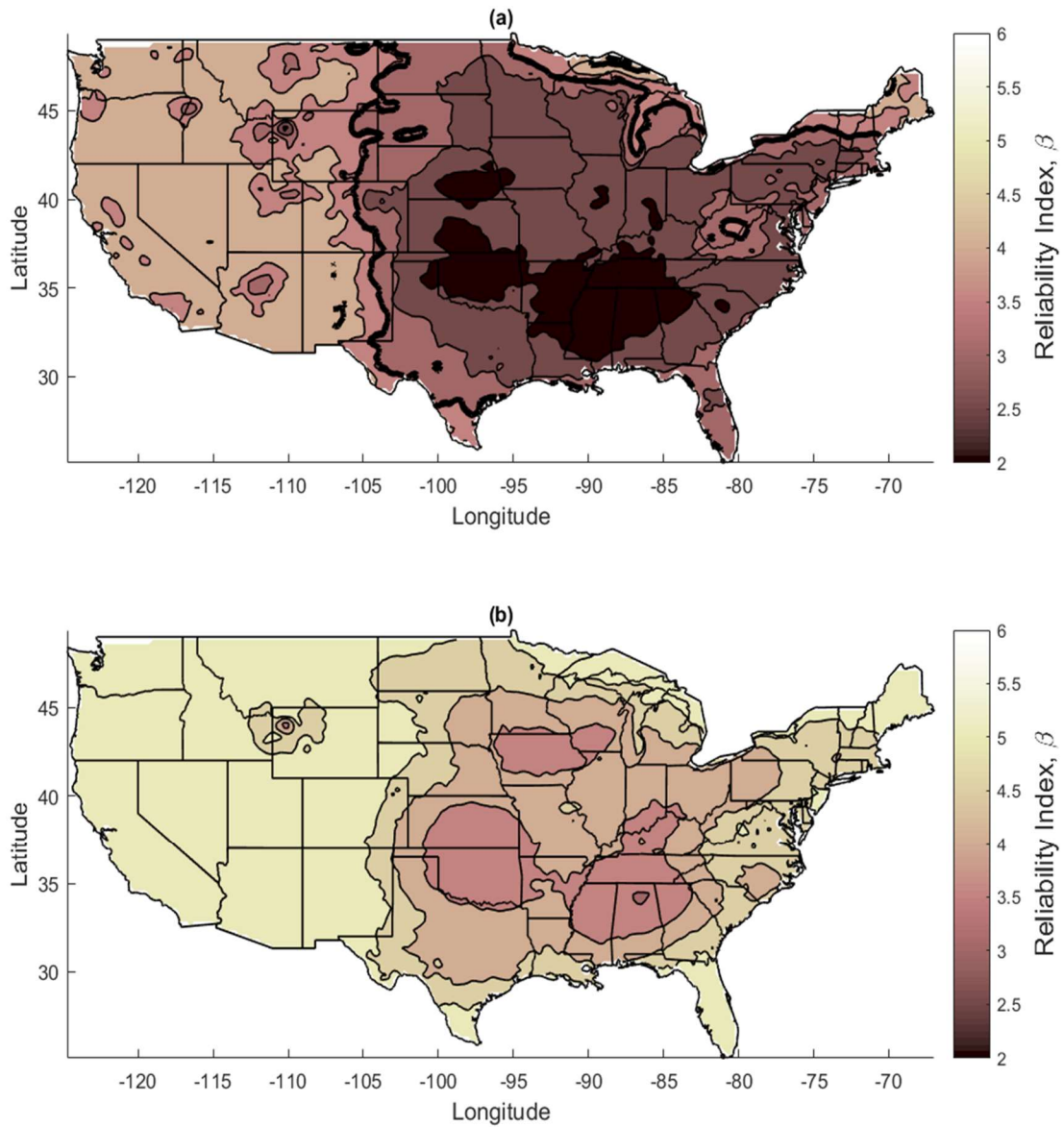


Figure 6.7: Reliability index for light-frame (a) and CLT (b) residential construction subject to tornado hazards

Examining the distribution and values of the reliability index underscores the improvement in performance from light-frame to CLT. Figure 6.8 shows the probability density function of reliability index for all locations fit to a generalized extreme value

distribution. More than 40% of the United States by area has a reliability index less than 3.0, with more than 71% having an index less than 4.0 for residential structures constructed using light-frame construction. Conversely, only 4.6% of residential structures in the United States would have a reliability index less than 4.0 if constructed using CLT. These results are summarized in Table 6.8.

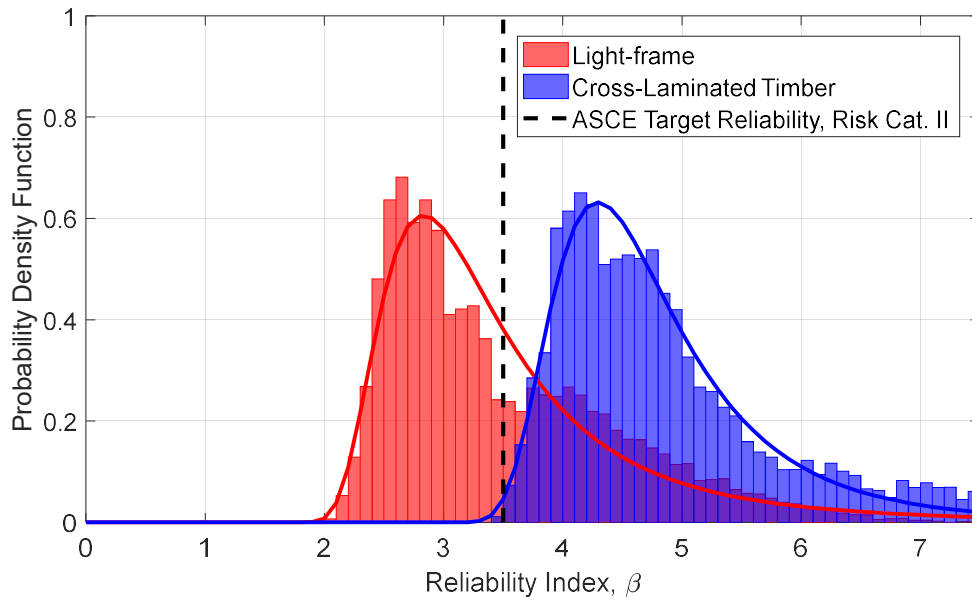


Figure 6.8: Probability density function of reliability index for light-frame and CLT residential structures

Table 6.8: Percentage of US by area with reliability index less than given value

Construction Type	Reliability Index		
	$\beta < 3.0$	$\beta < 3.5$	$\beta < 4.0$
LF	40.6%	59.2%	71.4%
CLT	0.0%	0.1%	11.6%

The cost comparison performed in this study only accounted for the changes in performance due to tornado hazard and neglect the differences in expected performance

due to non-tornadic wind hazards (e.g., downburst, hurricane and other non-tornado windstorms). Comparing the loss over time while considering a nominal 3% inflation produces a relationship between time and the comparative estimated losses from both light-frame and CLT residential structures across the United States and can be represented by Equation 6.9 where the cost after n years, C_n , is a function of the interest rate, I , and the annual average cost due to the comparative losses, C_l .

$$C_n = (1 + I)^{n-1} \times C_l \quad (6.9)$$

This comparison for each location in the United States shows that a point exists where the anticipated cost of light-frame surpasses that of CLT due to tornado induced damages and initial construction costs. This amount of time is dependent on the tornado hazard associated with each point, the size of the target in question, and the variation in up-front cost due to geographic variation in construction and material costs and assumes a uniform level of design for all locations.

Locations in the central and southeastern portion of the United States where tornado hazard were the greatest experienced the highest difference in comparative loss. For smaller target sizes more realistic for residential structures the difference in comparative loss peaked at between \$40,000 and \$45,000 over a time period of 50 years. This loss alone would not be significant enough to provide a financial benefit of building out of CLT, as the initial construction cost differential averaged approximately \$80,000. Considering a longer study period and accounting for other hazards such as the straight-line winds present in Figure 6.2 would decrease the difference in expected cost between light-frame and CLT construction. Figure 6.9 shows the amount of time before the estimated cost due

to initial construction costs and tornado loss is equal for light-frame and CLT residential construction. This value was computed by solving Equation 6.10 for the number of years, n , that the net present cost (initial construction cost plus, C_c , estimated comparative losses due to tornadoes, C_{bld} and C_{roof}) is equal for CLT and light-frame residential construction. For locations in the southeastern portion of the United States subject to a higher level of tornado hazard, the time before the expected cost due to initial construction cost and tornado losses varies between 90 and 100 years.

$$C_{c,CLT} + (1 + I)^{n-1} \times (C_{bld,CLT} + C_{roof,CLT}) = C_{c,LF} + (1 + I)^{n-1} \times (C_{roof,LF} + C_{fail,LF}) \quad (6.10)$$

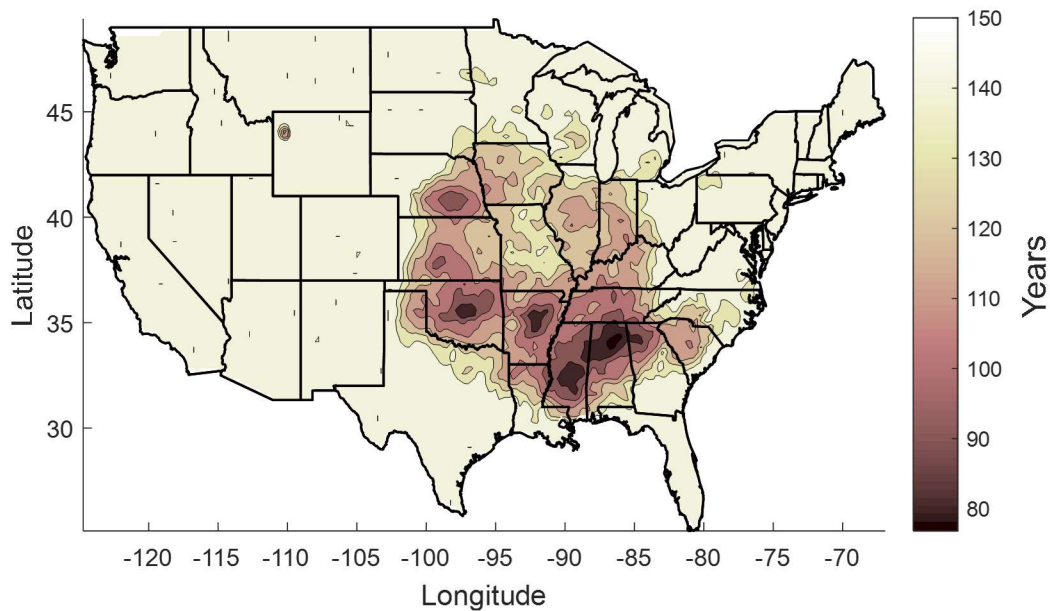


Figure 6.9: Time before net present cost is equal for light-frame and CLT construction

6.6 CASE STUDIES

Three case study locations were taken as an example of the tornado hazard analysis as it relates to the performance of residential construction. Each case study was meant to

represent a different class of hazard. Denver, CO represents low tornado hazards, Greenville, SC represents a moderate level of tornado hazard, and Huntsville, AL represent a level of high tornado hazard. The hazard curves for each of the case study locations are shown in Figure 6.10. This hazard is further quantified in Table 6.9 with coefficients describing Equation 6.1.

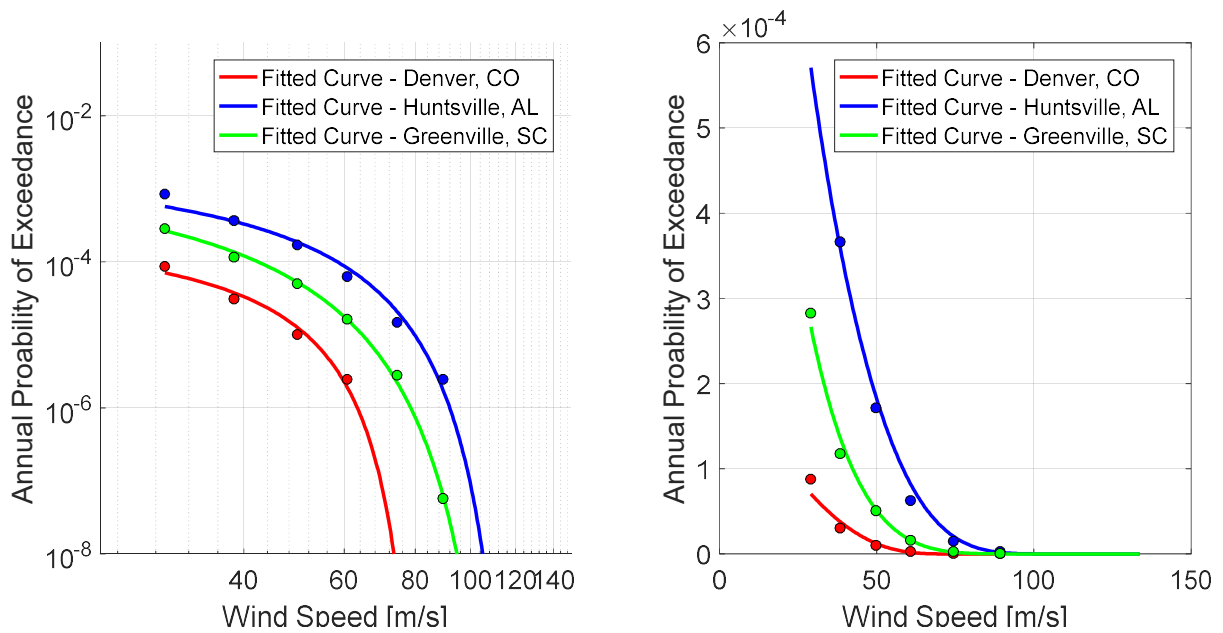


Figure 6.10: Tornado hazard for case study locations

Table 6.9: Tornado hazard equation coefficients for case study locations

Target Size	Huntsville, AL			Greenville, SC			Denver, CO		
	APE ₀	α	V _{max} [m/s]	APE ₀	α	V _{max} [m/s]	APE ₀	α	V _{max} [m/s]
Point	0.0046	3.18	134.1	0.00047	2.12	134.1	0.00047	2.12	89.4
Small	0.0073	3.18	134.1	0.00195	2.46	130.0	0.00195	2.46	91.2
Medium	0.0106	3.16	134.1	0.00384	2.56	129.4	0.00384	2.56	91.7
Large	0.0318	3.16	134.1	0.02400	2.90	128.9	0.02400	2.90	93.3

The hazard associated with a point estimate target size was used to perform all further calculations in this example. Convolution of the hazard curve shown in Figure 6.10

with the probability density function of the failure probability following Equation 6.3 is shown graphically in Figure 6.11. The hazard curve is plotted on the A residential structure constructed using CLT would have a significantly lower annual probability of failure than the same structure constructed using traditional light-frame construction. For each of the case study locations, the annual, 50-year, and 100-year probabilities of failure are summarized in Table 6.10. The values of reliability index shown describe the level of risk for current residential light-frame construction as higher than the values suggested by ASCE 7-16 for risk category II ($\beta=3.5$) in light-frame structures but shows adequate performance for CLT structures.

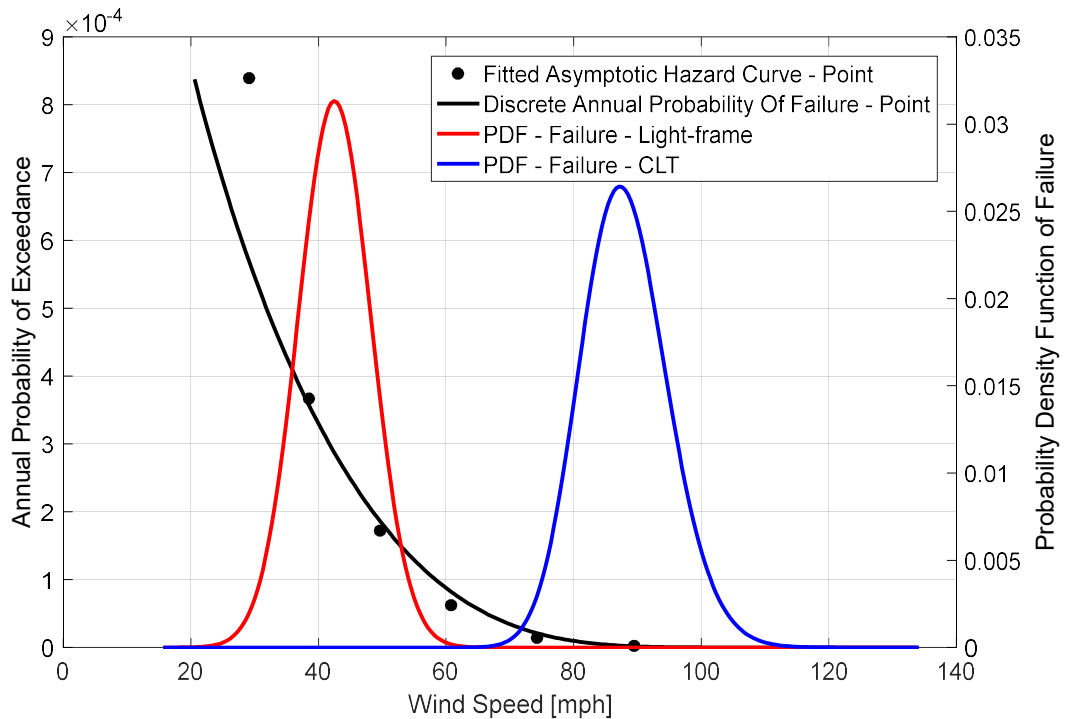


Figure 6.11: Hazard of tornado hazard and pdf of failure for CLT and light-frame for Huntsville, AL

Table 6.10: Summary of 1-year, 50-year, and 100-year P_F and β for Huntsville, AL

Construction Type	1-year		50-year		100-year	
	P_F	β	P_F	β	P_F	β
LF	2.97E-04	3.43	1.48E-02	2.18	2.93E-02	1.89
CLT	4.24E-06	4.45	2.12E-04	3.52	4.24E-04	3.34
LF	1.07E-04	3.70	5.33E-03	2.55	1.06E-02	2.30
CLT	3.05E-07	4.99	1.52E-05	4.17	3.05E-05	4.01
LF	2.88E-05	4.02	1.44E-03	2.98	2.88E-03	2.76
CLT	6.36E-10	6.07	3.18E-08	5.41	6.36E-08	5.28

An analysis of the comparative losses associated with tornado events, namely loss to roof sheathing/panel failure and total structural failure, was performed for each of the three locations. The summary of the results of this analysis are shown in Table 6.11 for a 50-year study period. The 50-year net present cost accounts for the differences in performance between light-frame and CLT construction due to tornado events and the initial cost of construction. For Huntsville, AL where the relative tornado hazard was much higher, the net present cost over a 50-year period was much closer for CLT and light-frame than it was for areas of lower tornado hazard like Denver, CO. In addition, the loss due to roof sheathing/panel failure and content loss was greater than the loss due to total failure due to the decreased likelihood of severe tornado events.

Table 6.11: Analysis of loss for comparison of light frame and CLT construction

Location	Construction Type	Initial Construction Cost	50-year Average: Roof Sheathing & Contents	50-year Average: Total Failure	Net Present Cost 50 year
Huntsville, AL	LF	\$373,588	\$4,465	\$12,528	\$390,582
	CLT	\$452,908	\$50.35	\$216.59	\$453,175
Greenville, SC	LF	\$371,072	\$1,149	\$4,476	\$376,697
	CLT	\$449,858	\$1.95	\$15.45	\$449,876
Denver, CO	LF	\$390,726	\$255	\$1,271	\$392,253
	CLT	\$473,686	\$0	\$0	\$473,686

The net present cost due to tornado events over time for light-frame and CLT residential construction is shown in Figure 6.12, where the point at which CLT construction becomes an economically competitive with light-frame construction is evident. For locations of high hazard like Huntsville, AL, this occurs after around 100 years. For locations of moderate hazard, this occurs after nearly 130 years. For low levels of hazard, it takes longer than 170 years for the comparative losses due to tornadoes to account for the difference in initial construction costs. Additional loss is expected for items such as roof cover and wall cover, but they were not analyzed in this study as they were assumed to be the same for light-frame and CLT residential construction. The hazards associated with straight-line wind shown in Figure 6.2 make it such that the structural advantages of CLT construction could reduce the amount of time before CLT and light-frame construction have comparable expected costs.

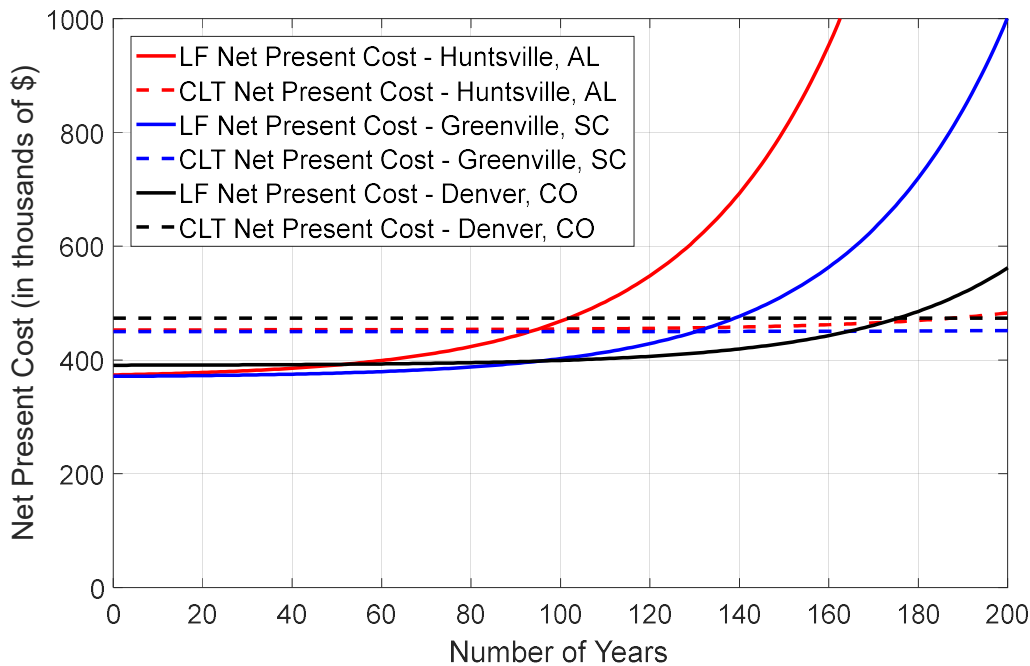


Figure 6.12: Estimated cost due to initial construction and estimated tornado loss for case study locations

6.7 CONCLUSIONS

The structural properties of Cross-Laminated Timber make it a building material that has the potential to resist loads associated with hazards such as tornadoes. To understand the feasibility of such a structural system as compared to more traditional light-frame construction, the structural reliability of residential structures subject to tornado hazards and estimated financial cost of such hazards was calculated for the contiguous United States. Considering only tornado hazards, the annual probability of failure was higher, and the reliability index was lower than the limits suggested by ASCE 7-16 for much of the portion of the United States with moderate level of tornado hazard. Using Cross-Laminated Timber construction significantly reduced the probability of failure and

increased the reliability index to levels that were considered acceptable by the same standards. The estimated loss due to tornado hazards projected that CLT construction would become cost competitive with light-frame construction after a period of nearly 100 years for the most severe tornado hazard locations. These estimates only account for the losses due to roof sheathing/panel failure and total structural failure as other losses in tornadoes like roof cover loss would likely remain constant for the two types of construction.

The calculations of loss in this study were only due to tornado hazards. Loss due to straight-line winds such as hurricanes would further reduce the amount of time before CLT became competitive. Additional indirect costs such as loss of life or injury were not accounted for in this study. It is also noted that other measures could be taken to improve the performance of light-frame construction including tighter nail spacing on roof sheathing elements and more connections between structural elements. Such methods could be more cost effective and ultimately bring the performance of light-frame construction to acceptable levels. Cross-Laminated Timber construction, as it becomes more economically competitive in terms of initial construction cost, could serve as a competitive alternative to light-frame construction, especially in locations where the hazard due to high winds is greatest.

6.8 REFERENCES

Kroll Brand Rating Agency. (2019, March 28). KBRA Releases Insurance Research: Insured Losses Rising for Tornadoes. Retrieved May 19, 2019. Retrieved from

<https://www.marketwatch.com/press-release/kbra-releases-insurance-research-insured-losses-rising-for-tornadoes-2019-03-28>.

ASCE. (2016). "Minimum design loads for buildings and other structures." Structural Engineering Institute, Reston, VA.

Fan, F., & Pang, W. (2019). Stochastic Track Model for Tornado Risk Assessment in the U.S. *Frontiers in Built Environment*, 5. doi: 10.3389/fbuil.2019.00037

Strader, S. M., Pingel, T. J., & Ashley, W. S. (2016). A Monte Carlo model for estimating tornado impacts. *Meteorological Applications*, 23(2), 269–281. doi: 10.1002/met.1552

Ellingwood, B. R., & Rosowsky, D. V. (2004). Fragility Assessment of Structural Systems in Light-Frame Residential Construction Subjected to Natural Hazards. *Structures 2004*. doi: 10.1061/40700(2004)119

Ashley, W. S. (2007). Spatial and Temporal Analysis of Tornado Fatalities in the United States: 1880–2005. *Weather and Forecasting*, 22(6), 1214–1228. doi: 10.1175/2007waf2007004.1

Amini, M., and van de Lindt, J. (2013). "Quantitative insight into rational tornado design wind speeds for residential wood-frame structures using fragility approach." *J. Struct. Eng.*, 10.1061/(ASCE)ST.1943-541X.0000914, 04014033.

Masoomi, H., & Lindt, J. W. V. D. (2018). Fatality and Injury Prediction Model for Tornadoes. *Natural Hazards Review*, 19(3), 04018009. doi: 10.1061/(asce)nh.1527-6996.0000295

- Standohar-Alfano, C. D., Freyne, S., Graettinger, A. J., Floyd, R. W., & Dao, T. N. (2015). Performance of Residential Shelters during the May 20, 2013, Tornado in Moore, Oklahoma. *Journal of Performance of Constructed Facilities*, 29(5), 04014143. doi: 10.1061/(asce)cf.1943-5509.0000636
- Roueche, D. B., Lombardo, F. T., & Prevatt, D. O. (2017). Empirical Approach to Evaluating the Tornado Fragility of Residential Structures. *Journal of Structural Engineering*, 143(9), 04017123. doi: 10.1061/(asce)st.1943-541x.0001854
- Twisdale, B. L. A., & Dunn, W. L. (1983). Probabilistic analysis of tornado wind risks, 109(2), 468–488.
- Bradley, B. A., Dhakal, R. P., Cubrinovski, M., Mander, J. B., & Macrae, G. A. (2007). Improved seismic hazard model with application to probabilistic seismic demand analysis. *Earthquake Engineering & Structural Dynamics*, 36(14), 2211–2225. doi: 10.1002/eqe.727
- Burback, B., & Pei, S. (2017). Cross-Laminated Timber for Single-Family Residential Construction: Comparative Cost Study. *Journal of Architectural Engineering*, 23(3), 06017002. doi: 10.1061/(asce)ae.1943-5568.0000267
- Plotner, S. C. (2019). Building construction costs with RSMeans data 2019. Rockland, MA: Gordian RSMeans Data.
- Truck Freight Rates. (2017). Retrieved from <https://truckerpath.com/blog/truck-freight-rates/>

- McDonald, James and Kishor C. Mehta (October 10, 2006). *A recommendation for an Enhanced Fujita scale (EF-Scale)*. Lubbock, Texas: Wind Science and Engineering Research Center, Texas Tech University. Retrieved January 2, 2018.
- EN 1990. (2002). Eurocode–Basis of structural design, CEN 2002. European Committee for Standardization (CEN) <http://www.cen.eu>.
- Rosowsky, D. V. (2001). Studies on probability-based design for residential construction. Corvallis, OR: Oregon State University.
- JCSS: Probabilistic model code. The Joint Committee on Structural Safety, 2001. <http://www.jcss.ethz.ch/>
- Vickery, P. J., Lin, J., Skerlj, P. F., Twisdale, L. A., & Huang, K. (2006). HAZUS-MH Hurricane Model Methodology. I: Hurricane Hazard, Terrain, and Wind Load Modeling. *Natural Hazards Review*, 7(2), 82–93. doi: 10.1061/(asce)152

CHAPTER SEVEN

SUMMARY, CONCLUSIONS, AND RECOMMENDATIONS

7.1 SUMMARY OF STUDY

Cross-Laminated Timber is an engineered wood product that, due to its dimensional stability, rigidity, and strength, show the capabilities to serve as structural material in residential structures that can reduce the risk associated with events such as tornadoes. In order to investigate the potential for CLT to serves such a role, a series of debris impact tests and experimental connection and shear wall tests were performed to quantitatively determine the response to the hazards most associated with tornado events. With this information, structural models were developed that predicted the response of residential archetypes designed using CLT to tornado events and attempted to quantify the variability associated with both the hazard and the material properties of the structures. These results were compared to similar models developed for light-frame construction with the goal of determining the increase in performance from light-frame to CLT residential structures. Finally, this information was coupled with information about the occurrence of tornado events in the United States. The analysis took the form of both quantitative risk through the reliability index and annual probability of failure due to tornado events as well as the estimated losses due to such events. These techniques determined the feasibility of using CLT as a residential structural material from both a cost perspective and a risk perspective.

7.2 CONCLUSIONS

7.2.1 Debris Impact Testing

A material's response to windborne debris plays a significant role in the performance of a structure in the event of a tornado. Experimental debris impact testing quantified the performance of 3-ply CLT to debris impacts based on impact location, CLT axis orientation, and connection orientation. The primary failure mechanisms were missile perforation and excessive panel deflection. The most vulnerable location on the CLT panels were the corner due to the lack of deformation capacity. Consequently, missile perforation occurred most frequently with impact located in the corner of panels. In addition, strong axis orientation panels were more likely to fail than the weak axis orientation panels. Finally, the weak connection orientation proved to be more vulnerable to debris impact failure than the strong connection orientation.

Use a lognormal fragility approach to summarize all experimental testing, a 3-ply CLT panel would experience failure nearly 54% of the time when subjected to the debris associated with an EF-5 level event as defined by relevant standards for tornado safe-room design. This probability drops to approximately 26% for debris associated with an EF-2 level event. Furthermore, a 3-ply CLT panel did not pass the experimental testing associated with tornado safe-rooms and storm shelters. Using a thicker panel (4-ply or 5-ply) would like result in an assembly that produces results consistent with those required for safe-room use.

7.2.2 Experimental Shear Wall Testing

In addition to the debris generated by tornado event, there are significant uplift and lateral forces that develop due to the wind-induced pressures. To investigate the performance of CLT lateral assemblies where out-of-plane wall are also present, experimental testing on such assemblies was performed. These types of configurations are often present in residential structures where there are more intersecting walls and the building dimensions create a more box-like behavior when subjected to lateral loading. In order to establish the behavior of connections used in the wall assembly testing, connection tests were performed on the screws and bracket-type connections. Additional information was estimated based on analytical and design code equations to develop numerical models of the wall assemblies.

Two wall assemblies were destructively tested, one with out-of-plane walls and one with in-plane walls only. The primary purpose of these tests was to determine the ability of out-of-plane loads to resist the uplift forces that develop. In addition, a simplified analytical approach to estimating the strength of the wall assembly was developed based on the design strength of the connecting elements. In addition to the destructive tests, stiffness tests were performed on the wall assemblies with and without the in-plane walls.

Results of the destructive tests indicate that the out-of-plane walls acted sufficiently to hold-down the boundary of the in-plane walls. The strength and stiffness of the wall with out-of-plane walls was higher than the assembly with only in-plane walls without reducing the ductility of the system. In addition, the primary deformation mechanism was present in the panel-to-panel connection.

The connection tests, stiffness tests, and destructive tests all informed a numerical model developed in *Timber3D* which served to predict the performance of the wall assemblies. Comparisons show that the numerical model and experimental testing agrees well with the stiffness, but the model significantly overestimates the strength. Further refinement of the models and the parameters used to estimate connection behavior would be required to better estimate the strength of the wall assembly.

A simplified analytical method was developed where the design strength of the wall is a function of the minimum of the design strengths of each of the following connection capacities: shear at the bottom of the assembly, shear at the top of the assembly, panel-to-panel shear capacity, hold-down capacity, and the shear capacity between the in-plane and out-of-plane walls when present. The walls designed for the purpose of the experimental testing were controlled by the panel-to-panel connection with an ASD capacity of 11.6 kN/m (792 plf). The ratio of ultimate tested capacity to ASD capacity was 5.8 for the wall test with out-of-plane walls suggesting that the analytical strategy does not account for the added strength gained by the out-of-plane walls. The ratio was 3.7 for the test with in-plane only walls suggesting a more appropriate estimation of the capacity of the system.

The results of the shear wall tests suggest that uplift that develops due to lateral loads can be resisted by out-of-plane walls given that there is enough shear capacity in the connection between the in-plane and out-of-plane walls. Furthermore, the capacity of the system can be approximated by the limiting connection capacity. Ultimately the strength and stiffness of the connections governed the behavior of the CLT wall assemblies. Further innovations in connections that provide sufficient strength, stiffness, and ductility for

seismic behavior are the most important factor that will lead towards the implementation of such lateral force resisting assemblies.

7.2.3 Structural Performance of CLT Residential Structures Subject to Tornadoes

In order to determine the total response of a CLT structure subject to a tornado event, a performance model was built. This model relied on relevant analytical methods for tornado induced wind loading, experimental material testing, and Monte Carlo Simulation. For this study, six archetype buildings developed by previous studies were designed using 3-ply CLT according to established design procedures for gravity and wind loads. Connectors matching the connections used in the experimental shear wall testing were used in the model which predicted the capacity of the archetypes in a variety of failure modes including wall and roof panel uplift failure, wall and roof panel connection failure, and system level failures like sliding and uplift/overturning. The demand for each panel and system were simulated based on statistics gathered from previous research about tornado induced loading. Using a Monte Carlo Simulation approach, the capacity and demand for each failure mode was simulated. Assumptions were also made about the amount and intensity of windborne debris and the connection spacing of bracket-type connections and screw connection at panel boundaries.

Results of the fragility analysis showed that the predominant failure mechanism was the roof and wall panels and their connections and the system level sliding failure. In addition, the assumptions about the amount of debris and the load path associated with system level failure of uplift/overturning did not significantly influence the overall performance of the archetypes. Certain archetypes were influenced more by the spacing

of bracket-type connectors while other were more significantly influenced by the screw spacing at panel boundaries. The archetypes studied collectively experienced an approximately 10% probability of failure during EF-4 level events which is an improvement when compared to the same archetypes designed analyzed using light-frame construction.

7.2.4 Hazard Assessment of Wood Residential Structures

In addition to the performance of CLT residential structures given a tornado event, understanding the risk associated with tornado hazards is essential to quantifying the benefit of a stronger but more expensive wood building material. Using a simulated database for the contiguous United States of one million years of tornadoes based on historical observations, hazard curves were developed which related a tornado induced wind speed with an annual probability of exceedance. These hazard curves could be used along with the fragilities developed by this study and previous research for CLT and light-frame residential archetypes respectively, to calculate the annual probability of failure due to tornado events. The annual probability of failure was used along with the reliability index to determine which portions of the United States satisfied target reliability indices from current design standards. Analysis of the reliability of light-frame residential structures shows that nearly 70% of the United States by area exhibit a greater level of risk than that recommended by design standards. Residential construction using CLT drops the portion of the country with risk greater than the target reliability to nearly 0%.

In addition, estimated comparative cost was used to determine the economic feasibility of using CLT as a residential construction material compared to light-frame.

Estimated comparative cost predicts only the loss due to tornadoes which would differ between a CLT and light-frame residential structure. When these costs are combined with the differences in upfront construction costs for CLT and light-frame, it was determined that for areas of high tornado hazard it would take approximately 100 years for CLT construction to be comparable with light-frame construction considering only tornado hazards. Hazards such as straight-line winds associated with hurricanes and indirect costs such as loss of life and injury were not considered and could potentially reduce the amount of time before a CLT residential structure would be economically competitive with light-frame construction.

7.3 LIMITATIONS AND RECOMMENDATIONS OF FUTURE WORK

As previously stated, the 3-ply CLT tested by this study did not pass the debris impact testing requirements for safe-rooms and storm shelters. Additional testing of 4-ply or 5-ply CLT would likely result in a passing test allowing for use in such applications. Furthermore, the number of experimental tests was low, and more tests would give better confidence to the fragilities developed by these studies. Limitations of the experimental test setup include the condition where two edges of the material remained unsupported. Because the relationship between stiffness and performance indicate that the stiffer configurations are more vulnerable than those configurations with more flexibility, this test setup may not represent the most vulnerable test scenario. While the support conditions are realistic for a panel located in the center of a longer wall segment, panels near the corner of a structure may be supported on three of the four sides rather than just on two edges. Additional debris impact testing according to less stringent impact testing standards like

those required for specific counties in Florida would be advantageous as well. Performing these tests on 3-ply CLT would further demonstrate the potential to resist debris associated with lower level events referenced by these standards.

The CLT shear wall testing performed in this study demonstrated the ability for out-of-plane walls to resist the uplift loads. While these tests confirmed this behavior for a single configuration, additional configurations could be tested to investigate the performance when different connection strengths control the capacity of the assembly. Further validation of the simplified analytical method through additional testing would also be recommended. Currently the analytical approach does not account for the increase in performance when out-of-plane wall are compositely utilized as part of the assembly. Considering such an increase in strength and stiffness would be advantageous to the design process of such systems. Additional connection testing would serve to calibrate the numerical *Timber3D* models and better predict the response of different connection configurations.

The performance models developed to quantify the performance of CLT residential construction relied heavily on load path assumptions and connection details used to develop the models. Verification of these assumptions comes only with post-event assessments of structures that are constructed using CLT. In addition, the hazard assessment of light-frame and CLT residential structures was performed using the database of simulated tornadoes. As tornado tracking and historical information is continually updated, the risk associated with these events needs to be re-evaluated. It is recommended that additional construction measures that improve the performance of light-frame

construction be considered. While the change from CLT to light-frame may not yet be economically feasible, smaller adjustments to the construction methods could increase the performance of light-frame construction to an acceptable level. In addition, the growth of the mass timber market could reduce upfront costs and would be worth exploring as the market continues to develop.

APPENDICES

APPENDIX A: Detailed Debris Impact Testing Results

Debris impact testing was performed in accordance with the setup in Chapter 3. Detailed pictures of each of the 16 panels which were tested in the study are shown and describe the panel number, axis orientation, connection orientation, location of impact, mass of missile, speed of missile, and whether the test passed or failed according to ICC 500/FEMA P-361 standards.



Figure A-1: Panel 1, weak-axis, strong-connection, center, 15-pound, 59.4 mph, passed test
(front of panel)



Figure A-2: Panel 1, weak-axis, strong-connection, edge, 15-pound, 59.4 mph, passed test
(front of panel)



Figure A-3: Panel 1, weak-axis, strong-connection, corner, 15-pound, 62.2 mph, passed
test (front of panel)



Figure A-4: Panel 2, weak-axis, strong-connection, center, 15-pound, 89.4 mph, passed test
(front-left, back right)



Figure A-5: Panel 2, weak-axis, strong-connection, edge, 15-pound, 84.1 mph, failed test
– dislodgement (back-left, front-right)



Figure A-6: Panel 2, weak-axis, strong-connection, corner, 15-pound, 80.9 mph, passed test (back of panel)



Figure A-7: Panel 3, weak-axis, strong-connection, center, 15-pound, 87.6 mph, failed – perforation (front-left, back-right)



Figure A-8: Panel 3, weak-axis, strong-connection, edge, 15-pound, 88.1 mph, failed – permanent deflection (back-left, front-right)



Figure A-9: Panel 3, weak-axis, strong-connection, corner, 15-pound, 91.9 mph, failed - perforation (front-left, back-right)



Figure A-10: Panel 4, weak-axis, strong-connection, center, 12-pound, 96.8 mph, failed – permanent deflection (front-left, back-right)



Figure A-11: Panel 4, weak-axis, strong-connection, edge, 12-pound, 100.2 mph, passed (front-left, back-right)



Figure A-12: Panel 4, weak-axis, strong-connection, corner, 12-pound, 102.4 mph, failed – perforation (front-left, back-right)



Figure A-13: Panel 5, weak-axis, strong-connection, center, 15-pound, 87.9 mph, passed (front-left, back-right)



Figure A-14: Panel 5, weak-axis, strong-connection, edge, 15-pound, 88.1 mph, passed (front-left, back-right)



Figure A-15: Panel 5, weak-axis, strong-connection, corner, 15-pound, 88.0 mph, passed (front-left, back-right)



Figure A-16: Panel 6, weak-axis, strong-connection, center, 12-pound, 75.2 mph, passed
(front-left, back-right)



Figure A-17: Panel 6, weak-axis, strong-connection, edge, 12-pound, 77.6 mph, passed
(front-left, back-right)



Figure A-18: Panel 6, weak-axis, strong-connection, corner, 12-pound, 69.7 mph, passed (front of panel)

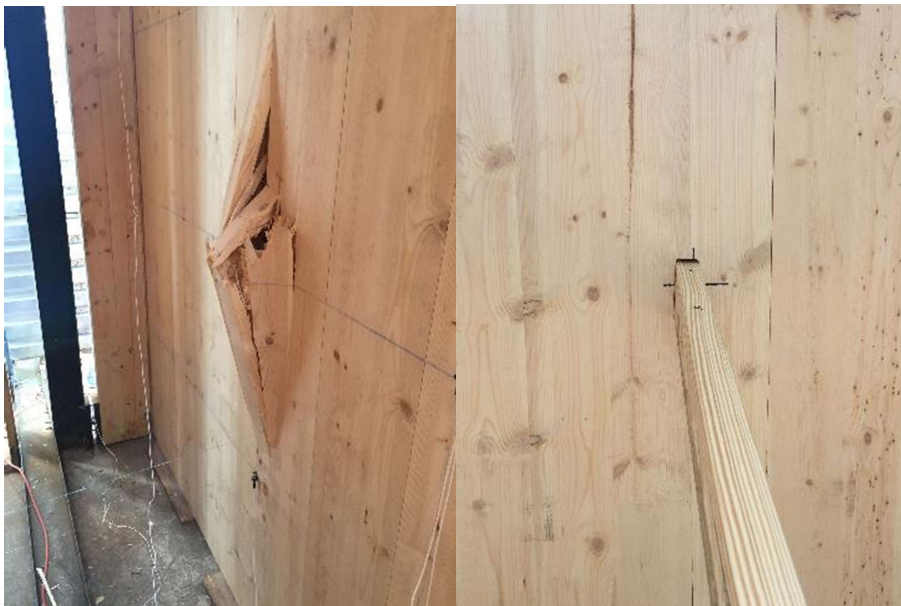


Figure A-19: Panel 7, weak-axis, strong-connection, center, 15-pound, 91.5 mph, failed – permanent deflection (back-left, front-right)

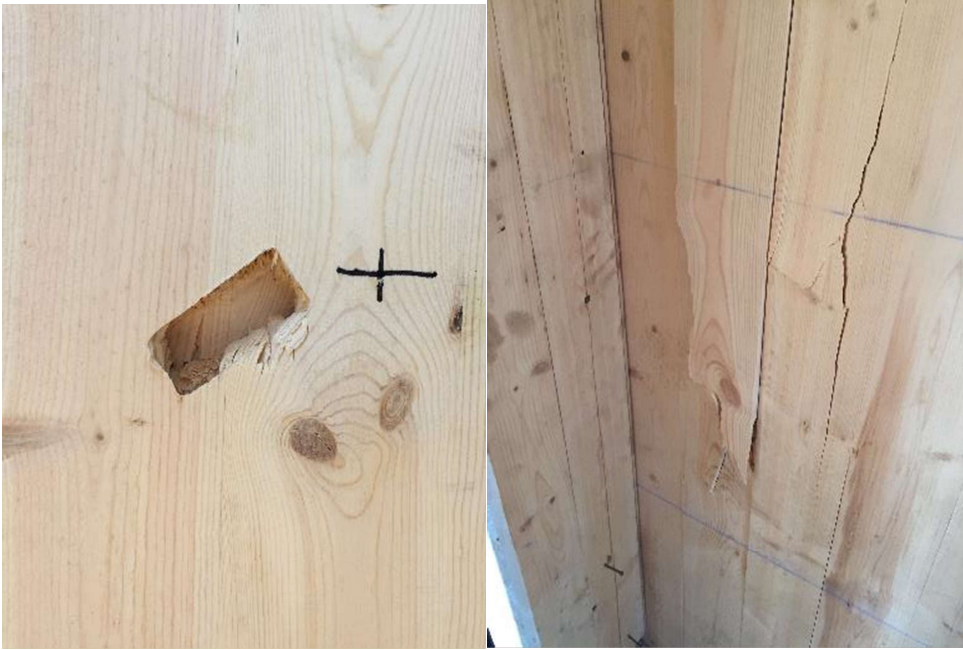


Figure A-20: Panel 7, weak-axis, strong-connection, edge, 15-pound, 90.9 mph, passed (front-left, back-right)



Figure A-21: Panel 7, weak-axis, strong-connection, corner, 15-pound, 89.9 mph, failed – dislodgement (front-left, back-right)



Figure A-22: Panel 8, strong-axis, strong-connection, center, 15-pound, 102.1 mph, passed (front-left, back-right)



Figure A-23: Panel 8, strong-axis, strong-connection, edge, 15-pound, 119.4 mph, passed (front-left, back-right)



Figure A-24: Panel 8, strong-axis, strong-connection, corner, 15-pound, 110.2 mph, passed (back-left, front-right)

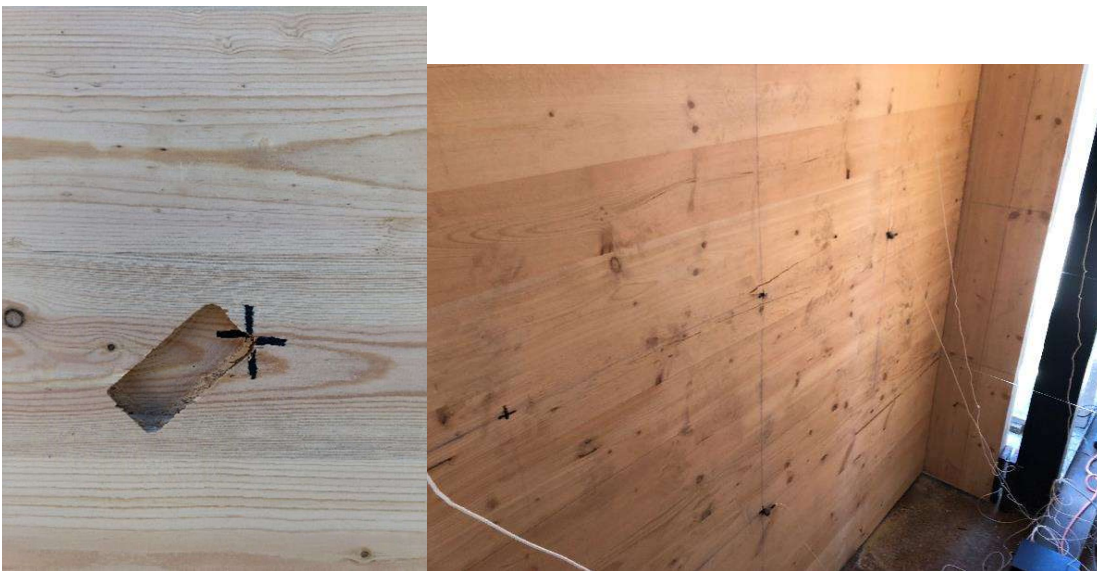


Figure A-25: Panel 9, strong-axis, weak-connection, center, 15-pound, 92.8 mph, passed (front-left, back-right)



Figure A-26: Panel 9, strong-axis, weak-connection, edge, 15-pound, 93.9 mph, passed (front-left, back-right)



Figure A-27: Panel 9, strong-axis, weak-connection, corner, 15-pound, 101.6 mph, failed – perforation/dislodgement (front-left, back-right)



Figure A-28: Panel 10, strong-axis, weak-connection, center, 15-pound, 104.3 mph, failed – perforation/dislodgement (front-left, back-right)



Figure A-29: Panel 10, strong-axis, weak-connection, edge, 15-pound, 112.8 mph, failed – perforation/dislodgement (back-left, front-right)



Figure A-30: Panel 10, strong-axis, weak-connection, corner, 15-pound, 112.7 mph, failed – perforation/dislodgement (front-left, back-right)



Figure A-31: Panel 11, strong-axis, strong-connection, center, 9-pound, 96.9 mph, passed (front-left, back-right)



Figure A-32: Panel 11, strong-axis, strong-connection, edge, 9-pound, 105.8 mph, failed
– permanent deflection (front-left, back-right)



Figure A-33: Panel 11, strong-axis, strong-connection, corner, 9-pound, 103.9 mph,
failed – permanent deflection (front-left, back-right)



Figure A-34: Panel 12, strong-axis, strong-connection, center, 14.5-pound, 96.9 mph, passed (front-left, back-right)



Figure A-35: Panel 12, strong-axis, strong-connection, edge, 14.5-pound, 105.8 mph, failed – perforation/dislodgement (front-left, back-right)



Figure A-36: Panel 12, strong-axis, strong-connection, corner, 14.5-pound, 103.9 mph, passed (front-left, back-right)



Figure A-37: Panel 13, weak-axis, weak-connection, center, 15-pound, 87.8 mph, passed (front-left, back-right)

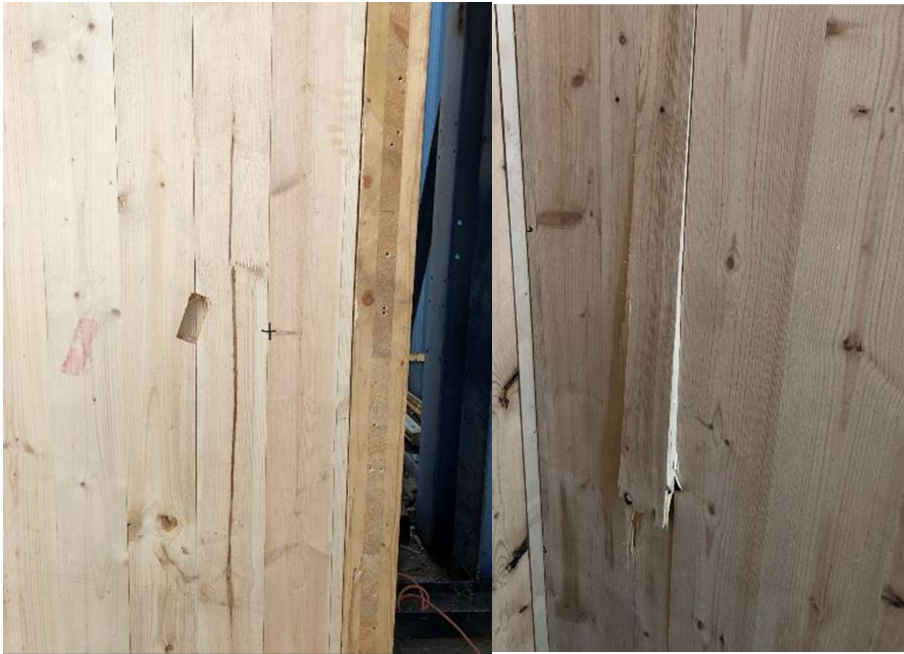


Figure A-38: Panel 13, weak-axis, weak-connection, edge, 15-pound, 87.3 mph, passed (front-left, back-right)



Figure A-39: Panel 13, weak-axis, weak-connection, corner, 15-pound, 89.4 mph, failed – perforation/dislodgement (front-left, back-right)



Figure A-40: Panel 14, weak-axis, weak-connection, center, 9-pound, 88.8 mph, passed (front-left, back-right)



Figure A-41: Panel 14, weak-axis, weak-connection, edge, 9-pound, 79.5 mph, passed (front-left, back-right)



Figure A-42: Panel 14, weak-axis, weak-connection, corner, 9-pound, 89.5 mph, failed – perforation/dislodgement (front-left, back-right)



Figure A-43: Panel 15, weak-axis, half-lap connection, center, 15-pound, 87.7 mph, failed – perforation/dislodgement (front-left, back-right)



Figure A-44: Panel 16, weak-axis, half-lap connection, center, 15-pound, 68.5 mph, passed (front-left, back-right)



Figure A-45: Panel 17, weak-axis, surface-spline connection, center, 15-pound, 76.3 mph, failed – permanent deflection (front-left, back-right)



Figure A-46: Panel 18, strong-axis, surface-spline connection, center, 15-pound, 85 mph, passed (front-left, back-right)

Appendix B: NDS Connection Capacity of Half-Lap Connection

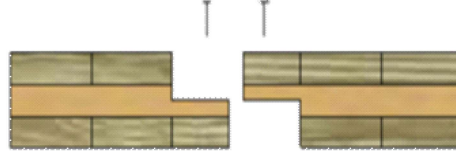
CLT Half Lap Connection Capacity

Screw Properties: Simpson SDS 25300

$$L_w := 3 \text{ in}$$

$$D := 0.242 \text{ in}$$

$$F_{yb} := 164000 \text{ psi}$$



CLT Properties: 3-ply SL-V4 CLT

$$SG_{SPF} := 0.36 \quad \text{SPF-S SG}$$

$$E_{CLT} := 1.1 \cdot 10^6 \text{ psi} \quad \text{Modulus of Elasticity}$$

$$t := 4.125 \text{ in} \quad \text{Overall thickness}$$

$$t_{ply} := 1.375 \text{ in} \quad \text{Thickness of one ply}$$

$$F_{eCLT1} := 16600 \cdot SG_{SPF}^{1.84} \text{ psi} = 2533 \cdot \text{psi} \quad \text{Bearing Strength if } D < 0.25$$

Connection Geometry:

$$L_{side} := \frac{t}{2} = 2.063 \cdot \text{in} \quad \text{Side member bearing length}$$

$$p := L - L_{side} = 0.937 \cdot \text{in} \quad 10 \cdot D = 2.42 \cdot \text{in} \quad 6D = 1.452 \cdot \text{in}$$

$$\theta_E := 31 \text{ deg} \quad \text{Angle of taper of screw tip}$$

$$E := \frac{\frac{D}{2}}{\tan\left(\frac{\theta_E}{2}\right)} = 0.436 \cdot \text{in} \quad \text{Length of tapered tip}$$

$$L_{main} := p - \frac{E}{2} = 0.719 \cdot \text{in} \quad \text{Main member bearing length}$$

Bearing Strengths:

$$F_{es} := F_{eCLT1} = 2533 \cdot \text{psi} \quad D = 0.242 \cdot \text{in} \quad \text{Side Member Bearing Strength}$$

$$F_{em} := F_{eCLT1} = 2533 \cdot \text{psi} \quad D = 0.242 \cdot \text{in} \quad \text{Main Member Bearing Strength}$$

Yield Mode Calculation Terms:

$$R_e := \frac{F_{em}}{F_{es}} = 1$$

$$R_t := \frac{L_{\text{main}}}{L_{\text{side}}} = 0.349$$

$$K_D := 10 \frac{D}{\text{in}} + 0.5 = 2.92 \quad R_D := K_D \quad \text{For } 0.17" < D < 0.25"$$

$$k_1 := \frac{\sqrt{R_e + 2 \cdot R_e^2 (1 + R_t + R_t^2) + R_t^2 \cdot R_e^3} - R_e \cdot (1 + R_t)}{(1 + R_e)} = 0.333$$

$$k_2 := -1 + \sqrt{2(1 + R_e) + \frac{2 \cdot F_{yb} \cdot (1 + 2 \cdot R_e) \cdot D^2}{3 \cdot F_{em} \cdot L_{\text{main}}^2}} = 3.319$$

$$k_3 := -1 + \sqrt{\frac{2 \cdot (1 + R_e)}{R_e} + \frac{2 \cdot F_{yb} \cdot (2 + R_e) \cdot D^2}{3 \cdot F_{em} \cdot L_{\text{side}}^2}} = 1.405$$

Yield Mode I_m :

$$Z_{Im} := \frac{D \cdot L_{\text{main}} \cdot F_{em}}{R_D} = 151 \cdot \text{lbf}$$

Yield Mode I_s :

$$Z_{Is} := \frac{D \cdot L_{\text{side}} \cdot F_{es}}{R_D} = 433 \cdot \text{lbf}$$

Yield Mode II:

$$Z_{II} := \frac{k_1 \cdot D \cdot L_{side} \cdot F_{es}}{R_D} = 144 \cdot \text{lb} \cdot \text{ft}$$

Yield Mode III_m:

$$Z_{III_m} := \frac{k_2 \cdot D \cdot L_{main} \cdot F_{em}}{(1 + 2 \cdot R_e) \cdot R_D} = 167 \cdot \text{lb} \cdot \text{ft}$$

Yield Mode III_s:

$$Z_{III_s} := \frac{k_3 \cdot D \cdot L_{side} \cdot F_{em}}{(2 + R_e) \cdot R_D} = 203 \cdot \text{lb} \cdot \text{ft}$$

Yield Mode IV:

$$Z_{IV} := \frac{D^2}{R_D} \cdot \sqrt{\frac{2 \cdot F_{em} \cdot F_{yb}}{3 \cdot (1 + R_e)}} = 236 \cdot \text{lb} \cdot \text{ft}$$

$$Z := \min(Z_{I_m}, Z_{I_s}, Z_{II}, Z_{III_m}, Z_{III_s}, Z_{IV}) = 144 \cdot \text{lb} \cdot \text{ft}$$

$$C_g := 1.0 \quad \text{NDS Eq. 11.3-1}$$

$$C_{\Delta} := 1.0 \quad \text{NDS 12.5.1.1}$$

$$C_m := 1.0 \quad C_{di} := 1.0 \quad C_{tn} := 1.0$$

$$C_t := 1.0 \quad C_{eg} := 1.0$$

$$K_F := 3.32 \quad \phi := 0.65 \quad \lambda := 1.0 \quad C_D := 1.6$$

$$Z'_{LRFD} := Z \cdot K_F \cdot \phi \cdot \lambda \cdot C_m \cdot C_t \cdot C_{eg} \cdot C_{di} \cdot C_{tn} \cdot C_g \cdot C_{\Delta} = 312 \cdot \text{lb} \cdot \text{ft}$$

LRFD Design Value

$$Z'_{ASD} := Z \cdot C_D \cdot (C_m \cdot C_t \cdot C_{eg} \cdot C_{di} \cdot C_{tn} \cdot C_g \cdot C_{\Delta}) = 231 \cdot \text{lb} \cdot \text{ft}$$

ASD Design Value

APPENDIX C: Individual Fragilities for CLT Panels in Residential Archetypes

The individual panel fragilities based on panel moment capacity and connection capacity for each unique CLT panel is shown in this Appendix. Each structure is shown with the corresponding roof panel labels (letters) and wall panel labels (numbers). For structure types 1-6, the fragilities for each wall panel, roof panel, and system level fragilities according to Chapter 5 are shown below. In addition, a table of wind load statistics for each panel shown.

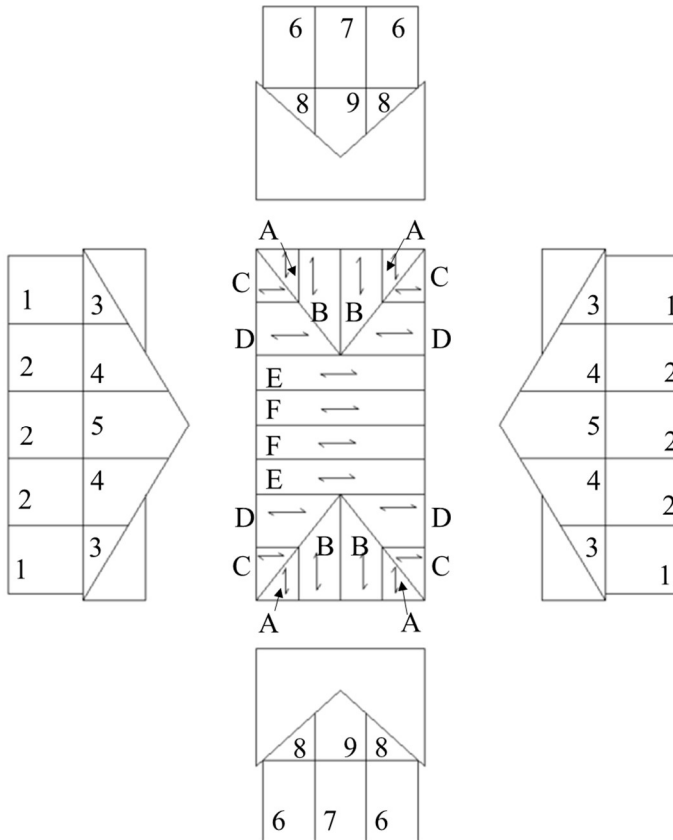


Figure C-1: Roof and wall panel labelling for Structure 1

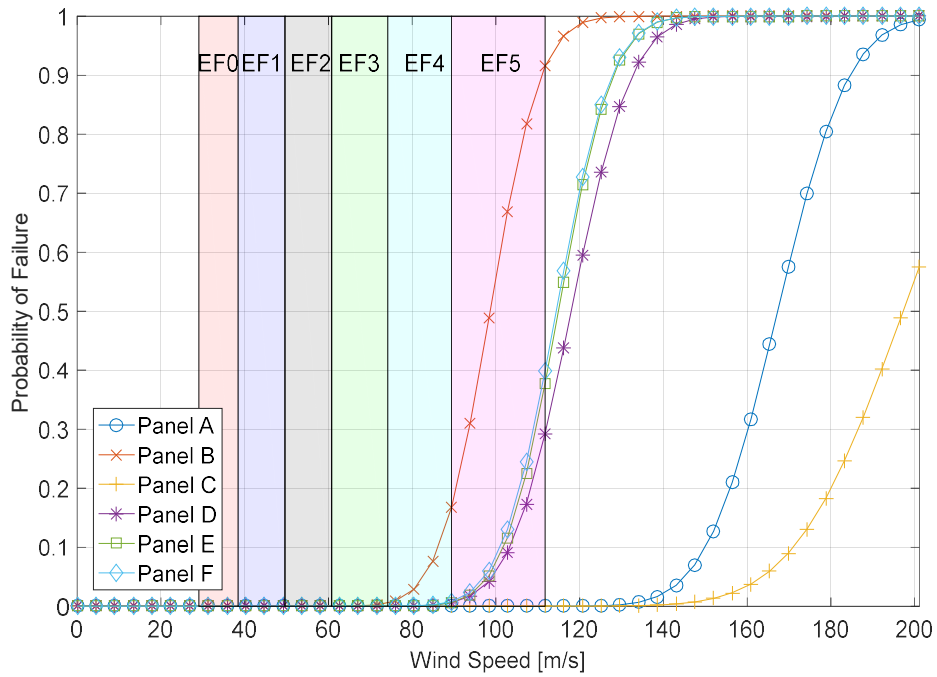


Figure C-2: Roof Panel Fragilities for Structure 1

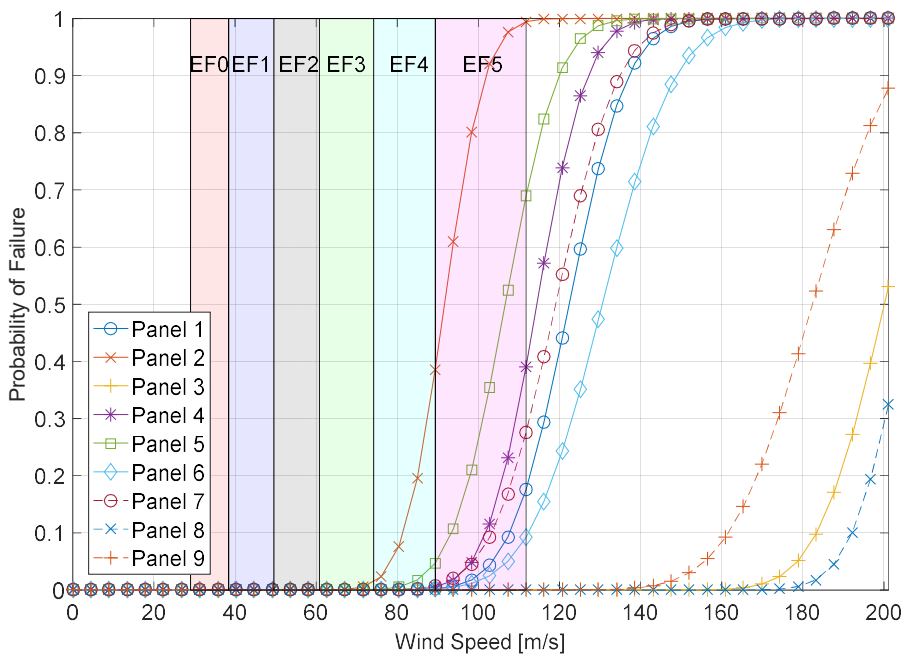


Figure C-3: Wall Panel Fragilities for Structure 1

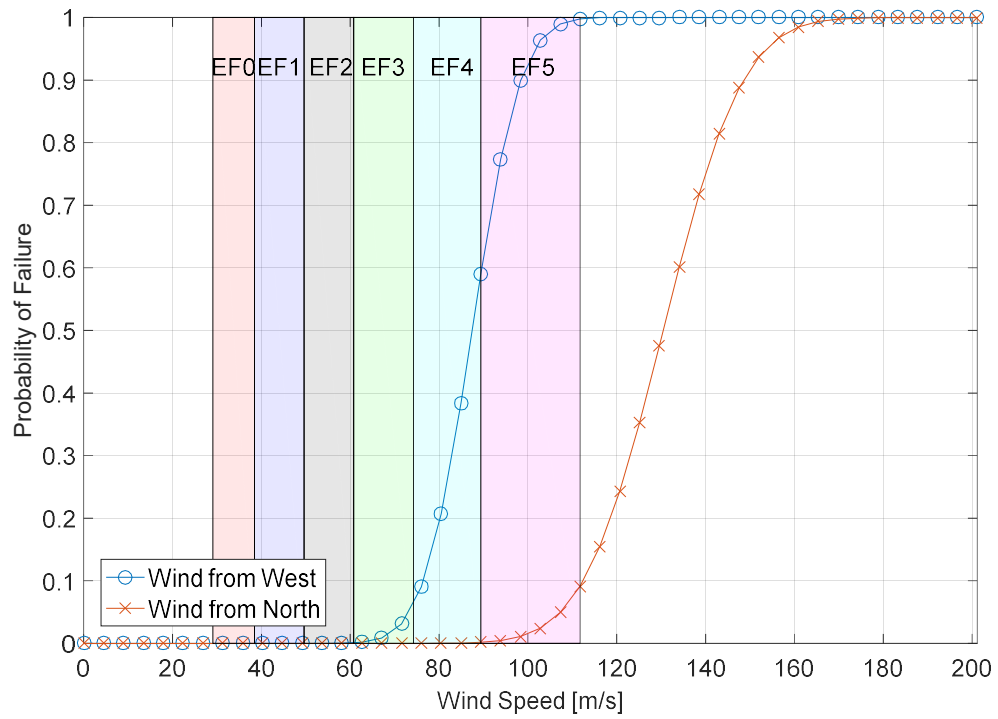


Figure C-4: System Level Fragilities for Structure 1

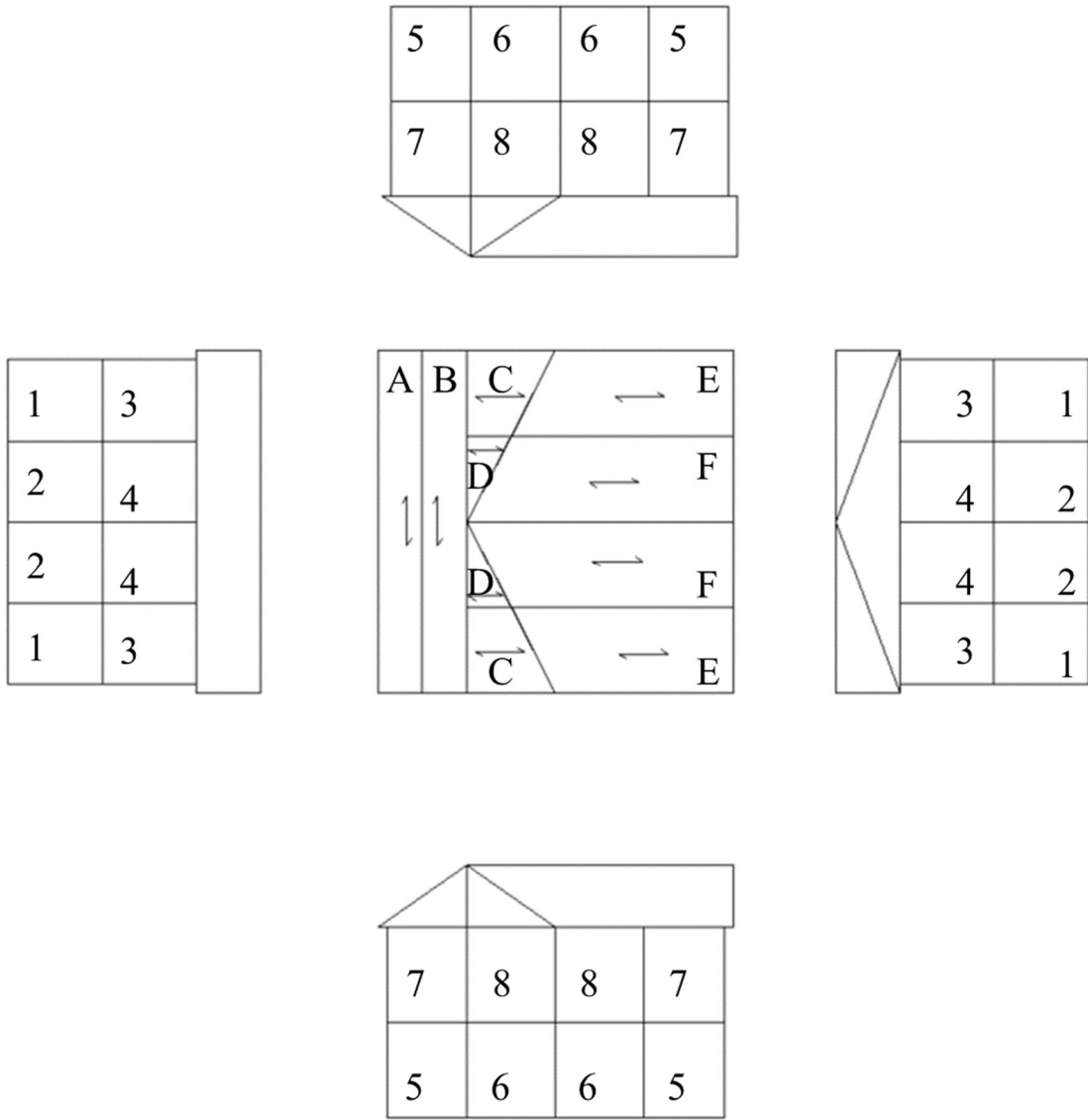


Figure C-5: Roof and wall panel labelling for Structure 2

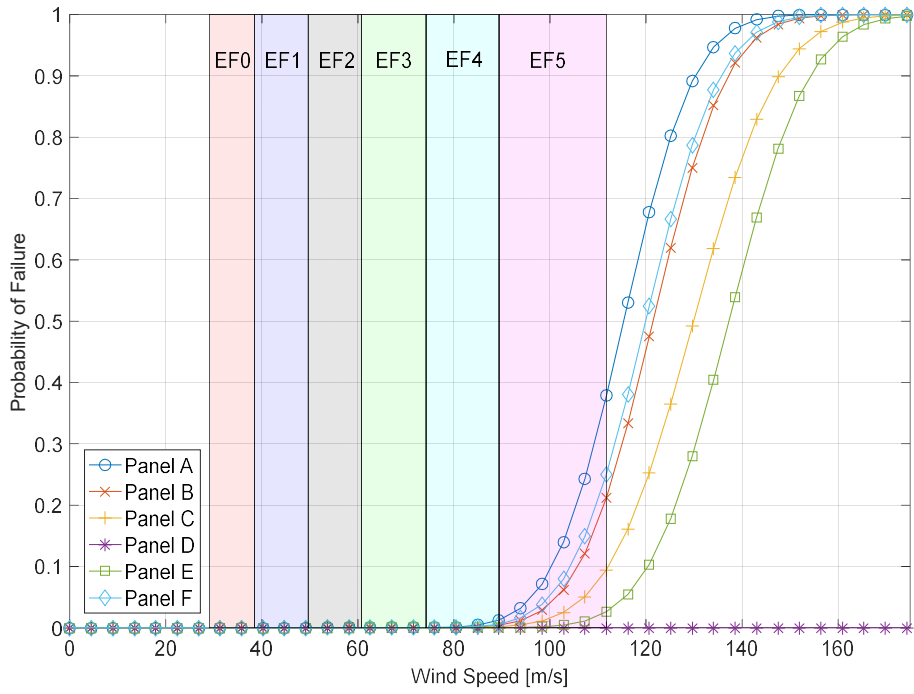


Figure C-6: Roof Panel Fragilities for Structure 2

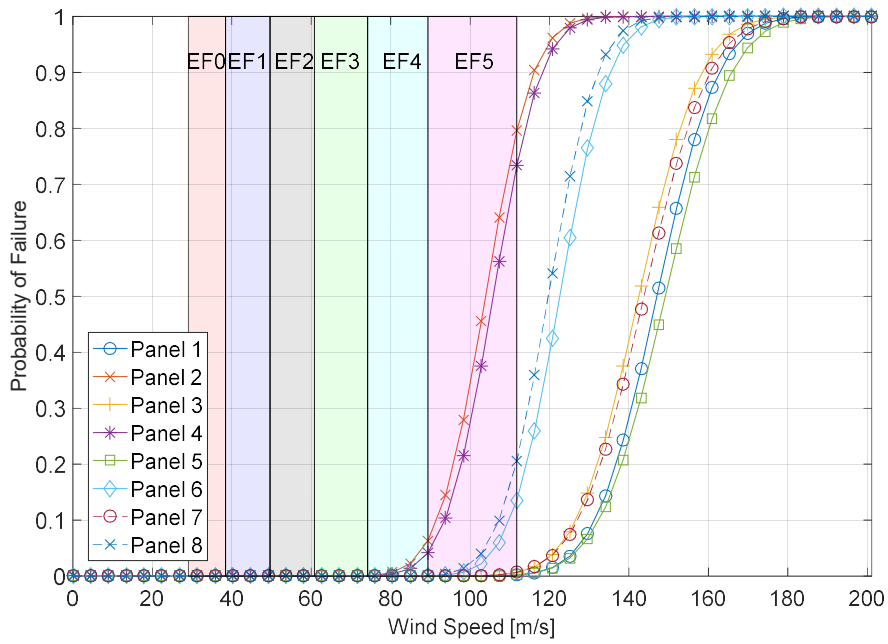


Figure C-7: Wall Panel Fragilities for Structure 2

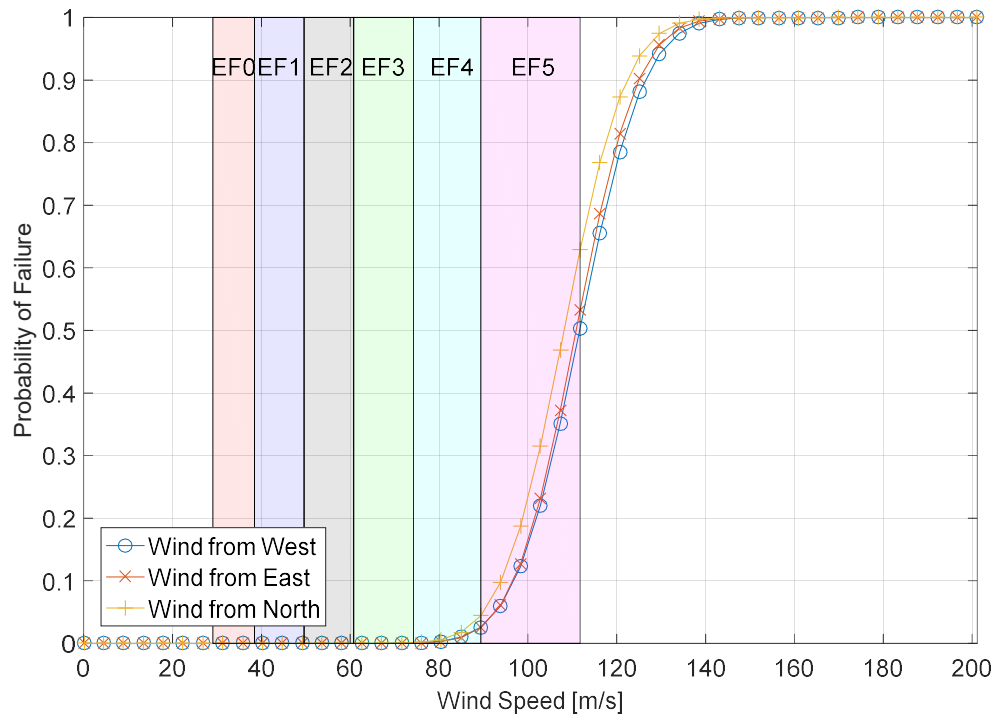


Figure C-8: System Level Fragilities for Structure 2

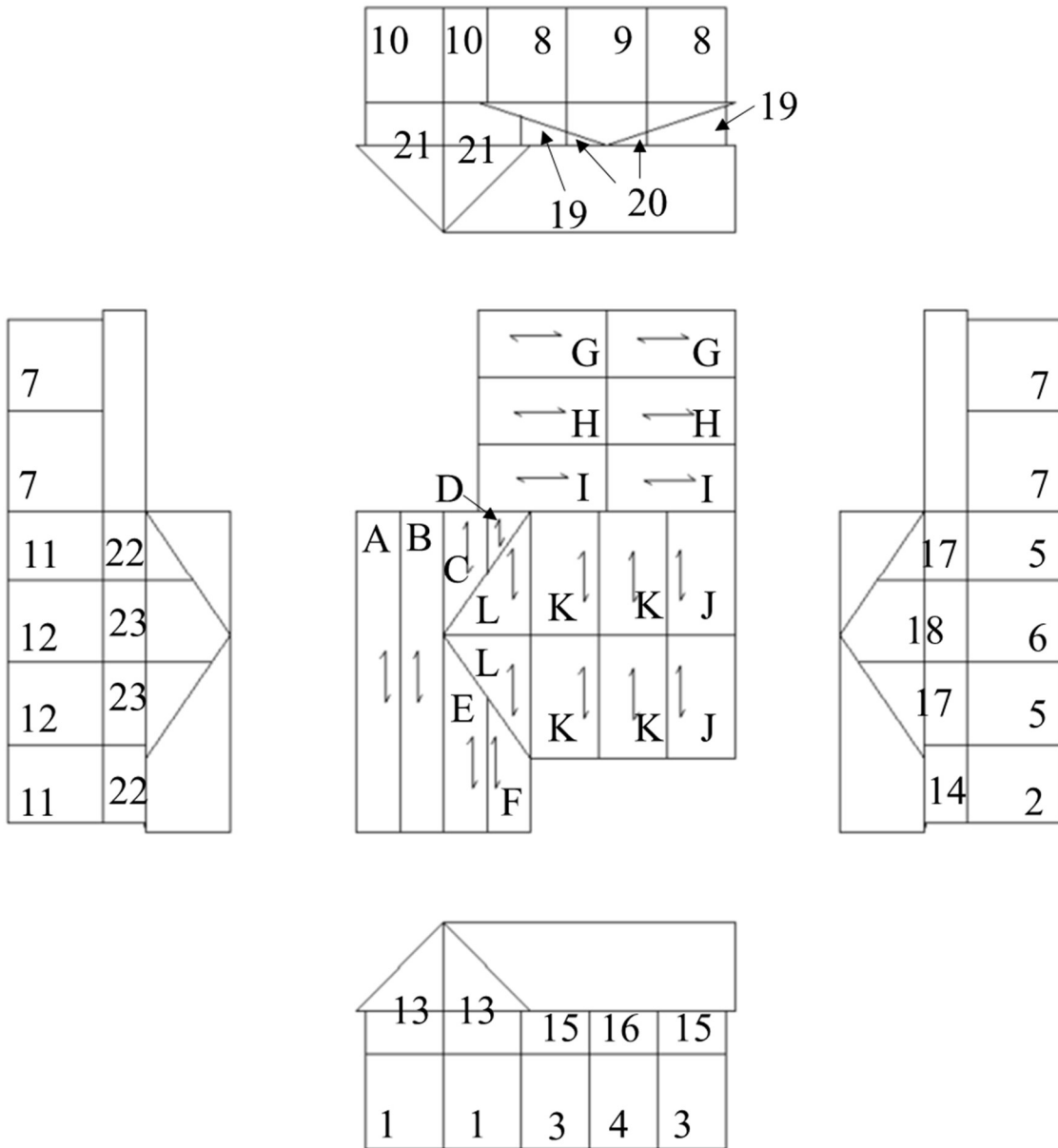


Figure C-9: Roof and wall panel labelling for Structure 3

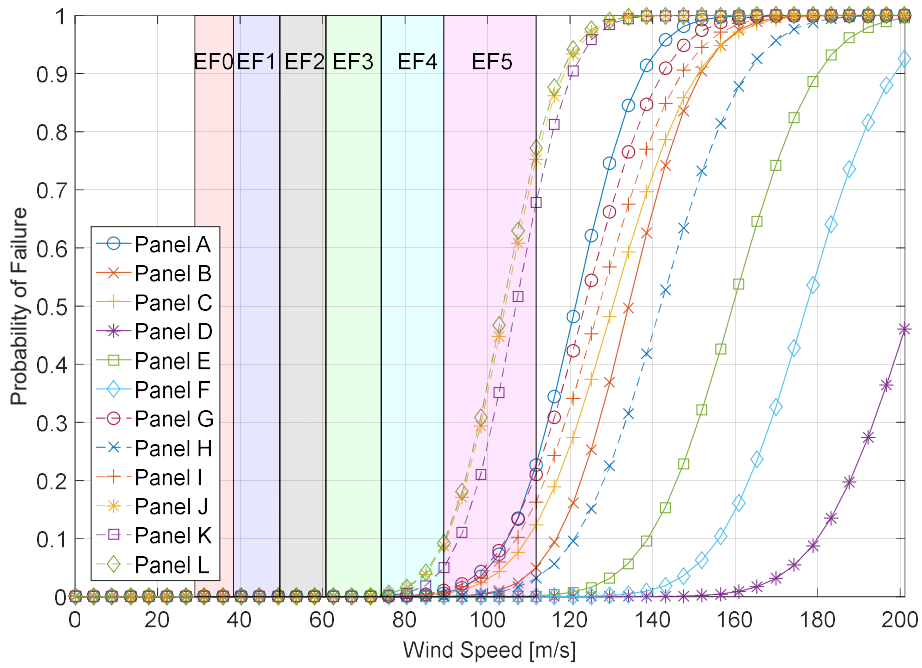


Figure C-10: Roof Panel Fragilities for Structure 3

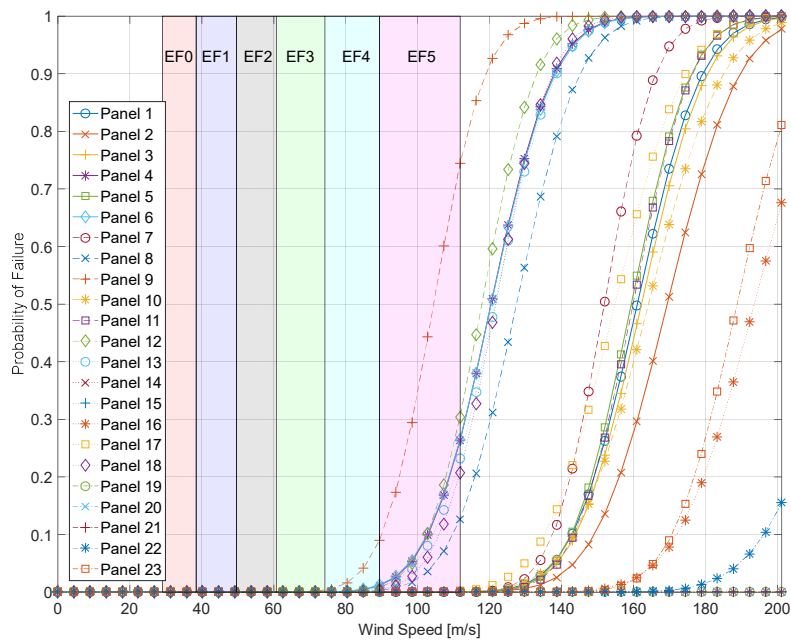


Figure C-11: Wall Panel Fragilities for Structure 3

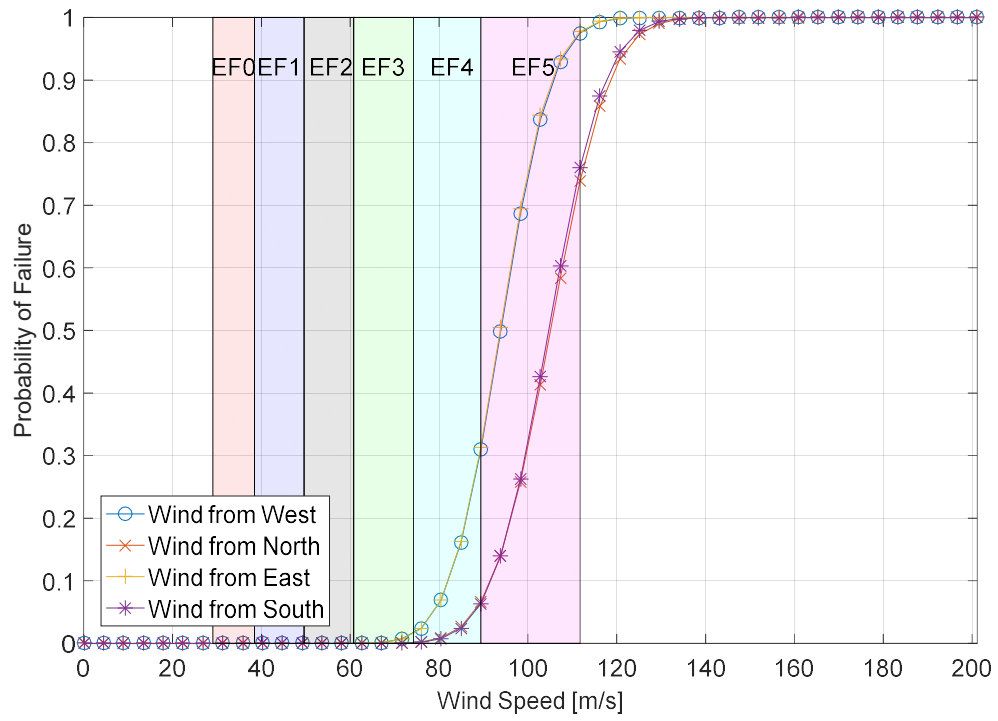


Figure C-12: System level Fragilities for Structure 4

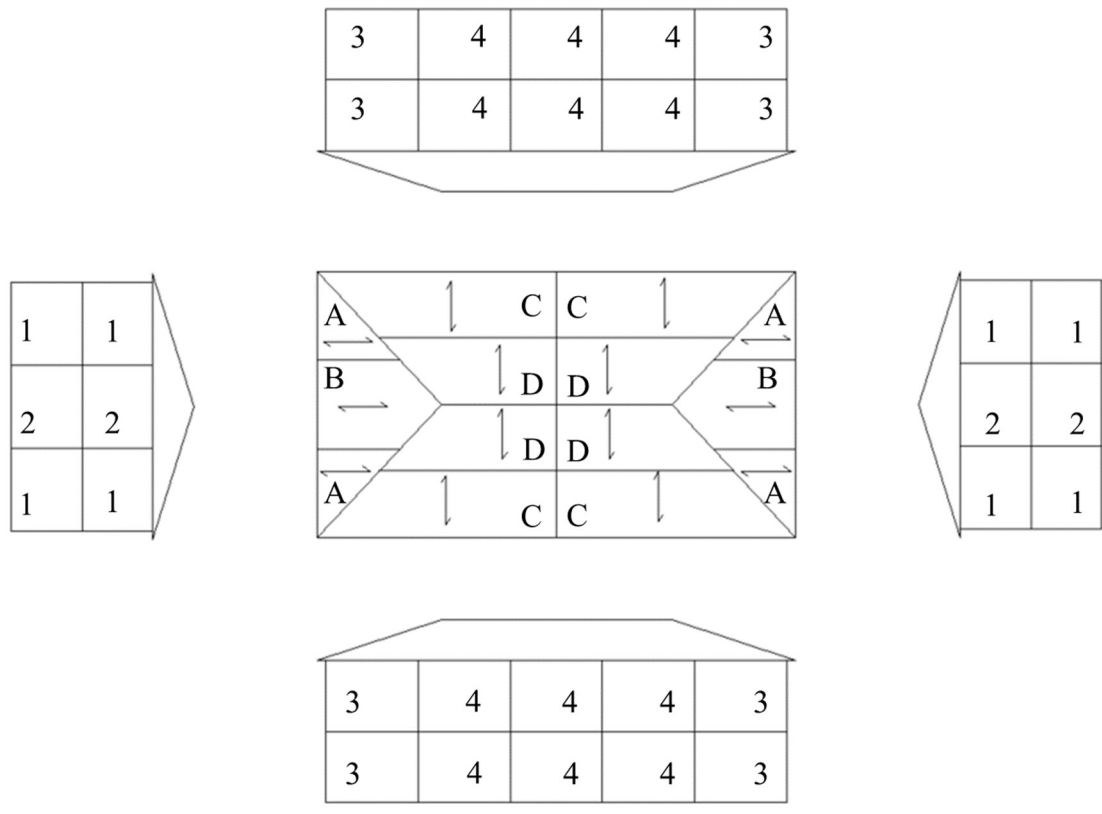


Figure C-13: Roof and wall panel labelling for Structure 4

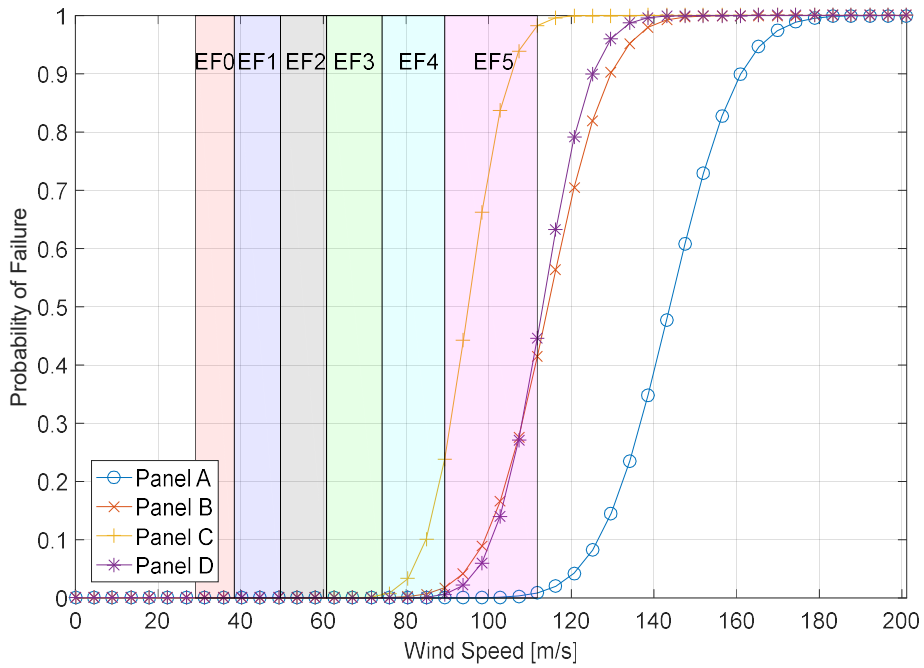


Figure C-14: Roof Panel Fragilities for Structure 4

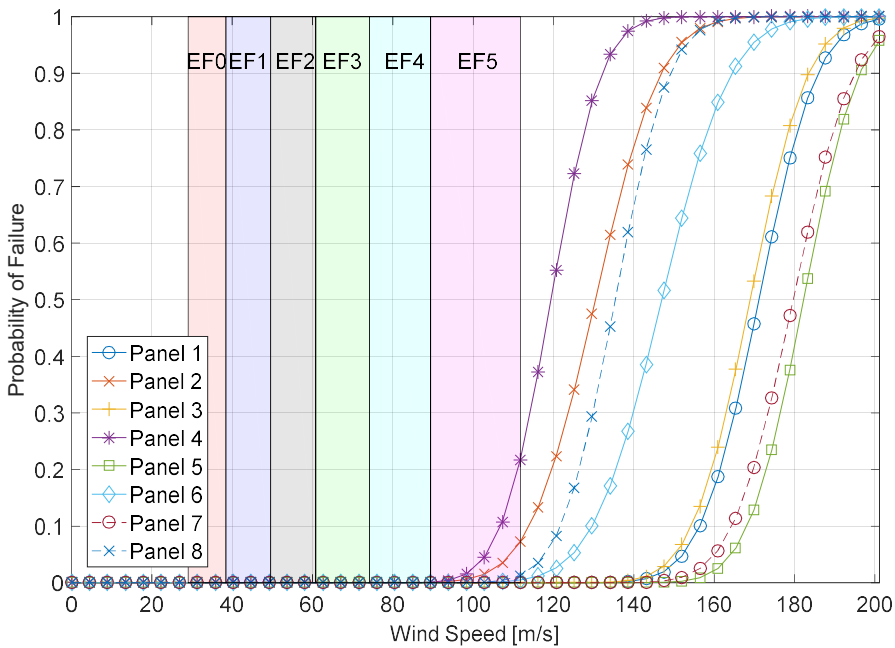


Figure C-15: Wall Panel Fragilities for Structure 4

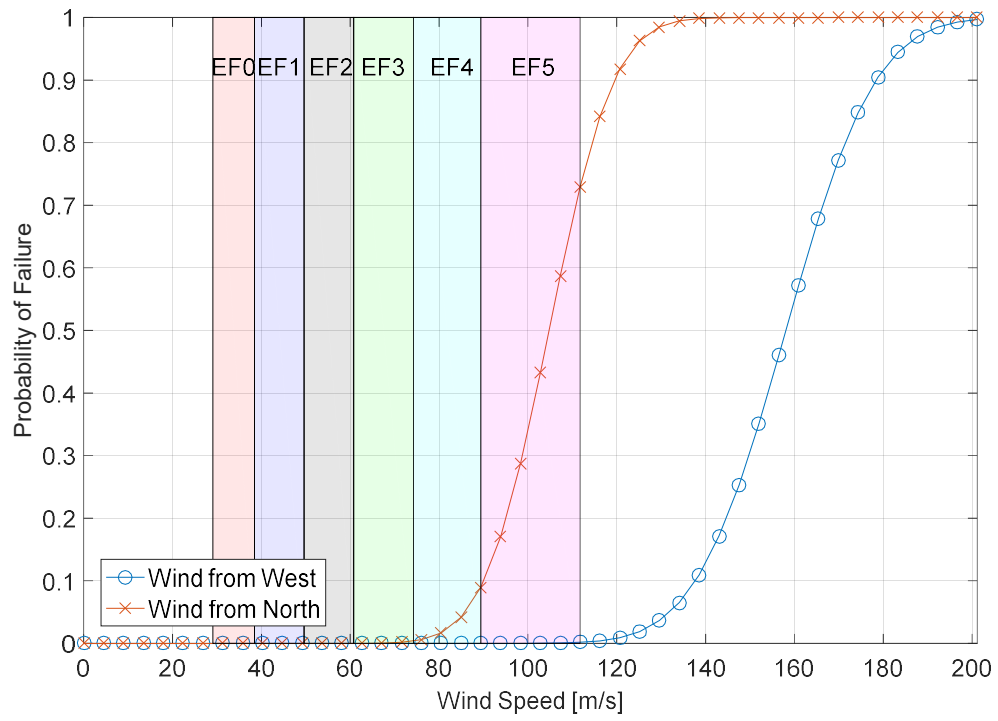


Figure C-16: System Level Fragilities for Structure 4

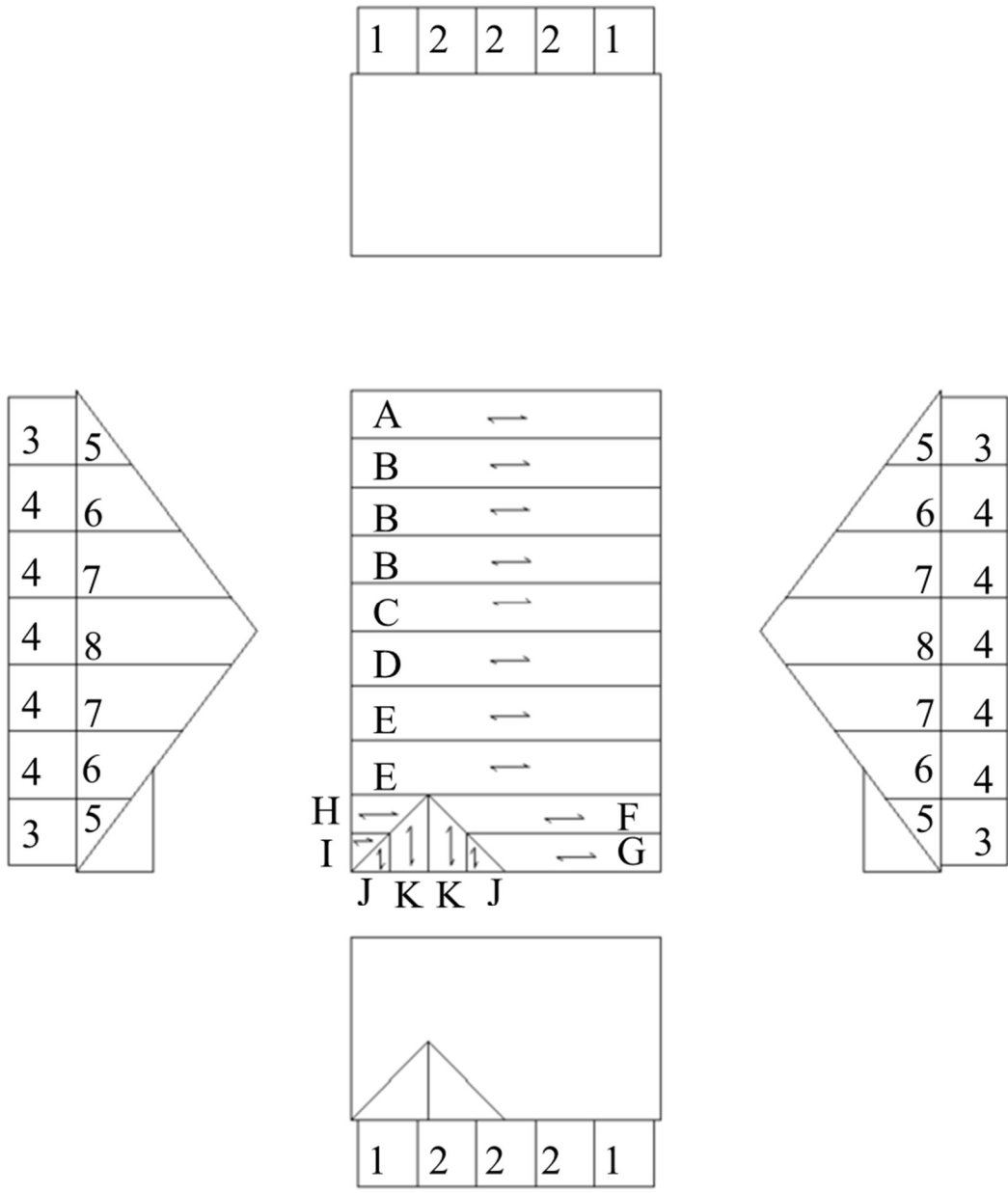


Figure C-17: Roof and wall panel labelling for Structure 5

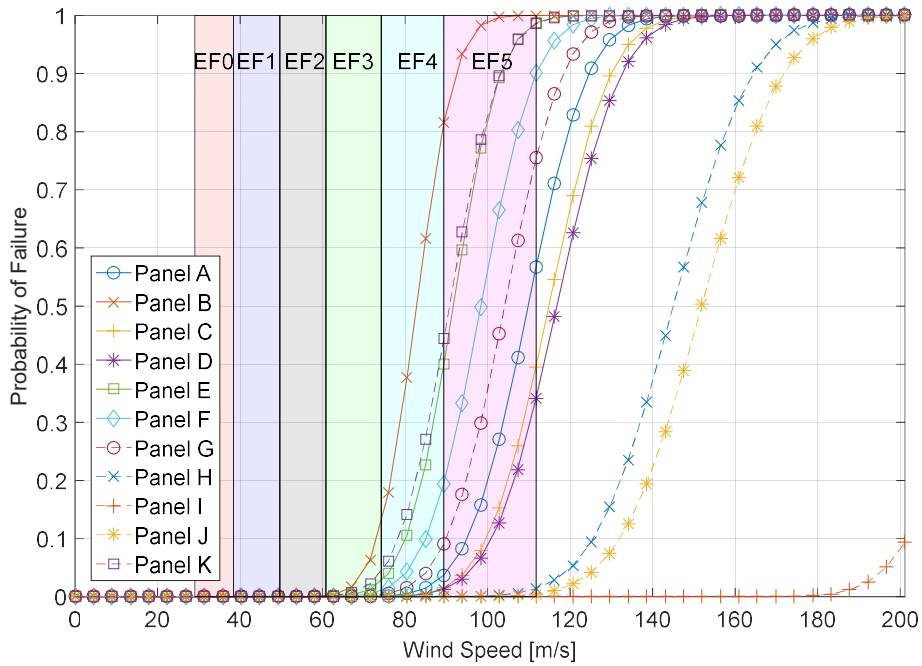


Figure C-18: Roof Panel Fragilities for Structure 5

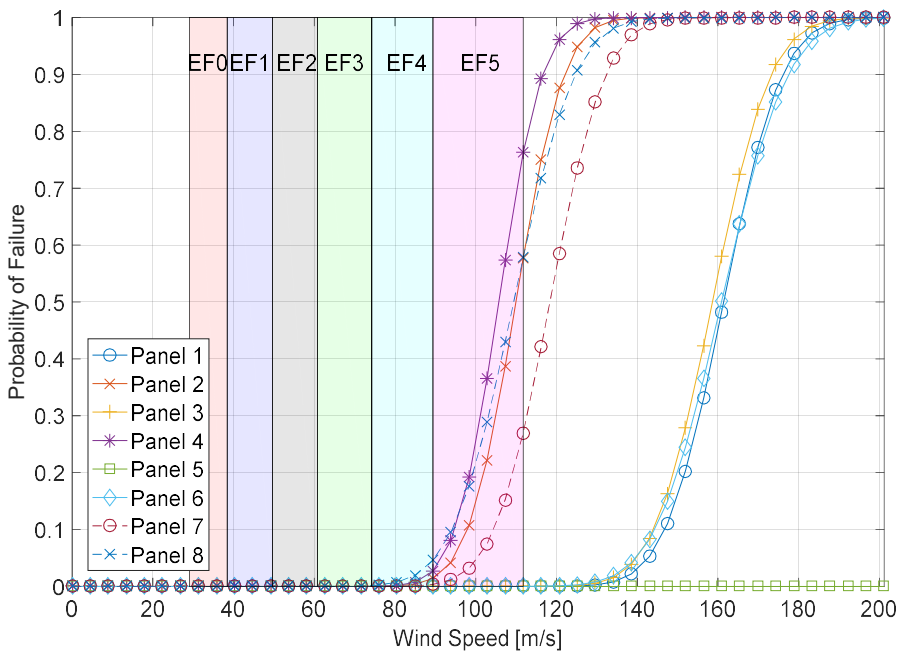


Figure C-19: Wall Panel Fragilities for Structure 5

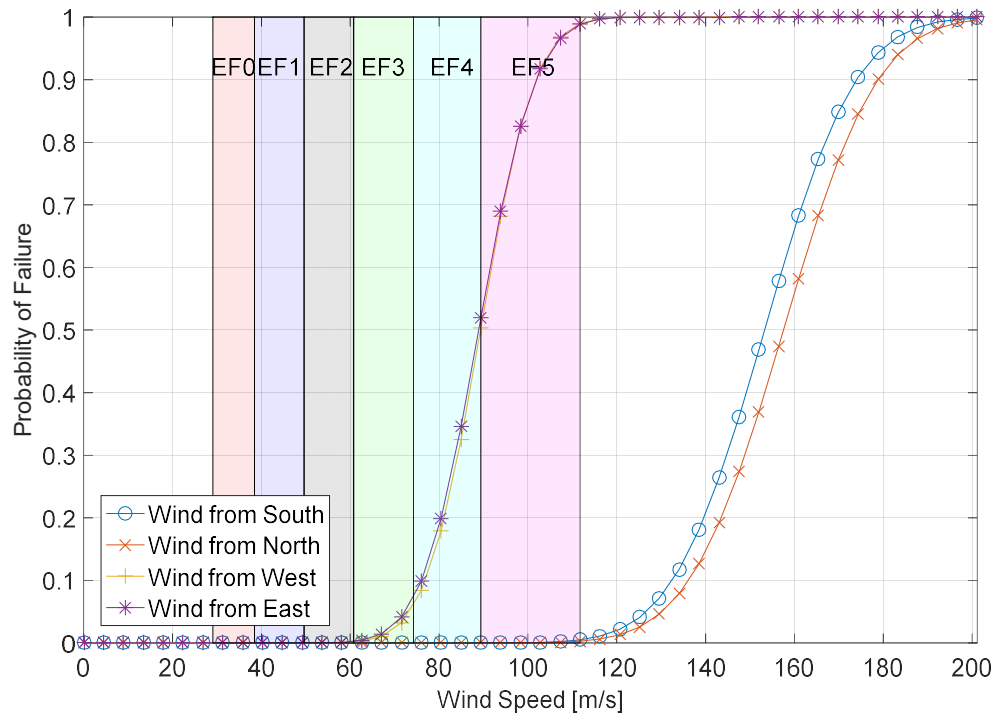


Figure C-20: System Level Fragilities for Structure 5

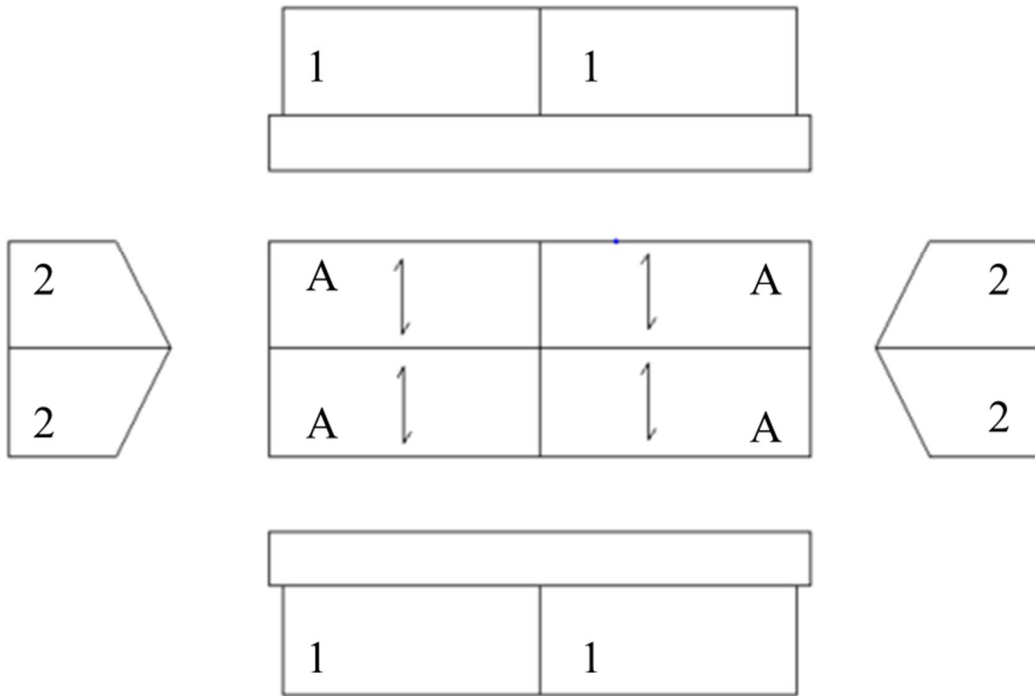


Figure C-21: Wall and roof panel labelling for Structure 6

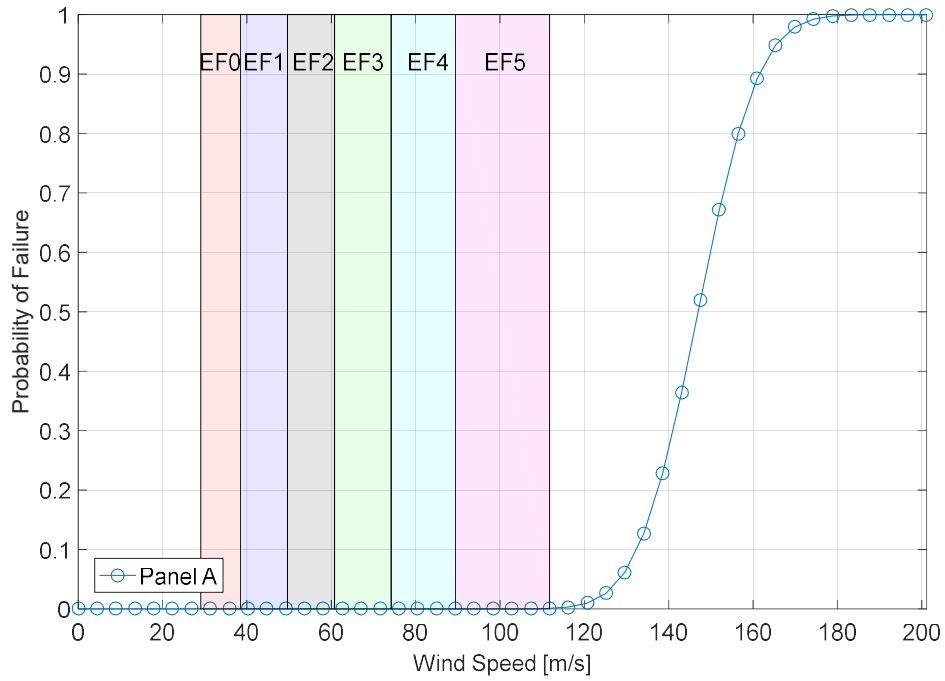


Figure C-22: Roof Panel Fragilities for Structure 6

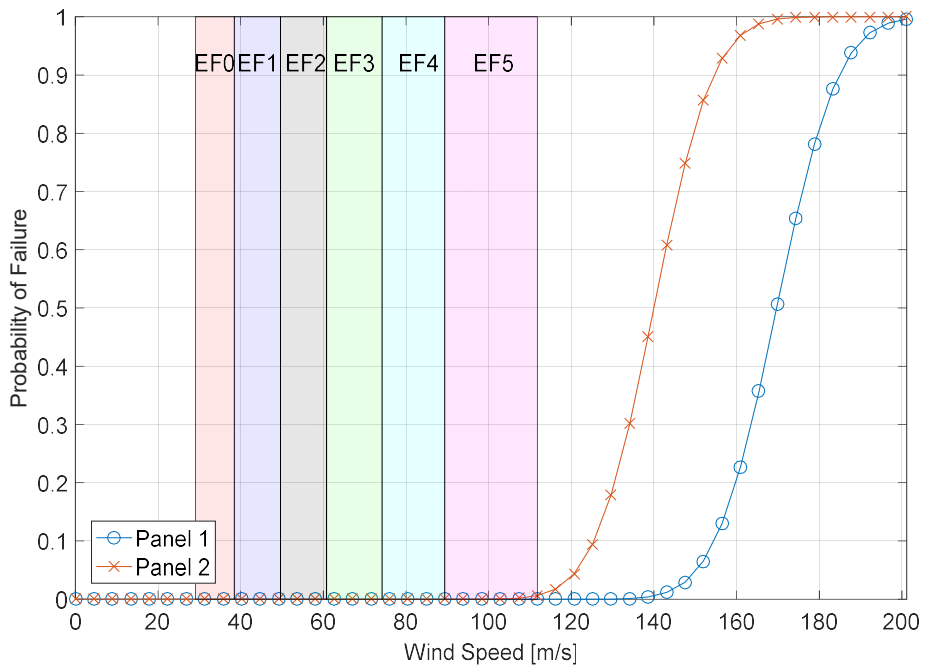


Figure C-23: Wall Panel Fragilities for Structure 6

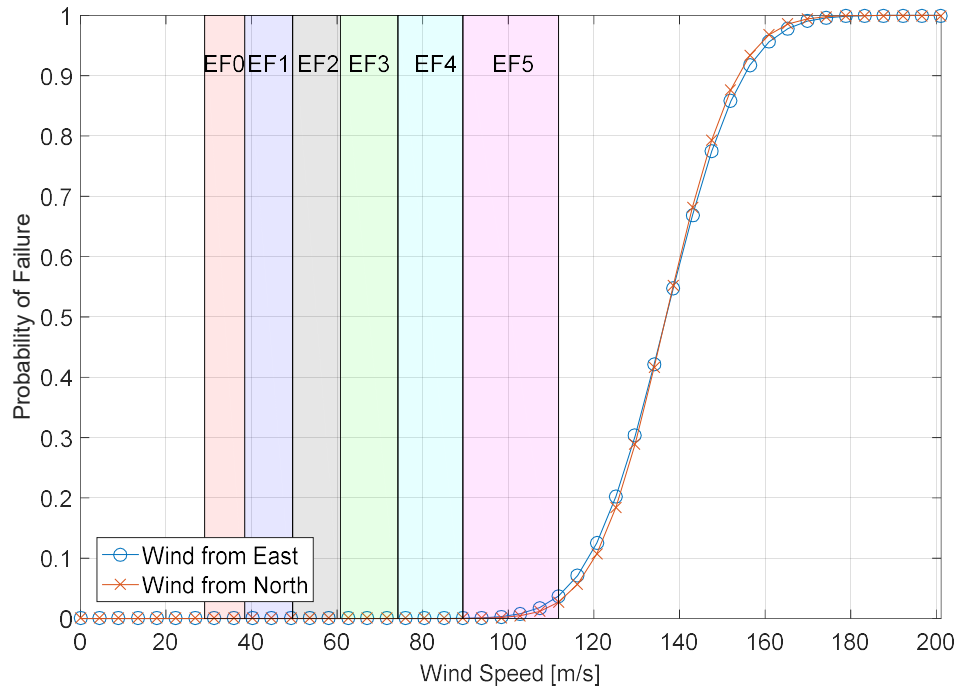


Figure C-24: System Level Fragilities for Structure 6

Appendix D - Roof and Wall Panel Parameters

Roof Panel Type	Average Length [ft]	Width [ft]	Area [ft ²]	Span Minimum [ft]	Span Maximum [ft]	Average +Cp	Average -Cp	Number of Panels	Kz-nominal	Kz-mean	Panel Area [ft ²]	Archetype Area [ft ²]	Archetype Perimeter [ft]	Panel Slope (in of rise/ft)
1A	4.0	8.7	34.6	0.0	8.0	0.70	1.81	4	0.87	0.81	138.4 ft ²	1591	150	11
1B	12.0	8.7	103.8	8.0	16.0	0.60	1.20	4	0.87	0.81	415.2 ft ²	1591	150	11
1C	3.2	8.0	25.5	0.0	6.4	0.85	2.13	4	0.91	0.85	102.0 ft ²	1591	150	11
1D	9.6	8.0	76.5	6.4	12.8	0.60	1.25	4	0.91	0.85	306.0 ft ²	1591	150	11
1E	25.5	6.2	157.5	12.8	12.8	0.60	1.19	2	0.91	0.85	314.9 ft ²	1591	150	4
1F	25.5	6.2	157.5	12.8	12.8	0.60	1.19	2	0.91	0.85	314.9 ft ²	1591	150	4
2A	39.0	6.1	236.3	13.0	13.0	0.60	1.31	1	0.95	0.89	236.3 ft ²	1745	150	8
2B	39.0	6.1	236.3	13.0	13.0	0.60	1.12	1	0.95	0.89	236.3 ft ²	1745	150	8
2C	9.1	9.8	88.6	6.1	12.1	0.55	1.24	2	0.95	0.89	177.3 ft ²	1745	150	8
2D	3.0	9.8	29.7	0.0	6.1	0.75	1.40	2	0.95	0.89	59.4 ft ²	1745	150	8
2E	22.7	10.3	233.0	10.1	12.6	0.30	0.80	2	0.95	0.89	466.0 ft ²	1745	150	4
2F	27.7	10.3	285.1	12.6	15.1	0.30	0.83	2	0.95	0.89	570.1 ft ²	1745	150	4
3A	35.0	6.7	235.2	11.7	11.7	0.60	1.32	1	0.9	0.84	235.2 ft ²	1929	188	12
3B	35.0	6.7	235.2	11.7	11.7	0.60	0.99	1	0.9	0.84	235.2 ft ²	1929	188	12
3C	10.1	6.7	68.0	6.8	13.5	0.60	1.19	1	0.9	0.84	68.0 ft ²	1929	188	12
3D	3.4	6.7	22.7	0.0	6.8	0.60	1.97	1	0.9	0.84	22.7 ft ²	1929	188	12
3E	18.1	6.7	121.8	7.4	10.8	0.60	1.11	1	0.9	0.84	121.8 ft ²	1929	188	12
3F	11.4	6.7	76.4	4.0	7.4	0.60	1.28	1	0.9	0.84	76.4 ft ²	1929	188	12
3G	14.8	7.3	108.2	14.8	14.8	0.30	1.21	1	0.85	0.79	108.2 ft ²	1929	188	4
3H	14.8	7.3	108.2	14.8	14.8	0.30	0.77	1	0.85	0.79	108.2 ft ²	1929	188	4
3I	14.8	7.3	108.2	14.8	14.8	0.30	1.14	1	0.85	0.79	108.2 ft ²	1929	188	4
3J	16.2	7.4	120.7	16.2	16.2	0.50	1.13	2	0.9	0.84	241.5 ft ²	1929	188	8
3K	16.2	7.4	120.7	16.2	16.2	0.50	0.85	4	0.9	0.84	483.0 ft ²	1929	188	8
3L	8.1	7.4	60.4	0.0	16.2	0.60	1.15	2	0.9	0.84	120.7 ft ²	1929	188	8
4A	4.9	10.0	49.0	0.0	9.8	0.40	1.55	4	0.88	0.82	196.0 ft ²	1700	160	4
4B	11.9	10.0	119.0	9.8	14.0	0.40	1.36	2	0.88	0.82	238.0 ft ²	1700	160	4
4C	23.5	7.9	185.9	7.9	7.9	0.40	1.52	4	0.88	0.82	743.5 ft ²	1700	160	4
4D	16.5	7.9	130.5	7.9	7.9	0.40	1.49	4	0.88	0.82	522.1 ft ²	1700	160	4
5A	45.0	8.8	393.8	15.0	15.0	0.60	1.04	1	0.95	0.89	393.8 ft ²	3870	222	9
5B	45.0	8.8	393.8	15.0	15.0	0.60	0.90	3	0.95	0.89	1181.3 ft ²	3870	222	9
5C	45.0	8.8	393.8	15.0	15.0	0.60	0.91	1	0.95	0.89	393.8 ft ²	3870	222	9
5D	45.0	9.4	356.3	15.0	15.0	0.60	0.97	1	0.95	0.89	356.3 ft ²	3870	222	9
5E	45.0	9.4	356.3	15.0	15.0	0.60	0.90	2	0.95	0.89	712.5 ft ²	3870	222	9
5F	30.9	7.9	289.3	14.1	16.9	0.60	0.87	1	0.95	0.89	289.3 ft ²	3870	222	9
5G	25.3	7.9	236.7	11.3	14.1	0.60	1.03	1	0.95	0.89	236.7 ft ²	3870	222	9
5H	8.4	7.9	78.9	5.6	11.3	0.60	1.27	1	0.95	0.89	78.9 ft ²	3870	222	9
5I	2.8	7.9	26.3	0.0	5.6	0.70	1.84	1	0.95	0.89	26.3 ft ²	3870	222	9
5J	4.7	8.0	37.2	0.0	9.4	0.70	1.68	2	0.91	0.85	74.4 ft ²	3870	222	12
5K	8.0	8.0	63.3	9.4	18.7	0.60	1.11	2	0.91	0.85	126.6 ft ²	3870	222	12
6A	20.0	8.0	160.0	10.0	10.0	0.30	1.09	4	0.85	0.79	640.0 ft ²	640	112	6

Appendix D - Roof and Wall Panel Parameters

Wall Panel Type	Average Length [ft]	Width [ft]	Area [ft ²]	Span Minimum [ft]	Span Maximum [ft]	Average +Cp	Average - Cp	MWFRS +Cp	MWFRS - Cp	Number of Panels	Kz-nominal	Kz-mean
1A	13.3	10.3	136.9	13.3	13.3	0.80	0.92	0.80	0.70	4	0.91	0.85
1B	13.3	10.3	136.9	13.3	13.3	0.80	0.90	0.80	0.70	6	0.91	0.85
1C	3.2	10.3	32.5	0.0	6.3	0.90	1.04	0.80	0.70	4	0.91	0.85
1D	9.5	10.3	97.5	6.3	12.7	0.85	0.93	0.80	0.70	4	0.91	0.85
1E	14.3	10.3	146.3	12.7	15.8	0.80	0.90	0.80	0.70	2	0.91	0.85
1F	13.3	7.8	104.4	13.3	13.3	0.85	0.94	0.80	0.70	2	0.91	0.85
1G	13.3	7.8	104.4	13.3	13.3	0.85	0.90	0.80	0.70	1	0.91	0.85
1H	3.2	7.8	24.8	0.0	6.3	0.95	1.00	0.80	0.70	2	0.91	0.85
1I	7.9	7.8	62.0	6.3	9.5	0.88	0.95	0.80	0.70	1	0.91	0.85
2A	10.5	9.3	97.1	10.5	10.5	0.83	0.95	0.80	0.70	4	0.95	0.89
2B	10.5	9.3	97.1	10.5	10.5	0.83	0.93	0.80	0.70	4	0.95	0.89
2C	11.0	9.3	101.8	11.0	11.0	0.83	0.95	0.80	0.70	4	0.95	0.89
2D	11.0	9.3	101.8	11.0	11.0	0.83	0.93	0.80	0.70	4	0.95	0.89
2E	10.5	9.3	98.0	10.5	10.5	0.83	0.95	0.80	0.70	4	0.95	0.89
2F	10.5	9.3	98.0	10.5	10.5	0.83	0.93	0.80	0.70	4	0.95	0.89
2G	11.0	9.3	102.7	11.0	11.0	0.83	0.95	0.80	0.70	4	0.95	0.89
2H	11.0	9.3	102.7	11.0	11.0	0.83	0.93	0.80	0.70	4	0.95	0.89
3A	10.3	8.5	87.8	10.3	10.3	0.825	0.98	0.80	0.70	2	0.9	0.84
3B	10.3	8.5	87.8	10.3	10.3	0.825	0.98	0.80	0.70	1	0.9	0.84
3C	10.3	7.4	76.9	10.3	10.3	0.85	1.007	0.80	0.70	2	0.9	0.84
3D	10.3	7.4	76.9	10.3	10.3	0.85	0.95	0.80	0.70	1	0.9	0.84
3E	10.3	9.0	93.0	10.3	10.3	0.825	0.98	0.80	0.70	2	0.9	0.84
3F	10.3	9.0	93.0	10.3	10.3	0.825	0.95	0.80	0.70	1	0.9	0.84
3G	10.3	10.5	108.5	10.3	10.3	0.82	0.95	0.80	0.70	4	0.9	0.84
3H	11.9	8.7	103.1	10.3	13.4	0.82	0.974	0.80	0.70	2	0.9	0.84
3I	14.2	8.7	123.3	13.4	15.0	0.82	0.974	0.80	0.70	1	0.9	0.84
3J	10.3	6.7	68.9	10.3	10.3	0.85	1.01	0.80	0.70	2	0.9	0.84
3K	10.3	8.3	85.2	10.3	10.3	0.825	0.98	0.80	0.70	2	0.9	0.84
3L	10.3	8.3	85.2	10.3	10.3	0.825	0.95	0.80	0.70	2	0.9	0.84
3A2	9.4	8.5	80.0	4.7	14.2	0.825	0.98	0.80	0.70	2	0.9	0.84
3B2	4.7	8.5	39.7	4.7	4.7	0.9	1.08	0.80	0.70	1	0.9	0.84
3C2	4.7	7.4	34.7	4.7	4.7	0.9	1.08	0.80	0.70	2	0.9	0.84
3D2	4.7	7.4	34.7	4.7	4.7	0.9	1	0.80	0.70	1	0.9	0.84
3E2	7.8	9.0	70.5	4.7	11.0	0.85	1.007	0.80	0.70	2	0.9	0.84
3F2	12.6	9.0	113.3	11.0	14.2	0.82	0.974	0.80	0.70	1	0.9	0.84
3H2	3.1	8.7	27.0	1.6	4.7	0.925	1.2	0.80	0.70	2	0.9	0.84
3I2	0.8	8.7	6.7	0.0	1.6	0.925	1.1	0.80	0.70	1	0.9	0.84
3J2	4.7	6.7	31.1	4.7	4.7	0.9	1.08	0.80	0.70	2	0.9	0.84
3K2	4.7	8.3	38.5	4.7	4.7	0.9	1.08	0.80	0.70	2	0.9	0.84
3L2	4.7	8.3	38.5	4.7	4.7	0.9	1.08	0.80	0.70	2	0.9	0.84
4A	8	9.33	74.6	8	8	0.875	1.00	0.80	0.70	4	0.88	0.82
4B	8	9.33	74.6	8	8	0.875	0.95	0.80	0.70	2	0.88	0.82
4C	8	10.2	81.6	8	8	0.875	1.00	0.80	0.70	4	0.88	0.82
4D	8	10.2	81.6	8	8	0.875	0.95	0.80	0.70	6	0.88	0.82
4A2	8	9.33	74.6	8	8	0.875	1.00	0.80	0.70	4	0.88	0.82
4B2	8	9.33	74.6	8	8	0.875	0.95	0.80	0.70	2	0.88	0.82
4C2	8	10.2	81.6	8	8	0.875	1.00	0.80	0.70	4	0.88	0.82
4D2	8	10.2	81.6	8	8	0.875	0.95	0.80	0.70	6	0.88	0.82
5A	8.7	9.0	78.0	8.67	8.67	0.85	1.00	0.80	0.70	4	0.95	0.89
5B	8.7	9.0	78.0	8.67	8.67	0.85	0.95	0.80	0.70	6	0.95	0.89
5C	8.7	9.7	84.2	8.67	8.67	0.85	1.00	0.80	0.70	4	0.95	0.89
5D	8.7	9.7	84.2	8.67	8.67	0.85	0.95	0.80	0.70	10	0.95	0.89
5E	2.3	9.7	22.5	0.00	4.64	0.90	1.10	0.80	0.70	2	0.95	0.89
5F	7.0	9.7	67.6	4.64	9.29	0.85	0.95	0.80	0.70	2	0.95	0.89
5G	11.6	9.7	112.7	9.29	13.93	0.81	0.90	0.80	0.70	2	0.95	0.89
5H	15.1	9.7	146.5	13.93	16.25	0.80	0.88	0.80	0.70	1	0.95	0.89
6A	8	20	160	8	8	0.80	0.90	0.80	0.70	4	0.85	0.79
6B	8	20	160	8	8	0.80	0.90	0.80	0.70	4	0.85	0.79

Appendix E: CLT Design Calculations

This program designs CLT based on the National Design Specification for Wood Construction

Input

Geometry			Cross Section		Roof Data	
Number of Layers	3	12" Strip	Fire	Normal	Number of Spans	2
	Parallel/Perpendicular	Thickness			Span in Direction of Slope	No
Layer #1	Parallel	1.375	1	1	Hor. Proj. Largest Span	19.00 ft
Layer #2	Perpendicular	1.375	2	3	Hor. Proj. Span 2 (double only)	19.00 ft
Layer #3	Parallel	1.375			Slope(in. per ft run)	2.00 in
Layer #4					Member Length Span 1	19.00 ft
Layer #5					Member Length Span 1	19.00 ft
Layer #6					Projection Loads (PSF)	
Layer #7					Self Weight	12.81
Layer #8					Self Weight Override	
Layer #9					Super Imposed Dead	15
Total Thickness	4.125 in				Live, Occupancy	20
Material Properties			Fire Thickness		Roof Live	0
Manufacture or CLT Grade/ Strength Direction	V3 - Major	Layer #1	1.375		Snow	0
		Layer #2	1.375		Adjusted Loads (PSF)	
		Layer #3	1.375		Self Weight	12.8
Modulus of Elasticity	1.4 x 10E6 psi	Layer #4		Super Imposed Dead	15.0	
Modulus of Elasticity, Perp.	1.3 x 10E6 psi	Layer #5		Live, Occupancy	20.0	
F _b	750 psi	Layer #6		Roof Live	0.0	
F _s	55 psi	Layer #7		Snow	0.0	
Specific Gravity	0.55	Layer #8		Wind (positive pressure)	0	
C _M	1.00	Layer #9		Wind (negative pressure)	0	
C _t	1.00			Fire Design Inputs		
				Fire Rating (hr)	0.0 hr	

Output

Section Properties	
GA_{eff}	$0.49 \times 10^6 \text{ lb-in}^2/\text{ft}$
EI_{eff}	$94.74 \times 10^6 \text{ lb-in}^2/\text{ft}$
EI_{app}	$90.86 \times 10^6 \text{ lb-in}^2/\text{ft}$

DOUBLE SPAN				
Strength				LRFD
	Capacity	Applied	Ratio	
Moment (lb-ft/ft)	3012	2950	0.98	
Shear (lb/ft)	3402	776	0.23	
Moment Ratio	98%			
Controlling M Combo #	2			
Controlling Moment Load Combo	1.2D+1.6L + 0.5(Lr or S or R)			
Shear Ratio	23%			
Controlling V Combo #	2			
Controlling Shear Load Combo	1.2D+1.6L + 0.5(Lr or S or R)			

Servicability						
	Limiting Ratio	Limiting Ratio Override	Limit	Actual	Ratio	Percentage
Total	180		1.27	0.824	277	65%
Live Load	240		0.95	0.454	503	48%
Long Term	180		1.27	1.196	191	94%

Vibration			Fire Design	
Span	11.91	ft	EI_{eff}	$94.61 \times 10^6 \text{ lb-in}^2/\text{ft}$
Frequency	14.10	Hz	S_{eff}	32.77 in^3
			n_{lim}	0
			a_{char}	0.00 in
			Max Moment	2149 lbf-ft
			Moment Ratio	0.43
			Max Shear	566 lbf
			Shear Ratio	0.10